

**Institut für Strömungsmechanik
und Elektron. Rechnen im Bauwesen
der Leibniz Universität Hannover**

Bericht Nr. 72/2006

Martin Kohlmeier

**Coupling of thermal, hydraulic and mechanical
processes for geotechnical simulations
of partially saturated porous media**

ISSN 0177 — 9028

Institut für Strömungsmechanik
und Elektronisches Rechnen im Bauwesen
Leibniz Universität Hannover
Appelstraße 9A, D – 30167 Hannover

Tel.: +49 – 511 – 762-3568

Fax.: +49 – 511 – 762-3777

URL: <http://www.hydromech.uni-hannover.de>

Von der Fakultät für Bauingenieurwesen und Geodäsie der Leibniz
Universität Hannover zur Erlangung des Grades Doktor – Ingenieur
genehmigte Dissertation.

Referent: Prof. Dr.-Ing. Werner Zielke

Korreferenten: Prof. Dr.-Ing. Udo Nackenhorst

Prof. Dr. rer. nat. Gerhard Starke

Tag der Promotion: 30. August 2006

Abstract

The description and numerical investigation of multi-phase flow processes in deformable solids of granular or skeletal structure are of great interest for geotechnical engineering. Geothermal applications as well as predictions of long term behavior of barrier systems often require the fully coupled thermal, hydraulic and mechanical modeling.

The subject of this work is the theoretical description as well as the numerical treatment and modeling of thermally affected fluid-solid problems in fully or partially saturated porous media without consideration of phase changes.

An overview of the Theory of Porous Media is given. Based on the geometrically linear theory the required kinematical quantities are derived and the characteristic properties are explicated in the context of the mixture theory. Within this approach the coupled processes are described and presented in form of coupled partial differential equations.

The numerical realization in the framework of the finite element method is explained and presented in detail for selected formulations of coupled problems. The resulting system of partial differential equations is solved by the finite element method. The correctness of the numerical realization of process couplings is proven by appropriate validating examples.

For a complete coverage of the often non-linear behavior of both fluid and solid phase, along with the couplings, an extensive description of the constitutive behavior is necessary. Thus, some selected constitutive models and their algorithmic formulations are presented. The correct implementation is demonstrated as well.

Due to the new requirements, the finite element code RockFlow has been extended in several areas, including linear and non-linear solid mechanics, process couplings and their control as well as the new graphical user interface. Nature and extent of the new developments are explicated and presented in detail.

The applicability of the developed algorithms is demonstrated by several engineering applications. The results are consistent to those of other international research groups working on the extension coupled simulation tools for multi-field problems. This work is a contribution to the continuously covered but still broad field of multidisciplinary modeling and particularly considers the modeling of geotechnical problems.

Keywords: Theory of Porous Media, coupled geotechnical modeling, finite element method.

Zusammenfassung

Die Beschreibung und die numerische Analyse von mehrphasigen Strömungsprozessen in deformierbaren Festkörpern von granularer oder skelettartiger Struktur ist von großem Interesse in der Geotechnik. Geothermische Anwendungen oder Vorhersagen zum Langzeitverhalten von Barriersystemen erfordern oftmals eine vollständig gekoppelte thermische, hydraulische und mechanische Modellierung.

Gegenstand dieser Arbeit ist die theoretische Beschreibung sowie die numerische Behandlung und Modellierung von thermisch beeinflussten gekoppelten Fluid-festkörperproblemen in voll- und teilgesättigten porösen Medien ohne Berücksichtigung von Phasenübergängen.

Es wird zunächst ein Überblick über die Theorie Poröser Medien gegeben. Basierend auf geometrisch linearer Theorie werden die benötigten kinematischen Größen hergeleitet und die notwendigen Kenngrößen im Rahmen der Mischungstheorie erläutert. Darauf aufbauend werden die gekoppelten Prozesse beschrieben und in Form gekoppelter partieller Differentialgleichungen dargestellt.

Ihre numerische Umsetzung im Rahmen der Finite-Elemente-Methode wird erläutert und anhand ausgewählter gekoppelter Problemformulierungen im Detail dargestellt. Das resultierende System von stark oder schwach gekoppelten partiellen Differentialgleichungen wird mit Hilfe der Finite-Elemente-Methode gelöst. Die korrekte numerische Umsetzung der Prozesskopplungen wird anhand geeigneter Validierungsbeispiele belegt.

Zur vollständigen Erfassung des meist nicht-linearen Verhaltens der flüssigen als auch der festen Phase sind neben den Kopplungen umfangreiche Materialbeschreibungen notwendig. Es werden daher ausgewählte konstitutive Modelle dargestellt, deren algorithmische Formulierung erläutert und ihre korrekte Implementierung demonstriert.

Aufgrund der neuen Erfordernisse ist das Finite-Element-Programm RockFlow in zahlreichen Bereichen erweitert worden. Dazu zählen die lineare und nicht-lineare Festkörpermechanik, die neuen Prozesskopplungen und ihre Steuerung sowie die graphische Benutzeroberfläche. Art und Umfang der neuen Erweiterungen werden erläutert und ausführlich dargestellt.

Die Anwendbarkeit der entwickelten Algorithmen wird anhand mehrerer Ingenieursanwendungen demonstriert. Die erzielten Ergebnisse stehen dabei im Einklang mit denen anderer internationaler Forschungsgruppen, die Simulationsprogramme für gekoppelte Mehrfeldprobleme nutzen und weiterentwickeln. Diese Arbeit stellt somit einen Beitrag zum beständig weiter erschlossenen aber noch immer umfangreichen Feld der multidisziplinären Modellierung dar und berücksichtigt dabei insbesondere die Modellierung geotechnischer Probleme

Schlagnworte: Theorie Poröser Medien, gekoppelte geotechnische Modellierung, Finite-Elemente-Methode.

Vorwort

Die vorliegende Arbeit ist während meiner Tätigkeit am Institut für Strömungsmechanik und Elektronisches Rechnen im Bauwesen der Leibniz Universität Hannover in den Jahren 2000–2006 entstanden. In dieser Zeit war ich zunächst im Rahmen eines Stipendiums der Deutschen Forschungsgemeinschaft im Graduiertenkolleg 615 „Interaktion von Modellbildung, Numerik und Software-Konzepten für technisch-wissenschaftliche Problemstellungen“ und im Anschluss als wissenschaftlicher Mitarbeiter tätig. Von besonderer Bedeutung für die Ausrichtung dieser Arbeit war meine Mitwirkung an Forschungsprojekten für die *Bundesanstalt für Geowissenschaften und Rohstoffe* (BGR) in Hannover.



Zunächst möchte ich Herrn Prof. W. Zielke für die fortwährende Unterstützung und für die Übernahme des Referats danken. Des Weiteren danke ich Herrn Prof. G. Starke vom Institut für Mathematik der Leibniz Universität Hannover und Herrn Prof. U. Nackenhorst vom Institut für Baumechanik und Numerische Mechanik der Leibniz Universität Hannover für die Übernahme der Korreferate.

Als großer Vorteil erwies sich die Tatsache, dass ich meine Arbeit auf bereits vorhandenen Entwicklungen der Arbeitsgruppe Grundwassermodellierung, die bis zum Jahr 2001 von Herrn Dr.-Ing. habil. O. Kolditz geleitet wurde, aufbauen konnte. Den bis dahin beteiligten Personen gilt daher mein ganz besonderer Dank, namentlich René Kaiser, Abderrahmane Habbar, Thomas Rother und Olaf Kolditz der mir beim Einstieg in die Thematik immer hilfreich zur Seite stand.

Im Jahr 2000 vergrößerte sich die Gruppe zunächst durch die Mitwirkung von Frau Sylvia Moenickes und später durch die neuen Kollegen Frau Gesa Zieffle und Herrn Jobst Massmann, so dass eine neue Generation der Arbeitsgruppe Geohydrologie und Geotechnik unter der Leitung von Herrn René Kaiser entstand. Sie alle haben in zahlreichen fachlichen Diskussionen immer wieder hilfreiche Anregungen für den Fortschritt meiner Arbeit geliefert. Ihnen gilt mein besonderer Dank.

Zahlreiche Anregungen lieferte auch die enge Zusammenarbeit mit der BGR vertreten durch Herrn H. Shao. Während der Bearbeitung der Forschungsprojekte für die BGR haben die Herrn T. Nowak, J. Hesser und H. Kunz neben dem nötigen Ansporn in Form wissenschaftlicher Zielsetzungen auch viele hilfreiche Hinweise gegeben. Vor allem aber haben sie den notwendigen Bezug zu praktischen Anwendungen geliefert. Dafür danke ich ihnen im besonderen Maße. Im direkten Zusammenhang dazu steht die Mitarbeit in den Projekten *DECOVALEX III* und *DECOVALEX THMC*, die im Rahmen einer internationalen Zusammenarbeit die Erarbeitung neuer Ideen forcierten und die Möglichkeit des vergleichenden Einsatzes der neuen Programmentwicklungen boten. Des Weiteren wurde dadurch der so wichtige wissenschaftliche Austausch auf Workshops ermöglicht und die Teilnahme an weiteren internationalen Kongressen initiiert.

Ohne die Mitwirkung von wissenschaftlichen Hilfskräften wären wohl zahlreiche Kleinigkeiten auf der Strecke geblieben und hätten einige wichtige Dinge nicht vollendet werden können. Für ihr Engagement im Rahmen von Studienarbeiten bzw. für ihren verlässlichen Einsatz als wissenschaftliche Hilfskraft möchte ich daher Gesa Zieffle, Meike Wulkau, Alireza Ahmari, Michael Plotkowiak und Xuan Li besonderen Dank aussprechen.

Mein Dank gilt insbesondere allen Kollegen des Instituts für die gute Zusammenarbeit aber insbesondere auch für das sehr gute Arbeitsklima. Dieser positive Rahmen stellte eine wichtige Grundlage für das Gelingen der Arbeit dar.

Ganz besonders großer Dank gebührt meiner Lebenspartnerin Nicole. Sie hat mich ermuntert, mich unterstützt und das notwendige Verständnis in der Endphase meiner Arbeit aufgebracht.

Hannover, Dezember 2006

Martin Kohlmeier

Contents

Abstract	i
Zusammenfassung	ii
Vorwort	iii
1 Introduction	1
1.1 Motivation	1
1.2 Problem, objectives and approach	1
1.2.1 Problem	1
1.2.2 Objectives	2
1.2.3 Approach	3
1.3 The finite element code RockFlow	5
1.4 Outline	5
2 Theory of Porous Media	7
2.1 Introduction	7
2.2 Overview of the historical development	8
2.3 Kinematics	8
2.3.1 Kinematics of a body	8
2.3.2 Mixtures theory and kinematics of a mixture	10
2.3.3 Concept of volume fractions	11
2.4 Kinematical quantities	14
2.4.1 Velocity and acceleration measures	14
2.4.2 Strain measures	14
2.4.3 Geometric linearization	15
2.4.4 Geometrically linearized measures	15
2.5 Balance equations of general mixtures	15
2.6 Balance equations of deformable porous media	16
2.6.1 Introduction	16
2.6.2 Mechanical equilibrium	17
2.6.3 Hydraulic equilibrium	17
2.6.4 Thermodynamical equilibrium	21
3 Governing equations	23
3.1 Introduction	23
3.2 Saturated flow in poro-thermo-elastic media	23
3.3 Partially saturated flow in poro-thermo-elastic media	24

4	The finite element method	27
4.1	Introduction	27
4.2	Finite element formulation	27
4.2.1	A general initial boundary value problem	28
4.2.2	Weak formulation	28
4.2.3	Spatial discretization	28
4.2.4	Numerical approximation	28
4.2.5	Numerical integration	29
4.2.6	Assembly	29
4.3	Temporal discretization	29
4.3.1	A general initial value problem	30
4.3.2	Numerical approximation of the time derivative	30
4.3.3	Numerical integration in time	31
4.4	Iterative techniques for nonlinear algebraic equations	32
4.4.1	Introduction	32
4.4.2	The Newton-Raphson method	33
4.4.3	Direct (Picard) iteration	34
4.5	Solution procedures for coupled equations	35
4.5.1	Introduction	35
4.5.2	Temporal discretization	36
4.5.3	Incremental formulation	36
4.5.4	Solving of coupled linear equations	36
4.5.5	Solving of coupled non-linear equations	37
4.5.6	Linearization of the residual	38
5	Coupling phenomena and associated numerical aspects	41
5.1	Coupling phenomena	41
5.1.1	Introduction	41
5.1.2	Coupling terms in the balance equations	42
5.1.3	Coupling terms in the constitutive equations	42
5.2	Numerical aspects	43
5.2.1	Formulation and assembly of the algebraic equation	43
5.2.2	Sparse storage scheme	45
5.2.3	Iterative solving of linear systems	45
6	Constitutive modeling	49
6.1	Linear elasticity	49
6.2	Anisotropic elasticity	50
6.2.1	Introduction	50
6.2.2	Notation	51
6.2.3	Transverse isotropy	51
6.2.4	Numerical example	52
6.3	Rate-independent plasticity	55
6.3.1	Governing equations	55
6.3.2	Continuum elasto-plastic tangent	57

6.3.3	Consistent elasto-plastic tangent	58
6.4	Yield criteria for isotropic material	58
6.4.1	Criteria for pressure insensitive material	59
6.4.2	Criteria for pressure sensitive material	59
6.5	Constitutive models with pressure insensitive yield criterion	59
6.5.1	Perfect plasticity – Prandtl-Reuss equation	61
6.5.2	J_2 plasticity with isotropic/kinematic hardening	63
6.6	Constitutive models with pressure sensitive yield criterion	65
6.6.1	Mohr-Coulomb model	65
6.6.2	Drucker-Prager model	66
6.7	Constitutive behavior of the fluid phase	70
6.7.1	Equation of state for water	70
6.7.2	Darcy’s law	70
6.8	Fourier’s law of heat conduction	71
7	Implementation	73
7.1	Introduction	73
7.2	The THM _{plus} model	73
7.2.1	The model-oriented approach	74
7.2.2	Processes in the THM _{plus} model	74
7.3	Created RockFlow objects	74
7.3.1	Control of processes and couplings	74
7.3.2	Finite elements with quadratic shape functions	75
7.3.3	Mesh generation	75
7.3.4	Input data description	75
7.4	Adapted RockFlow objects	77
7.4.1	Solver object for coupled problems	77
7.5	The graphical user interface RF ₊	78
7.5.1	Motivation and approach	78
7.5.2	Structure of the graphical user interface	79
7.5.3	Performance of the graphical user interface	81
8	Verification benchmarks	85
8.1	Mechanical analysis	85
8.1.1	Formulation of the problem	85
8.1.2	Plate with a hole	85
8.2	Thermo-mechanical analysis	90
8.2.1	Formulation of the problem	90
8.2.2	Stress concentrations around cavities in a steady heat flow	90
8.3	Hydraulic-mechanical analysis of saturated porous media	98
8.3.1	Formulation of the problem	98
8.3.2	One-dimensional consolidation of a saturated column	98
8.4	Hydraulic-mechanical analysis of partially saturated porous media	102
8.4.1	Formulation of the problem	102
8.4.2	Liakopoulos experiment	102

8.4.3	Localization analysis in a rigid footing	107
9	Applications	111
9.1	Coupled linear analysis of saturated poroelastic media	111
9.1.1	Poro-elastic consolidation – strip footing	111
9.1.2	Transport in an incompressible hydraulic system	114
9.2	Coupled analysis of thermo-poroelastic media	116
9.2.1	DECOVALEX-III – Task 3	116
9.2.2	Density driven flow in a thermo-poro-elastic medium	120
9.3	Coupled analysis of partially saturated thermoelastic and elasto-plastic media	122
9.3.1	DECOVALEX-THMC – Task D	122
9.3.2	Embankment problem	134
9.3.3	Slope stability problem	137
10	Conclusions and recommendations	141
10.1	Conclusions	141
10.2	Recommendations	142
	Notation	143
	Nomenclature	145
	Bibliography	149
A	Numerical methods and derivations	157
A.1	Convergence of iterative solution procedures	157
A.2	Derivation of finite elements	157
B	Application of the finite element method on a hydraulic-mechanically coupled saturated flow problem	161
B.1	Finite element formulation	161
B.2	Finite element matrices	163
C	Various derivations	165
C.1	Invariants of second order tensors	165
C.2	Thermoelasticity	167
C.3	Parameterization of transverse isotropy	168
	List of figures	172
	List of tables	177

Chapter 1

Introduction

1.1 Motivation

The range of applications of numerical modeling in the field of water resource and waste disposal management is continuously increasing. A security relevant aspect is to satisfy the need to predict environmental impacts which are often affected by a compound of several processes. Additionally, the interaction of these processes might be very complex.

In order to simplify the problem of coupled processes in a correct way, the evaluation of the degree of process interaction is of substantial interest. With this knowledge, either separate analysis of single processes or coupled analysis of only few processes arising in a coupled multi-field problem can successfully deliver equivalent results.

However, in most cases, a reliable analysis can only be achieved if the overall problem is treated with all its complex processes and interactions. Consequently, the analysis of coupled multi-field problems arising in engineering sciences is a challenging application of the finite element method.

1.2 Problem, objectives and approach

1.2.1 Problem

With the use of averaging strategies a deformable porous medium can be described by a continuum approach called *Theory of Porous Media* (TPM). The pores may be occupied by a single fluid (fully saturated single-phase flow) or by multiple fluids (partially saturated multi-phase flow). In both cases the approach results in a coupled formulation. The solving of this multi-field problem requires that both disciplines fluid and solid mechanics are considered.

Some applications comprises geothermal processes. The heat transport processes must be described as a conductive process in the solid and as a conductive/advective process in the liquid phase. Thermal strains have to be taken into account in the solid phase

as well as thermal expansion of the fluid phase. Usually, if the temperature changes are moderate, these processes can be incorporated in an isothermal approach that means that for example the thermal expansion coefficients can be assumed to be temperature independent. An isothermal approach also implies that no phase changes occur.

The fate and the behavior of substances in the environment is of great interest and sophisticated models are available. Physical as well as chemical processes might affect the integrity of *Engineered Barrier Systems* (EBSs). Thus, matter transport is of special interest in *Performance Assessment* (PA) studies. Additional geochemical modeling can improve the predictions of possible impact.

A thermo-hydro-mechanically coupled model has to be set up, also providing matter transport, and giving the opportunity of extensions towards geochemical modeling, in order to achieve an integral simulation tool for geotechnical investigations.

1.2.2 Objectives

The aim of this work is the numerical simulation of *initial boundary value problems* (IBVPs) based on the *Theory of Porous Media* (TPM). Soil mechanical problems are of main interest. Related topics like matter and heat transport in subsurface or engineered barrier systems broaden the range of intended types of applications. The resulting multi-field problem mainly is *thermo-hydro-mechanically* (THM) coupled while the conservative matter transport (C) can be treated as an add on.

Couplings. The realization of process couplings is an essential target of this work. A most natural concept is recommended that automatically activates couplings if the concerning process exists. In order to perform a step-by-step model approach an individual setting of the coupling specification should be provided.

Time scales. In a thermo-hydro-mechanical formulation two time dependent processes (fluid flow and heat transfer) are directly coupled to the quasi static process of structural mechanics. Caused by coupling effects within the multi-field problem its behavior usually differs significantly from that of the containing individual problems. Depending on the material properties, the coupling of two steady state processes can result in a transient multi-field problem (e.g. consolidation).

Non-linearities. The combination of rate-independent plasticity and partially saturated flow in the framework of the TPM has given rise to challenging research in the last decade.

Couplings result in further non-linear effects. Density dependencies can occur in the fluid phase due to dissolved substances or thermal gradients. In partially saturated fluid flow the capillary pressure as well as the relative permeability are usually highly non-linear functions of the saturation.

At high temperatures, moisture transport is an important non-isothermal process in partially saturated media. Here, a non-linear interaction of the temperature field with the pore pressure and saturation field has to be incorporated. Transitions between solid, liquid, and gaseous phases typically involve large amounts of energy compared to the specific heat. A phase change is accompanied by a relatively quick release or demand of energy compared to the specific heat. The latent heat of fusion or the latent heat of vaporization, for example, leads to a highly non-linear process. This work prepares the basis for the implementation of these non-isothermal effects.

Process sensitivities. A sufficient understanding of a system and its main processes is meaningful in many disciplines, especially if long-term processes are involved. The analysis of sensitivities is essential for the assessment of the long-term safety of repositories or underground storage sites. Public waste disposal authorities or *Nuclear Regulatory Commissions* (NRC) require the supply of decision criteria as they have to ensure the long-term safety performance of repositories for high-level radioactive waste. Thus, the classification of processes and couplings according to their importance is a significant result of the application of coupled numerical models to be developed.

Applicability. Coupled process modeling is requested in the international project *DECOVALEX* (acronym for DEvelopment of COupled models and their VALidation against EXperiments in nuclear waste isolation). One of the objectives is to study the influence of process interactions. Therefore, a strategy has to be developed that gives the opportunity to perform a process oriented implementation in combination with a control concept which allows the selective activation of processes. Furthermore, it is useful to consider selectable process couplings in order to accomplish sensitivity analyses.

Data management. The simulation of multi-field problems requires a user-friendly input and output management. A graphical user interface and the graphical visualization of simulation data implicates valuable assistance for both the developers and the users.

1.2.3 Approach

1.2.3.1 Starting point

The numerical algorithms required for the performance of the applications presented in this work have been implemented in the finite element code RockFlow. The basis for the development has been RockFlow 3.8. A historical overview of previous development stages of this code is presented in Sec. 1.3.

The range of applicability of the former version RockFlow 3.8 is single phase as well as multiphase flow in combination to matter or heat transport. Density dependent flow and reactive transport modeling is available as well. Occurring non-linearities are solved in an iterative *Picard* scheme. In this version of RockFlow, the solution of interacting

processes is performed in a *partitioned* approach, accompanied by a limited range of stability.

1.2.3.2 Established development

Single or multiple process strategy. The processes themselves are implemented independently in an object-oriented way and finally arranged in an integrating *model* which provides all the necessary data objects. An essential aspect of this strategy is the fact that the resulting RockFlow *model* is able to solve the coupled problem in a single-process or multiple-process approach. That means that processes as well as their couplings are selectable.

This strategy of object-oriented implementation of all processes is the basis to perform coupled analyses of multi-field problems or separate analyses of single problems. Thus, the significance of different kinds of couplings or dependencies of material properties can be estimated.

Modules and features. The main improvements of the finite element code RockFlow are the finite element set-up for mechanical analysis, its coupling to the heat transport part for thermo-elastic analysis and finally its coupling to fully or partially saturated fluid flow. Some further parts of improvements required for coupled analysis in RockFlow are listed below. They include

- the quadratic element types in two or three dimensions,
- the increase of degrees of freedom per node,
- the incorporation of new coupled finite element formulations and the combination to existing formulations in the framework of a new *model* named THM_{plus} ,
- the control concept for this THM_{plus} model,
- the direct solving strategy of the coupled formulations,
- associated with the required data objects,
- and accompanied by coupled and non-linear material formulations.

Graphical user interface. The achievement of user-friendly finite element software becomes even more important, when more processes come into play. The resulting increase in input data demands for an overall insight into the model's input data and its results. A graphical user interface was set-up in order to meet these demands. With this interface the structure and the definition of the input data is documented and made accessible for any user. The finite element results can be visualized in an controllable simulation sequence.

1.3 The finite element code RockFlow

At the Institute of Fluid Mechanics and Computer Applications in Civil Engineering the development of numerical models for the simulation of fluid flow and solute transport processes in porous and fractured porous media started in the mid eighties. These developments were performed and documented by Wollrath (1990) [107], Kröhn (1991) [60], Helmig (1993) [45], Shao (1994) [92] and Lege (1995) [63]. During this phase the first version of the program system RockFlow appeared in the language Fortran 77. It consisted of independent modules for the numerical analysis of incompressible or compressible flow (SM/GM), solute transport (TM) and density driven flow. Later these modules were combined in a single finite element code and called RockFlow *models*.

In the mid nineties, the need of adaptive algorithms especially for advective transport processes became obvious. Thus, the next meaningful step in the history of RockFlow was the development of an adaptive transport module (aTM) by Schulze-Ruhfus [91] and Barlag [1] in 1997. As a basic system for h -adaptive methods it was the foundation for further developments. Analogously, these developments were the beginning of the transition phase towards new object-oriented programming techniques provided by ANSI-C.

The third step of the RockFlow development was initiated in the late nineties. It took place in alliance with the above mentioned achievements of the development of an adaptive transport module in ANSI-C. Within this phase the former modules were combined in an model-oriented structure. The sub-division of processes finally was the basis of RockFlow Version 3.0. It was developed with the strict usage of dynamic data structures and object-oriented methods, see for example Kolditz et al. (1998) [57].

During this period of RockFlow development coupled models for multiphase and density driven flow and reactive transport modeling were created by Thorenz [101] and Habbar [41], respectively. Both models were embedded in a grid adaptive frame for coupled processes developed by Kaiser [50]. In 2001, these developments led to RockFlow 3.8 which finally marks the starting point of the work at hand.

1.4 Outline

The work at hand is structured as follows:

Chapter 1 *Introduction.* The motivation of processing coupled modeling, the arising objectives and the approach for achieving the aims of the work at hand are given in this chapter.

Chapter 2 *Theory of Porous Media.* The Theory of Porous Media which is the theoretical basis of the formulation of coupled problems in porous media is outlined. After a short historical review, the kinematics of porous media and the resulting conservation equations are presented.

Chapter 3 *Formulations of coupled problems.* The governing equations representing saturated and unsaturated flow processes in porous media are summarized.

Chapter 4 *The finite element method.* This chapter is devoted to the finite element method which is used for the numerical solution. The general approach of a finite element formulation is given. Further aspects on the numerical treatment of coupled transient problems are addressed in detail.

Chapter 5 *Coupling phenomena and associated numerical aspects.* Coupling phenomena arising in geotechnical applications are introduced in this chapter that also gives an insight into the strategy of numerical and computational solution strategies.

Chapter 6 *Constitutive modeling.* The theory of elasticity, elasto-plasticity and unsaturated fluid flow is introduced with special attention to constitutive modeling of geotechnical material and with respect to hydraulic-mechanical coupling.

Chapter 7 *Implementation.* The strategy of implementing coupled process formulations is presented here including the computation methods and software concepts for solving coupled thermo-hydro-mechanical problems and integrating the finite element code into a computational framework for graphical visualization.

Chapter 8 *Verification benchmarks.* Separated into well-defined groups of process interaction verification benchmarks and corresponding analytical solutions are presented.

Chapter 9 *Applications.* Different applications of particular scientific and engineering aspects are reflecting the applicability of the numerical implementation.

Chapter 10 *Conclusions and recommendations.* The final chapter discusses the contributed achievements and sketches perspectives of future research activities.

Chapter 2

Theory of Porous Media

The most incomprehensible thing about the world is that it is comprehensible.

Albert Einstein (1879 - 1955).

2.1 Introduction

Geomaterials like soils or rocks as well as artificial material like concrete or buffer materials for technical applications consist of granular and brittle materials. They have a porous skeleton. The pores are filled by a single or by multiple fluids. The behavior of the aggregate body is defined by the properties of its solid and fluid constituents. The structure of both the solid skeleton and the boundary layers of the fluids is usually not known. Thus, an averaging process is necessary to build up a continuum model. A macroscopic approach is the *Theory of Porous Media* (TPM) based on the classical mixture theory of superposed continua. The microscopic composition of the mixture is described by a structural quantity, the volume fraction.

In this work a geometrically linear three-phasic formulation of a deformable porous medium is derived. The governing equations of the resulting hydraulic-mechanically coupled problem are summarized in Chapter 3. The used multi-phase flow formulation is an approximation which assumes that the gaseous phase remains at atmospheric pressure. The transport of heat or solute matter are incorporated in the formulation but not addressed in detail. Thermal effects are restricted to the isothermal case. In the presented formulation non-linear behavior of solid and liquid phase are considered. Linear or non-linear processes can be coupled by linear or non-linear couplings. (see Chapter 5).

2.2 Overview of the historical development

First important developments of the Theory of Porous Media became manifest in the 1930s by Fillunger and Terzaghi. Their work was concerned with uplift, friction, capillarity and effective stress. Thereby they introduced the concept of volume fraction in a framework of a liquid-saturated rigid porous solid. The first ideas of effective stress go back to Terzaghi who finally stated a mathematical formulation of the consolidation process [99, 100]. Fundamental equations of the porous media theory were developed by Fillunger in 1936 who introduced a two-phase formulation consisting of a pore-water moving in a deformable porous skeleton of soil (see [38]).

The theory of consolidation developed by Terzaghi was generalized and extended to the three-dimensional case by Biot [6]. He also investigated elastic waves in poroelastic media [7, 8]. In 1957, Biot and Willis [9] determined and interpreted the elastic coefficients, for example the coefficient describing the interaction of fluid pressure and volumetric strain of the porous medium.

The modern Theory of Porous Media was founded by Bowen in the 1980s. He derived a two-phase model with incompressible and compressible constituents, respectively (see [14, 15]). Formulations of a modern treatment of the TPM are given by de Boer and Ehlers [24], Ehlers [31] or Ehlers and Bluhm [34]. For the historical development of fluid-saturated porous media the reader should refer to de Boer [23].

In the development of the recent years the theory of porous media has been extended to dynamically deforming as well as to thermally influenced porous solids, see for example Schrefler and Scotta [88] or Lewis and Schrefler [64].

The existence of heat in multi-phase flow processes causes the transfer of energy between the fluid phases. In case of high temperatures non-isothermal approaches are necessary. In 2002, Class et al. [21, 20] present numerical simulations of non-isothermal multi-phase flow in rigid porous media.

2.3 Kinematics

2.3.1 Kinematics of a body

Definition 2.1. Reference and current configuration. Let $\Omega_R \subset \mathbb{R}^{n_{\text{dim}}}$ be the reference configuration of the material body \mathcal{B} , where n_{dim} is the space dimension. The domain is bounded by a smooth boundary $\partial\Omega_R$.

Definition 2.2. Material and spatial coordinates. Each material point $\mathcal{P} \in \mathcal{B}$ has a reference and current localization, P_R and P , respectively. According to these representations *material* coordinates \mathbf{X} and *spatial* coordinates \mathbf{x} are introduced as shown in Fig. 2.1.

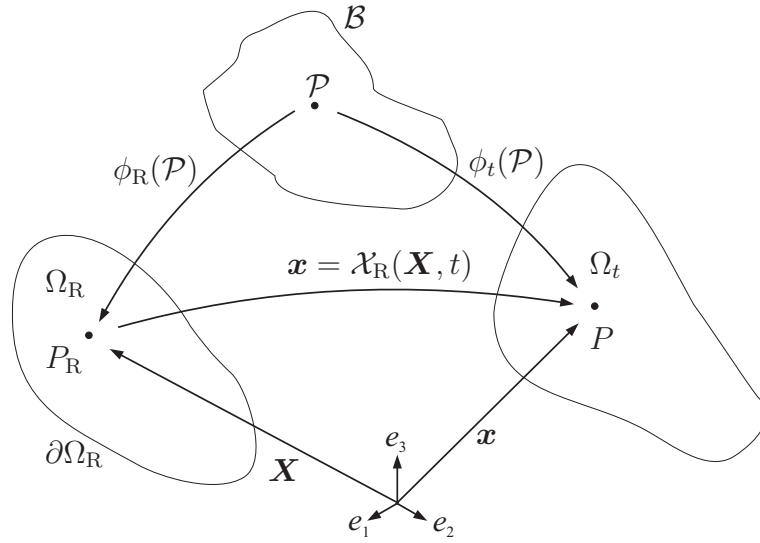


Figure 2.1: Motion of a material body in a Euclidian space, represented in relative to a frame of reference.

Definition 2.3. Motion of a material point. Let $[0, T] \subset \mathbb{R}_+$ be the time interval of interest. Then the motion of a material point \mathcal{P} at current time t is described by its spatial coordinates \mathbf{x} in the current configuration. The motion is as follows

$$\mathbf{x} = \mathcal{X}_R(\mathbf{X}, t) = \phi_t(\phi_R^{-1}(\mathcal{P})(\mathbf{X})). \quad (2.1)$$

Definition 2.4. Reference configuration at initial time. Since the choice of the reference configuration is arbitrary, the configuration at a fixed time t_0 is chosen to be the reference configuration with $\Omega_0 = \phi_0[\mathcal{B}]$ according to Fig. 2.2. Thus the material and spatial coordinates can be expressed by

$$\mathbf{X} = \phi_0(\mathcal{P}) \Leftrightarrow \mathcal{P} = \phi_0^{-1}(\mathbf{X}) \quad (2.2)$$

and

$$\mathbf{x} = \mathcal{X}_0(\mathbf{X}, t). \quad (2.3)$$

Definition 2.5. Displacement vector. The *displacements* of particles are described by a vector field

$$\mathbf{u} : \Omega_0 \times [0, T] \rightarrow \mathbb{R}^{\text{ndim}}. \quad (2.4)$$

with a reference position $\mathbf{X} \in \Omega_0$ at time t_0 . Then, the displacement vector is defined to be $\mathbf{u}(\mathbf{X}, t)$ the difference between the current and the reference position vector

$$\mathbf{u}(\mathbf{X}, t) = \mathbf{x} - \mathbf{X} = \mathcal{X}_0(\mathbf{X}, t) - \mathbf{X}. \quad (2.5)$$

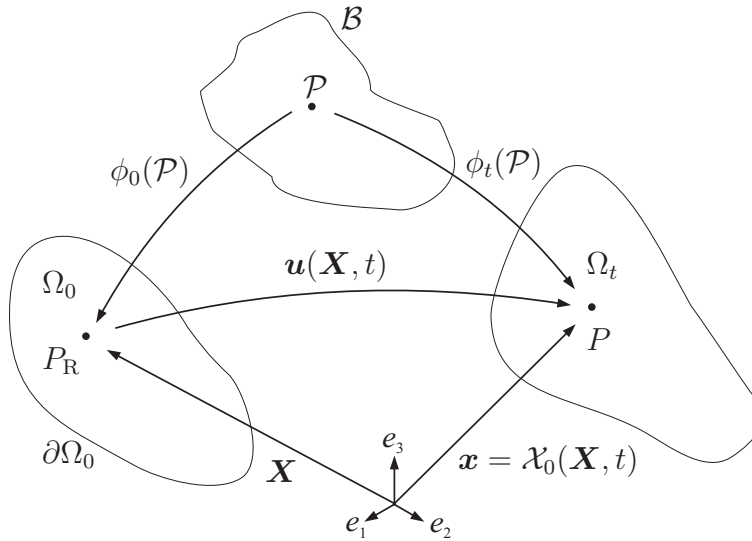


Figure 2.2: Motion of a material body in a Euclidian space, represented in relative to the configuration at time t_0 as a chosen frame of reference.

2.3.2 Mixtures theory and kinematics of a mixture

2.3.2.1 Mixture theory

Mixtures of a given amount of immiscible substances can be described by the mixture theory (see [104, 103, 75, 13]). Within this macroscopic description it is assumed that the constituent of the mixture are not located in microscopic subareas but exist simultaneously within the considered domain. Thus, a homogenization or an averaging process is needed to transform the microscopic structure to a macroscopic representation, see Fig. 2.3 or refer to [42, 43, 81].

Definition 2.6. A mixture or multi-phase continuum φ is a compound of several partial continua, named constituents φ^α . The terms constituent and phase are used synonymously.

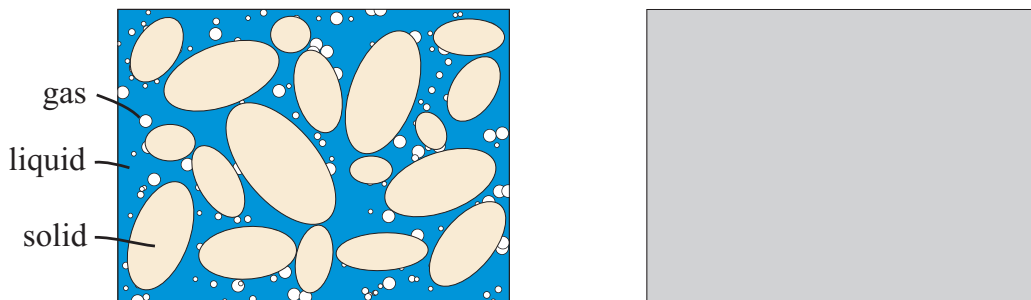


Figure 2.3: Real geometric structure of the representative element volume (REV) (left) and its smeared representation of a porous medium (right).

The resulting quantities of a macroscopic representation may be used to describe the physical process within the scale of the representative elementary volume (REV) suitable for the system. The REV is the smallest area the macroscopic theory is capable for. Within larger scales heterogeneities have to be quantified by the discretization of their material boundaries or upscaling strategies have to be applied (see e.g. [17]).

2.3.2.2 Kinematics of a mixture

Definition 2.7. Partial bodies. In the mixture theory the mixture is treated as a superposition of *partial bodies* \mathcal{B}^α .

The *reference* and *current* configuration of partial bodies \mathcal{B}^α can be defined according to Def. 2.1.

Material and spatial coordinates are defined for the partial bodies (see Def. 2.2) and finally the displacement vector of a phase is defined in Def. 2.8 as follows.

Definition 2.8. Displacement vector of a phase. The *displacements* of particles of phase φ^α are described by a vector field

$$\mathbf{u}^\alpha : \Omega_0 \times [0, T] \rightarrow \mathbb{R}^{\text{n dim}}. \quad (2.6)$$

with a reference position $\mathbf{X}^\alpha \in \Omega_0$ at initial time t_0 . Then the displacement vector $\mathbf{u}(\mathbf{X}^\alpha, t)$ is the difference between the current and the reference position vector

$$\mathbf{u}^\alpha(\mathbf{X}^\alpha, t) = \mathbf{x}^\alpha - \mathbf{X}^\alpha \quad (2.7)$$

$$= \mathcal{X}_R^\alpha(\mathbf{X}^\alpha, t) - \mathbf{X}^\alpha \quad (2.8)$$

$$= \mathcal{X}_0^\alpha(\mathbf{X}^\alpha, t) - \mathbf{X}^\alpha. \quad (2.9)$$

In the mixture theory approach it is presupposed that all phases are present and identifiable any time. Thus, a total phase change due to temperature or chemical reactions is not possible.

2.3.3 Concept of volume fractions

The mixture theory is not able to describe the internal structure of a mixture. Therefore, the theory of porous media makes use of the volume fraction whenever a structural quantity is needed in the formulation.

The resulting volumetric homogenization process for a granular material consisting of two fluid phases (gaseous and liquid) is depicted in Fig. 2.4. It is assumed that the representative element volume of the porous solid describes a control space. Only the liquids or gases filling the pores can leave this control space. Within the control space all phases and the pores, respectively, are assumed to be statistically distributed.

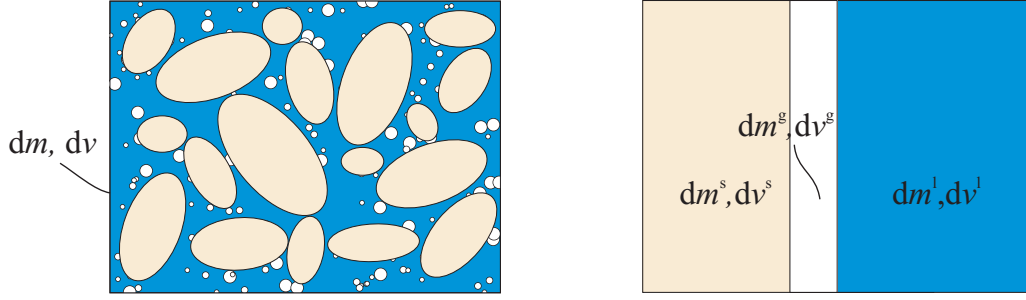


Figure 2.4: The concept of volume fraction. Schematic representation of the real REV (left) with a total volume of dv and the porous medium (right) described by its partial volumes.

Definition 2.9. Volume fraction. The volume fraction is a scalar field $n^\alpha : \Omega_t \rightarrow \mathbb{R}$ which assigns each spatial point $\mathbf{x} \in \Omega_t$ of the current configuration to the local volume fraction of the phase φ^α as a portion of the total volume as follows

$$n^\alpha = \frac{dv^\alpha}{dv}. \quad (2.10)$$

Thus, the partial volume V^α of the phase φ^α is defined by

$$V^\alpha = \int_{\Omega_t} n^\alpha(\mathbf{x}) dv. \quad (2.11)$$

It is supposed that the pores are completely filled by the constituent. Therefore, as the total volume V is the sum of the partial volumes V^α the sum of the volume fractions n^α is

$$\sum_{\alpha} n^\alpha = 1. \quad (2.12)$$

Definition 2.10. Saturation. The saturation of a fluid constituent is the local volume fraction of the fluid phase φ^{α_f} as a portion of the total *fluid* volume dv^f . Thus it is defined as follows

$$S^{\alpha_f} = \frac{dv^{\alpha_f}}{dv^f} \quad \alpha_f = \{l, g\} \quad (2.13)$$

where the total volume of the fluid phases dv^f is equal to the pore space.

Definition 2.11. Porosity. The porosity n is the proportion of the non-solid volume to the total volume. As the non-solid volume equals the fluid volume the porosity is defined by the sum of the volume fractions of the fluid phases φ^{α_f}

$$n = \frac{dv^f}{dv} \quad \alpha_f = \{l, g\} \quad (2.14)$$

$$= \sum_{\alpha_f} n^{\alpha_f} \quad (2.15)$$

$$= n^l + n^g. \quad (2.16)$$

Equivalently, the porosity can be defined by the solid fraction n^s as follows

$$n = 1 - n^s. \quad (2.17)$$

Definition 2.12. Partial density. The *partial density* $\rho_{\text{partial}}^\alpha$ of a phase is the local mass of the phase φ^α as a portion of the total volume dv , thus it is defined by

$$\rho_{\text{partial}}^\alpha = \frac{dm^\alpha}{dv}. \quad (2.18)$$

The partial density of the solid phase ρ_{partial}^s is the bulk density which is the mass of the dry particles divided by the total volume. For the formulation of equations of state it is more appropriate to use the real density and the saturation of a phase defined below.

Definition 2.13. Material density. The *material density* (real density) or simply the density ρ^α of a phase is the local mass of the phase φ^α as a portion of the partial volume dv^α , thus it is defined by

$$\rho^\alpha = \frac{dm^\alpha}{dv^\alpha}. \quad (2.19)$$

The material density of the solid ρ^s is equal to the particle density which is the mass of the solid particles divided by its volume. In this work usually the material density is used instead of the partial density. The *partial density* and the *material density* are related as follows

$$\rho_{\text{partial}}^\alpha = n^\alpha \rho^\alpha. \quad (2.20)$$

Definition 2.14. Mixture density. The *mixture density* ρ is the sum of the *partial densities* defined by

$$\rho = \sum_{\alpha} \rho_{\text{partial}}^\alpha, \quad \alpha_f = \{l, g\}. \quad (2.21)$$

Usually the effective densities and the fluid saturation are used to evaluate the *mixture density*. According to Eq. (2.13) and (2.14) the fluid volume fraction is $n^{\alpha_f} = n S^{\alpha_f}$.

Using the definition of porosity (2.17) and Eq. (2.20) for deriving the partial density of the solid the density of the mixture results in

$$\rho = (1 - n) \rho^s + n \sum_{\alpha_f} S^{\alpha_f} \rho^{\alpha_f}. \quad (2.22)$$

2.4 Kinematical quantities

2.4.1 Velocity and acceleration measures

Definition 2.15. Velocity of a phase. The velocity \mathbf{v}^α of a phase is defined as follows

$$\mathbf{v}^\alpha(\mathbf{X}, t) = \frac{d\mathcal{X}_R^\alpha(\mathbf{X}^\alpha, t)}{dt}. \quad (2.23)$$

Definition 2.16. Acceleration of a phase. The acceleration \mathbf{a}^α of a phase is defined as follows

$$\mathbf{a}^\alpha(\mathbf{X}, t) = \frac{d^2\mathcal{X}_R^\alpha(\mathbf{X}^\alpha, t)}{dt^2} \quad (2.24)$$

$$= \dot{\mathbf{v}}^\alpha(\mathbf{X}, t) \quad (2.25)$$

$$= \frac{\partial \mathbf{v}^\alpha(\mathbf{X}, t)}{\partial t} + [\text{grad } \mathbf{v}^\alpha(\mathbf{X}, t)] \cdot \mathbf{v}^\alpha(\mathbf{X}, t) \quad (2.26)$$

Definition 2.17. Relative velocity of a fluid phase. The relative velocity $\mathbf{v}^{\alpha_{fs}}$ of a fluid phase φ^{α_f} is defined with respect to the motion of the solid phase φ^s

$$\mathbf{v}^{\alpha_{fs}} = \mathbf{v}^{\alpha_f} - \mathbf{v}^s. \quad (2.27)$$

Definition 2.18. Relative acceleration of a fluid phase. The relative acceleration $\mathbf{a}^{\alpha_{fs}}$ of a fluid phase φ^{α_f} is defined with respect to the motion of the solid phase φ^s

$$\mathbf{a}^{\alpha_{fs}} = \mathbf{a}^{\alpha_f} - \mathbf{a}^s. \quad (2.28)$$

The acceleration of a fluid phase \mathbf{a}^{α_f} can be formulated in terms moving with the solid phase φ^s . Then the time derivative moving with the solid phase d^s/dt has to be taken. It follows

$$\begin{aligned} \mathbf{a}^{\alpha_f} &= \frac{d^s}{dt}(\mathbf{v}^s + \mathbf{v}^{\alpha_{fs}}) \\ &= \mathbf{a}^s + \mathbf{a}^{\alpha_{fs}} + [\text{grad } \mathbf{v}^{\alpha_f}] \cdot \mathbf{v}^{\alpha_{fs}}. \end{aligned} \quad (2.29)$$

2.4.2 Strain measures

Definition 2.19. The material gradient of motion

$$\mathbf{F}(\mathbf{X}, t) = \text{Grad } \mathcal{X}_R(\mathbf{X}, t) \quad (2.30)$$

is referred to as the deformation gradient.

Definition 2.20. The material gradient of the displacement vector is defined by

$$\mathbf{H}(\mathbf{X}, t) = \text{Grad } \mathbf{u}^s(\mathbf{X}, t). \quad (2.31)$$

2.4.3 Geometric linearization

Definition 2.21. The motion of a body is described by *small deformations* if

$$\delta = \|\mathbf{H}\| \ll 1 \quad (2.32)$$

throughout the motion as well as

$$|\mathbf{u}^s(\mathbf{X}, t)| \ll L, \quad (2.33)$$

where L is a characteristic length of the body under observation.

If the assumption of small deformations is valid, then all kinematic quantities expressed in terms of the displacement gradient \mathbf{H} can be linearized with regard to \mathbf{H} . This process is called *geometric linearization*. For more details refer to Haupt (2000) [44].

In case of small deformations the current configuration is close to the reference configuration. Thus, the difference between the material and the spatial representation is negligible, $\mathbf{u}^s(\mathbf{X}, t) = \mathbf{u}^s(\mathbf{x}, t)$, and

$$\mathbf{H} = \text{Grad } \mathbf{u}^s(\mathbf{X}, t) = \text{grad } \mathbf{u}^s(\mathbf{x}, t) + \mathbf{O}(\delta^2). \quad (2.34)$$

2.4.4 Geometrically linearized measures

Definition 2.22. The tensor

$$\boldsymbol{\varepsilon} = \frac{1}{2}(\mathbf{H} + \mathbf{H}^\top) \quad (2.35)$$

is called *linearized strain tensor*.

According to Eq. (2.34), the linearized strain tensor is

$$\boldsymbol{\varepsilon} = \frac{1}{2}(\text{grad } \mathbf{u}^s(\mathbf{x}, t) + \text{grad } \mathbf{u}^s(\mathbf{x}, t)^\top) + \mathbf{O}(\delta^2). \quad (2.36)$$

2.5 Balance equations of general mixtures

The formulation of balance equations is based on the *3 metaphysical principles* proposed by Truesdell (1984) [103]:

1. *All properties of the mixture must be mathematical consequences of properties of the constituents.*

2. So as to describe the motion of a constituent, we may in imagination isolate it from the rest of the mixture, provided we allow properly for the actions of the other constituents upon it.
3. The motion of the mixture is governed by the same equations as is a single body.

According to the above principles the global balance equation of conserved quantity Ψ in a mixture φ can be derived by

$$\frac{d}{dt} \int_{\mathcal{B}} \Psi \, dv = \int_{\partial \mathcal{B}} \boldsymbol{\phi} \cdot \mathbf{n} \, da + \int_{\mathcal{B}} \sigma \, dv + \int_{\mathcal{B}} \hat{\Psi} \, dv \quad (2.37)$$

where \mathbf{n} is the outward normal, $\boldsymbol{\phi} \cdot \mathbf{n}$ is the outward flux vector associated with Ψ , σ is the external supply of Ψ and $\hat{\Psi}$ is the net production of Ψ .

Applying the *Gauss* theorem on the surface integral results in the local form of the balance equation of the mixture

$$\dot{\Psi} + \Psi \nabla \cdot \dot{\mathbf{x}} = \nabla \cdot \boldsymbol{\phi} + \sigma + \hat{\Psi}. \quad (2.38)$$

According to *Truesdell's* principles the local conservation of a constituent φ^α is described analogously to Eq. (2.38) by

$$\dot{\Psi}^\alpha + \Psi^\alpha \nabla \cdot \dot{\mathbf{x}}_\alpha = \nabla \cdot \boldsymbol{\phi}^\alpha + \sigma^\alpha + \hat{\Psi}^\alpha. \quad (2.39)$$

An important aspect is that the conservation of a quantity in the mixture and its conservation within a single phase are not independent. In fact, the sum of each single term of the phase balance equation over all constituent has to result in the respective term in the conservation equation of the mixture. *Remark:* The before mentioned summation is valid only if the relative velocity of the phase φ^α with respect to the mixture φ is equal zero.

2.6 Balance equations of deformable porous media

2.6.1 Introduction

In the present section the balance equations of the thermo-hydro-mechanical formulations of saturated and partially saturated porous media are summarized. We are starting with a general approach consisting of the three phases, the solid, the liquid and the gaseous phase, referred to as φ^s , φ^l and φ^g , respectively. For more details see Lewis and Schrefler (1998) [64]. As mentioned in the previous section the conservation of a quantity can be formulated with respect to a single constituent or with respect to the mixture.

2.6.2 Mechanical equilibrium

2.6.2.1 Balance of mass

The macroscopic mass balance equation for the solid phase divided by the solid density ρ^s is as follows

$$\frac{(1-n)}{\rho^s} \frac{\partial \rho^s}{\partial t} - \frac{\partial n}{\partial t} + (1-n) \nabla \cdot \frac{\partial \mathbf{u}}{\partial t} = 0. \quad (2.40)$$

2.6.2.2 Balance of linear momentum

The conservation of linear momentum of the solid phase leads to the following equation

$$\nabla \cdot (\boldsymbol{\sigma} - \alpha p \mathbf{1}) + \rho \mathbf{g} = \mathbf{0}, \quad (2.41)$$

where $\boldsymbol{\sigma}$ and p are the effective stress of the solid skeleton and the excess pore pressure, respectively. The density of the mixture is denoted by ρ , \mathbf{g} is the gravity vector and α is the *Biot* coefficient defined by Eq. (2.47). In the following the two terms ρ and p are defined separately for saturated and unsaturated media.

I. Saturated medium. In case of a fully saturated medium the density of the fluid-solid mixture ρ_b is

$$\rho = (1-n) \rho^s + n \rho^l \quad (2.42)$$

and the excess pore pressure p is the fluid pressure p^f .

II. Unsaturated medium. In case of a partially saturated medium the density of the liquid-gas-solid mixture ρ is

$$\rho = (1-n) \rho^s + n S^l \rho^l + n S^g \rho^g \quad (2.43)$$

and the excess pore pressure p is defined to be the sum of the partial pressure of the liquid and the gaseous phase

$$p = S^l p^l + S^g p^g. \quad (2.44)$$

2.6.3 Hydraulic equilibrium

2.6.3.1 Balance of mass

I. Saturated flow. The hydraulic balance equation is based on the conservation of fluid mass. A volumetric formulation is derived by the division of the mass balance equation by the fluid density. The consideration of thermal expansion effects results in the following equation

$$\nabla \cdot \underbrace{(n \mathbf{v}^{ls})}_{\mathbf{q}} + S \frac{\partial p^l}{\partial t} - n \beta_T^l \frac{\partial T}{\partial t} - \beta_T^s (\alpha - n) \frac{\partial T}{\partial t} + \alpha \nabla \cdot \frac{\partial \mathbf{u}}{\partial t} = 0 \quad (2.45)$$

where S is the storativity term for a fluid saturated porous medium defined below. The volumetric thermal expansion of the fluid and the solid are defined by the coefficients β_T^1 and β_T^s .

Due to the fluid-solid coupling the storativity S depends not only on the compressibility of the fluid (K^f - bulk modulus of the fluid) but also on the relation between the compressive behavior of the solid skeleton (K_s - bulk modulus of the solid skeleton) and the solid grains (K_T - bulk modulus of the solid grains). The storativity is as follows ([64])

$$S = \frac{1}{K^f} + \frac{\alpha - n}{K_s}, \quad (2.46)$$

where α is the *Biot* coefficient defined by

$$\alpha = 1 - \frac{K_T}{K_s}. \quad (2.47)$$

By applying the *Biot* coefficient, the influence of compressible solid grains is incorporated into the formulation in which the bulk modulus of the solid skeleton only represents the averaged value compressibility. The assumption of incompressible grains results in a Biot coefficient of $\alpha = 1$.

The thermal expansion of the fluid is regarded in the second term of Eq. (2.45). Thermal strains on the small scale of the solid grains are not regarded in the overall parameter of thermal expansion of the solid skeleton. The thermal expansion of the solid grains has to be considered separately applying the third term of Eq. (2.45).

The most significant coupling term arises from the fluid-solid interaction, namely the volumetric strain rate of the solid. The effect of internal compressibility is again incorporated by the consideration of the Biot coefficient α .

II-a. Multiphase flow. For the sake of completeness, the formulation of multiphase flow in deformable porous media is outlined. In multiphase flow application the sources and sinks appearing in the interior of the domain may be of special interest. They are incorporated in terms of net production Q^α for each phase φ^α . The derivation of the general mass balance equation for the fluid phase in a rigid skeleton is given by Bear and Bachmat (1990) [4] as follows

$$\frac{\partial}{\partial t}(nS^\alpha \rho^\alpha) + \nabla \cdot (nS^\alpha \rho^\alpha \mathbf{v}^\alpha) - Q_{\rho^\alpha} = 0, \quad \alpha = 1, g. \quad (2.48)$$

Considering a deformable porous medium the following volumetric form of the fluid mass balance equation is obtained

$$\begin{aligned} S^\alpha \frac{\partial n}{\partial t} + \frac{nS^\alpha}{\rho^\alpha} \frac{\partial \rho^\alpha}{\partial t} + n \frac{\partial S^\alpha}{\partial t} + \frac{1}{\rho^\alpha} \nabla \cdot \underbrace{(nS^\alpha \rho^\alpha \mathbf{v}^{\alpha s})}_{\mathbf{J}^{\alpha s}} \\ + nS^\alpha \nabla \cdot \frac{\partial \mathbf{u}}{\partial t} - \frac{1}{\rho^\alpha} Q_{\rho^\alpha} = 0, \quad \alpha = 1, g. \end{aligned} \quad (2.49)$$

Using Eq. 2.40 eliminates the porosity derivative $\partial n/\partial t$ and the following balance equation is derived

$$S^\alpha \frac{(1-n)}{\rho^s} \frac{\partial \rho^s}{\partial t} + \frac{nS^\alpha}{\rho^\alpha} \frac{\partial \rho^\alpha}{\partial t} + n \frac{\partial S^\alpha}{\partial t} + \frac{1}{\rho^\alpha} \nabla \cdot \mathbf{J}^{\alpha s} + S^\alpha \nabla \cdot \frac{\partial \mathbf{u}}{\partial t} - \frac{1}{\rho^\alpha} Q_{\rho^\alpha} = 0, \quad \alpha = 1, g. \quad (2.50)$$

In the next steps the treatment of the density derivatives is considered. The material derivative of the of the solid density $\partial \rho^s/\partial t$ in Eq. (2.50) is replaced by the following term ([64])

$$\frac{1}{\rho^s} \frac{\partial \rho^s}{\partial t} = \frac{1}{1-n} \left[\frac{\alpha-n}{K_s} \frac{\partial}{\partial t} (S^g p^g + S^l p^l) - \beta_T^s (\alpha-n) \frac{\partial T}{\partial t} - (1-\alpha) \nabla \cdot \frac{\partial \mathbf{u}}{\partial t} \right] \quad (2.51)$$

The derivatives of the liquid and the gaseous density are derived from the equations of state which are linear or non-linear functions of the fluid pressure p^α and the temperature T , respectively.

Further constraints are necessary to reduce the number of unknown quantities in Eq. (2.50).

1. The time derivatives of the saturation can be reformulated by applying

$$\frac{\partial S^g}{\partial t} = - \frac{\partial S^l}{\partial t} \quad (2.52)$$

which is directly derived from the requirement that the sum of the saturations equal unity $S^g + S^l = 1$.

2. The capillary pressure p_c is defined as the pressure difference of the gas phase and the liquid phase

$$p_c = p^g - p^l. \quad (2.53)$$

The capillary pressure p_c is a non-linear function of the liquid saturation S^l .

Using the above mentioned constitutive equations and constraints Eq. (2.50) can be reformulated into two separate equations each consisting of a single primary variable. The *pressure-saturation* formulation for multiphase flow is robust and widely used [101].

II-b. Multiphase flow – one-phase formulation. The formulation of the mass balance equation presented here is based on the assumption of an unsaturated medium in which the gaseous phase flows without resistance and thus, remains at atmospheric pressure. This pressure is chosen to be the reference pressure with $p^g = 0$. In the unsaturated zones the liquid pressure p^l is negative while a positive pressure indicates saturated zones.

The mass balance equation of the liquid phase can be formulated using Eq. (2.50) but neglecting the gas phase. Inserting the density derivative of the solid given in Eq. (2.51) yields

$$\begin{aligned} S^l \frac{\alpha - n}{K_s} \frac{\partial(S^l p^l)}{\partial t} - S^l \beta_T^s (\alpha - n) \frac{\partial T}{\partial t} + \frac{n S^l}{\rho^l} \frac{\partial \rho^l}{\partial t} + n \frac{\partial S^l}{\partial t} \\ + \frac{1}{\rho^l} \nabla \cdot \mathbf{J}^{ls} + S^l \alpha \nabla \cdot \frac{\partial \mathbf{u}}{\partial t} - \frac{1}{\rho^l} Q_{\rho^l} = 0. \end{aligned} \quad (2.54)$$

The time derivative of the density is replaced using the equation of state of the liquid phase given by

$$\frac{1}{\rho^l} \frac{\partial \rho^l}{\partial t} = \frac{1}{K^l} \frac{\partial p}{\partial t} - \beta_T^l \frac{\partial T}{\partial t}, \quad (2.55)$$

thus it yields

$$\begin{aligned} \left(S^{l^2} \frac{\alpha - n}{K_s} + n S^l \frac{1}{K^l} \right) \frac{\partial p^l}{\partial t} + \left(\frac{\alpha - n}{K_s} p^l S^l + n \right) \frac{\partial S^l}{\partial t} \\ - (S^l \beta_T^s (\alpha - n) + n S^l \beta_T^l) \frac{\partial T}{\partial t} \\ + \frac{1}{\rho^l} \nabla \cdot \mathbf{J}^{ls} + S^l \alpha \nabla \cdot \frac{\partial \mathbf{u}}{\partial t} - \frac{1}{\rho^l} Q_{\rho^l} = 0. \end{aligned} \quad (2.56)$$

2.6.3.2 Balance of linear momentum

Balance equations of linear momentum are formulated for the gaseous and the liquid phase as follows

$$n^\alpha \rho^\alpha \mathbf{a}^\alpha - \nabla \cdot (n^\alpha p^\alpha \mathbf{1}) + n^\alpha \rho^\alpha \mathbf{g} - n^\alpha \mathbf{R}^\alpha \mathbf{v}^{\alpha s} = 0. \quad (2.57)$$

The transformation using Eq. (2.29) for the fluid acceleration and the application of the vector identity for the divergence of the stress in the fluid phase yields

$$n^\alpha \mathbf{v}^{\alpha s} = n^\alpha (\mathbf{R})^{-1} (-\nabla p^\alpha + \rho^\alpha (\mathbf{g} - \mathbf{a}^s - \mathbf{a}^{\alpha s})). \quad (2.58)$$

The permeability \mathbf{k} and the relative permeability factor k_{rel}^α are introduced as follows

$$n^\alpha (\mathbf{R})^{-1} = \frac{\mathbf{k} k_{\text{rel}}^\alpha}{\mu^\alpha} \quad (2.59)$$

where μ^α is the viscosity of the fluid phase. Neglecting the solid acceleration \mathbf{a}^s and the relative acceleration of the fluid $\mathbf{a}^{\alpha s}$ finally yields the modified *Darcy's law*

$$n^\alpha \mathbf{v}^{\alpha s} = \frac{\mathbf{k} k_{\text{rel}}^\alpha}{\mu^\alpha} (-\nabla p^\alpha + \rho^\alpha \mathbf{g}). \quad (2.60)$$

The above mentioned derivation of the modified *Darcy's law* from the momentum balance equation is described in detail by Bear and Bachmat (1990) [4] and Lewis and Schrefler (1998) [64].

Remark: *Darcy's law* is an equation describing the motion of the fluid occupying the void space. As mentioned above, its derivation implies several assumptions. Its application for the unsaturated case requires the specification of an additional soil water retention curve for example the popular van Genuchten function ([106]). This unsaturated soil hydraulic conductivity is a non-linear empirical function of the saturation. In view of these facts, the modified *Darcy law* as well as its linear form will be referred to as a constitutive equation defining the flux term in the fluid mass balance equation.

2.6.4 Thermodynamical equilibrium

I. Saturated flow. The conservation of heat energy in a fully saturated porous medium is described by the following balance equation

$$((1 - n) c^s \rho^s + n c^l \rho^l) \frac{\partial T}{\partial t} + \nabla \cdot \mathbf{J}_t + c^l \rho^l \mathbf{q}^{ls} \cdot \nabla T = 0. \quad (2.61)$$

where \mathbf{J}_t is the conductive heat flux defined by *Fourier's law* in Sec. 6.8.

II. Multiphase flow. In case of multiphase flow, the balance equation of heat energy reads as follows

$$((1 - n) c^s \rho^s + n (S^l c^l \rho^l + S^g c^g \rho^g)) \frac{\partial T}{\partial t} + \nabla \cdot \mathbf{J}_t + (c^g \mathbf{J}^{gs} + c^l \mathbf{J}^{ls}) \cdot \nabla T = 0. \quad (2.62)$$

Chapter 3

Governing equations

The mere formulation of a problem is far more often essential than its solution, which may be merely a matter of mathematical or experiment skill.

Albert Einstein (1879 - 1955).

3.1 Introduction

In this section the governing equations of the *thermo-hydro-mechanically* (THM) coupled problem are summarized for both the saturated and the partially saturated porous medium. The solid is considered to behave as a thermoelastic material and the liquid phase is assumed to be incompressible.

3.2 Saturated flow in poro-thermo-elastic media

In Box 3.1 the balance equations for the thermo-hydro-mechanically coupled saturated flow problem are summarized. The fluid is assumed to be compressible. The material properties are derived from the equations of state given in Sec. 6.7.1. A constitutive equation has to be formulated for the stress strain relation of the linear thermoelastic material. It is described by the generalized Hooke's law

$$\boldsymbol{\sigma} = \lambda \operatorname{tr} \boldsymbol{\varepsilon}^{\text{el}} \mathbf{1} + 2G \boldsymbol{\varepsilon}^{\text{el}} \quad (3.1)$$

where $\boldsymbol{\varepsilon}^{\text{el}}$ is the elastic strain. Total strain $\boldsymbol{\varepsilon}$ is additively composed by elastic and thermal strain $\boldsymbol{\varepsilon}^{\text{t}}$, thus the elastic strain is as follows

$$\boldsymbol{\varepsilon}^{\text{el}} = \boldsymbol{\varepsilon} - \boldsymbol{\varepsilon}^{\text{t}} \quad \boldsymbol{\varepsilon}^{\text{t}} = \alpha_T (T - T_{\text{ref}}) \mathbf{1}$$

The equation for the fluid flux, derived from the conservation of linear momentum in the fluid, is *Darcy's law*

$$\mathbf{q} = \frac{\mathbf{k}}{\mu_1} (-\nabla p^l + \rho^l \mathbf{g}). \quad (3.2)$$

The conductive thermal flux \mathbf{J}_t is

$$\mathbf{J}_t = -\mathbf{D} \nabla T, \quad \mathbf{D} = ((1-n)\lambda^s + n\lambda^l) \mathbf{1} \quad (3.3)$$

where \mathbf{D} is the second order tensor of heat conduction.

Box 3.1: Thermo-hydro-mechanically coupled fully saturated flow formulation.
Balance equations.

Conservation of linear momentum of the solid phase:

$$\nabla \cdot (\boldsymbol{\sigma} - \alpha p^l \mathbf{1}) + \rho_b \mathbf{g} = \mathbf{0} \quad (3.4)$$

$$\text{where} \quad \rho_b = n \rho^l + (1-n) \rho^s$$

Conservation of mass:

$$\nabla \cdot \mathbf{q} + S \frac{\partial p^l}{\partial t} + \alpha \nabla \cdot \frac{\partial \mathbf{u}}{\partial t} = 0 \quad (3.5)$$

$$\text{where} \quad S = \frac{n}{K_f} + \frac{\alpha-n}{K_s}, \quad \alpha = 1 - \frac{K_T}{K_s}$$

Conservation of heat energy:

$$\nabla \cdot \mathbf{J}_t + c\rho \frac{\partial T}{\partial t} + c^l \rho^l \mathbf{q} \nabla T = 0 \quad (3.6)$$

$$\text{where} \quad c\rho = n c^l \rho^l + (1-n) c^s \rho^s$$

3.3 Partially saturated flow in poro-thermo-elastic media

In this section the governing equations of the thermo-hydro-mechanically coupled problem in the framework of partially saturated porous media are presented in the one-phase formulation, see for example Lewis and Schrefler (1998) [64].

We assume an incompressible liquid in a moving porous solid and negligible gas pressure gradients (Richards' approximation). That means that in the partially saturated zone the gaseous phase flows without resistance. Consequently, the gaseous phase remains

at atmospheric pressure, which is taken as reference pressure. It is straightforward to distinguish between saturated and unsaturated zone: in the saturated zone we have positive pore pressures, whereas the pressure is negative in the unsaturated zone. The two zones are separated by the free surface which can be obtained by the isobar of zero pore pressure. Effects due to vapor transport are neglected in the formulation. Its balance equations are summarized in Box 3.2.

Box 3.2: Thermo-hydro-mechanically coupled partially saturated one-phase flow formulation. Balance equations.

Conservation of linear momentum of the solid phase:

$$\nabla \cdot (\boldsymbol{\sigma} - \alpha S^l p^l \mathbf{1}) + \rho_b \mathbf{g} = \mathbf{0} \quad (3.7)$$

$$\text{where} \quad \rho_b = n S^l \rho^l + (1 - n) \rho^s$$

Conservation of mass:

$$\begin{aligned} \left(S^{l2} \frac{\alpha - n}{K_s} + n S^l \frac{1}{K^l} \right) \frac{\partial p^l}{\partial t} + \left(\frac{\alpha - n}{K_s} p^l S^l + n \right) \frac{\partial S^l}{\partial t} \\ - \left(S^l \beta_T^s (\alpha - n) + n S^l \beta_T^l \right) \frac{\partial T}{\partial t} \\ + \frac{1}{\rho^l} \nabla \cdot \mathbf{J}^{ls} + S^l \alpha \nabla \cdot \frac{\partial \mathbf{u}}{\partial t} = 0. \end{aligned} \quad (3.8)$$

$$\text{where} \quad \alpha = 1 - \frac{K_T}{K_s}$$

Conservation of heat energy:

$$\nabla \cdot \mathbf{J}_t + c \rho \frac{\partial T}{\partial t} + c^l \rho^l \mathbf{q} \nabla T = 0 \quad (3.9)$$

$$\text{where} \quad c \rho = n c^l S^l \rho^l + (1 - n) c^s \rho^s$$

The constitutive equation for the stresses is equivalent to stress strain relation (3.1) defined within the saturated flow formulation. The equation for the fluid flux, derived from the conservation of linear momentum in the liquid phase, is the modified form *Darcy's law*

$$\mathbf{q} = \frac{\mathbf{k} k_{\text{rel}}^l}{\mu_l} (-\nabla p + \rho^l \mathbf{g}). \quad (3.10)$$

The time derivative of the saturation $\partial S^l / \partial t$ appearing in the mass balance equation (3.8) is usually replaced by $\frac{\partial S^l}{\partial p^l} \frac{\partial p^l}{\partial t}$. Then, the required derivative $\partial S^l / \partial p^l$ is obtained from the capillary pressure-saturation relation. The heat conduction for the multi-phase system needed in balance equation (3.9) is given by Eq. (6.64) in Sec. 6.8.

Chapter 4

The finite element method

4.1 Introduction

In the present section, a general approach for the finite element formulation of a generic time dependent coupled problem, defined in Sec. 4.2.1, is outlined and the required iterative techniques and numerical methods are presented.

4.2 Finite element formulation

The general finite element solution process is presented in the next sections. It consists of the following steps:

1. Formulation of the differential equation governing the problem under consideration (see Sec. 4.2.1).
2. Derivation of the weak form of the differential equation (see Sec. 4.2.2).
3. Approximation of state variables and their derivatives (see Sec. 4.2.4).
4. Computing of derived values of the state variables (for example fluxes).
5. Performing the integration over each element (see Sec. 4.2.5).
6. Assembly of the element contributions from previous item (see Sec. 4.2.6).
7. Incorporation of the *Dirichlet* boundary conditions.
8. Solving of the resulting system of equations (see Sec. 4.5).
9. Update of the field of unknown values and evaluation of desired derived values.

4.2.1 A general initial boundary value problem

The formulation of the finite element method presented in the following sections is derived according to a general coupled *initial boundary value problem* (IBVP). The considered problem is defined as follows

$$\begin{aligned} \frac{\partial u}{\partial t} &= \mathcal{F}(u(x, t), t) && \text{in } \Omega \times [0; T], \\ u(x, t_0) &= u_0 && \text{in } \Omega, \\ u(x) &= \bar{u}(t) && \text{on } \Gamma, \end{aligned} \quad (4.1)$$

where $\mathcal{F}(u(x, t), t)$ is a linear or non-linear function of $u(x, t)$ and t and $u(x, t_0)$ is the initial value of $u(x, t)$ at time t_0 .

4.2.2 Weak formulation

In order to obtain a variational formulation, each balance equation is multiplied by a test function. Integration by parts and application of the Gauss theorem leads to the weak form (see App. A.2). By applying this procedure, the natural or *Neumann* boundary conditions are incorporated.

4.2.3 Spatial discretization

The spatial domain Ω is approximated by $\hat{\Omega}$ composed of n_{el} non overlapping finite elements Ω^e as follows

$$\Omega \approx \hat{\Omega} = \bigcup_{e=1}^{n_{\text{el}}} \Omega^e. \quad (4.2)$$

The geometry of these elements is approximated by shape functions. Usually identical shape functions are used to approximate the displacements. This kind of element formulation is called *isoparametric*. The decomposition of the domain into finite elements and the use of shape functions for integration of the weak formulation at the element level lead to a set of linear or non-linear equations. The number of equations is equivalent to the number of degrees of freedom at the element nodes.

4.2.4 Numerical approximation

The finite element formulation is usually derived by applying the well known *Bubnov-Galerkin* method in which the *weighting* or *test* functions are approximated by the same shape function that are used for the approximation of the process dependent state variables like displacements, pressure or temperature.

In case of advective transport processes, a different choice of weighting function is useful for stabilization. Here, special shape functions are used which are modified according

to the current velocity field. This method is called *Streamline Upwind/Petrov-Galerkin* (SUPG).

As also known from mechanical mixed finite element formulations, the ansatz-space of coupled formulations for fluid-saturated poro-mechanics has to be chosen carefully (see [113, 114, 108], amongst others). In mixed formulations the finite element spaces must satisfy compatibility conditions in order to fulfill the stability criteria dictated by the *Babuška–Brezzi* theory, obtained independently by Babuška and Brezzi [18]. For proofing the stability of mixed formulations the inf-sup condition, has to be fulfilled (see [16]). Hence, linear and quadratic shape functions are used for pressure und displacements, respectively.

4.2.5 Numerical integration

The element contributions are the weighted integrals of the stiffness, conductivity or storage terms, the internal fluxes or internal loads, and the external loads or sources. Internal fluxes are stresses, heat flux, volume flux or mass flux. Internal loads can arise from gravitational acceleration. External loads can be distributed along edges, on surfaces or within the domain of an element.

The numerical integration is presented in App. A.2. With the performed integration the weak form of the problem results in a nodal representation of the equation system. Summing up of the contributions of each node results in a set of equation equivalents to the number of nodes.

4.2.6 Assembly

The nodal contributions of each element are added to the algebraic system of equations. In a coupled formulation the dimensions of the element contributions are non-uniform as the approximations of the weighting functions are of different order.

4.3 Temporal discretization

General transient dynamic problems can be described by equations of the following form

$$\mathcal{A}\ddot{u} + \mathcal{B}\dot{u} + \mathcal{C}u = \mathcal{F} \quad (4.3)$$

where u is a set of state variables. Assuming a quasi static problem in soil mechanics the dynamic behavior is of no importance. Thus, the term \mathcal{A} can be omitted. The first time derivative term \mathcal{B} describes the transient behavior, defining e.g. the damping of temporal fluctuations in the fluid pressure field. Both, the term \mathcal{B} as well as \mathcal{C} describing the static response, e.g. the stress or the fluid flow, may depend non-linearly on the system variable u or on further internal variables.

4.3.1 A general initial value problem

An initial value problem (IVP) is defined by

$$\begin{aligned} \frac{\partial u}{\partial t} &= \mathcal{F}(u(t), t) \quad \text{in } [0; T], \\ u(t_0) &= u_0, \end{aligned} \quad (4.4)$$

where $\mathcal{F}(u(t), t)$ is a linear or non-linear function of $u(t_0)$ and t and $u(t_0)$ is the initial value of $u(t_0)$ at time t_0 . The time domain is discretized by equidistant time steps, thus $\Delta t = t_{n+1} - t_n$.

4.3.2 Numerical approximation of the time derivative

Single-step methods. The time operator in Eq. (4.4) can be expressed in finite differences using a Taylor's series expansion. Incorporation of the left and right endpoint of a single time step results in

$$\frac{\partial u}{\partial t} = \frac{u_{n+1} - u_n}{\Delta t} + \mathcal{O}(\Delta t). \quad (4.5)$$

If this approximation is used in the forward *Euler* scheme, which evaluates the state of the system at current time t_n as depicted in Fig. 4.1, the resulting solution u_{n+1} can directly be estimated in an explicit formula. The backward *Euler* method, calculating the state of the system at the new time t_{n+1} , is depicted in Fig. 4.2 and consequently results in an implicit solution.

Second order accuracy can be achieved with the family of *Newmark* methods which is well-established in structural dynamics, see e.g. Hughes (2000) [46]. Higher order of accuracy is gained by *Runge-Kutta* methods. They are easy to implement and very stable. The primary disadvantage of *Runge-Kutta* methods is that they require significantly more computer time than multi-step methods of comparable accuracy.

Multi-step methods. In contrast to single-step methods, multi-step methods use values from previous time steps. Thus, they are not self-starting, i.e. some single-steps have to be performed before a multi-step integration is possible.

The *leapfrog* strategy is a centered scheme, depicted in Fig. 4.3. It is developed around the current time t_n , thus it yields

$$\frac{\partial u}{\partial t} = \frac{u_{n+1} - u_{n-1}}{2\Delta t} + \mathcal{O}(\Delta t^2). \quad (4.6)$$

The accuracy of this scheme is of second order. Other multi-step methods are for example Predictor-Corrector methods and various *Adams* methods.

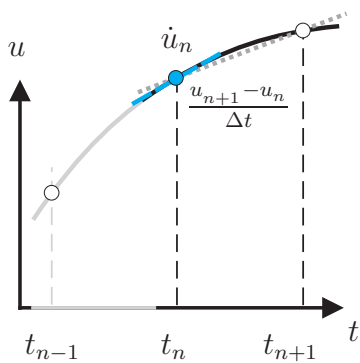


Figure 4.1: Single-step method. Explicit *Euler*. System state evaluation at current time t_n .

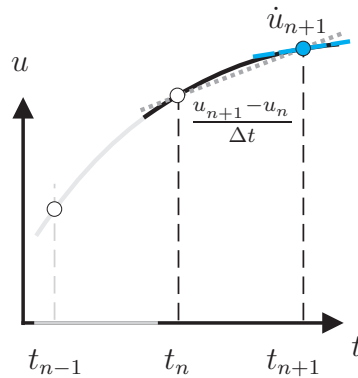


Figure 4.2: Single-step method. Implicit *Euler*. System state evaluation at new time t_{n+1} .

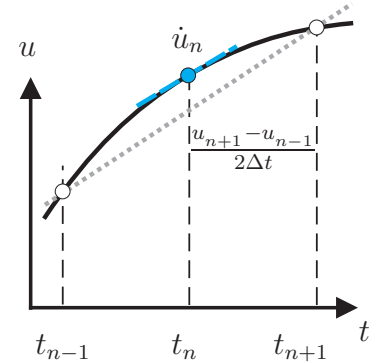


Figure 4.3: Multi-step method with approximation around t_n . *Leapfrog*: centered explicit. System state evaluation at current time t_n .

4.3.3 Numerical integration in time

The exact integration of (4.4) in time yields

$$\int_{t_n}^{t_{n+1}} \frac{\partial u}{\partial t} dt = u_{n+1} - u_n = \int_{t_n}^{t_{n+1}} \mathcal{F}(t, u(t)) dt. \quad (4.7)$$

This differential equation can be replaced by finite differences according to Eq. (4.5) while the function \mathcal{F} can be evaluated at time t_n and t_{n+1} and then weighted by the time collocation factor θ as follows

$$\frac{u_{n+1} - u_n}{\Delta t} = \theta \mathcal{F}(t_{n+1}, u_{n+1}) + (1 - \theta) \mathcal{F}(t_n, u_n) + \mathcal{O}, \quad 0 \leq \theta \leq 1. \quad (4.8)$$

Depending on the time collocation, several time-stepping schemes of different order of accuracy are possible:

1. $\theta = 0$. The fully explicit forward *Euler* scheme, see Fig. 4.4. is 1st order accurate

$$u_{n+1} = u_n + \Delta t \mathcal{F}(t_n, u_n) + \mathcal{O}(\Delta t^2). \quad (4.9)$$

The forward *Euler* scheme is not neutral for various problems, in the sense that some quantities such as mass, momentum or energy are not conserved but may decay or grow as the simulation is advanced in time. When these quantities grow with time, the model is of course unstable. The explicit *leapfrog* scheme is neutral and conditionally stable.

2. $\theta = 0.5$. The semi-implicit *Crank-Nicolson* scheme (cf. [22]), see Fig. 4.5 is 2nd order accurate

$$u_{n+1} = u_n + \Delta t \frac{1}{2} (\mathcal{F}(t_{n+1}, u_{n+1}) + \mathcal{F}(t_n, u_n)) + \mathcal{O}(\Delta t^3). \quad (4.10)$$

The advantage of the semi-implicit treatment is that the time-operator is centered. Thus, this scheme (centered in time) is neutral.

3. $\theta = 1.0$. The fully-implicit backward *Euler* scheme, see Fig. 4.6, is 1st order accurate

$$u_{n+1} = u_n + \Delta t \mathcal{F}(t_{n+1}, u_{n+1}) + \mathcal{O}(\Delta t^2). \quad (4.11)$$

This fully-implicit scheme is not neutral but unconditionally stable.

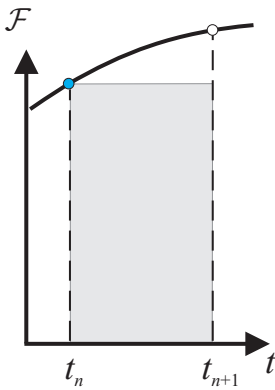


Figure 4.4: Forward *Euler* (left endpoint).

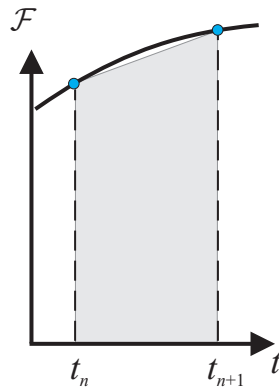


Figure 4.5: *Crank-Nicolson* (trapezoidal).

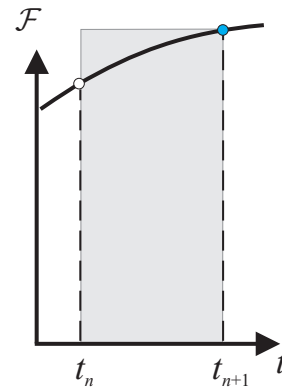


Figure 4.6: Backward *Euler* (right endpoint).

Usually fully implicit schemes are preferred in mechanical analysis in order to ensure the stability of the algorithm. In transient transport analysis the accuracy is of great importance, thus the semi-implicit *Crank-Nicolson* scheme is of special interest. For more details on stability and accuracy the reader should refer to Knabner and Angermann (2003) [53] amongst others.

4.4 Iterative techniques for nonlinear algebraic equations

4.4.1 Introduction

Non-linear problems generally result non-linear algebraic equations of the following form

$$\mathbf{G}(\mathbf{a}) = \mathbf{f} - \mathbf{P}(\mathbf{a}) = \mathbf{0}, \quad (4.12)$$

where \mathbf{a} is the set of discretized solution parameters, \mathbf{f} is a vector which is independent of the parameters while \mathbf{P} is a vector dependent on the parameters.

A discretization due to load or time steps yields

$$\mathbf{G}_{n+1} = \mathbf{G}(\mathbf{a}_{n+1}) = \mathbf{f}_{n+1} - \mathbf{P}(\mathbf{a}_{n+1}) = \mathbf{0}. \quad (4.13)$$

Assuming an iterative procedure with a solution increment

$$d\mathbf{a}_n^i = \mathbf{a}_{n+1}^{i+1} - \mathbf{a}_{n+1}^i \quad (4.14)$$

the Taylor series expansion of $\mathbf{G}(\mathbf{a}_{n+1})$ about the last iterative solution \mathbf{a}_{n+1}^i is as follows

$$\mathbf{G}(\mathbf{a}_{n+1}^{i+1}) = \mathbf{G}(\mathbf{a}_{n+1}^i) + \left(\frac{\partial \mathbf{G}}{\partial \mathbf{a}} \right)_{n+1}^i d\mathbf{a}_n^i + \left(\frac{\partial^2 \mathbf{G}}{\partial \mathbf{a}^2} \right)_{n+1}^i (d\mathbf{a}_n^i)^2 + \dots = \mathbf{0} \quad (4.15)$$

With a given change in the forcing function

$$\mathbf{f}_{n+1} = \mathbf{f}_n + \Delta \mathbf{f}_n \quad (4.16)$$

the new solution can be gained starting from the last solution \mathbf{a}_n by iterative determination of the total increment $\Delta \mathbf{a}_n$ (*Newton-Raphson* method)

$$\mathbf{a}_{n+1} = \mathbf{a}_n + \Delta \mathbf{a}_n^i \quad (4.17)$$

or by direct evaluation of the solution vector \mathbf{a}_{n+1} (*Picard* iteration).

For solving non-linear equations governing flow in partially saturated porous media the *Picard* iteration is widely used. A comparison of *Picard* and *Newton* scheme according to this problem can be found in Paniconi and Putti (1994) [80]. In non-linear structural analysis the *Newton* or modified *Newton* methods are usually applied ([115, 108]).

4.4.2 The Newton-Raphson method

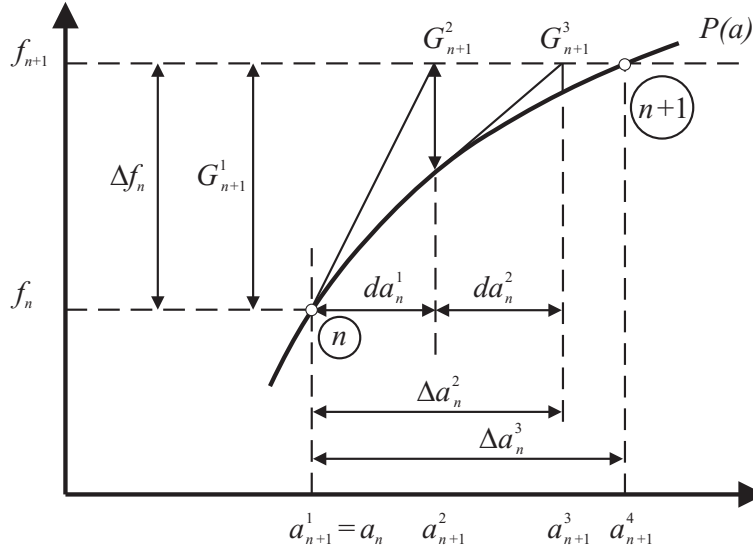
Assuming that an initial solution is available and no divergence occurs in the following iterative procedure, the *Newton-Raphson* method achieves a quadratic order of convergence. The method was derived by Newton and Raphson independently. A brief review of its origin can be found in Bicanic and Johnson (1979) [5].

Omitting the quadratic terms in the Taylor series (4.15) the non-linear problem (4.12) is approximated linearly by

$$\mathbf{G}(\mathbf{a}_{n+1}^{i+1}) \approx \mathbf{G}(\mathbf{a}_{n+1}^i) + \left(\frac{\partial \mathbf{G}}{\partial \mathbf{a}} \right)_{n+1}^i d\mathbf{a}_n^i = \mathbf{0} \quad (4.18)$$

where $d\mathbf{a}_n^i$ is the solution increment of iteration i . The Jacobian matrix $\partial \mathbf{G} / \partial \mathbf{a}$ (or the tangential stiffness \mathbf{K}_T) corresponding to the tangent direction $\partial \mathbf{P} / \partial \mathbf{a}$ given by

$$\mathbf{K}_T = \frac{\partial \mathbf{P}}{\partial \mathbf{a}} = - \frac{\partial \mathbf{G}}{\partial \mathbf{a}} \quad (4.19)$$

Figure 4.7: The *Newton-Raphson* method.

is used to derive the iterative correction defined in Eq. (4.18) as follows

$$d\mathbf{a}_n^i = (\mathbf{K}_T^i)^{-1} \mathbf{G}_{n+1}^i. \quad (4.20)$$

The final solution is achieved by a series of successive approximations, illustrated in Fig. 4.7,

$$\mathbf{a}_{n+1}^{i+1} = \mathbf{a}_{n+1}^i + d\mathbf{a}_n^i \quad (4.21)$$

$$= \mathbf{a}_n + \Delta\mathbf{a}_n^i \quad (4.22)$$

where

$$\Delta\mathbf{a}_n^i = \sum_{k=1}^i d\mathbf{a}_n^k. \quad (4.23)$$

4.4.3 Direct (Picard) iteration

Assume the non-linear problem of the following form

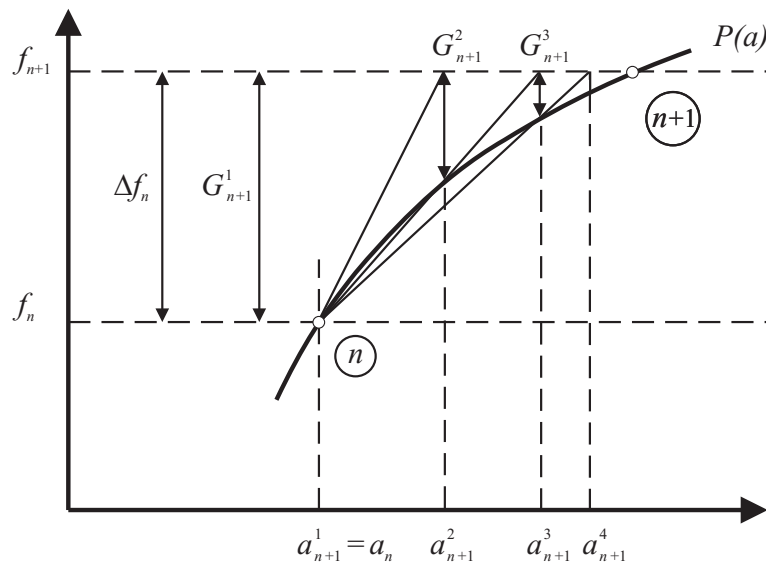
$$\mathbf{G}(\mathbf{a}) = \mathbf{f} - \mathbf{K}(\mathbf{a})\mathbf{a} = \mathbf{0} \quad (4.24)$$

which can be approximated by

$$\mathbf{G}(\mathbf{a}_{n+1}^{i+1}) \approx \overbrace{\mathbf{f}_{n+1} - \mathbf{K}(\mathbf{a}_{n+1}^i)\mathbf{a}_{n+1}^i}^{\mathbf{G}(\mathbf{a}_{n+1}^i)} - \overbrace{\left(\mathbf{K}(\mathbf{a}_{n+1}^i) + \frac{\partial \mathbf{K}(\mathbf{a}_{n+1}^i)}{\partial \mathbf{a}_{n+1}^i} \mathbf{a}_{n+1}^i\right)}^{\mathbf{K}_T} d\mathbf{a}_n^i. \quad (4.25)$$

By neglecting the second term of \mathbf{K}_T and replacing $d\mathbf{a}_n^i$ by $\mathbf{a}_{n+1}^{i+1} - \mathbf{a}_{n+1}^i$ we get a linear form

$$\mathbf{G}(\mathbf{a}_{n+1}^{i+1}) \approx \mathbf{f}_{n+1} - \mathbf{K}(\mathbf{a}_{n+1}^i)\mathbf{a}_{n+1}^{i+1} = \mathbf{0} \quad (4.26)$$

Figure 4.8: Direct (*Picard*) iteration.

which finally results in the following iterative update procedure

$$\mathbf{a}_{n+1}^{i+1} = [\mathbf{K}(\mathbf{a}_{n+1}^i)]^{-1} \mathbf{f}_{n+1}. \quad (4.27)$$

4.5 Solution procedures for coupled equations

4.5.1 Introduction

The governing equation of the thermo-hydro-mechanically coupled formulation of single-phase flow in porous media is outlined in Sec. 3.2. A coupled system of algebraic equations arises from spatial discretization of the weak formulation of this transient coupled problem. It can be written in a concise form that reads as follows

$$\mathbf{B} \frac{\partial \mathbf{Y}}{\partial t} + \mathbf{C} \mathbf{Y} = \mathbf{F} \quad (4.28)$$

where the matrices \mathbf{B} and \mathbf{C} represent the transient and the steady state response of the problem. The matrices are usually unsymmetric and may depend on the configuration vector \mathbf{Y} . The right hand side \mathbf{F} implies the load vectors and additional coupling terms that can not be incorporated on the left hand side matrices, for example the term representing thermal expansion.

The thermo-hydro-mechanically coupled formulation, containing the thermal process P_T describing the heat flow, the hydraulic process P_p representing the fluid flow, and the mechanical process P_u for the estimation of solid deformations reads

$$\begin{bmatrix} 0 & 0 & 0 \\ \mathbf{C}_{pu} & \mathbf{S}_{pp} & \mathbf{C}_{pT} \\ 0 & 0 & \mathbf{S}_{TT} \end{bmatrix} \frac{\partial}{\partial t} \begin{Bmatrix} \mathbf{u} \\ p \\ T \end{Bmatrix} + \begin{bmatrix} \mathbf{K}_{uu} & \mathbf{C}_{up} & \mathbf{C}_{uT} \\ 0 & \mathbf{K}_{pp} & 0 \\ 0 & \mathbf{C}_{pT} & \mathbf{K}_{TT} \end{bmatrix} \begin{Bmatrix} \mathbf{u} \\ p \\ T \end{Bmatrix} = \begin{Bmatrix} \mathbf{F}_u \\ \mathbf{F}_p \\ \mathbf{F}_T \end{Bmatrix} \quad (4.29)$$

where the processes are described by stiffness or conductivity matrices \mathbf{K} , capacitance or storage matrices \mathbf{S} and coupling matrices \mathbf{C} . The configuration vector is composed by the state variables $\{\mathbf{u}, p, T\}^\top$.

4.5.2 Temporal discretization

The discretization in time is carried out using an implicit scheme, thus at time $t_{n+\theta}$ Eq. (4.28) results in

$$\left[\frac{1}{\Delta t} \mathbf{B} + \theta \mathbf{C} \right] \mathbf{Y}_{n+1} = \left[\frac{1}{\Delta t} \mathbf{B} + (1 - \theta) \mathbf{C} \right] \mathbf{Y}_n + \mathbf{F}_{t+\theta} \quad (4.30)$$

where Δt is the time step length, \mathbf{Y}_n and \mathbf{Y}_{n+1} are the state vectors at times t_n and t_{n+1} . Parameter θ with limits $0 \leq \theta \leq 1$ is the time collocation introduced in Sec. 4.3.

4.5.3 Incremental formulation

The temporal discretization given in Eq. (4.30) is formulated in an incremental form

$$\left[\frac{1}{\Delta t} \mathbf{B} + \theta \mathbf{C} \right] \Delta \mathbf{Y}_n^i = - \left[\frac{1}{\Delta t} \mathbf{B} + \theta \mathbf{C} \right] \mathbf{Y}_n^i + \left[\frac{1}{\Delta t} \mathbf{B} + (1 - \theta) \mathbf{C} \right] \mathbf{Y}_n + \mathbf{F}_{t+\theta} \quad (4.31)$$

In an iterative scheme the update of the configuration vector is

$$\mathbf{Y}_{n+1}^{i+1} = \mathbf{Y}_{n+1}^i + \Delta \mathbf{Y}_n^i. \quad (4.32)$$

4.5.4 Solving of coupled linear equations

4.5.4.1 Monolithic and partitioned approach

The incremental solutions of Eq. (4.31) can be gained within a monolithic scheme resulting in one system of coupled equations. A partitioned approach which solves the equations separately may have certain advantages concerning

- the reduction of the size of the system matrices,
- and the smaller condition numbers of the separated system matrices.

In soil consolidation problems distinct couplings between the equilibrium and mass balance equations occur. A procedure for judging the strength of the coupling is given in Lewis et al. (1991) [65].

A monolithic approach has been chosen for solving the coupled solid-fluid problem while the thermal problem is solved separately. Both systems of equations are solved in an iterative scheme until satisfying convergence is achieved.

The incremental update of the configuration vector \mathbf{Y} , pointed out in the previous section, has been chosen only for the solid problem. The resulting system of equations for the solid-fluid problem is

$$\begin{aligned}
& \left(\frac{1}{\Delta t} \begin{bmatrix} 0 & 0 \\ \mathbf{C}_{pu} & \mathbf{S}_{pp} \end{bmatrix} + \theta \begin{bmatrix} \mathbf{K}_{uu} & \mathbf{C}_{up} \\ 0 & \mathbf{K}_{pp} \end{bmatrix} \right) \begin{Bmatrix} \Delta \mathbf{u}_n^i \\ p_{n+1}^i \end{Bmatrix} \\
& = - \left(\frac{1}{\Delta t} \begin{bmatrix} 0 & 0 \\ \mathbf{C}_{pu} & 0 \end{bmatrix} + \theta \begin{bmatrix} \mathbf{K}_{uu} & \mathbf{C}_{up} \\ 0 & 0 \end{bmatrix} \right) \begin{Bmatrix} \mathbf{u}_{n+1}^i \\ 0 \end{Bmatrix} \\
& + \left(\frac{1}{\Delta t} \begin{bmatrix} 0 & 0 \\ \mathbf{C}_{pu} & \mathbf{S}_{pp} \end{bmatrix} + (1-\theta) \begin{bmatrix} \mathbf{K}_{uu} & \mathbf{C}_{up} \\ 0 & \mathbf{K}_{pp} \end{bmatrix} \right) \begin{Bmatrix} \mathbf{u} \\ p \end{Bmatrix}_n \\
& + \begin{bmatrix} \mathbf{C}_{uT} \\ \frac{1}{\Delta t} \mathbf{C}_{pT} \end{bmatrix} (\{ T_{n+1}^i \} - \{ T_n \}) + \begin{Bmatrix} \mathbf{F}_u \\ \mathbf{F}_p \end{Bmatrix}_{t+\theta}
\end{aligned} \tag{4.33}$$

and the thermal problem is

$$\begin{aligned}
& \left(\frac{1}{\Delta t} [\mathbf{S}_{TT}] + \theta [\mathbf{K}_{TT}] \right) \{ T \}_{n+1}^{i+1} \\
& = \left(\frac{1}{\Delta t} [\mathbf{S}_{TT}] + (1-\theta) [\mathbf{K}_{TT}] \right) \{ T \}_n + \{ \mathbf{F}_T \}_{t+\theta}.
\end{aligned} \tag{4.34}$$

The update of the configuration vector is

$$\begin{Bmatrix} \mathbf{u} \\ p \\ T \end{Bmatrix}_{n+1}^{i+1} = \begin{Bmatrix} \mathbf{u} \\ p \\ T \end{Bmatrix}_{n+1}^i + \begin{Bmatrix} \Delta \mathbf{u} \\ 0 \\ 0 \end{Bmatrix}_n. \tag{4.35}$$

The derivation of the finite element formulation for the solid-fluid problem and the resulting finite element matrices are given in App. A.2.

4.5.5 Solving of coupled non-linear equations

4.5.5.1 Formulation of the residual

This section is devoted to the treatment of non-linearities occurring in the coupled set of balance equations of the hydraulic-mechanical problem. The non-linear equation system resulting from the finite element formulation can be written in the following compact form

$$\mathbf{G}(\mathbf{Y}) = \mathbf{0}, \tag{4.36}$$

where the configuration vector is

$$\mathbf{Y} = \begin{Bmatrix} \mathbf{u} \\ p \end{Bmatrix}. \quad (4.37)$$

For the numerical solution of the non-linear problem it has to be linearized at $\bar{\mathbf{Y}}$ with respect to $\Delta\mathbf{Y}$

$$\mathbf{G}(\bar{\mathbf{Y}}, \Delta\mathbf{Y}) \cong \mathbf{G}(\bar{\mathbf{Y}}) + \mathbf{D}_{\bar{\mathbf{Y}}}\mathbf{G}(\bar{\mathbf{Y}}) \cdot \Delta\mathbf{Y}. \quad (4.38)$$

where $\mathbf{D}_{\bar{\mathbf{Y}}}\mathbf{G} \cdot \Delta\mathbf{Y}$ is the *Gâteaux* derivative.

It follows, that for given initial data of the last time step t_n $\mathbf{Y}^n = \{\mathbf{u}^n, p^n\}$ and in respect of the corresponding internal quantities describing the non-linear behavior the resulting equilibrium problem is to find

$$\mathbf{Y}^{n+1} \text{ such that } \mathbf{G}^{n+1}[\mathbf{Y}^{n+1}] = \mathbf{0}. \quad (4.39)$$

4.5.6 Linearization of the residual

In view of a Newton algorithm for solving the finite element discretized counterpart of the equilibrium problem (4.39) a linearization of the residual \mathbf{G}^{n+1} with respect to the configuration vector \mathbf{Y}^{n+1} becomes necessary. The application of the *Gâteaux* derivative $\Delta_{\mathbf{Y}}(\bullet)^{n+1}$

$$\Delta_{\mathbf{Y}}(\bullet)^{n+1} = \frac{d(\bullet)}{d\mathbf{Y}^{n+1}} \cdot \Delta\mathbf{Y} = \frac{d}{d\epsilon} \{(\bullet)[\mathbf{Y}^{n+1} + \epsilon\Delta\mathbf{Y}]\}_{\epsilon=0} \quad (4.40)$$

leads to the following result

$$\Delta_{\mathbf{Y}}\mathbf{G}^{n+1} = \begin{bmatrix} \Delta_{\mathbf{Y}}F_s^{n+1} + \Delta t \Delta_{\mathbf{Y}}G_s^{int,n+1} \\ \Delta_{\mathbf{Y}}F_f^{n+1} - \Delta t \Delta_{\mathbf{Y}}G_f^{int,n+1} \end{bmatrix} \quad (4.41)$$

where

1. $\Delta_{\mathbf{Y}}F_s^{n+1} = \Delta_{\mathbf{u}}F_s^{n+1} + \Delta_pF_s^{n+1}$
 - a. $\Delta_{\mathbf{u}}F_s^{n+1} = \int_{\Omega} \frac{\rho_b}{\theta \Delta t} \delta \mathbf{u} \cdot \Delta \mathbf{u} dV$
 - b. $\Delta_pF_s^{n+1} = 0$
2. $\Delta_{\mathbf{Y}}G_s^{int,n+1} = \Delta_{\mathbf{u}}G_s^{int,n+1} + \Delta_pG_s^{int,n+1}$
 - a. $\Delta_{\mathbf{u}}G_s^{int,n+1} = \int_{\Omega} \nabla_x \delta \mathbf{u} : \mathbb{C}_{11}^{n+\theta} : \nabla_x \Delta \mathbf{u} dV$
 - b. $\Delta_pG_s^{int,n+1} = \int_{\Omega} -\text{div} \delta \mathbf{u} \theta \Delta p dV$

describe in the solid sub-problem and

$$\begin{aligned}
1. \quad & \Delta_{\mathbf{Y}} F_f^{n+1} = \Delta_{\mathbf{u}} F_f^{n+1} + \Delta_p F_f^{n+1} \\
& a. \quad \Delta_{\mathbf{u}} F_f^{n+1} = 0 \\
& b. \quad \Delta_p F_f^{n+1} = \int_{\Omega} S \delta p \Delta p dV \\
2. \quad & \Delta_{\mathbf{Y}} G_f^{int,n+1} = \Delta_{\mathbf{u}} G_f^{int,n+1} + \Delta_p G_f^{int,n+1} \\
& a. \quad \Delta_{\mathbf{u}} G_f^{int,n+1} = -\frac{1}{\theta \Delta t} \int_{\Omega} \delta p \operatorname{div} \Delta \mathbf{u}^{n+\theta} dV + \int_{\Omega} \nabla_{\mathbf{x}} \delta p \mathbb{C}_{21}^{n+\theta} : \nabla_{\mathbf{x}} \Delta \mathbf{u} dV \\
& b. \quad \Delta_p G_f^{int,n+1} = \int_{\Omega} \theta \nabla_{\mathbf{x}} \delta p \cdot \mathbb{C}_{22}^{n+\theta} \cdot \nabla_{\mathbf{x}} \Delta p dV
\end{aligned}$$

are according to the the fluid sub-problem. It remains to determine the following consistent moduli

$$\mathbb{C}_{11}^{n+\theta} = \frac{\partial \boldsymbol{\sigma}^{n+\theta}}{\partial \boldsymbol{\varepsilon}^{n+1}}, \quad \mathbb{C}_{21}^{n+\theta} = \frac{\partial \mathbf{q}^{n+\theta}}{\partial \boldsymbol{\varepsilon}^{n+1}}, \quad \mathbb{C}_{22}^{n+\theta} = \frac{\partial \mathbf{q}^{n+\theta}}{\partial (\nabla_{\mathbf{x}} p)^{n+1}}. \quad (4.42)$$

The consistent tangent moduli $\partial \boldsymbol{\sigma}^{n+\theta} / \partial \boldsymbol{\varepsilon}^{n+1}$ of the solid problem are derived in Chapter 6. The term $\partial \mathbf{q}^{n+\theta} / \partial \boldsymbol{\varepsilon}^{n+1}$ arises from the coupling between solid and fluid and $\partial \mathbf{q}^{n+\theta} / \partial (\nabla_{\mathbf{x}} p)^{n+1} = \mathbf{k} / \mu^f$ is addressed in Chapter 3. Corresponding derivations for the analysis of rock salt can be found in Mahnken and Kohlmeier (1999) [69].

Chapter 5

Coupling phenomena and associated numerical aspects

The diversity of the phenomena of nature is so great, and the treasures hidden in the heavens so rich, precisely in order that the human mind shall never be lacking in fresh nourishment.

Johannes Kepler (1571 - 1630).

German astronomer.

5.1 Coupling phenomena

5.1.1 Introduction

The assessment of geotechnical constructions or engineered barrier systems requires extensive numerical simulations of meaningful scenarios. The numerical simulation of geotechnical problems, which usually are multi-field problems, requires the solving of a compound of sub-problems.

In geomechanics the all-important sub-problems are the solid mechanics and the fluid mechanics. The interaction of both is founded in the fluid pressure and the volumetric deformation rate of the solid. Whereas the solid mechanical problem itself could usually be formulated quasi-static, the coupling to the transient fluid flow results in a time dependent problem. Due to its impact, the consideration of fluid-solid couplings in geotechnical simulations results in much more reliable predictions.

The third sub-problem is thermodynamics. Numerous additional coupling phenomena arise if thermal effects have to be taken into account. Thermal effects are the thermal

expansion of the solid or the fluid phase, respectively. The fluid and the fluid flow are associated with conductive and convective heat transport, respectively. A back coupling may occur if the thermal expansion of the solid causes additional fluid flow that transports the heat. Heat conduction is of interest in geothermal applications. In case of high temperature conditions vaporization has to be taken into account.

The forth sub-problem mentioned in this work is the transport of matter. The transport process only becomes relevant if persistent flow processes occur. These flow processes can be caused by volumetric deformation. Solid deformations might also generate additional or close existing flow paths and thus influence the matter transport.

5.1.2 Coupling terms in the balance equations

Fluid-solid interaction The hydraulic-mechanical interaction in a poro-elastic or poro-plastic formulation is governed by the Biot coefficient α that scales the fluid pressure term and the volumetric strain rate. The fluid-solid coupling in a linear elastic porous medium is presented in Sec. 9.1.1. Physical or geometrical non-linearities may occur in the coupling terms. Formulations of finite poroelasticity are given by Eipper (1998) [36]. A highly non-linear coupling occurs if partially saturated media are considered. In this case, the coupling term is additionally affected by the saturation S^α of the fluid phases (see for example [35] or [56]). A numerical application of fluid flow in a partially saturated poro-elastic medium is given in Sec. 9.3.2.1.

Thermal expansion. A transient temperature field results in transient thermal expansion or contraction. The governing parameter is the linear thermal expansion coefficient α_T . Thermal stresses occur if the displacements are restraint or in case of thermal gradients. The mechanical response due to thermal load in a thermo-hydro-mechanically coupled framework is addressed in Sec. 9.3.1 (see [55]).

Transport. The couplings arising in transport phenomena are caused by the fluid flux terms in the respective balance equation of the transported media. Consequently, coupling is restricted to the advective part of the transport process. Diffusive transport can be treated as a single process without interactions. The advective transport of matter can be induced by solid deformations via the fluid-solid coupling. The corresponding numerical example is given in Sec. 9.1.2.

5.1.3 Coupling terms in the constitutive equations

The coupling of different processes is reflected in the constitutive behavior of fluids or solids. An overview of couplings arising in the framework of geotechnical applications is given below.

Permeability and porosity. The fluid flux is governed by the permeability k . The permeability is scaled by a factor called relative permeability that depends on the saturation. The capillary-pressure saturation relations and relative permeability saturation relations are described in Sec. 6.7.2. These relations can be highly non-linear.

The deformation of a porous medium usually results in a change of void space if volumetric strains are present. The associated changes in compressibility, porosity and permeability are important issues (see e.g. [36] or [111]).

Swelling and shrinkage. Saturation induced swelling or shrinkage of expansive soils is caused by the transient evolution of saturation caused by humidity changes or vapor transport. The swelling may cause a change of porosity and permeability especially if a free swelling is restrained (see e.g. [93] [70], [110] or [54]). The swelling behavior of bentonite material is of interest in the simulation performed in Sec. 9.3.1. In case of a decrease of saturation, a restrained shrinkage causes fracturing that opens additional flow paths.

Plastic behavior. The yielding of plastic materials, especially granular soils, strongly depends on the mean effective normal stress that is influenced by the fluid pressure. Thus, the fluid pressure is an significant coupling factor in elasto-plastic analysis of soils. The deviatoric plastic strain rate can be accompanied by a volumetric part, which directly interacts with the fluid flow. The corresponding analyses are presented in Sec. 8.4.3 and Sec. 9.3.3.

Density dependence. Gradients in temperature or concentration fields result in significant spatial density variations of the transporting fluid. The analysis of variable density flows in groundwater systems, considering the thermohaline *Elder* problem [37], can be found in Kolditz et al. (1988) [58], Diersch and Kolditz (1988) [29], Johannsen (2002) [48], amongst others. An example of a thermo-hydro-mechanically coupled density flow is presented in Sec. 9.2.2 (see [55]).

5.2 Numerical aspects

5.2.1 Formulation and assembly of the algebraic equation

In this section, the computational formulation of coupled problems is outlined. The chosen problem consists of three processes: a hydraulic-mechanically coupled sub-problem, with its finite element formulation presented in App. B.1, and a thermal sub-problem. For the numerical implementation of these finite element algorithms, a process oriented approach has been chosen. Each process provides its own function for the set-up of necessary finite element matrices. Moreover, the finite element function is responsible for all the coupling matrices that provide the interaction directed from all other processes to itself.

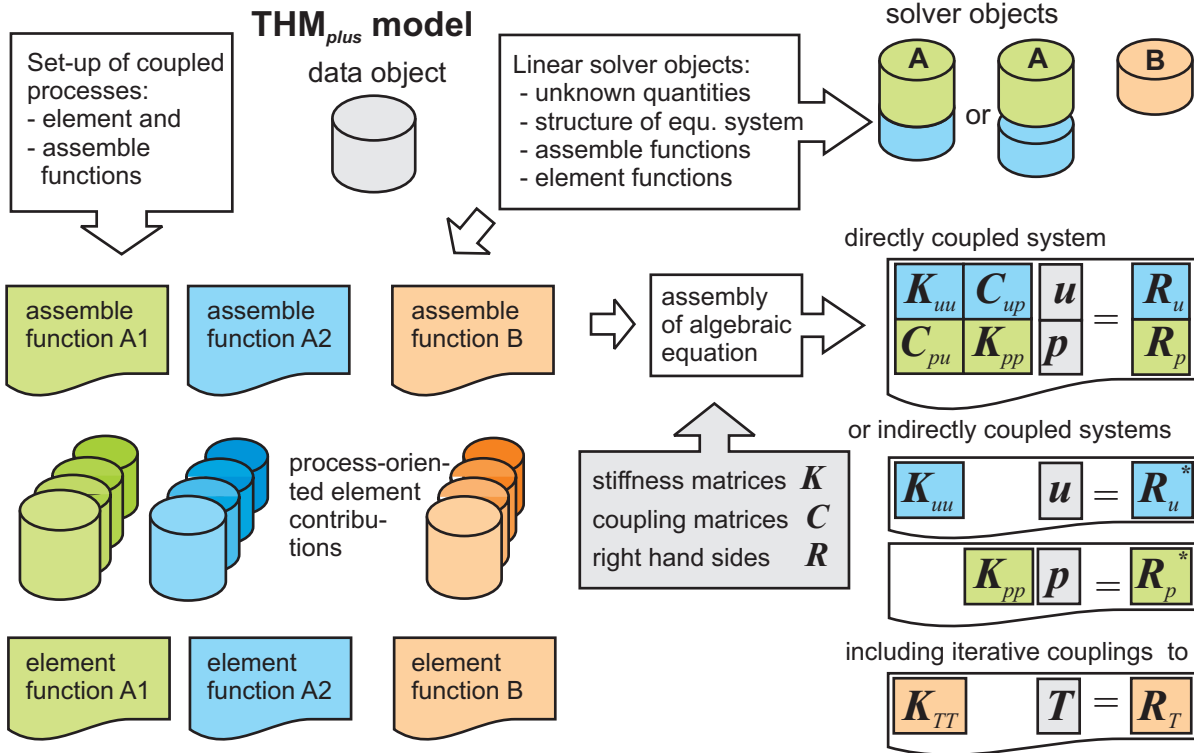


Figure 5.1: Schematic description of the set-up of a linear equation system with direct (monolithic) or indirect (partitioned) treatment of the couplings.

A schematic visualization of this approach is given in Fig. 5.1, assuming a fully coupled hydraulic-mechanical sub-problem which is iteratively coupled with the thermal sub-problem. This approach results in a coupled formulation equivalent to the following algebraic system of equations

$$\begin{bmatrix} \mathbf{K}_{uu} & \mathbf{C}_{up} \\ \mathbf{C}_{pu} & \mathbf{K}_{pp} \end{bmatrix} \begin{Bmatrix} \Delta \hat{\mathbf{u}} \\ \hat{\mathbf{p}} \end{Bmatrix} = \begin{Bmatrix} \mathbf{R}_u \\ \mathbf{R}_p \end{Bmatrix} \quad (5.1)$$

and

$$\begin{bmatrix} \mathbf{K}_{TT} \end{bmatrix} \begin{Bmatrix} \hat{\mathbf{T}} \end{Bmatrix} = \begin{Bmatrix} \mathbf{R}_T \end{Bmatrix}. \quad (5.2)$$

If the fluid-solid coupling is weak, the multi-field problem can also be arranged separately in order to formulate an iterative scheme that solves all sub-problems successively. In this case, the contributions of the coupling terms, provided by the finite element functions, are assembled on the right hand side of the equation system.

The advantage of the approach presented here is its flexibility. Whole processes as well as single process couplings can be cut off or deactivated in an easy and convincing way. This approach also provides a basis for the formulation of constitutively coupled material behavior often requiring a set of multiple processes.

5.2.2 Sparse storage scheme

The coefficient matrix of an algebraic equation system resulting from a finite element formulation is a sparse matrix, as the element matrices are overlapping only by the contributions of neighboring elements. The structure of this sparse matrix, more precisely the distribution of the non-zero entities, is symmetric. In order to avoid the wasting of memory only non-zero values are considered in the applied sparse storage scheme. The standard storage of a structurally symmetric sparse matrix with unsymmetric entity values is depicted in Fig. 5.2. In Fig. 5.3 the strategy of column compressed sparse storage technique is applied. As the matrix is supposed to have unsymmetric entity values, the diagonal part and both the upper and lower triangle parts have to be stored. Nevertheless, the symmetric structure of the matrix can still be taken into consideration for reducing the memory demand of the sparse storage scheme.

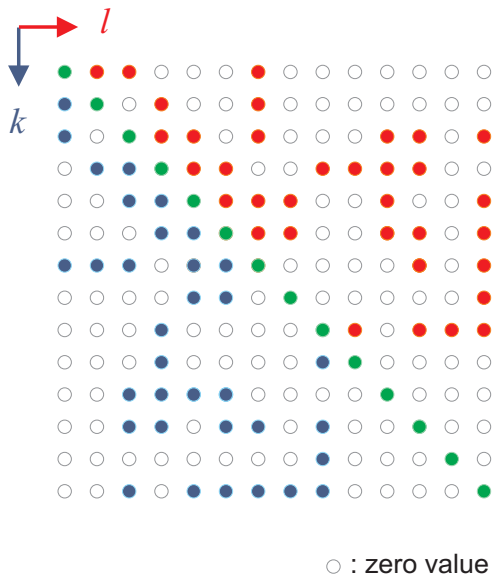


Figure 5.2: Standard storage of a structurally symmetric sparse matrix.

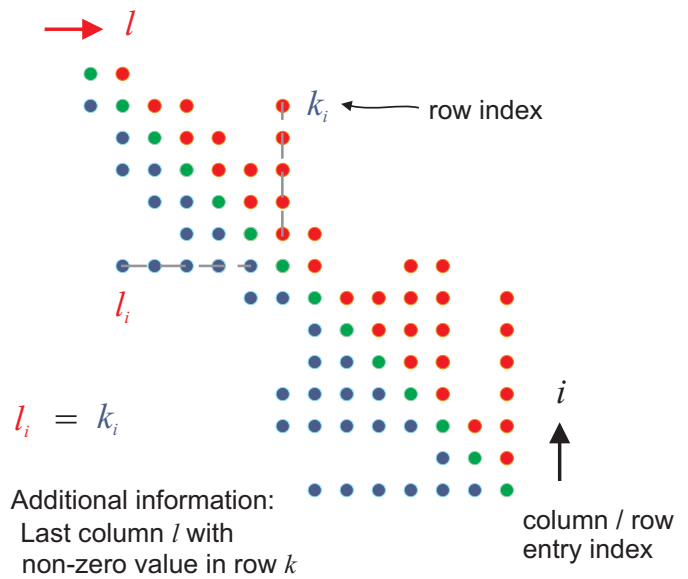


Figure 5.3: Column compressed storage of a structurally symmetric sparse matrix. The coefficient are addressed using the indices (i, l) instead of (k, l) .

5.2.3 Iterative solving of linear systems

In this section some aspects of iterative solvers for linear equations are mentioned. In particular, the solving of linear equations involving unsymmetric matrices is addressed here. A broad overview is given in Kanzow (2005) [51] amongst others. The chosen algorithm consists of an indirect solver with bandwidth reduction and preconditioning. Some important aspects of this solving method are presented in the next sections.

5.2.3.1 Iterative solver

The discretized form of coupled equations usually results in algebraic systems of linear equations consisting of an unsymmetric coefficient matrix. For the solution of such non-symmetric linear equations the *Biconjugate Gradient Stabilized* method (BiCGSTAB) of van der Vorst (1992) [105] is a commonly used method.

5.2.3.2 Preconditioning

The linear system is preconditioned by an *incomplete lower-upper* (ILU) decomposition combined with a diagonal preconditioning. In order to achieve an optimal ILU decomposition, the bandwidth of the matrix is optimized by a grid node reordering. Some aspects of bandwidth reduction for coupled equation systems are addressed in the next section.

5.2.3.3 Bandwidth reduction

In order to achieve an optimal performance of the sparse storage scheme and the above mentioned ILU decomposition an optimal matrix bandwidth reduction is important. For a good performance of larger problems treated in this work, a reordering of the grid nodes has been necessary. The reverse *Cuthill-McKee* algorithm or the *Gibbs-Poole-Stockmeyer* (GPS) [40] algorithm can be applied.

The resulting matrix of a hydraulic-mechanically coupled formulation consisting of six straight-lined hexahedral elements is presented here. Suppose that the structure of the linear equation system is according to the type of unknowns (displacement u_x, u_y, u_z and fluid pressure p) and no reordering scheme is applied, then the matrix has a poor bandwidth depicted in Fig. 5.4. If a grid node reordering is applied the resulting matrix consists of several diagonal bands according to the number of unknowns. This matrix type is depicted in Fig. 5.5. A small bandwidth and an optimal reduction of the number of iterations needed is achieved if the system of equations is arranged according to the reordered nodal structure. It has to be taken into account, that the nodes have either four ($3 \times u_i, p$) or three (u_i) degrees of freedom.

The increase in performance of the solution procedure according to the bandwidth reduction results from fewer iterations and faster access to the sparse matrix coefficients. The length of time required for the solving of coupled problems is reduced up to ten times if an adequate bandwidth reduction can be achieved.

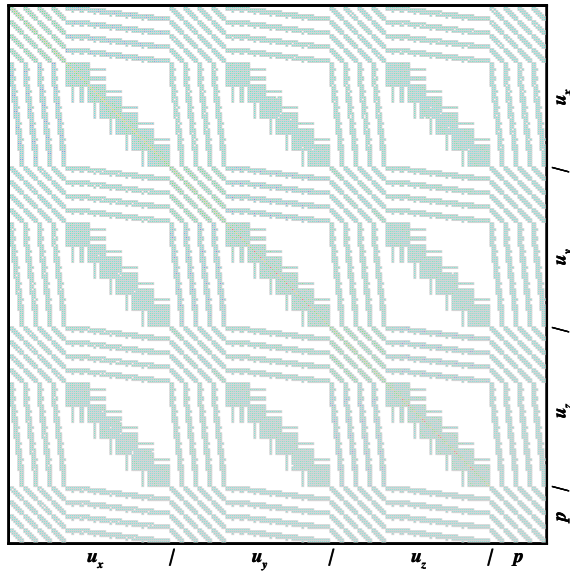


Figure 5.4: Hydraulic-mechanically coupled system of six elements. Matrix structure resulting from a block-wise composition of unknowns without grid node reordering.

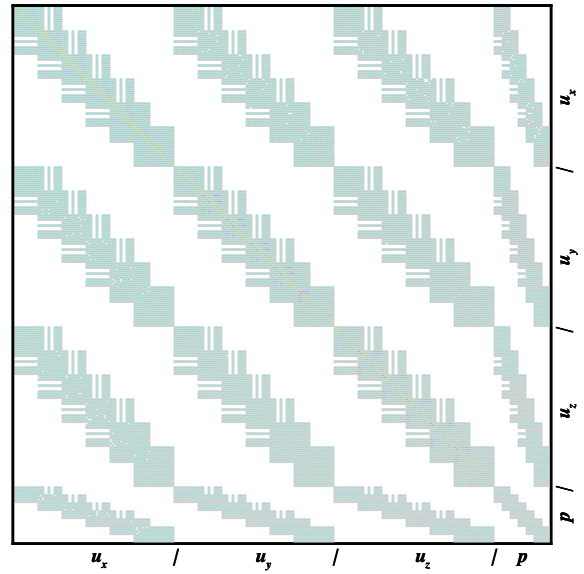


Figure 5.5: Hydraulic-mechanically coupled system of six elements. Matrix structure resulting from a block-wise composition of unknowns with grid node reordering.

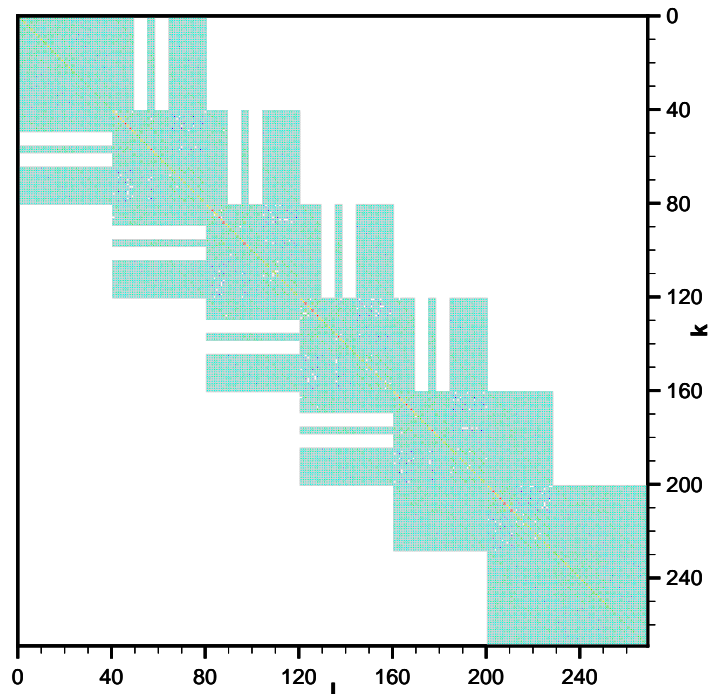


Figure 5.6: Hydraulic-mechanically coupled system of six elements. Matrix structure resulting from a node oriented composition with grid node reordering.

Chapter 6

Constitutive modeling

Obstacles are those frightful things we see when we take our eyes off our goals.

Henry Ford.

6.1 Linear elasticity

The simplest formulation of a constitutive equation, provided by the hyperelastic material model, the stress strain response is derived from a stored energy function given in Def. 6.1.

Definition 6.1. Stored energy and stress response. Let W be the stored energy function

$$W : \Omega_t \times \mathbb{S} \rightarrow \mathbb{R}, \quad (6.1)$$

such that the stress $\boldsymbol{\sigma}$ can be derived as follows

$$\boldsymbol{\sigma}(\boldsymbol{x}) = \frac{\partial W[\boldsymbol{x}, \boldsymbol{\varepsilon}(\boldsymbol{x})]}{\partial \boldsymbol{\varepsilon}}. \quad (6.2)$$

Definition 6.2. Elasticity tensor. The fourth order tensor \mathbb{C} derived by

$$\mathbb{C}(\boldsymbol{x}) = \frac{\partial^2 W[\boldsymbol{x}, \boldsymbol{\varepsilon}(\boldsymbol{x})]}{\partial \boldsymbol{\varepsilon}^2} \quad (6.3)$$

is called elasticity tensor describing the stress-strain relation and consisting of 21 independent parameters.

Definition 6.3. Isotropic elasticity. If W does not depend on $\mathbf{x} \in \mathcal{B}$ the material is *homogeneous*. If W is rotationally invariant the material behavior is *isotropic*. In case of additionally constant \mathbb{C} the material is linear elastic and

$$\mathbb{C} = \lambda \mathbf{1} \otimes \mathbf{1} + 2G \mathbf{II}. \quad (6.4)$$

where $\mathbf{1}$ is the second order and \mathbf{II} is the fourth-order identity tensor defined by

$$\mathbf{II}_{ijkl} := \frac{1}{2}[\delta_{ik}\delta_{jl} + \delta_{il}\delta_{jk}].$$

The two components, λ and G are the Lamé constants. If the matrix notation defined in Eq. (6.7) is used, the elastic tangent \mathbb{C} can also be defined by

$$\mathbb{C} = \begin{pmatrix} C_{11} & C_{12} & C_{12} & 0 & 0 & 0 \\ C_{12} & C_{11} & C_{12} & 0 & 0 & 0 \\ C_{12} & C_{12} & C_{11} & 0 & 0 & 0 \\ 0 & 0 & 0 & \frac{C_{11}-C_{12}}{2} & 0 & 0 \\ 0 & 0 & 0 & 0 & \frac{C_{11}-C_{12}}{2} & 0 \\ 0 & 0 & 0 & 0 & 0 & \frac{C_{11}-C_{12}}{2} \end{pmatrix} \quad (6.5)$$

where

$$\begin{aligned} C_{11} &= \lambda + 2G = \frac{E}{1+\nu} \frac{1-\nu}{1-2\nu}, \\ C_{12} &= \lambda = \frac{E}{1+\nu} \frac{\nu}{1-2\nu}, \\ \frac{C_{11}-C_{12}}{2} &= G. \end{aligned}$$

6.2 Anisotropic elasticity

6.2.1 Introduction

In general, geomaterials can be assumed to be isotropic. However, geologic observations show that rocks, soils, and fault zones typically have anisotropic and inhomogeneous material properties. The most common type of anisotropy found in geomaterials is the transverse isotropy, where there is an axis of elastic symmetry, generally vertical, and isotropy is found only inside the planes perpendicular to that axis.

Thus, for example the mechanical behavior of layered inclined soil or rock formations can be approximated by transversely isotropic elasticity. The required theory and its application in a verification example will be presented in this section. An application within a geotechnical framework using RockFlow's unsaturated flow model is given by Shao et al. (2006) [93]. They are analyzing the saturated-unsaturated behavior of anisotropic formations of clay materials.

6.2.2 Notation

For the implementation of material laws the second and fourth order tensors are expressed in terms of vectors and matrices, respectively. The resulting notation is called *contracted notation* or *Voigt-Kelvin notation*, see e.g. Reddy (2002) [82]. With the following change of subscripts

$$11 \rightarrow 1, 22 \rightarrow 2, 33 \rightarrow 3, 23 \rightarrow 4, 13 \rightarrow 5, 12 \rightarrow 6.$$

the stress and strain tensors are expressed in a single-subscript notation

$$\begin{pmatrix} \sigma_1 \\ \sigma_2 \\ \sigma_3 \\ \sigma_4 \\ \sigma_5 \\ \sigma_6 \end{pmatrix} = \begin{pmatrix} \sigma_{11} \\ \sigma_{22} \\ \sigma_{33} \\ \sigma_{23} \\ \sigma_{13} \\ \sigma_{12} \end{pmatrix}, \quad \begin{pmatrix} \varepsilon_1 \\ \varepsilon_2 \\ \varepsilon_3 \\ \varepsilon_4 \\ \varepsilon_5 \\ \varepsilon_6 \end{pmatrix} = \begin{pmatrix} \varepsilon_{11} \\ \varepsilon_{22} \\ \varepsilon_{33} \\ \varepsilon_{23} \\ \varepsilon_{13} \\ \varepsilon_{12} \end{pmatrix} \quad (6.6)$$

and the stiffness tensor is expressed analogously with two subscript components

$$\{C_{ijkl} | \{i, j, k, l\} = 1, 2, 3\} \rightarrow \{C_{\alpha\beta} | \{\alpha, \beta\} = 1, \dots, 6\}. \quad (6.7)$$

6.2.3 Transverse isotropy

An *orthotropic* body has material properties that are different in three mutually perpendicular directions at a point in the body and, further, have three mutually perpendicular planes of material symmetry. Thus, the properties are a function of orientation at a point in the body. A special class of *orthotropic* materials is a material which has the same properties in one plane but different properties in the direction normal to this plane. Such a material class is called *transversely isotropic*.

A transversely isotropic material is described by five independent elastic coefficients λ , G_T , G_L , α and β . The direction \mathbf{a} ($\|\mathbf{a}\| = 1$) perpendicular to the plane of isotropy is called axis of transverse isotropy. The derivation and formulation of transversely isotropic material is given in detail by Schröder (1996) [90]. In tensor notation, the material is described by the following expression

$$\mathbb{C} = \lambda \mathbf{1} \otimes \mathbf{1} + 2G_T \mathbb{I} + \alpha [\mathbf{a} \otimes \mathbf{a} \otimes \mathbf{1} + \mathbf{a} \otimes \mathbf{a} \otimes \mathbf{1}] + 2(G_L - G_T) \mathbf{a} \mathbb{I} \mathbf{a} + \beta \mathbf{a} \otimes \mathbf{a} \otimes \mathbf{a} \otimes \mathbf{a}. \quad (6.8)$$

In case of an axis of isotropy \mathbf{a} lying parallel to direction 3 Eq. (6.8) leads to the following matrix representation

$$\mathbb{C} = \begin{pmatrix} \lambda + 2G_T & \lambda & \lambda + \alpha & 0 & 0 & 0 \\ \lambda & \lambda + 2G_T & \lambda + \alpha & 0 & 0 & 0 \\ \lambda + \alpha & \lambda + \alpha & \lambda + 2\alpha + \beta + 4G_L - 2G_T & 0 & 0 & 0 \\ 0 & 0 & 0 & G_L & 0 & 0 \\ 0 & 0 & 0 & 0 & G_L & 0 \\ 0 & 0 & 0 & 0 & 0 & G_T \end{pmatrix}. \quad (6.9)$$

Consequently, transverse isotropic material is defined by the following five independent parameters

$$\mathbb{C} = \begin{pmatrix} C_{11} & C_{12} & C_{13} & 0 & 0 & 0 \\ C_{12} & C_{11} & C_{13} & 0 & 0 & 0 \\ C_{13} & C_{13} & C_{33} & 0 & 0 & 0 \\ 0 & 0 & 0 & C_{44} & 0 & 0 \\ 0 & 0 & 0 & 0 & C_{44} & 0 \\ 0 & 0 & 0 & 0 & 0 & \frac{1}{2}(C_{11} - C_{12}) \end{pmatrix}. \quad (6.10)$$

The description of transversely isotropic material in an invariant formulation is given in Table C.1. The parameters in engineering representation depend on the axis of isotropy. In App. C.3 the parameters needed in case of direction 1, 2 and 3 are summarized in Tables C.2, C.3 and C.4, respectively.

6.2.4 Numerical example

A tensile test is carried out in plane strain conditions according to an example proposed by Schröder (1996) [90]. The orientation of the material properties is rotated during the simulation.

6.2.4.1 Set-up

The set-up is depicted in Fig. 6.1. The behavior of the material is transversely isotropic. During the simulation the axis of transverse isotropy is rotated counter-clockwise with time starting with $\gamma = 0^\circ$ and ending with $\gamma = 180^\circ$.

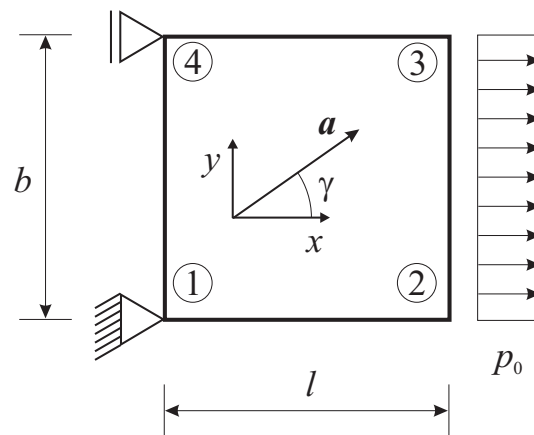


Figure 6.1: Tensile test. Set-up.

6.2.4.2 Representation of anisotropic material parameters

Invariant representation. The applied load, the geometry data and material properties in invariant representation are given in Table 6.1. *Remark:* In this invariant representation the x -direction of the prescribed coordinate system is always chosen to be the axis of transverse isotropy \mathbf{a} .

Table 6.1: Load, material and geometric properties.

	Parameter	Value
Load	p_0	0.2 MPa
Material	λ	1000 MPa
	G_L	375 MPa
	G_T	175 MPa
	α	10 MPa
	β	10 MPa
Local coordinate system	$\gamma(t)$	$0^\circ \dots 180^\circ$
Geometry	b	10 mm
	l	10 mm

Representation in terms of engineering elastic properties. Two further simulations are carried out for the purpose of comparison using equivalent elastic properties. Now, these properties are given in engineering representation. The resulting values remain unchanged.

The two sets of parameters for two different axis of transverse isotropy (first case x and second case y) are given in Table 6.2 and 6.3, respectively. For the first set of parameters ($\mathbf{a} = x$ -direction), the rotation of the local coordinate system starts with the initial global coordinate system: the angle is $\gamma = 0^\circ \dots 180^\circ$.

Table 6.2: Engineering representation of elastic properties with axis of transverse isotropy in x -direction.

	Parameter	Value
Material	E_1	1311.82972 MPa
	$E_2 = E_3$	561.121223 MPa
	ν_{12}	0.18383691
	ν_{23}	0.60320349
	G_{12}	375.0 MPa
Local coordinate system	$\gamma(t)$	$0^\circ \dots 180^\circ$

The application of the second set of parameters ($\mathbf{a} = y$ -direction) requires the rotation of the coordinate system in a way that the local y -axis is mapped on the global x -axis: the angle is $\gamma = -90^\circ \dots 90^\circ$. In both cases, the same results are obtained (c.f. Fig. 6.2).

Table 6.3: Engineering representation of elastic properties with axis of transverse isotropy in y -direction.

	Parameter	Value
Material	E_2	1311.82972 MPa
	$E_1 = E_3$	561.121223 MPa
	ν_{21}	0.18383691
	ν_{13}	0.60320349
	G_{21}	375.0 MPa
Local coordinate system	$\gamma(t)$	$-90^\circ \dots 90^\circ$

6.2.4.3 Numerical results

The numerical results determined with RockFlow are compared to values given in [90] in Fig. 6.2. The results show a good agreement.

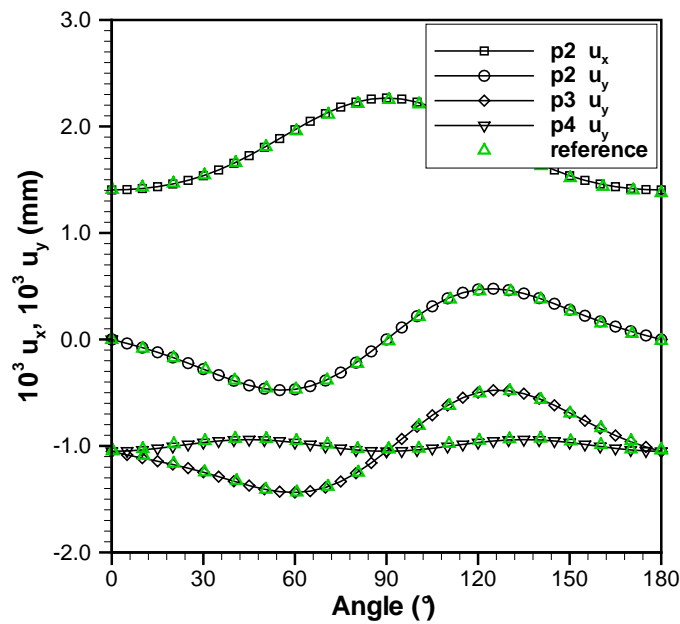


Figure 6.2: Tensile test. RockFlow results and reference values taken from Schröder (1996) [90].

6.3 Rate-independent plasticity

In this section a short introduction to the numerical treatment of plastic material behavior is given. A broad overview of theoretical and computational aspects of inelasticity are given by Simo and Hughes (1998) [94] or by Wriggers (2001) [108].

The classical theory of plasticity expounds the idea that a linear solid passes into a flowing state as soon as a critical state of stress is reached. The location of this stress state is defined by the yield surface bounding the elastic region in the stress space.

Several yield surfaces are presented in Sec. 6.4.1 and Sec. 6.4.2. Formulations of elastoplasticity and the resulting numerical algorithms are summarized in Sec. 6.5.1 and Sec. 6.5.2.

6.3.1 Governing equations

6.3.1.1 Additive decomposition of the strain tensor

It is assumed that the strain tensor $\boldsymbol{\varepsilon}$ can be decomposed into an elastic and a plastic part

$$\boldsymbol{\varepsilon} = \boldsymbol{\varepsilon}^{\text{el}} + \boldsymbol{\varepsilon}^{\text{pl}}. \quad (6.11)$$

Since the strain tensor $\boldsymbol{\varepsilon}$ is an independent variable and the evolution of the plastic part $\boldsymbol{\varepsilon}^{\text{pl}}$ is defined by the flow rule (6.16) given below. Eq. (6.11) defines the elastic strain tensor with $\boldsymbol{\varepsilon}^{\text{el}} := \boldsymbol{\varepsilon} - \boldsymbol{\varepsilon}^{\text{pl}}$.

6.3.1.2 Stress response

The stress tensor is related to the elastic strain $\boldsymbol{\varepsilon}^{\text{el}}$ by means of a stored energy function $W : \mathcal{B} \times \mathbb{S} \rightarrow \mathbb{R}$ according to the (hyperelastic) relationship (cf. Eq. (6.2))

$$\boldsymbol{\sigma}(\boldsymbol{x}) = \frac{\partial W[\boldsymbol{x}, \boldsymbol{\varepsilon}^{\text{el}}(\boldsymbol{x})]}{\partial \boldsymbol{\varepsilon}^{\text{el}}}. \quad (6.12)$$

In linearized elasticity, the stored energy function W is a quadratic form in the elastic strain, i.e., $W = \frac{1}{2} \boldsymbol{\varepsilon}^{\text{el}} : \mathbb{C} : \boldsymbol{\varepsilon}^{\text{el}}$ and with assumption (6.11) we get the relationship

$$\boldsymbol{\sigma} = \mathbb{C} : [\boldsymbol{\varepsilon} - \boldsymbol{\varepsilon}^{\text{pl}}]. \quad (6.13)$$

6.3.1.3 Elastic domain and yield condition

The function $f : \mathbb{S} \times \mathbb{R} \rightarrow \mathbb{R}$ called *yield criterion* constrains the admissible states $\{\boldsymbol{\sigma}, \boldsymbol{q}\} \in \mathbb{S} \times \mathbb{R}$ in stress space to lie in the set $\mathbb{E}_{\boldsymbol{\sigma}}$ defined by

$$\mathbb{E}_{\boldsymbol{\sigma}} := \{(\boldsymbol{\sigma}, \boldsymbol{q}) \in \mathbb{S} \times \mathbb{R} \mid f(\boldsymbol{\sigma}, \boldsymbol{q}) \leq 0\}. \quad (6.14)$$

The interior of \mathbb{E}_σ is called the elastic domain, whereas the boundary of \mathbb{E}_σ , denoted by $\partial\mathbb{E}_\sigma$ and defined by

$$\partial\mathbb{E}_\sigma := \{(\boldsymbol{\sigma}, \mathbf{q}) \in \mathbb{S} \times \mathbb{R} \mid f(\boldsymbol{\sigma}, \mathbf{q}) = 0\}, \quad (6.15)$$

is called the *yield surface* in stress space. It is important to notify that states $\{\boldsymbol{\sigma}, \mathbf{q}\}$ outside \mathbb{E}_σ are nonadmissible and ruled out in classical plasticity.

6.3.1.4 Flow rule and hardening law

The nature of irreversibility is defined by the equations of evolution for plastic strain rate $\dot{\boldsymbol{\varepsilon}}^{\text{pl}}$ and the evolution of the internal variables $\dot{\mathbf{q}}$. The equations, called flow rule and hardening law, are prescribed functions

$$\dot{\boldsymbol{\varepsilon}}^{\text{pl}} = \gamma \mathbf{r}(\boldsymbol{\sigma}, \mathbf{q}), \quad (6.16)$$

$$\dot{\mathbf{q}} = -\gamma \mathbf{h}(\boldsymbol{\sigma}, \mathbf{q}), \quad (6.17)$$

where $\mathbf{r} : \mathbb{S} \times \mathbb{R} \rightarrow \mathbb{S}$ and $\mathbf{h} : \mathbb{S} \times \mathbb{R} \rightarrow \mathbb{R}$ define the direction of plastic flow and the type of hardening, respectively. The parameter γ is called consistency parameter and has to obey the *Kuhn-Tucker complementary conditions*

$$\gamma \geq 0, \quad f(\boldsymbol{\sigma}, \mathbf{q}) \leq 0, \quad \gamma f(\boldsymbol{\sigma}, \mathbf{q}) = 0 \quad (6.18)$$

and the *consistency requirement*

$$\gamma \dot{f}(\boldsymbol{\sigma}, \mathbf{q}) = 0. \quad (6.19)$$

The evaluation of condition (6.19) provides a derivation of the consistency parameter γ and is shown in Section 6.3.1.6.

6.3.1.5 Loading/unloading conditions

The investigation of the *Kuhn-Tucker* conditions (6.18) and the consistency requirement (6.19) results in the following possible situations

$$\left\{ \begin{array}{l} f \Leftrightarrow (\boldsymbol{\sigma}, \mathbf{q}) \in \text{int}(\mathbb{E}_\sigma) \\ f \Leftrightarrow (\boldsymbol{\sigma}, \mathbf{q}) \in \partial\mathbb{E}_\sigma \end{array} \right. \Rightarrow \left\{ \begin{array}{ll} \gamma = 0 & \text{elastic,} \\ \dot{f} < 0 \Rightarrow \gamma = 0 & \text{elastic unloading,} \\ \dot{f} = 0 \text{ and } \gamma = 0 & \text{neutral loading,} \\ \dot{f} = 0 \text{ and } \gamma > 0 & \text{plastic loading.} \end{array} \right. \quad (6.20)$$

6.3.1.6 Consistency condition

In order to exploit the consistency requirement (6.19), the time derivative of the yield function f at $(\boldsymbol{\sigma}, \mathbf{q}) \in \mathbb{E}_\sigma$ is evaluated

$$\dot{f} = \partial_\sigma f : \dot{\boldsymbol{\sigma}} + \partial_q f \cdot \dot{\mathbf{q}} \quad (6.21)$$

$$= \partial_\sigma f : \mathbb{C} : [\dot{\boldsymbol{\varepsilon}} - \dot{\boldsymbol{\varepsilon}}^{\text{pl}}] + \partial_q f \cdot \dot{\mathbf{q}} \quad (6.22)$$

$$= \partial_\sigma f : \mathbb{C} : \dot{\boldsymbol{\varepsilon}} - \gamma [\partial_\sigma f : \mathbb{C} : \mathbf{r} + \partial_q f \cdot \mathbf{h}] \leq 0. \quad (6.23)$$

It can be shown that the following inequality holds for *associated perfect plasticity*

$$[\partial_{\sigma} f : \mathbb{C} : \mathbf{r} + \partial_{\mathbf{q}} f \cdot \mathbf{h}] > 0, \quad (6.24)$$

for all admissible states $\{\boldsymbol{\sigma}, \mathbf{q}\} \in \partial \mathbb{E}_{\sigma}$ and thus, the following equivalence can be derived from Eq. (6.19)

$$\dot{f} = 0 \quad \Leftrightarrow \quad \gamma = \frac{\langle \partial_{\sigma} f : \mathbb{C} : \dot{\boldsymbol{\epsilon}} \rangle}{\partial_{\sigma} f : \mathbb{C} : \mathbf{r} + \partial_{\mathbf{q}} f \cdot \mathbf{h}} \quad (6.25)$$

where $\langle \bullet \rangle := [\bullet + |\bullet|]/2$ denotes the ramp function. In view of (6.24) and (6.25) we can also conclude that for $f = 0$ and $\dot{f} = 0$

$$\gamma \geq 0 \Leftrightarrow \partial_{\sigma} f : \mathbb{C} : \mathbf{r} + \partial_{\mathbf{q}} f \cdot \mathbf{h} \geq 0. \quad (6.26)$$

This inequality also gives a geometric interpretation of plastic ($\Theta < 90^\circ$) and neutral $\Theta = 90^\circ$ loading conditions depicted in Fig. 6.3.

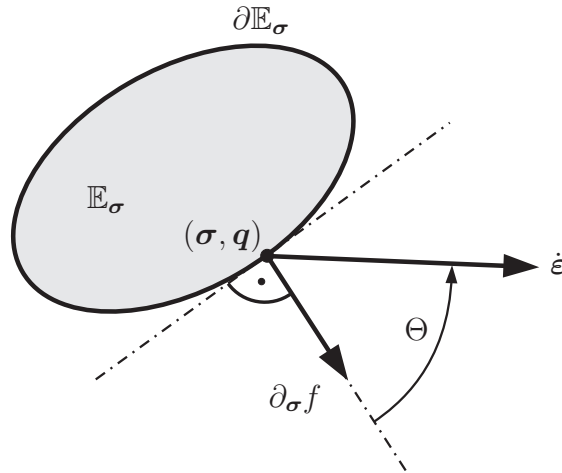


Figure 6.3: Geometric interpretation of plastic loading ($\gamma > 0$) at angles $\Theta < 90^\circ$.

6.3.2 Continuum elasto-plastic tangent

Using (6.13) and the flow rule (6.16) we get

$$\dot{\boldsymbol{\sigma}} = \mathbb{C} : [\dot{\boldsymbol{\epsilon}} - \dot{\boldsymbol{\epsilon}}^{\text{pl}}] = \mathbb{C} : [\dot{\boldsymbol{\epsilon}} - \gamma \mathbf{r}]. \quad (6.27)$$

With the substitution of γ in Eq. (6.27) by the derivation of (6.25), the change of $\boldsymbol{\sigma}$ in terms of the total strain rate $\dot{\boldsymbol{\epsilon}}$ is

$$\dot{\boldsymbol{\sigma}} = \mathbb{C}^{\text{ep}} : \dot{\boldsymbol{\epsilon}}, \quad (6.28)$$

where \mathbb{C}^{ep} is the so-called tensor of elastoplastic moduli given by

$$\mathbb{C}^{\text{ep}} = \begin{cases} \mathbb{C} & \text{if } \gamma = 0, \\ \mathbb{C} - \frac{\mathbb{C} : \mathbf{r} \otimes \mathbb{C} : \partial_{\sigma} f}{\partial_{\sigma} f : \mathbb{C} : \mathbf{r} + \partial_{\mathbf{q}} f \cdot \mathbf{h}} & \text{if } \gamma > 0. \end{cases} \quad (6.29)$$

For arbitrary $\mathbf{r}(\boldsymbol{\sigma}, \mathbf{q})$ the elasto-plastic tangent \mathbb{C}^{ep} is generally non-symmetric, except of the case that the following equivalence holds

$$\mathbf{r}(\boldsymbol{\sigma}, \mathbf{q}) = \partial_{\sigma} f(\boldsymbol{\sigma}, \mathbf{q}) \quad (6.30)$$

which defines the *associative flow rule*.

6.3.3 Consistent elasto-plastic tangent

The evolution equation of plastic strain $\boldsymbol{\varepsilon}^{\text{pl}}$ and internal variables \mathbf{q} has to be integrated in time. Starting from the temporal discretization and the selection of an appropriate time integration scheme outlined in Sec. 4.3, it becomes obvious that the *continuum* tangent, presented in Section 6.3.2, has to be modified as it is valid only for small time steps as $\Delta t \rightarrow 0$ comprises $\Delta \gamma \rightarrow 0$.

The derivation of the elasto-plastic tangent moduli reflecting the incremental characteristic of the integration algorithm finally results in a *consistent* linearization. With this *consistent* or *algorithmic* tangent at hand, a quadratic rate of (asymptotic) convergence (see App. A.1) can be assured for the solution of the non-linear problem as described by Simo and Taylor (1985) [95].

The procedure is equivalent with the derivation of the tangent of the continuum problem, but additionally the algorithmic expression of $\boldsymbol{\sigma}_{n+1}$ is being regarded and differentiated with respect to the strain tensor $\boldsymbol{\varepsilon}_{n+1}$. According to Eq. (6.27) and (6.16) the partial derivatives of the consistency parameter γ , the direction of plastic flow \mathbf{r} and finally the integration algorithm itself come into play. The procedure of linearization and the resulting *algorithmic* (consistent) tangent moduli in case of associative J_2 flow rules with general nonlinear kinematic and isotropic hardening are given by Simo and Taylor (1985) [95] also mentioning non-associative pressure sensitive yield criteria (e.g. *Drucker-Prager*). Derivations for the *Cam-clay* plasticity models are given by Borja and Lee (1990) [12]. More details can be found in Simo and Hughes (1998) [94] or Wriggers (2001) [108] among others.

6.4 Yield criteria for isotropic material

In this section a brief review of yield criteria is given. For isotropic materials, the yielding only depends on the magnitudes of the principle stresses, thus the yield function f is $f(I_1, I_2, I_3)$. Criteria, which are dependent on deviatoric stresses, are given in Section 6.4.1, while those criteria which also include the influence of hydrostatic pressure are summarized in Section 6.4.2. The yield surface has been evaluated within

a cylindrical domain around the hydrostatic axis. The segment at the upper left part of the yield surface has been omitted for the purpose of a better visualization.

The evaluation of yield surfaces has been used for the prediction of safety factors and threshold levels of damage in Task C of the DECOVALEX-THMC project (see [110, 84]).

6.4.1 Criteria for pressure insensitive material

For metallic material experimental evidence allows to assume that the hydrostatic pressure has no effect on plastic yielding. The yield function F can be expressed by $f = f(J_2)$ for the *von Mises* (Fig. 6.4) or by $f = f(J_2, J_3)$ for the *Tresca* (Fig. 6.5) yield criterion.

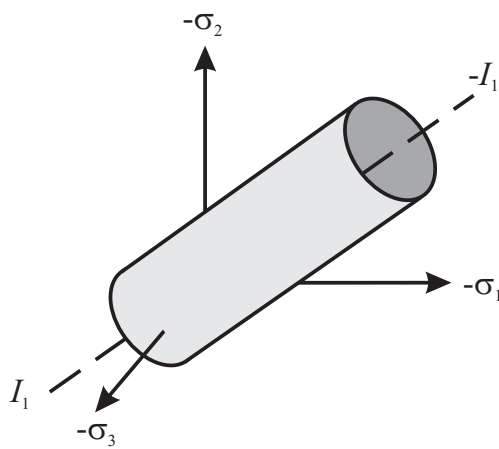


Figure 6.4: Yield surface of *von Mises* criterion.

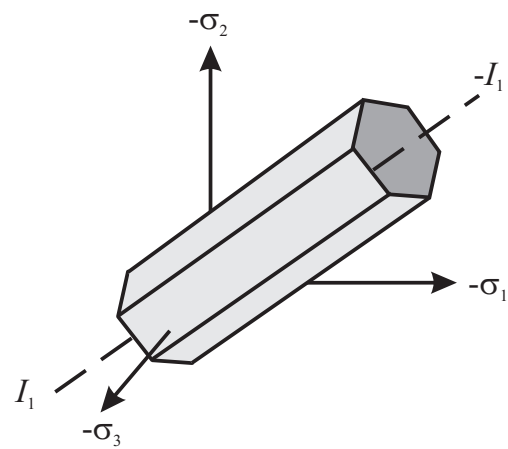


Figure 6.5: Yield surface of *Tresca* criterion.

6.4.2 Criteria for pressure sensitive material

The yielding of porous materials is pressure sensitive. The yield function F can be expressed by $f = f(I_1, J_2)$ representing the yield surface of the *Drucker-Prager* model depicted in Fig. 6.6.

For granular media, yielding and plastic flow are known to be influenced by all three stress invariants I_1 , J_2 and J_3 , thus $f = f(I_1, J_2, J_3)$. The *Mohr-Coulomb* model or *Ehlers's* single surface model belong to this group. Their yield surfaces are depicted exemplarily in Figs. 6.7 and 6.8.

6.5 Constitutive models with pressure insensitive yield criterion

A broad overview of the theory of elasto-plasticity, especially metal plasticity, its algorithmic formulation and numerical implementation can be found in Miehe (1993) [72] or Simo and Hughes (1993) [94].

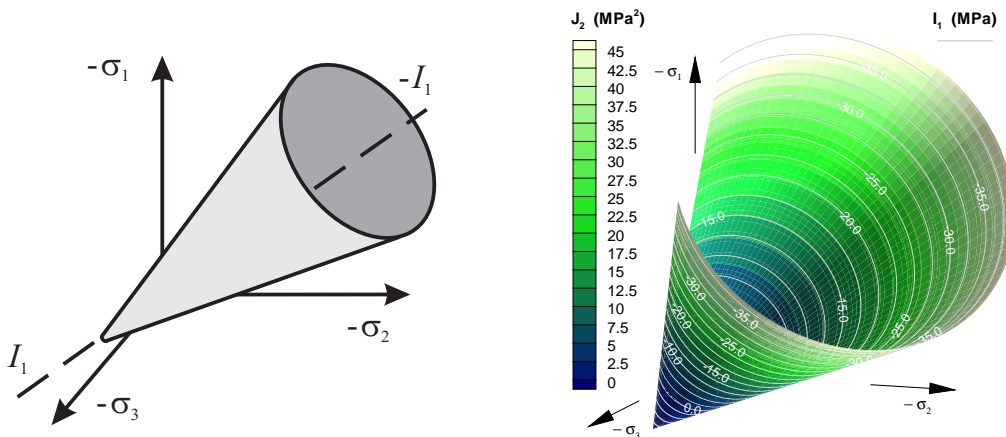


Figure 6.6: Yield surface of *Drucker-Prager* criterion.

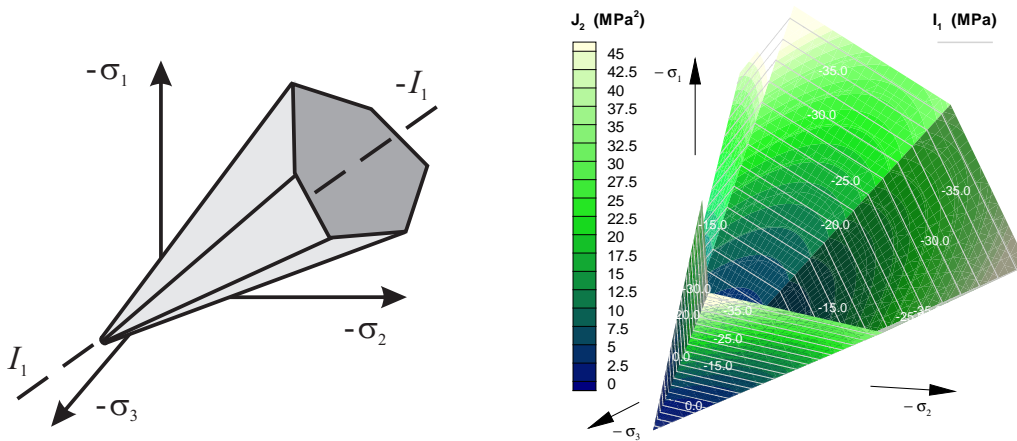


Figure 6.7: *Mohr-Coulomb* yield surface.

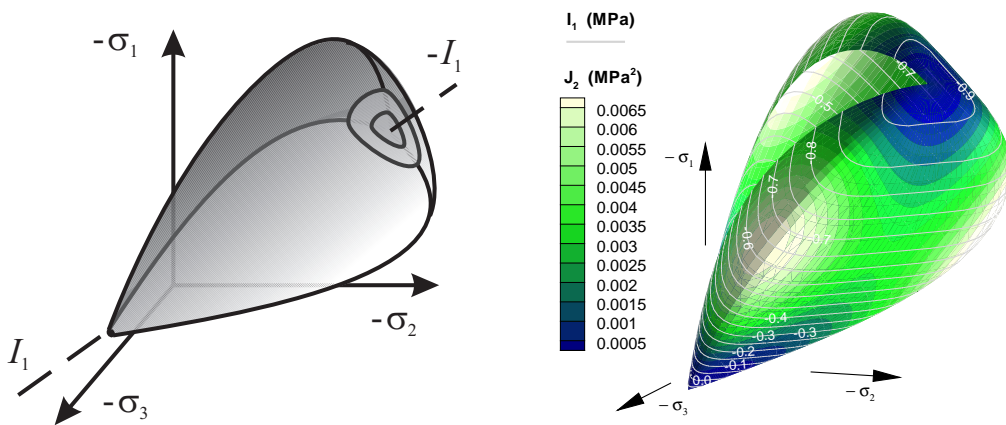


Figure 6.8: Single yield surface. Material properties are taken from Ehlers (2002) [33] (p. 58).

6.5.1 Perfect plasticity – Prandtl-Reuss equation

6.5.1.1 Model formulation

The classical *Prandtl-Reuss* equations of perfect plasticity are derived from the following assumptions

1. The elastic response is linear isotropic.
2. The *Huber–von Mises* yield condition

$$f(\mathbf{s}) = \|\mathbf{s}\| - R = f(J_2) = \sqrt{2} \sqrt{J_2} - \sqrt{2} R \quad (6.31)$$

is used, where \mathbf{s} is the deviatoric part of the stress tensor, R is the radius of the yield surface defined by $R = \sqrt{\frac{2}{3}} \sigma_Y$.

3. The associated *Levy–Saint Venant* flow rule is used.
4. No hardening occurs i.e. $\mathbf{h} \equiv 0$.

A short overview of the basic equations characterizing perfect plasticity is given in Box. 6.1.

Box 6.1: Formulation of perfect plasticity.

Elastic strain	$\boldsymbol{\varepsilon}^{\text{el}} = \boldsymbol{\varepsilon} - \boldsymbol{\varepsilon}^{\text{pl}}$
	$\varepsilon_v^{\text{el}} = \text{tr} \boldsymbol{\varepsilon}^{\text{el}}, \quad \mathbf{e}^{\text{el}} = \boldsymbol{\varepsilon}^{\text{el}} - \frac{1}{3} \varepsilon_v^{\text{el}} \mathbf{1}$
Stored energy function	$W = K \frac{1}{2} (\varepsilon_v^{\text{el}})^2 + G \text{tr}(\mathbf{e}^{\text{el}})^2$
Stress	$\boldsymbol{\sigma} = K \varepsilon_v^{\text{el}} \mathbf{1} + 2G \mathbf{e}^{\text{el}}$
Yield function	$f = f(\mathbf{s}) = \ \mathbf{s}\ - \sqrt{\frac{2}{3}} \sigma_Y$
Flow rule	$\dot{\boldsymbol{\varepsilon}}^{\text{pl}} = \gamma \mathbf{n}, \quad \mathbf{n} := \frac{\partial f(\mathbf{s})}{\partial \boldsymbol{\sigma}} = \frac{\mathbf{s}}{\ \mathbf{s}\ }$
Kuhn Tucker loading/unloading conditions	$\gamma \geq 0, \quad f(\mathbf{s}) \leq 0, \quad \gamma f(\mathbf{s}) = 0$

6.5.1.2 Consistent elasto-plastic tangent moduli

The consistent elasto-plastic tangent is

$$\mathbb{C}_{n+1}^{\text{algo}} = K\mathbf{1} \otimes \mathbf{1} + 2G\beta_{n+1}[\mathbb{I} - \frac{1}{3}\mathbf{1} \otimes \mathbf{1}] - 2G\beta_{n+1}\mathbf{n}_{n+1} \otimes \mathbf{n}_{n+1} \quad (6.32)$$

where

$$\beta_{n+1} := 1 - \frac{2G\Delta\gamma}{\|\mathbf{s}_{n+1}^{\text{trial}}\|}. \quad (6.33)$$

6.5.1.3 Algorithmic formulation

The algorithmic formulation is summarized in Box 6.2.

Box 6.2: Radial return algorithm. Perfect plasticity.

1. Trial step.

- (a) $\boldsymbol{\varepsilon}_{n+1}^{\text{el,trial}} = \boldsymbol{\varepsilon}_n^{\text{el}} + \Delta\boldsymbol{\varepsilon}_{n+1}^{\text{el}}$
- (b) $\boldsymbol{\sigma}_{n+1}^{\text{trial}} = \mathbb{C}^{\text{el}}\boldsymbol{\varepsilon}_{n+1}^{\text{el,trial}}$
- (c) $f_{n+1}^{\text{trial}} = f(\mathbf{s}_{n+1}^{\text{trial}})$

2. (a) Elastic deformation or (b) plastic correction.

(a) $f_{n+1}^{\text{trial}} \leq 0 \Rightarrow$ elastic deformation

- i. $\boldsymbol{\sigma}_{n+1} = \boldsymbol{\sigma}_{n+1}^{\text{trial}}$
- ii. $\boldsymbol{\varepsilon}_{n+1}^{\text{el}} = \boldsymbol{\varepsilon}_{n+1}^{\text{el,trial}}$
- iii. Next load step (1.)

(b) $f_{n+1}^{\text{trial}} > 0 \Rightarrow$ plastic correction.

- i. $\boldsymbol{\varepsilon}_{n+1}^{\text{el}} = \boldsymbol{\varepsilon}_{n+1}^{\text{el,trial}} - \boldsymbol{\varepsilon}_{n+1}^{\text{pl}}, \quad \boldsymbol{\varepsilon}_{n+1}^{\text{pl}} = \boldsymbol{\varepsilon}_n^{\text{pl}} + \Delta\boldsymbol{\varepsilon}^{\text{pl}}$
 where $\Delta\boldsymbol{\varepsilon}^{\text{pl}} = \Delta\gamma\mathbf{n}, \quad \mathbf{n} = \frac{\partial f_{n+1}^{\text{trial}}}{\partial \boldsymbol{\sigma}_{n+1}^{\text{trial}}} = \frac{\mathbf{s}_{n+1}^{\text{trial}}}{\|\mathbf{s}_{n+1}^{\text{trial}}\|}$

$$\Delta\gamma = \frac{f_{n+1}^{\text{trial}}}{2G}$$

- ii. $\boldsymbol{\sigma}_{n+1} = \boldsymbol{\sigma}_{n+1}^{\text{tr}} - \mathbb{C}^{\text{ep}}\Delta\boldsymbol{\varepsilon}^{\text{pl}}$
- iii. Next iterative step (1.)

3. Next load step (1.)

6.5.2 J_2 plasticity with isotropic/kinematic hardening

6.5.2.1 Model formulation

J_2 plasticity with isotropic/kinematic hardening is formulated as follows

1. The elastic response is linear isotropic.
2. The yield condition is defined by

$$f(\mathbf{s}) = \|\boldsymbol{\xi}\| - \sqrt{\frac{2}{3}} H_{\text{iso}}(e_q^{\text{pl}}) \quad (6.34)$$

with $\boldsymbol{\xi} = \mathbf{s} - \boldsymbol{\beta}$.

3. The flow rule is associated and a purely deviatoric plastic strain rate \dot{e}^{pl} is derived as follows

$$\dot{e}^{\text{pl}} = \gamma \frac{\boldsymbol{\xi}}{\|\boldsymbol{\xi}\|}. \quad (6.35)$$

4. Isotropic and kinematic hardening occurs. Isotropic hardening $H_{\text{iso}}(e_q^{\text{pl}})$ is a function of the equivalent plastic strain e_q^{pl} . The derivative of this invariant is directly determined by

$$\dot{e}_q^{\text{pl}} = \gamma \sqrt{\frac{2}{3}} \quad (6.36)$$

using Eq. (6.35) and Eq. (C.4).

Kinematic hardening dislocates the center of the *von Mises* yield surface in the deviatoric stress space and is defined by the back stress $\boldsymbol{\beta}$ with $\text{tr} \boldsymbol{\beta} := 0$. Its derivative is as follows

$$\dot{\boldsymbol{\beta}} = \gamma \frac{\boldsymbol{\xi}}{\|\boldsymbol{\xi}\|} \frac{2}{3} H'_{\text{kin}}(e_q^{\text{pl}}). \quad (6.37)$$

6.5.2.2 Consistent elasto-plastic tangent moduli

The consistent elasto-plastic tangent is

$$\mathbb{C}_{n+1}^{\text{algo}} = K \mathbf{1} \otimes \mathbf{1} + 2G \theta_{n+1} [\mathbb{I} - \frac{1}{3} \mathbf{1} \otimes \mathbf{1}] - 2G \bar{\theta}_{n+1} \mathbf{n}_{n+1} \otimes \mathbf{n}_{n+1} \quad (6.38)$$

where

$$\begin{aligned} \theta_{n+1} &:= 1 - \frac{2G \Delta\gamma}{\|\boldsymbol{\xi}_{n+1}^{\text{trial}}\|} \\ \bar{\theta}_{n+1} &:= \frac{1}{1 + \frac{[H'_{\text{iso}}(e_q^{\text{pl}}) + H'_{\text{kin}}(e_q^{\text{pl}})]_{n+1}}{3G}} - (1 - \theta_{n+1}). \end{aligned} \quad (6.39)$$

Box 6.3: The *von Mises* model with non-linear isotropic/kinematic hardening.
Radial return algorithm (cf. [94]).

1. Compute *trial elastic* stress.

$$\begin{aligned} \mathbf{e}_{n+1} &= \boldsymbol{\varepsilon}_{n+1} - \frac{1}{3}(\text{tr}[\boldsymbol{\varepsilon}_{n+1}]) \mathbf{1} \\ \mathbf{s}_{n+1}^{\text{trial}} &= 2G (\mathbf{e}_{n+1} - \mathbf{e}_n^{\text{pl}}) \\ \boldsymbol{\xi}_{n+1}^{\text{trial}} &= \mathbf{s}_{n+1}^{\text{trial}} - \boldsymbol{\beta}_n \end{aligned}$$

2. Check yield condition.

$$f_{n+1}^{\text{trial}} := \|\boldsymbol{\xi}_{n+1}^{\text{trial}}\| - \sqrt{\frac{2}{3}} H_{\text{iso}}([e_q^{\text{pl}}]_n)$$

IF $f_{n+1}^{\text{trial}} \leq 0$ THEN:

$$\text{Set } (\bullet)_{n+1} = (\bullet)_{n+1}^{\text{trial}} \ \& \ \text{EXIT.}$$

ENDIF.

3. Compute \mathbf{n}_{n+1} and find $\Delta\gamma$ in local iteration.

$$\begin{aligned} \mathbf{n}_{n+1} &:= \frac{\boldsymbol{\xi}_{n+1}^{\text{trial}}}{\|\boldsymbol{\xi}_{n+1}^{\text{trial}}\|} \\ [e_q^{\text{pl}}]_{n+1} &:= [e_q^{\text{pl}}]_n + \sqrt{\frac{2}{3}} \Delta\gamma \end{aligned}$$

4. Update back stress, strain and stress.

$$\begin{aligned} \boldsymbol{\beta}_{n+1} &= \boldsymbol{\beta}_n + \sqrt{\frac{2}{3}} [H_{\text{kin}}([e_q^{\text{pl}}]_{n+1}) - H_{\text{kin}}([e_q^{\text{pl}}]_n)] \mathbf{n}_{n+1} \\ \mathbf{e}_{n+1}^{\text{pl}} &= \mathbf{e}_n^{\text{pl}} + \Delta\gamma \mathbf{n}_{n+1} \\ \boldsymbol{\sigma}_{n+1} &= K \text{tr} \boldsymbol{\varepsilon}_{n+1} \mathbf{1} + \mathbf{s}_{n+1}^{\text{trial}} - 2G \Delta\gamma \mathbf{n}_{n+1} \end{aligned}$$

5. Compute *consistent* elasto-plastic tangent moduli given in (6.38).

6.5.2.3 Algorithmic formulation

The algorithmic formulation is summarized in Box 6.3.

6.6 Constitutive models with pressure sensitive yield criterion

In this section, a short introduction to selected material models for cohesive-frictional soils is given. For more details the reader should refer to Khan and Huang (1995) [52], Chen and Baladi (1985) [19] or Desai and Siriwardane (1984) [28], amongst others.

The yielding of porous materials is usually characterized by a pressure sensitive behavior. Thus, the yield criterion for these materials has to incorporate the influence of the hydrostatic pressure. Material models of this type are for example the *Mohr-Coulomb* model or the *Drucker-Prager* model. Both models are characterized by yield functions that linearly depend on the deviatoric and hydrostatic parts of the stress tensor. As these models tend to overestimate the shear strength at higher compressive mean stress, models with a non-linear increase of shear strength, e. g. described by Ehlers (1995) [32], are advantageous.

A significant disadvantage of the *Mohr-Coulomb* model emerges because of the corners of the hexagonal yield surface leading to numerical instability. In order to avoid these problems smooth approximations of the hexagonal yield surface have been used in Lade and Duncan (1975) [62] and Lade (1977) [61]. A smooth yield surface that very well approximates the *Mohr-Coulomb* criterion has also been presented by Matsuoka and Nakai (1974) [71].

In more general formulation based on three invariants, the conical yield surfaces of *Drucker-Prager*, *Matsuoka-Nakai* and *Lade-Duncan* can be represented and additionally extended by a non-linear pressure sensitive cone. Formulations and comparative investigation can be found in Ehlers (1995) [32] or Borja and Aydin (2004) [11], respectively.

The above mentioned family of three-invariant plasticity models including a compression cap is able to capture the entire spectrum of yielding of geomaterials including simple shearing, pure compaction or dilation.

6.6.1 Mohr-Coulomb model

This model is based on the *Coulomb* friction failure law, which can be expressed in terms of principle stresses as follows

$$(\sigma_1 - \sigma_3) = 2 C \cos \phi - (\sigma_1 + \sigma_3) \sin \phi \quad (6.40)$$

where σ_1 and σ_3 are principle stresses, C is the cohesion and ϕ is the angle of internal friction. For more details refer to Khan and Huang (1995) [52]. The yield function f bounding the elastic domain ($f < 0$) is given by

$$f(\sigma_1, \sigma_3) = (\sigma_1 - \sigma_3) + (\sigma_1 + \sigma_3) \sin \phi - 2 C \cos \phi = f(I_1, J_2, J_3) \quad (6.41)$$

where I_1 is the first invariant of the stress tensor and J_2 , J_3 are the second and third invariant of the deviatoric stress tensor, respectively. As usual in continuum mechanics the tensile stresses are positive.

With the definition of the Lode angle (cf. Fig 6.9)

$$\cos 3\theta = \frac{3\sqrt{3}}{2} \frac{J_3}{J_2^{3/2}} \quad (0 \leq \theta \leq 60^\circ) \quad (6.42)$$

the principle values σ_1 and σ_3 can be replaced by

$$\sigma_1 = \frac{1}{3}I_1 + \frac{2}{\sqrt{3}}\sqrt{J_2} \cos \theta \quad (6.43)$$

$$\sigma_3 = \frac{1}{3}I_1 + \frac{2}{\sqrt{3}}\sqrt{J_2} \cos (\theta + 120^\circ) \quad (6.44)$$

and the yield function for the standard *Mohr-Coulomb* model finally is defined by

$$\frac{1}{3}I_1 \sin \phi + \sqrt{J_2} \left[\sin (\theta + 60^\circ) + \frac{1}{\sqrt{3}} \sin \phi \cos(\theta + 60^\circ) \right] = C \cos \phi. \quad (6.45)$$

6.6.2 Drucker-Prager model

6.6.2.1 Introduction

Drucker and Prager (1952) suggested the following elasto-plastic model treating the yield surface as a smooth circular cone. The yielding is based on the following pressure dependent yield function

$$f(I_1, J_2) = \alpha_\phi I_1 + \sqrt{J_2} - \kappa \quad (6.46)$$

representing a conical surface. Contrary to the *von Mises* yield criterion a hydrostatic stress term appears controlled by the friction coefficient α_ϕ . The parameters α_ϕ and κ can be determined in such a way that the *Drucker-Prager* yield surface coincides the outer corners of the *Mohr-Coulomb* yield surface. If the circular cone shall coincide with the outer apexes (yield stress in compression) of the hexagonal one of the *Mohr-Coulomb* type the parameters are

$$\alpha_\phi = \frac{2 \sin \phi}{\sqrt{3} (3 - \sin \phi)} \quad (6.47)$$

$$\kappa = \frac{6 C \cos \phi}{\sqrt{3} (3 - \sin \phi)}. \quad (6.48)$$

Further values are summarized in Table 6.4 according to Fig 6.9 for the case coinciding with the inner apexes (yield stress in tension) and for a yield surface lying in between or internal.

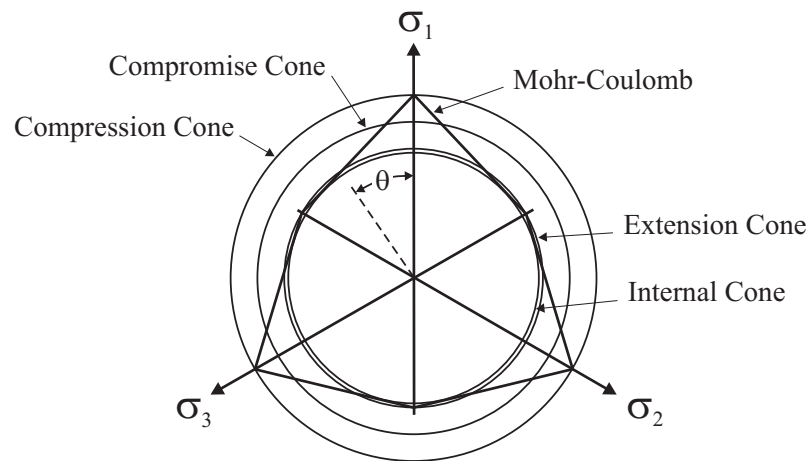


Figure 6.9: Approximation of the *Mohr-Coulomb* yield criterion by a model of *Drucker-Prager* type with compromise cone.

Table 6.4: Parameters of the *Mohr-Coulomb* yield criterion approximated by a model of *Drucker-Prager* type with compromise cone.

Approximation	Friction coefficient	Dilatancy coefficient	Cohesion parameter
Compression Cone	$\alpha_\phi = \frac{2 \sin \phi}{\sqrt{3} (3 - \sin \phi)}$	$\alpha_\psi = \frac{2 \sin \psi}{\sqrt{3} (3 - \sin \psi)}$	$\kappa = \frac{6 C \cos \phi}{\sqrt{3} (3 - \sin \phi)}$
Extension Cone	$\alpha_\phi = \frac{2 \sin \phi}{\sqrt{3} (3 + \sin \phi)}$	$\alpha_\psi = \frac{2 \sin \psi}{\sqrt{3} (3 + \sin \psi)}$	$\kappa = \frac{6 C \cos \phi}{\sqrt{3} (3 + \sin \phi)}$
Compromise Cone	$\alpha_\phi = \frac{2 \sin \phi}{3\sqrt{3}}$	$\alpha_\psi = \frac{2 \sin \psi}{3\sqrt{3}}$	$\kappa = \frac{6 C \cos \phi}{3\sqrt{3}}$
Internal Cone	$\alpha_\phi = \frac{\sin \phi}{\sqrt{3} (3 + \sin^2 \phi)^{1/2}}$	$\alpha_\psi = \frac{\sin \psi}{\sqrt{3} (3 + \sin^2 \psi)^{1/2}}$	$\kappa = \frac{3 C \cos \phi}{\sqrt{3} (3 + \sin^2 \phi)^{1/2}}$

An illustration of a *Drucker-Prager* yield surface lying in between the inner and outer edges of the *Mohr-Coulomb* yield surface is given in Fig. 6.10. The parameters are given in Table 6.5.

Table 6.5: Parameters of the *Mohr-Coulomb* yield criterion approximated by *Drucker-Prager* type.

Parameter	Symbol	Value
Cohesion	C	1.4 MPa
Angle of internal friction	ϕ	20°

In contrast to metals the behavior of geomaterials, e.g. dense or loose sands, show dilatant as well as contractant behavior. In case of an associated flow rule the volumetric plastic strain rate is often over- or underestimated. In order to avoid this, a non-associated flow rule is used. Here, the plastic flow is derived from a plastic potential that differs from the yield function.

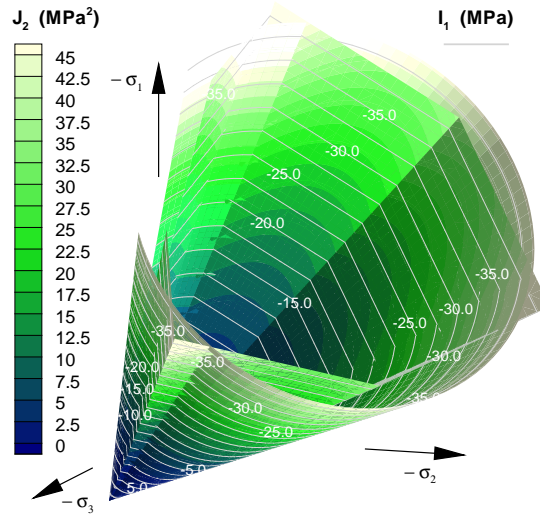


Figure 6.10: Approximation of the *Mohr-Coulomb* yield criterion by a *Drucker-Prager* model.

The plastic potential is

$$g(I_1, J_2) = \alpha_\psi I_1 + \sqrt{J_2} \quad (6.49)$$

where α_ψ is the dilatancy coefficient. An associated model with $\alpha_\phi = \alpha_\psi$ would overestimate the dilatancy. Consequently, the dilatancy coefficient is usually chosen smaller than the friction coefficient.

6.6.2.2 Algorithmic formulation

A short introduction of the algorithmic formulation is given here. For more details the reader should refer to de Borst and Groen [25, 26, 27], Runesson (1987) [86], Loret and Prevost [67, 68] or Panesso (1998) [79], amongst others. For a convenient algorithmic formulation the yield criterion (6.46) is formulated as follows

$$f(\boldsymbol{\sigma}, \mathbf{s}) = \ell \operatorname{tr} \boldsymbol{\sigma} + \|\mathbf{s}\| - \beta_n \frac{2}{3} (C_0 + h e_q^{\text{pl}}) \quad (6.50)$$

and the plastic potential is

$$g(\boldsymbol{\sigma}, \mathbf{s}) = \chi \operatorname{tr} \boldsymbol{\sigma} + \|\mathbf{s}\| - \beta_n \frac{2}{3} (C_0 + h e_q^{\text{pl}}) \quad (6.51)$$

where C_0 is an initial value of cohesion and h is a hardening coefficient. According to Eq. (6.47) the coefficients ℓ and χ depend on the angle of internal friction ϕ and the angle of dilatancy ψ

$$\ell = 2\sqrt{\frac{2}{3}} \frac{\sin \phi}{3 - \sin \phi} \quad \chi = 2\sqrt{\frac{2}{3}} \frac{\sin \psi}{3 - \sin \psi}. \quad (6.52)$$

The coefficient β_n (cf. Eq. (6.48)) is defined as follows

$$\beta_n = 6 \frac{\cos \phi}{3 - \sin \phi}. \quad (6.53)$$

The flow rule, derived from the plastic potential (6.51) is

$$\dot{\boldsymbol{\epsilon}}^{\text{pl}} = \gamma \frac{\partial g}{\partial \boldsymbol{\sigma}} = \gamma \left(\chi \mathbf{1} + \frac{\mathbf{s}}{\|\mathbf{s}\|} \right) = \gamma (\chi \mathbf{1} + \mathbf{n}). \quad (6.54)$$

For the evaluation of the increment $\Delta\gamma$, the consistency requirement (6.19) has to be exploited using the derivative of the yield function f for t_{n+1} that reads

$$\frac{\partial f_{n+1}}{\partial \Delta\gamma_{n+1}} = -9\ell\chi K - 2G - \beta_n \sqrt{\frac{2}{3}} h \sqrt{1 + 3\chi^2}. \quad (6.55)$$

6.6.2.3 Consistent elasto-plastic tangent moduli for dilatant/contractant plastic flow

The consistent elasto-plastic tangent is as follows

$$\mathbb{C}_{n+1}^{\text{algo}} = c_1 \mathbf{1} \otimes \mathbf{1} + c_2 [\mathbb{I} - \frac{1}{3} \mathbf{1} \otimes \mathbf{1}] + c_3 \mathbf{n}_{n+1} \otimes \mathbf{n}_{n+1} + c_4 \mathbf{n}_{n+1} \otimes \mathbf{1} + c_5 \mathbf{1} \otimes \mathbf{n}_{n+1} \quad (6.56)$$

where

$$\begin{aligned} c_1 &= 1 - \frac{9\ell\chi K}{d_1} \\ c_2 &= 2G \left[1 - 2G \frac{\Delta\gamma_{n+1}}{\|\mathbf{s}_{n+1}^{\text{trial}}\|} \right] \\ c_3 &= -4G^2 \left[\frac{1}{d_1} - \frac{\Delta\gamma_{n+1}}{\|\mathbf{s}_{n+1}^{\text{trial}}\|} \right] \\ c_4 &= -\frac{6\ell K G}{d_1} \quad c_5 = -\frac{6\chi K G}{d_1} \\ d_1 &= 9\ell\chi K + 2G + \beta_n h \sqrt{\frac{2}{3}} (1 + 3\chi^2). \end{aligned}$$

6.6.2.4 Consistent elasto-plastic tangent moduli for deviatoric plastic flow

For convenience and useful for comparison the consistent elasto-plastic tangent is also given for a pressure sensitive yield function and a plastic flow of *von Mises* type (cf. [95]). Let f be a pressure sensitive yield function of the form

$$f(\mathbf{s}, \sigma) = \|\mathbf{s}\| - \sqrt{\frac{2}{3}} \kappa(\sigma) \quad (6.57)$$

where $\kappa(\sigma)$ is a non-linear function defining a pressure sensitive yield stress. A non-associated plastic potential g is defined by

$$g(\mathbf{s}) = \|\mathbf{s}\| \quad (6.58)$$

Then, the resulting consistent elasto-plastic tangent is

$$\mathbb{C}_{n+1}^{\text{algo}} = K\mathbf{1} \otimes \mathbf{1} + 2G\beta_{n+1}[\mathbb{I} - \frac{1}{3}\mathbf{1} \otimes \mathbf{1}] - 2G\beta_{n+1}\mathbf{n}_{n+1} \otimes \mathbf{n}_{n+1} + K\sqrt{\frac{2}{3}}\kappa'(\sigma_{n+1})\mathbf{n}_{n+1} \otimes \mathbf{1}, \quad (6.59)$$

where

$$\beta_{n+1} := \sqrt{\frac{2}{3}} \frac{\kappa(\sigma_{n+1})}{\|\mathbf{s}_{n+1}^{\text{trial}}\|}.$$

6.7 Constitutive behavior of the fluid phase

6.7.1 Equation of state for water

The density of the water can be obtained by a linearization of the equation of state

$$\frac{1}{\rho_0^f} \frac{\partial \rho^w}{\partial t} = K_w^{-1} \frac{\partial p^w}{\partial t} - \beta_T \frac{\partial T}{\partial t}. \quad (6.60)$$

where K_w is the bulk modulus of water and β_T is the volumetric thermal expansion coefficient.

6.7.2 Darcy's law

The fluid flux in saturated porous media is described by *Darcy's* law

$$\mathbf{q} = \frac{\mathbf{k}}{\mu_1} (-\nabla p^l + \rho^l \mathbf{g}) \quad (6.61)$$

which may also be derived from the macroscopic balance equation of the fluid momentum. A modification of *Darcy's* law is used for the evaluation of motion of the fluid phase $\varphi^\alpha = \{\varphi^l, \varphi^g\}$ in an unsaturated porous medium. For more details see for example Bear and Bachmat (1990) [4]. It reads as follows

$$\mathbf{J}^{\alpha s} = nS^\alpha \rho^\alpha (\mathbf{v}^\alpha - \mathbf{v}^s) = \rho^\alpha \frac{k_{\text{rel}}^\alpha \mathbf{k}}{\mu^\alpha} (-\nabla p^\alpha + \rho^\alpha \mathbf{g}) \quad (6.62)$$

where the non-linear relative permeability saturation relation $k_{\text{rel}}^\alpha(S^l)$ has to be defined by separate equations, see for example van Genuchten (1980) [106].

6.8 Fourier's law of heat conduction

The heat flux is assumed to obey the generalized version of *Fourier's* law. For the saturated porous medium it can be formulated as follows

$$\mathbf{J}_t = -\mathbf{D} \nabla T, \quad \mathbf{D} = ((1 - n)\lambda^s + n\lambda^l) \mathbf{1} \quad (6.63)$$

where \mathbf{D} is the second order tensor of heat conduction. For the partially saturated case the heat flux \mathbf{J}_t is

$$\mathbf{J}_t = -\mathbf{D} \nabla T, \quad \mathbf{D} = \lambda_b \mathbf{1} \quad (6.64)$$

where

$$\lambda_b = (1 - n) \lambda_s + n S^l \lambda^l + n S^g \lambda^g. \quad (6.65)$$

Chapter 7

Implementation

The whole is more than the sum of its parts.

Metaphysica. Aristotle.

Greek critic, philosopher, physicist, & zoologist.

7.1 Introduction

The derived algorithms presented in the previous chapters have been implemented in the finite element code RockFlow developed at the Institute of Fluid Mechanics and Computer Applications in Civil Engineering. A historical view of the code has been given in Sec. 1.3. For the application of thermo-hydro-mechanical analysis a new model has been set up. This model and the required code improvements are described in the following sections.

7.2 The THM_{plus} model

For the performance of coupled thermo-hydro-mechanical analysis a new model has been created within the framework of the finite element code RockFlow. This new model is called THM_{plus}. In fact, it is a sub module set-up within the model oriented approach of RockFlow. The next sections describe both the model-oriented approach and the processes available in the THM_{plus} model.

7.2.1 The model-oriented approach

The software package RockFlow has been developed in an object-oriented way. The resulting structure provides all objects needed for applying the finite element method. The main part of this structure is a set of *models* containing and defining the model specific data, the objects of the algebraic equations, objects for the control of the simulation cycle and finally interface functions providing access by model independent objects. These additional objects contain the geometric description of the domain, the parameterization of material properties, the temporal discretization, initial and boundary conditions and the finite element formulation of the numerical problems involved.

7.2.2 Processes in the THM_{plus} model

The new model THM_{plus} is aimed to be the framework for the implementation of thermo-hydro-mechanically coupled processes. The processes currently provided by the model are listed in Table 7.1. The extension by further processes or process formulations is possible.

Table 7.1: THM_{plus} model. Available processes and associated keywords.

Heat transport	T	#PROCESS_HEAT_TRANSPORT
Fluid flow	H	#PROCESS_FLUID_FLOW
Solid mechanics	M	#PROCESS_SOLID_DEFORMATION
Matter transport	+	#PROCESS_MASS_TRANSPORT

A process is activated if its keyword appears in the input file followed by specific parameters. Couplings are activated automatically, if multiple processes exists.

For the set-up of the THM_{plus} model some new objects had to be created and the adaptation of existing objects was necessary. The realized developments are described in Sec. 7.3 and Sec. 7.4, respectively.

7.3 Created RockFlow objects

7.3.1 Control of processes and couplings

An object for the control and the definition of processes has been set up. All processes available in RockFlow are defined separately by a particular keyword (see e.g. Fig. 7.11). Due to the existence of these keywords in the input file a process is activated in a coupled simulation. With this approach, a fully defined multi-field problem can easily be reduced by removing a process keyword or, vice versa, an initially defined single process can be extended step-by-step by additional processes. The processing of an active process can be restricted by defining the sub-keyword \$ACTIVATION (see Fig. 7.11). If a process is deactivated, its initial conditions are completely incorporated but the process itself

remains in a steady state. Couplings of a deactivated process to other processes are treated as if the process was active.

The control of couplings of processes is also possible. The corresponding data object is defined by the sub-keyword `$INFLUENCING_PROCESSES` (see Fig. 7.11). It defines restrictions in the interaction of a single process to other coupled processes. These restrictions can easily be incorporated into the finite element formulation. Thus, an estimation of the sensitivity of selected couplings is possible.

7.3.2 Finite elements with quadratic shape functions

The available standard elements of RockFlow have linear shape functions. For the hydraulic-mechanically coupled formulation elements with quadratic shape functions are required. Thus the finite element functions for 9-node and 20-node elements has been implemented, see Fig. 7.1. In the coupled formulation the fluid pressure is approximated linearly and the displacements are approximated quadratically. This results in non-uniform numbers of unknowns in both processes involved and has to be taken into account in the solving procedure.

It is possible to declare elements with coinciding nodes for the representation of degenerated elements. This provides the possibility to compare formulations based on quadrilateral or hexahedral elements with those of triangular, tetrahedral or prismatic element types.

7.3.3 Mesh generation

Algorithms for complex three-dimensional grid generation for hydrogeological models of the finite element code RockFlow have been developed by Rother (2001) [85] and Moenickes (2004) [74]. They have been implemented in the preprocessor HGM.

In order to perform a structured mesh generation, the tool OMEGA (**O**pen **M**esh **G**eneration and **A**daptation) has been developed and integrated in RockFlow. The meshes used in the numerical examples presented within this work have all been generated with the meshing tool OMEGA. The mesh generation algorithms are entirely defined by keywords which can be individually parameterized and composed by the user. Consequently, the tool provides an optimal degree of flexibility.

7.3.4 Input data description

The availability of user manuals and its continuous update is a common problem of finite element codes developed for research purpose. In order to avoid a necessary update of the manual whenever a new version is released, an alternative has been developed in terms of a self-documenting code. The basis of this feature is the availability of standard definitions for all the input functionalities needed.

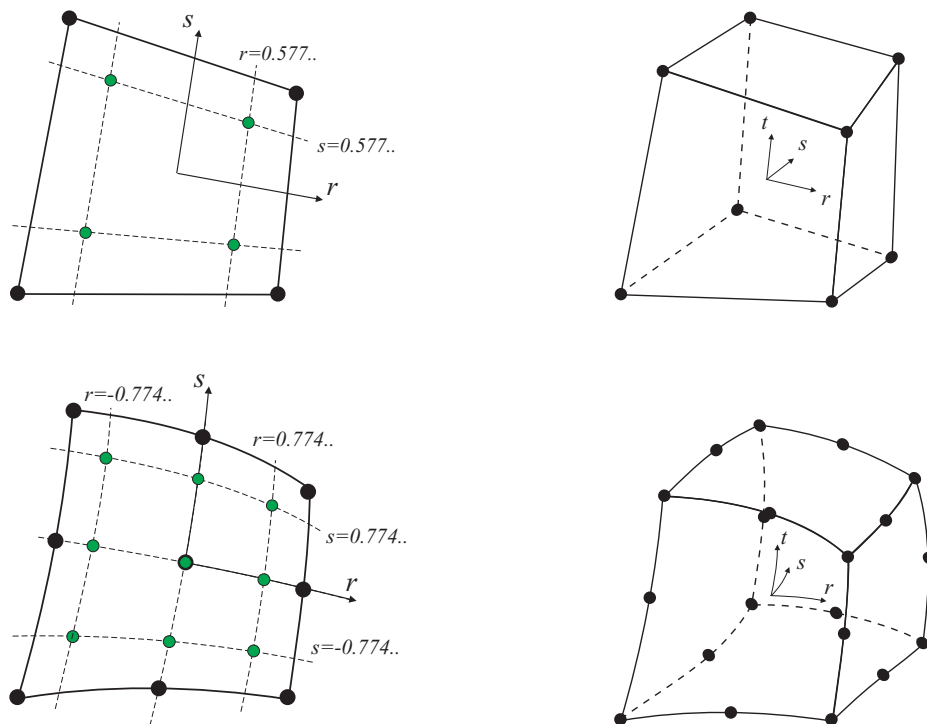


Figure 7.1: 2-D and 3-D elements with linear (above) and quadratic (below) shape functions. The location of the integration points is depicted in 2-D for a reliable integration order of 2×2 for linear and 3×3 quadratic approximation.

For this purpose, a data base was set up by Wulkau (2005) [109]. This data base is part of RockFlow and stores a description of the structure of the input data, its documentation and the link to the data object that finally stores the information.

Default objects, containing the complete input description, are compiled in the data base. During the reading of input data files, specific objects are created that contain only the specified part of input values and its description. The data stored in the default data objects is prepared by the developer and assembled by data base functions.

With the information provided by the data base all the input data operations performed in RockFlow are entirely defined, for example the reading of input files or the writing of the error message file. For documentation purposes a compilation of the default input descriptions can be done automatically. Various configurations are provided and different formats like XML or LaTeX are selectable.

Finally, this input data base, containing the whole structure of input data, allows lots of potential further developments directed towards a more user-friendly finite element simulation tool. The possibility to visualize the default descriptions of individual keywords has already been implemented in the graphical user interface. The results are presented in Sec. 7.5.3.3.

7.4 Adapted RockFlow objects

7.4.1 Solver object for coupled problems

The simulation of a coupled process in the framework of the THM_{plus} model requires a finite element data management for element and node data and for the solving procedure. The element and node data base itself is not affected by the existence of couplings but the finite element routines must provide the necessary coupling terms if interactions shall be considered. Thus, coupling-specific information of the solving procedure has to be transferred from the model to the finite element routines, to the assemble functions and to the solver as well.

The solver data object has finally been chosen to be the central part of the coupled solving strategy. In the solver object all the data concerning the coupling of processes is centrally stored. Therefore, this object had to be extended in order to control all parts of the coupled solving strategy.

7.4.1.1 Indirect solving scheme

Habbar [41] and Thorenz [101] describe the indirect solving of coupled processes. The couplings are considered in a scheme that reiteratively solves a cycle of single processes until the error is in an acceptable range. Using this strategy, the processes can easily be combined. Non-linearities are handled in an iterative scheme of a *Picard* type. The applicability of this approach is usually restricted to weakly coupled problems as the scheme is only conditionally stable. For strongly coupled problems a direct scheme should be used. Its implementation is presented in the next section.

7.4.1.2 Direct solving schemes

For the direct solving of an algebraic equation arising from a coupled finite element formulation the solving concept had to be made more flexible. The overall procedure is depicted in Fig. 7.2.

For each process the finite element matrices are formulated separately and assembled individually. Thus, the coupled formulation originates from process and coupling matrices on its left hand side. The right hand side vector is a compound of load terms, terms due to the chosen time stepping scheme or due to coupling terms which are incorporated indirectly. After the assembly the boundary conditions for all processes are incorporated. Due to different degrees of freedom, resulting from shape functions of different order, the dimensions of the process unknowns are non-uniform. This has to be considered for example whenever data is exchanged with the algebraic system of equations, for example when the nodal values of the current time step are updated by the resulting solution vector. An appropriate update has to be chosen according to the iterative scheme which may be of *Picard* or *Newton* type. In order to store the information needed, a new object containing data for each unknown was added to the *linear solver object* described in Fig 7.3.

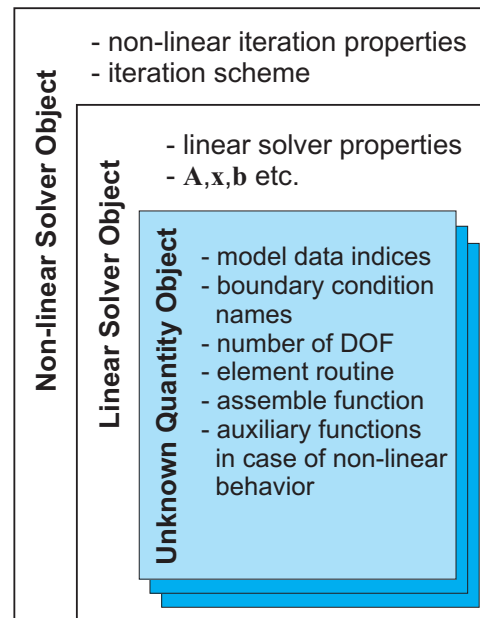
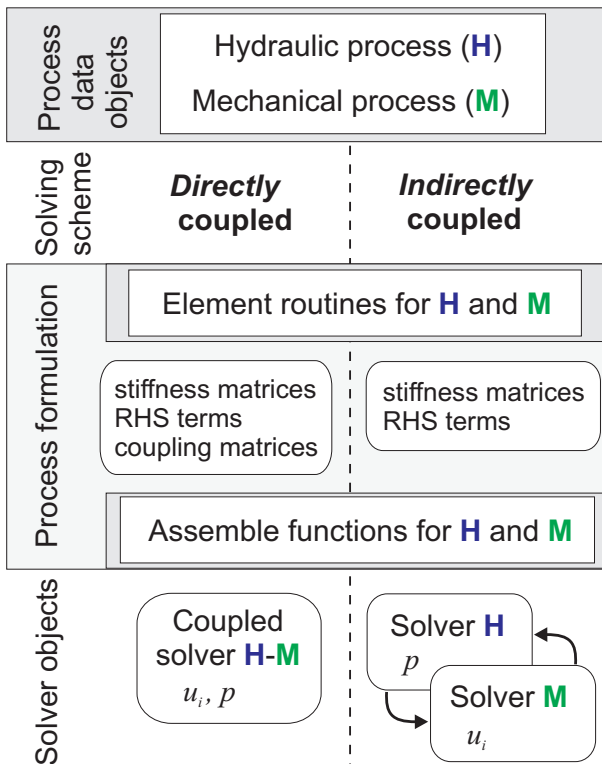


Figure 7.2: Procedure for direct or indirect solution of a coupled process. Figure 7.3: The non-linear solver object.

7.5 The graphical user interface RF₊

7.5.1 Motivation and approach

The simulation of coupled processes associated with numerous pieces of different types of information requires a possibility to check the consistency of the input data. The graphical visualization is an important aspect in achieving this aim.

In order to assist the users as well as the developers of the finite element code RockFlow, a framework of a *graphical user interface* (GUI) has been designed. The development was guided by the following main features including

- the straightforward integration of the text terminal version of RockFlow into the new framework,
- the independent development of both graphical user interface and RockFlow code,
- the possibility of cross-platform development allowing the development of a single code for Windows and Linux applications,
- and finally the realization within the modern C++ programming language.

The developed graphical user interface has been named RF₊. In order to achieve a platform independent code TROLLTECH®'s application framework Qt 3.2.1 has been chosen.

TROLLTECH®'s Qt uses the class based programming language C++ and provides OpenGL functionality for three-dimensional visualization in graphical applications. The development of graphical forms for the user interface is assisted by several libraries included in the Qt framework.

Data interfaces have been realized for the data interchange between the graphical user interface RF₊ and the object-oriented RockFlow code. The interfaces ensure an almost independent development of the GUI code. The structure of the resulting framework, its classes and the integration of RockFlow are described in Sec. 7.5.2. Its performance is addressed in Sec. 7.5.3.1 and some additional features like cross-platform applicability and the user-friendly visualization of input data are presented in Sec. 7.5.3.2 and 7.3.4, respectively.

7.5.2 Structure of the graphical user interface

The structure of the GUI framework and its C++ classes are depicted in Fig. 7.4.

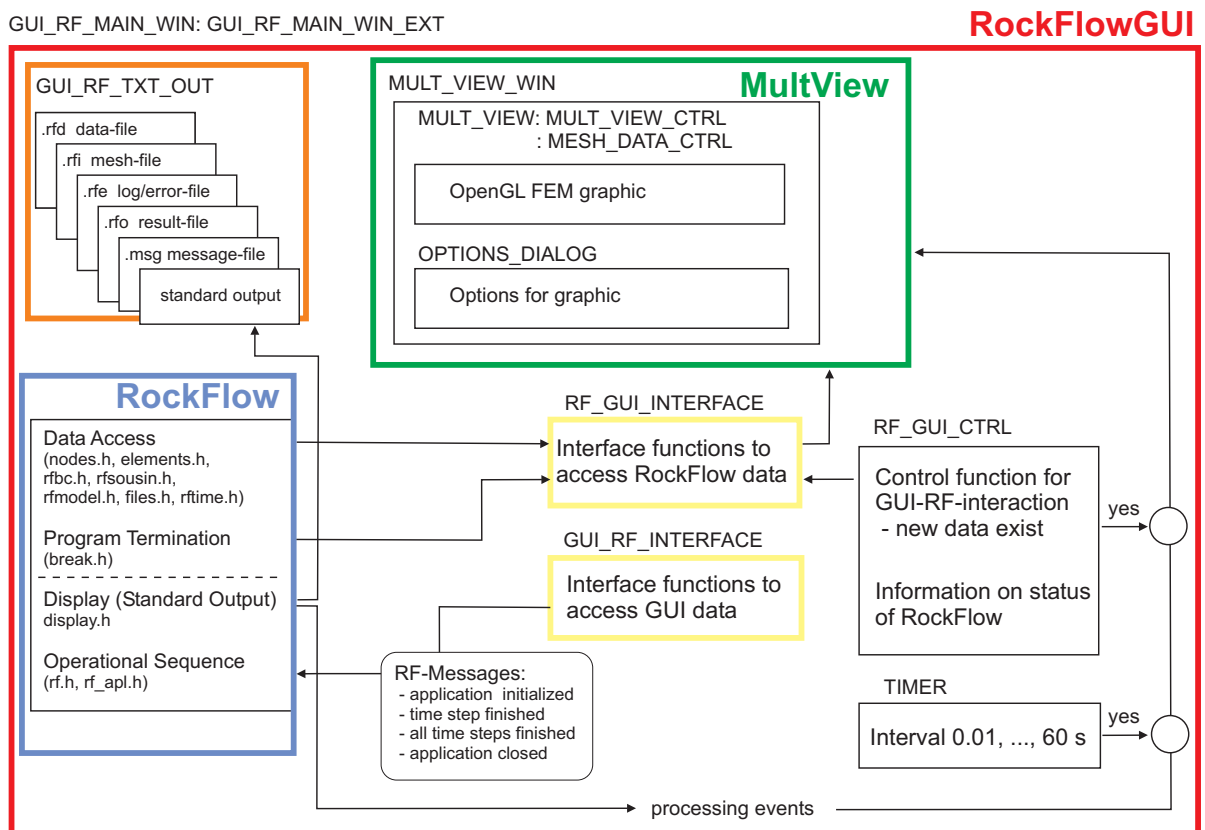


Figure 7.4: Classes of the GUI framework for RockFlow.

Interface functions for the communication between GUI and the standard finite element code ensure the possibility of a simultaneous development of both RockFlow and its graphical user interface. The visualization is performed by the graphical output class named MULT_VIEW. This class has been developed independently from the graphical user interface and thus could be used in further applications for graphical visualization, for example in WaveLoads [73].

Within the developed framework the standard text based RockFlow which is still applied as a terminal version can be integrated without adjustments. Communication and data exchange is performed via the classes RF_GUIINTERFACE and GUI_RF_INTERFACE, respectively. The text output is performed by the class GUI_RF_TXT_OUT. This class is also assigned to accomplish file access, the colored visualization of input data and the online documentation of keywords (see Fig. 7.11). The processing of RockFlow is controlled by the class RF_GUICTRL. For the execution of a test cycle of benchmarks RF₊ can be started without user interference.

The fact that all resulting output files of RockFlow and RF₊ are equivalent simplifies the development of the codes and ensures the enduring consistency of both applications.

The class MULT_VIEW. This class has been developed independently in the visualization project MultiView. It can directly be integrated into the RF₊ framework. Its task is the visualization of one-dimensional, two-dimensional or three-dimensional rendered or wire framed finite element objects. All the graphical objects are defined by OpenGL functions provided by Qt. The depiction of material groups and the numbering of nodes and elements is presented in Fig. 7.5 and Fig. 7.6.

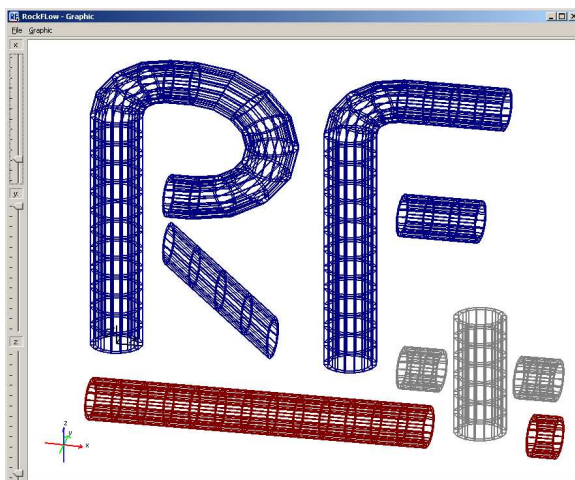


Figure 7.5: Wire frame representation of the finite element mesh with differently colored material groups.

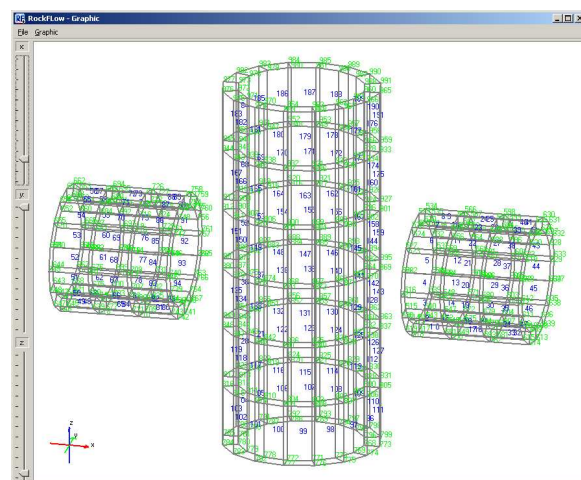


Figure 7.6: Selection of one material group. Node and element numbers are visualized.

In addition, the MultiView graphic allows the coloring of element surfaces for contour plots, depicted in Fig. 7.7. The relocation of the mesh according to scaled values of,

for example, resulting displacements, shown in Fig. 7.8, is a useful option which can be supplemented by the setting of a light source for a realistic visualization in three-dimensional simulations.

The class RF_GUIINTERFACE and GUIRF_INTERFACE. The finite element code RockFlow is a standard text terminal window application. All code files belonging to this base application are usually developed independently from any graphical application.

For the purpose of data interchange between RockFlow and the GUI, RF₊ is provided with two interface classes called RF_GUIINTERFACE and GUIRF_INTERFACE. They are able to transfer data in both directions. As these two interfaces are the only link between graphical user interface and the finite element objects, only minor adjustments are necessary if data objects of RockFlow has been modified.

The class RF_GUICTRL. The graphical user interface is able to process events while the simulation is running. These events can be caused by the user or by the running simulation of RockFlow in terms of signals indicating the completion of the initializing process, the beginning of a new time step or the finalizing of a simulation run.

The processing of these events results in a better control of a simulation run. The initialization of RockFlow or the start of the simulation is controlled by events initiated by the user. Possible events are *Initialize*, *Run*, *Next Time Step*, *Stop* or *Exit*. These options enable the user to interrupt a running simulation and to continue with it after evaluation of current results.

7.5.3 Performance of the graphical user interface

7.5.3.1 Visualization of finite element results

The development of the graphical user interface aims to give a direct and instantaneous insight into mesh properties, material properties or initial and boundary conditions. Additionally, it provides the visualization of all kinds of numerical results. Exemplary visualizations are portrayed in Fig. 7.7 and Fig. 7.8. The graphical user interface centralizes all input and output files of a simulation. It provides visualizations of functional relationships and numerous forms of facilities for a user friendly performance.

7.5.3.2 Visualization on different platforms

At all times, the finite element code RockFlow has been used on different computer platforms. The TROLLTECH[®] application framework has been selected as it allows the development of a single code for graphical applications on different platforms and operating systems.

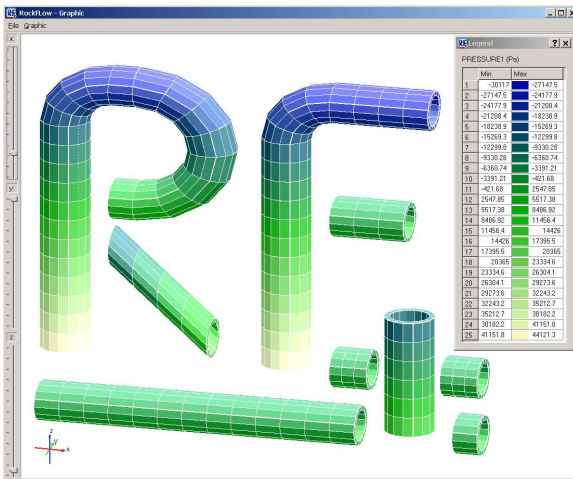


Figure 7.7: Visualization of a hydrostatic pressure field contour.

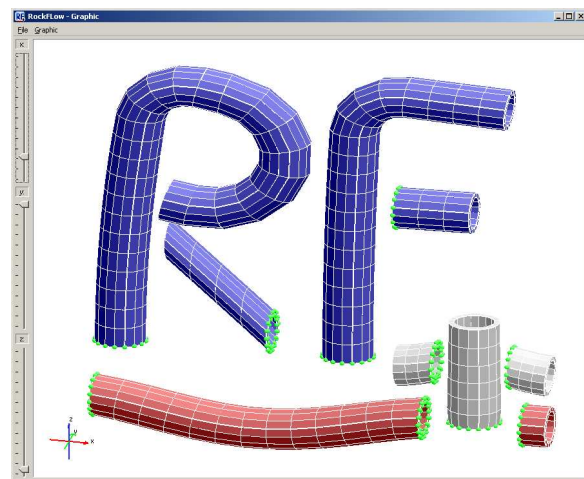


Figure 7.8: Visualization of material groups and deformation due to gravity. *Dirichlet* boundary nodes are marked by green dots. The displacements are scaled by the factor 1000.

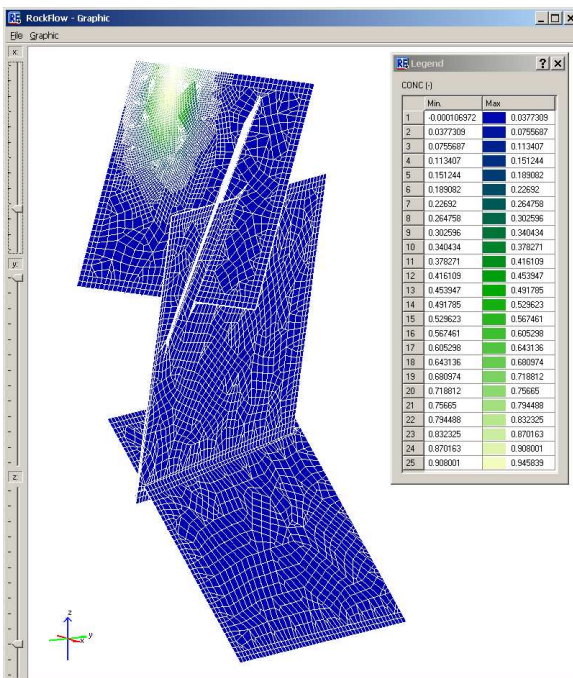


Figure 7.9: Grimsel 2.75-D application [74]. 2.5-D fracture network and its concentration field. Windows view.

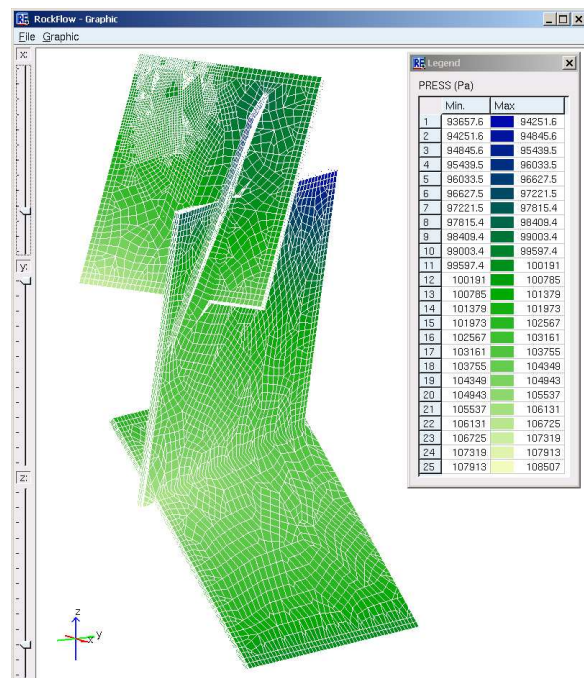
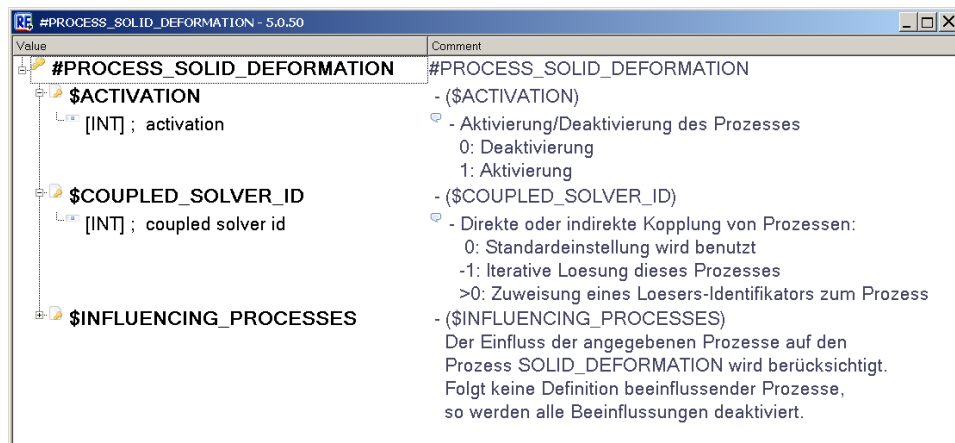


Figure 7.10: Grimsel 2.75-D application [74]. 3-D matrix blocks around 2.5-D fracture network and its pressure field. Linux view.

The resulting graphical output is equivalent on different operating systems. A comparison of a Linux Suse 9.0 and a Windows 2000 view of an extensive finite element model is shown in Fig. 7.9 and Fig. 7.10. Here, a 2.75-D model created by Moenickes (2004) [74] is presented. It consists of a 2-D fracture network which is extended by 3-D matrix elements representing the near-field rock surrounding of the fractures. For the simulation of the transport problem grid adaptive methods implemented by Kaiser (2001) [50] have been applied.

7.5.3.3 Visualization of the input data description of in RF₊

The input data base of RockFlow is described in Sec. 7.3.4. In the graphical user interface RF₊ a visualization of an XML based keyword description has been realized. By an interactive selection of a keyword appearing in the input data file the user can obtain information on the parameter set of an unfamiliar keyword. The resulting description of the keyword #SOLID_DEFORMATION is shown in Fig. 7.11.



Value	Comment
#PROCESS_SOLID_DEFORMATION	#PROCESS_SOLID_DEFORMATION
\$ACTIVATION	-\$ACTIVATION
[INT]; activation	- Aktivierung/Deaktivierung des Prozesses 0: Deaktivierung 1: Aktivierung
\$COUPLED_SOLVER_ID	-\$COUPLED_SOLVER_ID
[INT]; coupled solver id	- Direkte oder indirekte Kopplung von Prozessen: 0: Standardeinstellung wird benutzt -1: Iterative Loesung dieses Prozesses >0: Zuweisung eines Loesers-Identifikators zum Prozess
\$INFLUENCING_PROCESSES	-\$INFLUENCING_PROCESSES
	Der Einfluss der angegebenen Prozesse auf den Prozess SOLID_DEFORMATION wird berücksichtigt. Folgt keine Definition beeinflussender Prozesse, so werden alle Beeinflussungen deaktiviert.

Figure 7.11: Visualization of an XML based keyword description.

Chapter 8

Verification benchmarks

Doubt is not a pleasant condition, but certainty is absurd.

Voltaire.
French philosopher.

8.1 Mechanical analysis

8.1.1 Formulation of the problem

The examples in this section are concerned with linear elastic and elasto-perfectly plastic material behavior. The governing equations of perfect elasto-plasticity are summarized in Box 6.1.

8.1.2 Plate with a hole

The benchmark presented here has been used in the joint research project 'Adaptive Finite-Element-Methods in Computational Mechanics' supported by the German National Science Foundation.

8.1.2.1 Set-up

A two-dimensional system of a quadratic steel plate with a circular hole under plane strain conditions is stretched in one direction, see Fig. 8.1. More details on this benchmark and reference solutions using adaptive refinement can be found in [96].

The geometric properties and the loading are listed in Table 8.1. The results of elastic and elasto-plastic analysis are presented in the ensuing section.

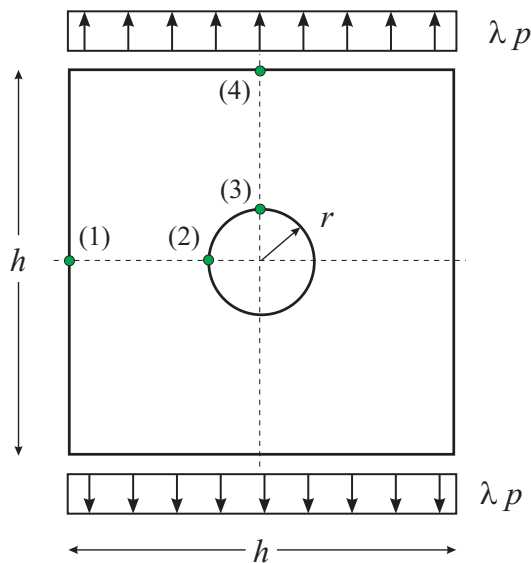


Figure 8.1: Geometry of the plate with a hole benchmark problem.

Table 8.1: Geometry and load setup.

Parameter	Value
height, width	h 200 mm
radius	r 10 mm
load	p 100 MPa
load factor	λ

8.1.2.2 Elastic analysis

As reference, the maximum vertical stress appearing at point (2) is analyzed here. The properties of the linear elastic material are given in Table 8.2. The comparison of reference values, taken from Stein et al. 2002 [96], and the results evaluated with RockFlow shows a good agreement (see Tab. 8.3).

Table 8.2: Material Properties.

Parameter	Value
Young's modulus	E 206899.94 MPa
Poisson's ratio	ν 0.29

8.1.2.3 Elastic-perfectly plastic analysis

Here the plate is assumed to have an elastic-perfectly plastic behavior. Its material properties are shown in Table 8.4. The analyses are performed with a monotonic and a cyclic loading λ , respectively. First plastic deformations occur at a load step $\lambda_0 = 1.68$ and the critical load is reached at $\lambda_{\text{crit.}} = 4.76$ ([96]).

Table 8.3: Reference values and RockFlow results ($\lambda = 4.5$).

Quantity	Symbol	Value
max. displacement	u_y	
reference, [96]		0.20951 mm
RockFlow		0.20950668 mm
max. stress	σ_{yy}	
reference, [96]		1388.732343 MPa
RockFlow		1380.596418 MPa

Table 8.4: Material properties.

Parameter		Value
Young's modulus	E	206899.94 MPa
Poisson's ratio	ν	0.29
initial yield stress	σ_Y	450.00 MPa

Results for monotonic loading. A monotonic increase of the applied load until a maximum load of $\lambda_{\max} = 4.65$ is analyzed. During the loading phase a local unloading occurs in point (2). The horizontal displacement u_x of this point till reaching the final sub-critical load of $\lambda = 4.65$ is shown in Fig 8.2 with the well matching reference values added. The equivalent stress and the accumulated plastic strain fields occurring at the final load step $\lambda_{\max} = 4.65$ are depicted in Figs. 8.3 and 8.4. The yield stress of $\sigma_Y = 450$ MPa is reached in almost the whole domain, thus, only an area of minor extent remains elastic.

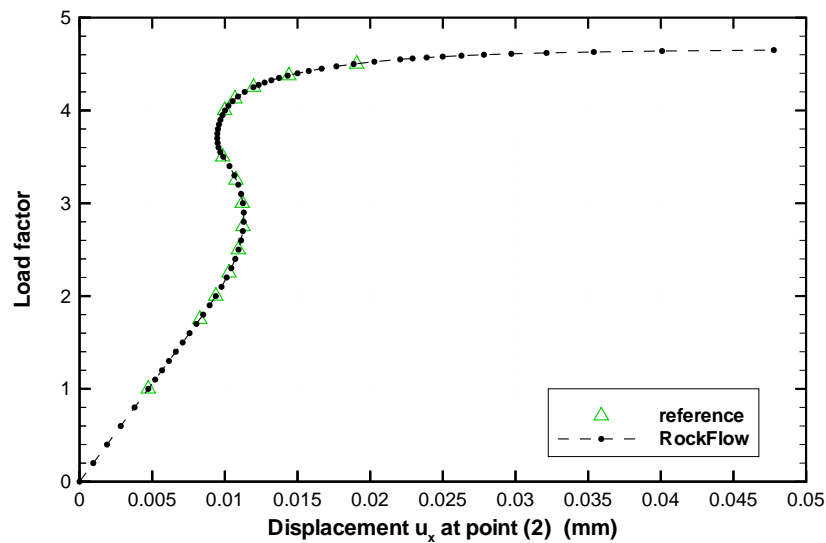


Figure 8.2: Monotonic loading: local unloading in point (2).

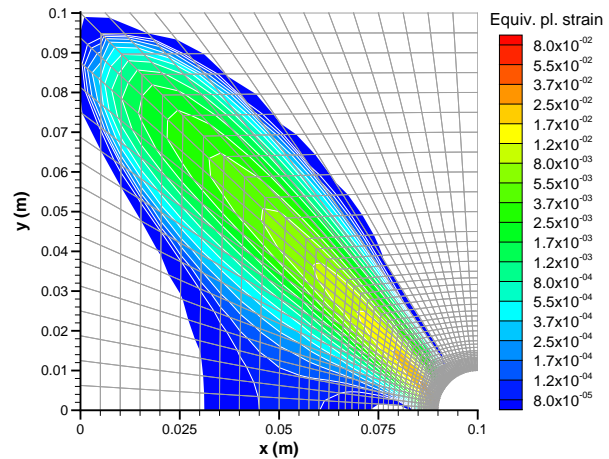
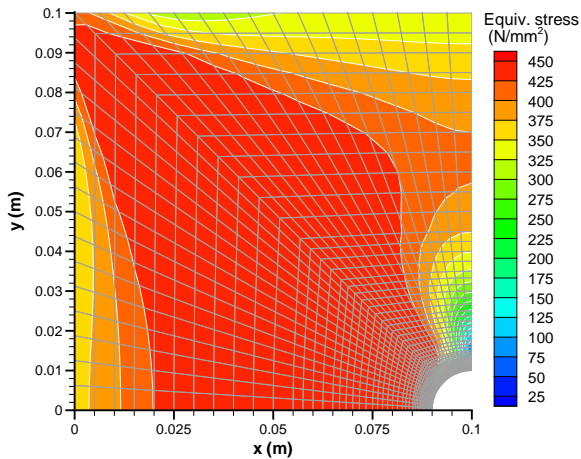


Figure 8.3: Monotonic loading: equivalent stress at $\lambda = 4.65$.

Figure 8.4: Monotonic loading: accumulated plastic strain at $\lambda = 4.65$.

Results for cyclic loading. A cyclic loading and unloading of the specimen is analyzed here. The variation of load λ is in a range of -4.5 to 4.5 . The deformation of the plate at several load steps is depicted in Fig. 8.5.

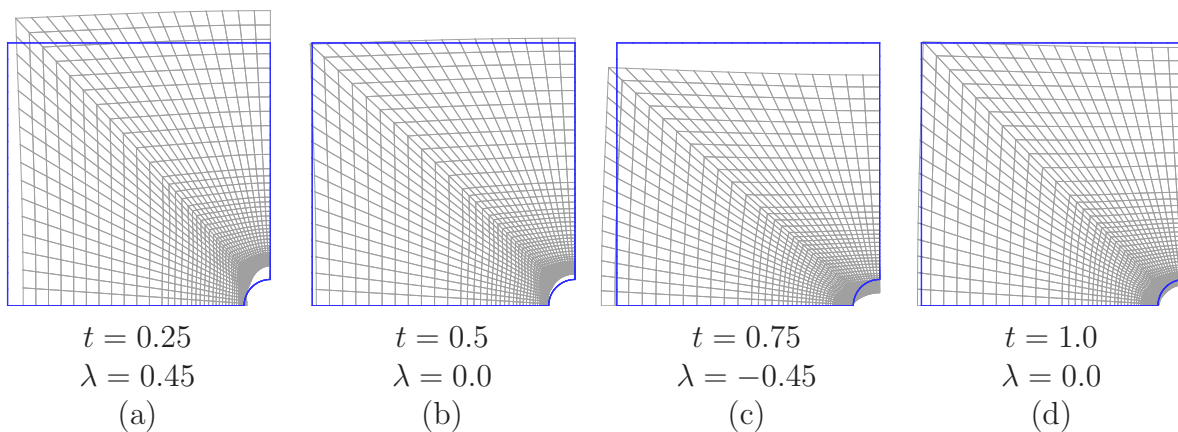
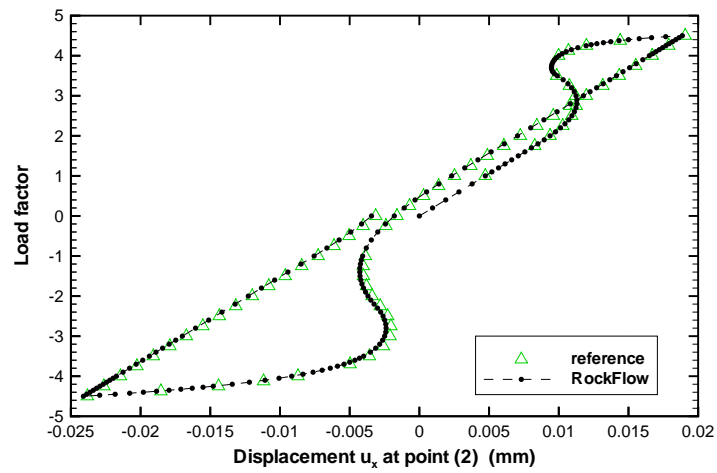
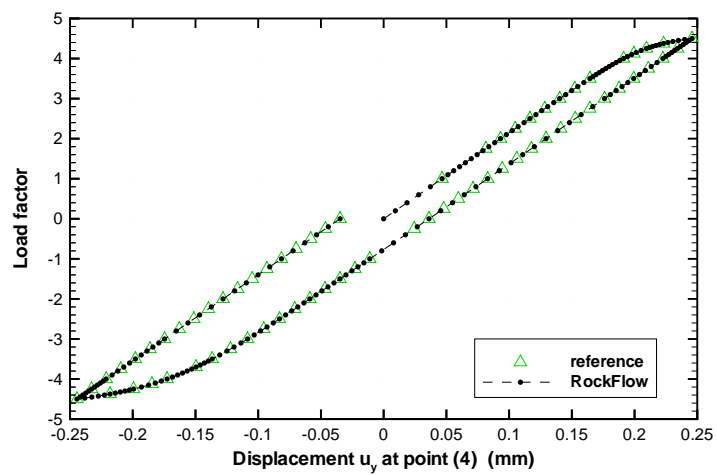


Figure 8.5: Cyclic loading: deformation at sequenced load steps.

The resulting displacements and stresses evaluated at the observation points (see Fig 8.1) are depicted in Fig. 8.6 and Fig. 8.7, respectively. The mesh used here is pre-refined around the circular hole. With the help of the pre-refinement it was possible to reproduce the reference values correctly. These reference values have been predicted with adaptively refined meshes and summarized in Stein et al. (2002). The resulting equivalent stress and the accumulated plastic strain at load step $\lambda = 4.5$ are given in Figs. 8.8 and 8.9.



(a)



(b)

Figure 8.6: Cyclic loading: displacement u_x in point (2) (a) and u_y in point (4) (b).

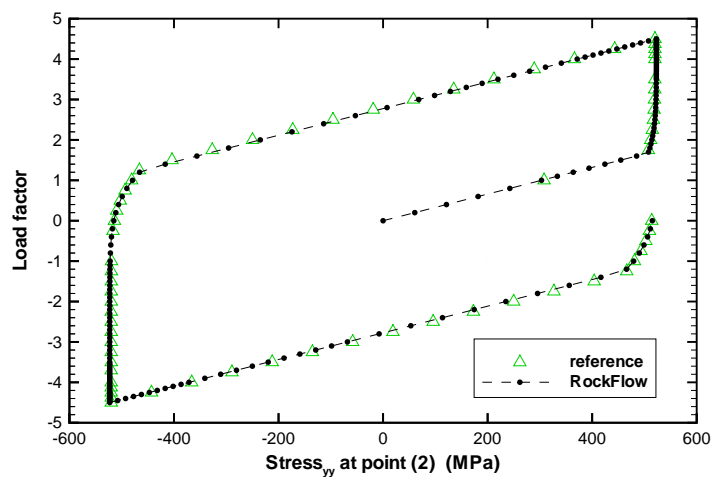


Figure 8.7: Cyclic loading: stress σ_{yy} in point (2).

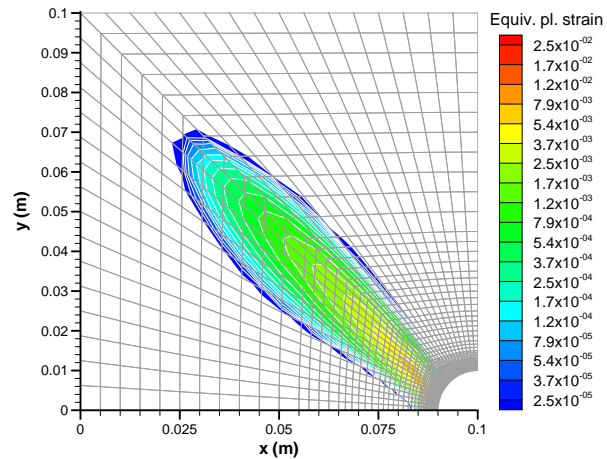
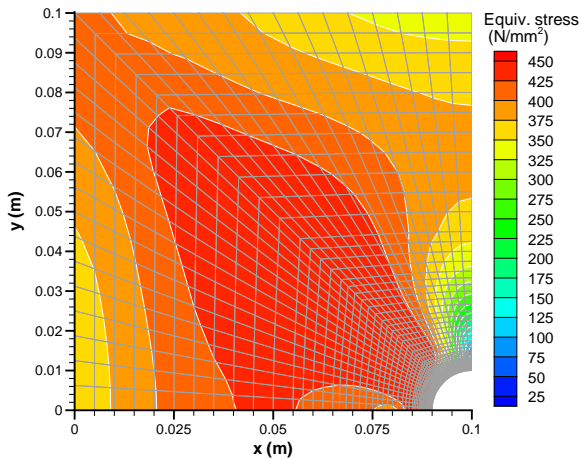


Figure 8.8: Cyclic loading: equivalent stress at $\lambda = 4.5$. Figure 8.9: Cyclic loading: accumulated plastic strain at $\lambda = 4.5$.

8.2 Thermo-mechanical analysis

8.2.1 Formulation of the problem

In this section, thermomechanical applications, carried out in two and three dimensions, are presented. The resulting temperatures and the accompanied thermally induced stresses are compared to analytical solutions. For convenience, the formulation of two- and three-dimensional thermo-elasticity is summarized in Appendix C.2.

8.2.2 Stress concentrations around cavities in a steady heat flow

The basis of this benchmark is the analysis of thermal stresses, which are induced by the disturbance of a uniform heat flow through a domain of infinite extent. The origin of the disturbance are single cavities in the solid material acting like obstacles in the heat flow and creating peaks in the temperature and stress fields. Solutions for this problem of thermo-elasticity for differently shaped cavities can be found in [39] and [102] or in the collection of Kachanov et al. (2003) [49].

8.2.2.1 Analytical solution

A steady heat flow with gradient τ in an infinite domain of thermo-elastically responding porous material is assumed. The heat flow is disturbed by a spherical or cylindrical cavity of radius a . The analytical solutions of this coupled problem are given by Florence and Goodier (1959) [39]. Their derivations for two and three dimensional cavities lead to the following equations.

Analytical three-dimensional solution. The temperature and stresses in spherical coordinates (r, θ, φ) defined in Fig 8.10 are as follows:

$$T(r, \theta) = \tau \left(r + \frac{a^3}{2r^2} \right) \cos \theta \quad (8.1)$$

$$\sigma_{\theta\theta} = \sigma_{\varphi\varphi} = -\frac{E}{4(1-\nu)} \alpha_T \tau a \left(\frac{a^2}{r^2} + \frac{a^4}{r^4} \right) \cos \theta \quad (8.2)$$

$$\sigma_{\max} = \frac{1}{2} E \alpha_T \tau a / (1 - \nu) \quad (8.3)$$

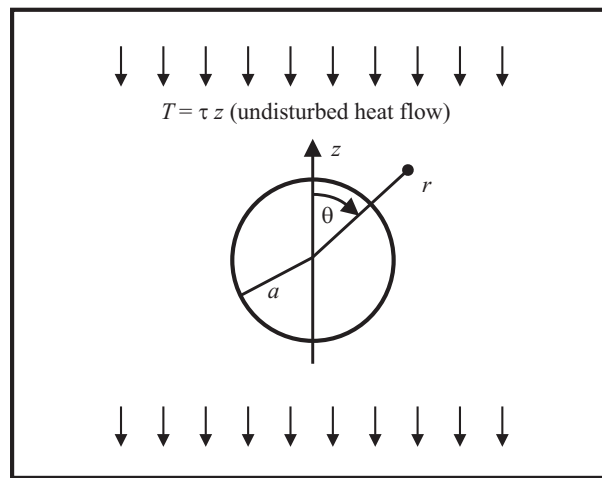


Figure 8.10: Heat flow around spherical cavity.

Analytical plane stress solution. The temperature and stresses in cylindrical coordinates (r, φ, z) defined in Fig 8.11 are as follows:

$$T(r, \varphi) = \tau \left(r + \frac{a^2}{r} \right) \sin \varphi \quad (8.4)$$

$$\sigma_{\varphi\varphi} = -\frac{1}{2} E \alpha_T \tau a \left(\frac{a}{r} + \frac{a^3}{r^3} \right) \sin \varphi \quad (8.5)$$

$$\sigma_{\max} = E \alpha_T \tau a \quad (8.6)$$

Analytical plane strain solution. The resulting values for the plane strain state are achieved by replacing E and α_T according to Appendix C.2:

$$T(r, \varphi) = \tau \left(r + \frac{a^2}{r} \right) \sin \varphi \quad (8.7)$$

$$\sigma_{\varphi\varphi} = -\frac{E}{2(1-\nu)} \alpha_T \tau a \left(\frac{a}{r} + \frac{a^3}{r^3} \right) \sin \varphi \quad (8.8)$$

$$\sigma_{\max} = E \alpha_T \tau a / (1 - \nu) \quad (8.9)$$

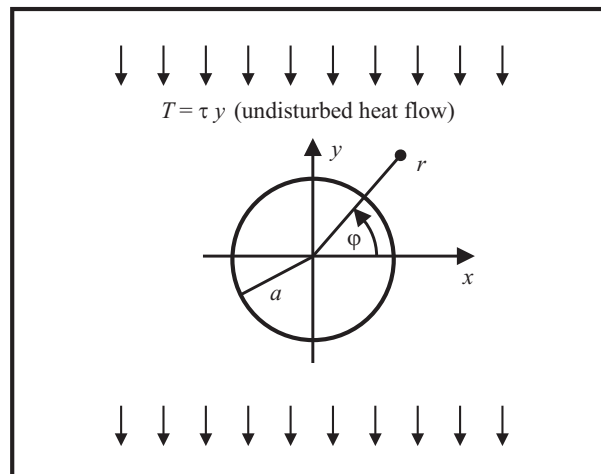


Figure 8.11: Heat flow around 2-D circular hole.

8.2.2.2 Numerical simulation

According to the analytical solutions, it can be seen that the stress concentration towards the cavity is a fourth order function in case of a spherical shape but only a third order function in case of a circular shape. The stress increase is caused by the temperature disturbance around the cavity. This disturbance reduces cubically with the radial distance to the sphere but quadratically with the distance to the circular shaped cavity. Consequently, the resulting maximum stress at the surface of the circular cavity is two times higher than the stress at the sphere's surface.

Due to the above mentioned reasons, the size of the domain for the circular case is chosen four times larger than the domain used for the spherical case. The mesh properties for three cases (a) spherical cavity, (b) circular cavity in two dimensions and (c) in three dimensions are summarized in Table 8.5.

Table 8.5: Model geometry and mesh size.

Value	Type of model realization		
	Spherical cavity	Circular hole 2-D	Circular hole 3-D
Radius, a	0.01 m	0.01 m	0.01 m
Size			
max x	$10 \times a$	$40 \times a$	$40 \times a$
max y	$10 \times a$	$40 \times a$	$40 \times a$
max z	$10 \times a$		$1 \times a$
Number of elements	4416	2064	4128

The chosen material and heat flow parameters are given in Table 8.6. Using these parameters, the maximum values stress and temperature are estimated and presented in the next sections and finally summarized in Table 8.7.

Table 8.6: Material and heat flow parameters.

Parameter		Value
Young's modulus	E	206900.0 MPa
Poisson's ratio	ν	0.29
Linear thermal expansion	α_T	$1.2 \times 10^{-6} \text{ K}^{-1}$
Heat flow gradient	τ	100 K m^{-1}

Three-dimensional analysis of the spherical cavity problem. Due to symmetries in the xy -plane as well as in the yz -plane only a quarter of the whole domain is analyzed as depicted in Fig. 8.12. The disturbance of the heat flow and the caused variation in temperature gradients around the sphere is visualized in Fig. 8.13. Analytical solution and numerical results of temperature and stress σ_{xx} are depicted in Figs. 8.14 and 8.15 along the central axis or the sphere's surface, respectively (gray line). The comparison of both values indicates that the refinement at the sphere's surface is not yet sufficient for an exact peak stress prediction.

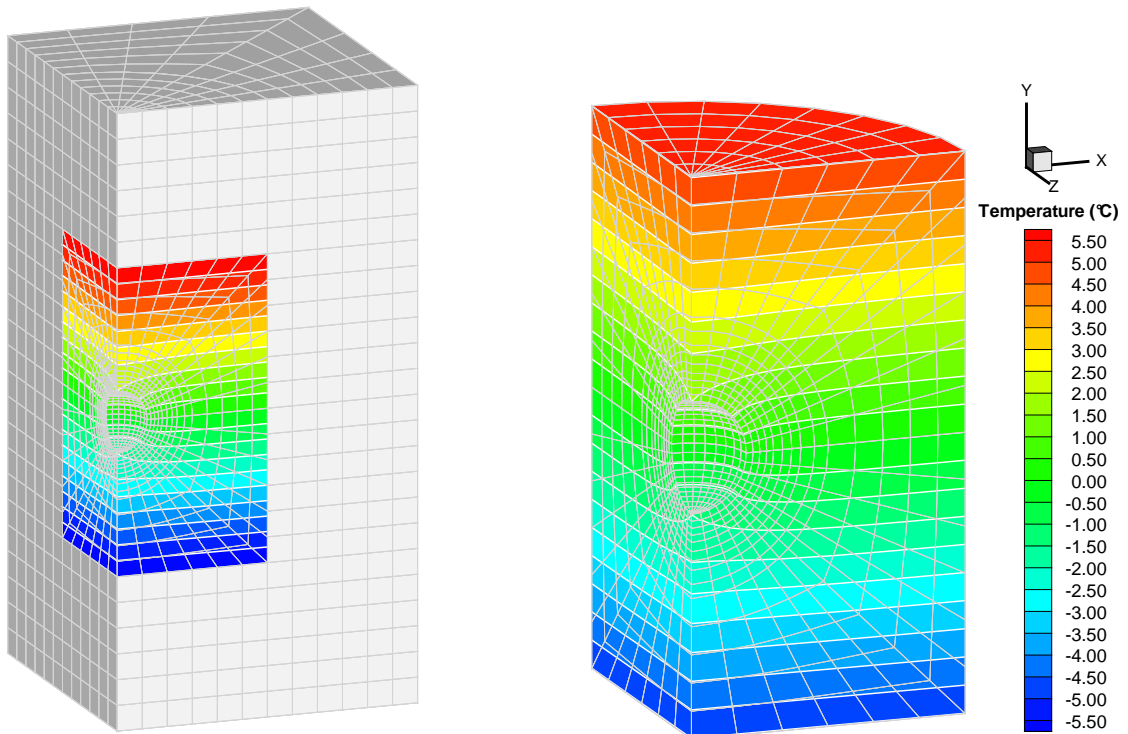


Figure 8.12: 3-D spherical cavity. Domain with colored near field.

Figure 8.13: 3-D spherical cavity. Temperature in the near field.

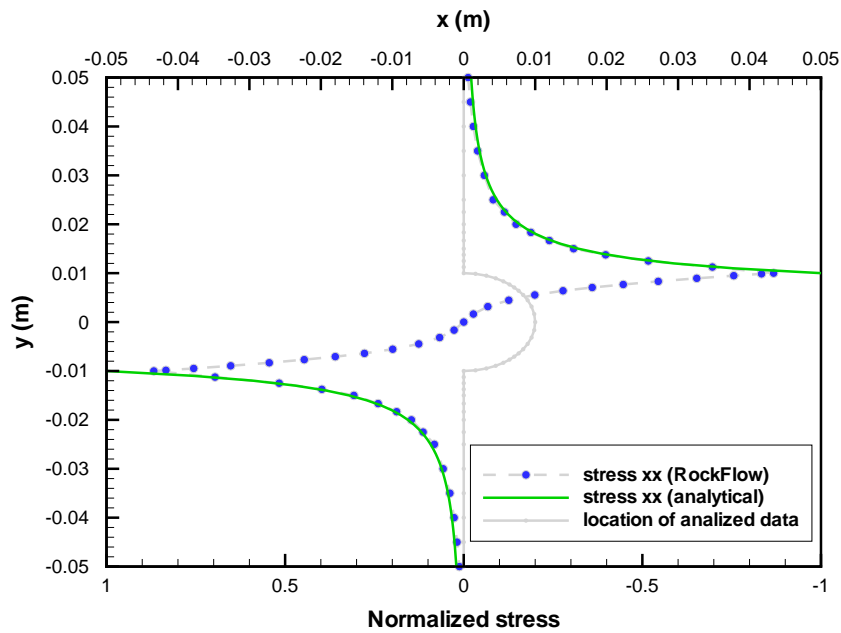


Figure 8.14: 3-D spherical cavity. Stress σ_{xx} versus height in the near field.

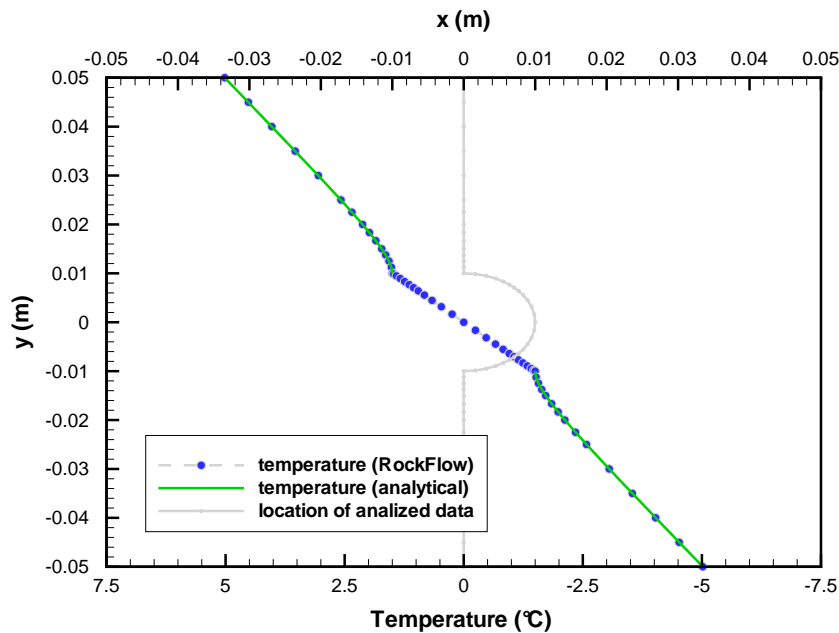


Figure 8.15: 3-D spherical cavity. Temperature versus height in the near field.

Two-dimensional analysis of the circular cavity problem in plane strain conditions. A circular cylinder with infinite length in the third direction is assumed. Due to the symmetry, the system can be reduced as depicted in Fig. 8.16. The increase in temperature due to the cylindrical obstacle in the heat flow is two times higher than

the increase around a spherical obstacle (cf. Table 8.7). The extensive disturbance becomes obvious in Fig. 8.17. Finally, the extension of the mesh size by a factor of four, in comparison to the 3-D case, generates reasonable results (Figs. 8.18 and 8.19).

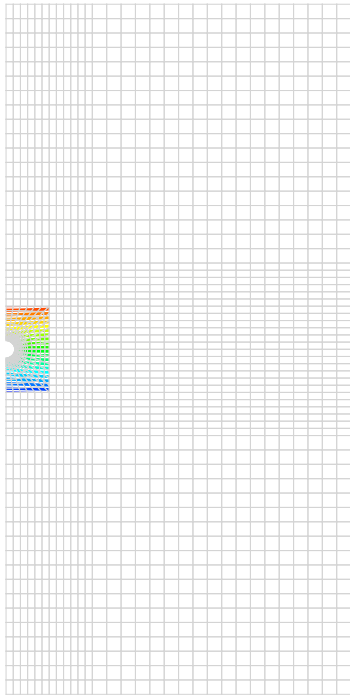


Figure 8.16: 2-D circular hole. Domain with colored near field.

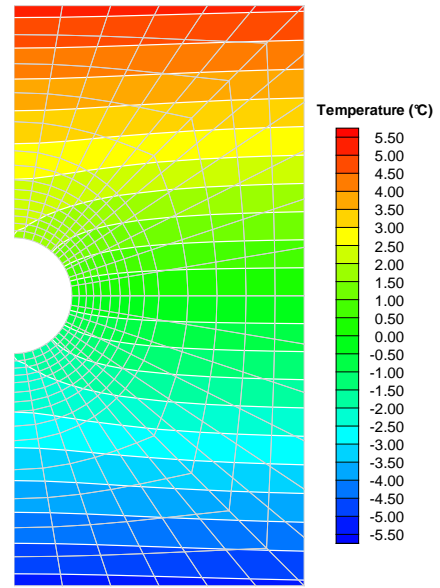


Figure 8.17: 2-D circular hole. Temperature in the near field.

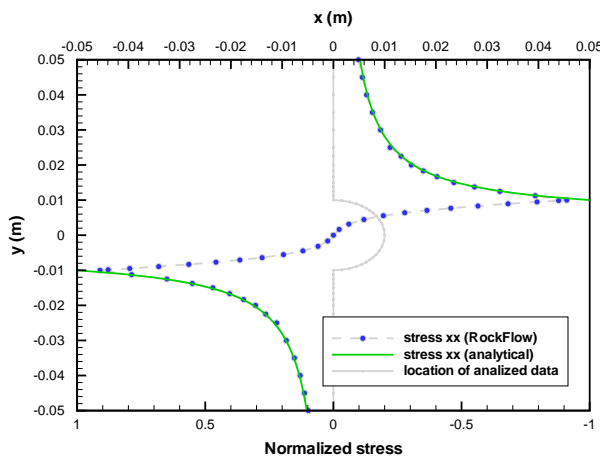


Figure 8.18: 2-D circular hole. Stress σ_{xx} in the near field.

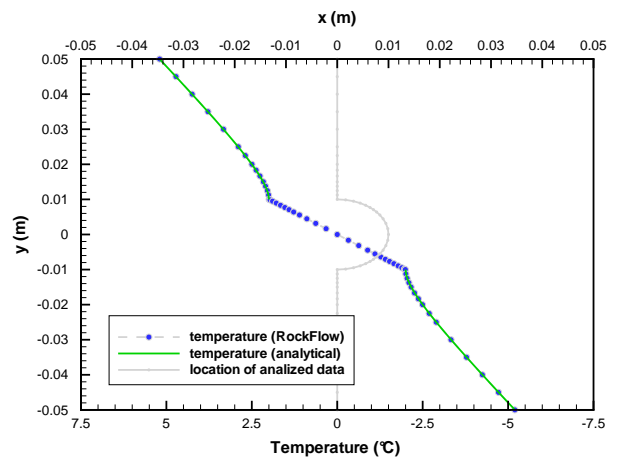


Figure 8.19: 2-D circular hole. Temperature versus height in the near field.

Three-dimensional analysis of the circular cavity problem in plane strain conditions. The three-dimensional analysis presented here has been carried out for reasons of comparison only. While the temperature values are equal (Fig. 8.22), slight differences in stress analysis (Fig. 8.23) become apparent when the maximum values in Table 8.7 are compared.

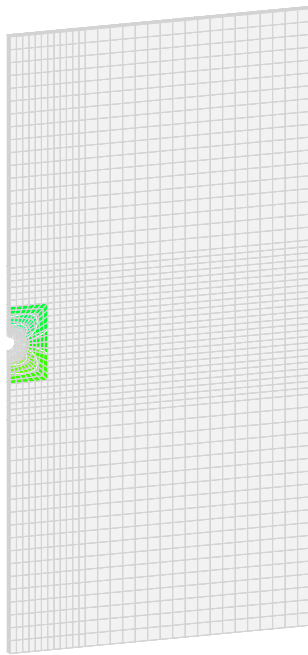


Figure 8.20: 3-D circular hole. Domain with colored near field.

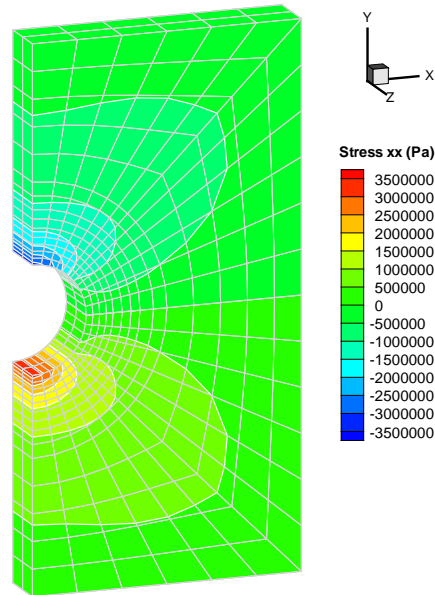


Figure 8.21: 3-D circular hole. Stress σ_{xx} in the near field.

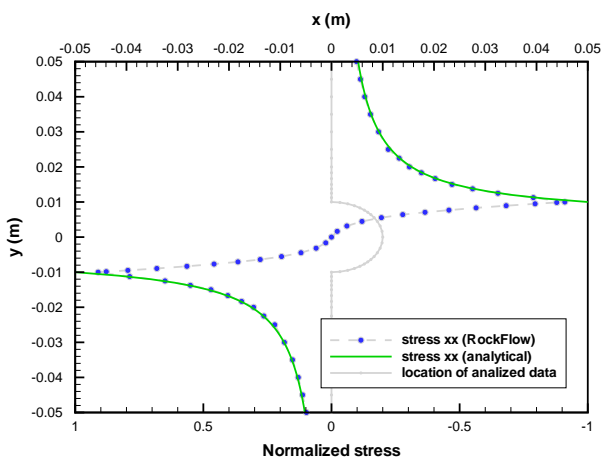


Figure 8.22: 3-D circular hole. Stress σ_{xx} versus height in the near field.

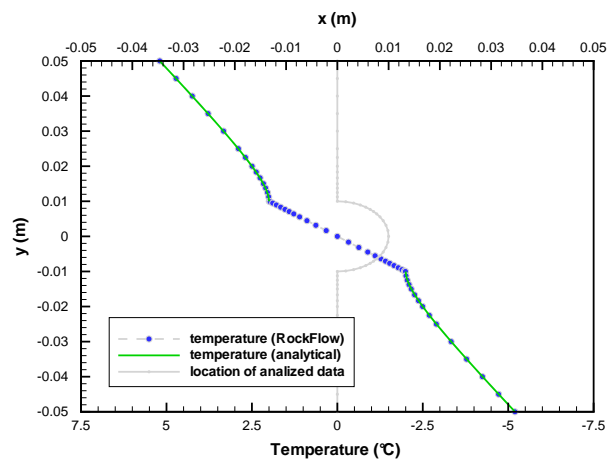


Figure 8.23: 3-D circular hole. Temperature versus height in the near field.

8.2.2.3 Conclusions

For the purpose of comparison, the analytical results and the numerical approximations at crucial points at the surface of the cavities are summarized in Table 8.7. The temperature values are approximated very well, while the correct approximation of the peak stress values requires a better mesh refinement towards the cavity surface.

Table 8.7: Comparison of analytical and numerical results.

Value	Type of model realization		
	Spherical cavity	Circular hole 2-D	Circular hole 3-D
Temperature at cavity's surface			
analytical	1.5 °C	2.0 °C	2.0 °C
RockFlow	1.4993 °C	1.9934 °C	1.9934 °C
Peak stress at cavity's surface			
analytical	1748.5 kPa	3496.9 kPa	3496.9 kPa
RockFlow	1516.7 kPa	3183.6 kPa	3184.1 kPa

8.3 Hydraulic-mechanical analysis of saturated porous media

8.3.1 Formulation of the problem

In case of a fully saturated medium ($S^l = 1$) the solid phase (φ^s) and the liquid phase (φ^l) in the pore space is considered. The resulting set of governing equations is summarized in Box 8.1.

Box 8.1: The hydraulic-mechanically coupled single-phase flow problem. Set of governing equations.

I. Balance equations

Conservation of mass (volumetric form) – Eq. (2.45)

$$\nabla \cdot \underbrace{(n \mathbf{v}^{ls})}_{\mathbf{q}} + S \frac{\partial p^l}{\partial t} - n \beta_T^l \frac{\partial T}{\partial t} - \beta_T^s (\alpha - n) \frac{\partial T}{\partial t} + \alpha \nabla \cdot \frac{\partial \mathbf{u}}{\partial t} = 0$$

Conservation of linear momentum – Eq. (3.4)

$$\nabla \cdot (\boldsymbol{\sigma} - \alpha p^l \mathbf{1}) + \rho_b \mathbf{g} = \mathbf{0}$$

II. Constitutive equation

Fluid flux – Eq. (6.61)

$$\mathbf{q} = \frac{\mathbf{k}}{\mu_l} (-\nabla p^l + \rho^l \mathbf{g})$$

Effective stresses – Eq. (3.1)

$$\boldsymbol{\sigma} = \lambda \operatorname{tr} \boldsymbol{\varepsilon}^{el} \mathbf{1} + 2G \boldsymbol{\varepsilon}^{el}$$

8.3.2 One-dimensional consolidation of a saturated column

This benchmark comprises a one-dimensional consolidation problem taken for comparison against an analytical solution. The consolidation takes place in a porous column bounded by rigid and impermeable walls. On the top which is free to drain a load σ_0 is applied. The column is of height H . The set-up of the consolidation problem is depicted in Fig. 8.24.

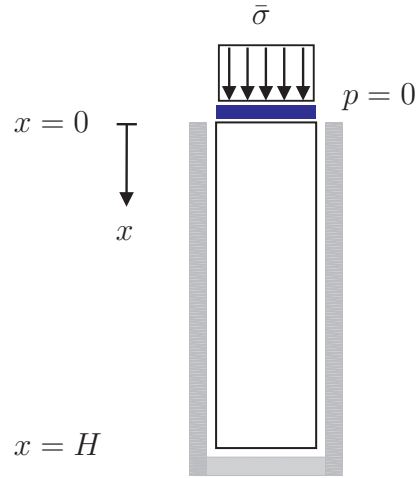


Figure 8.24: One-dimensional consolidation. Geometry and boundary conditions.

8.3.2.1 Analytical solution

The boundary and initial conditions of the problem according to Fig. 8.24 are defined by

$$\sigma = -\bar{\sigma}, \quad p = 0 \quad \text{on} \quad x = 0 \quad (8.10)$$

$$u = 0, \quad \frac{\partial p}{\partial x} = 0 \quad \text{on} \quad x = H \quad (8.11)$$

$$\frac{\partial u}{\partial x} = 0 \quad \text{in} \quad (0, H) \quad \text{for} \quad t = 0. \quad (8.12)$$

An analytical solution for this initial boundary value problem has been given by Murad and Loula (1992) [76]. It can be formulated as follows

$$\sigma^* = -1 + \sum_{n=0}^{\infty} \frac{2}{M} \sin(M x^*) e^{-M^2 t^*} \quad (8.13)$$

$$u^* = 1 - x^* - \sum_{n=0}^{\infty} \frac{2}{M^2} \cos(M x^*) e^{-M^2 t^*} \quad (8.14)$$

$$p^* = \sum_{n=0}^{\infty} \frac{2}{M} \sin(M x^*) e^{-M^2 t^*} \quad (8.15)$$

where

$$x^* = x/H, \quad t^* = (\lambda + 2G)k t / \mu^w H^2, \quad M = \frac{1}{2}\pi(2n + 1) \quad (8.16)$$

are non-dimensional quantities, and

$$\sigma^* = \sigma/\bar{\sigma} \quad u^* = u(\lambda + 2G) / \bar{\sigma} H, \quad p^* = p/\bar{\sigma} \quad (8.17)$$

are non-dimensional effective stress, displacement and pore pressure, respectively.

8.3.2.2 Numerical results

The geometric and material properties chosen for this benchmark are summarized in Table 8.8. The numerical simulation is performed on a two-dimensional mesh discretized by 100 quadrilateral elements. The total simulation time is 100 s. In order to cope with the strongly time dependent behavior of this problem, the discretization in time has been adapted. The time step lengths are the following: 10×0.01 s, 9×0.1 s, 9×1.0 s and 9×10.0 s.

Table 8.8: One-dimensional consolidation. Geometry and material properties.

Parameter		Value	Unit
Height	H	1.0	m
Young's modulus	E	3.0×10^4	MPa
Poisson's ratio	ν	0.2	
Permeability	k	1.0×10^{-10}	m^2
Water viscosity	μ^w	1.0×10^{-3}	Pa s

In Fig. 8.25 the resulting numerical approximation of fluid pressure, vertical stress and vertical displacement along the column depth x is depicted for several time steps. Some discrete points of the analytical solution are added. The comparison of the analytical values and the numerical predictions of RockFlow shows a satisfying agreement.

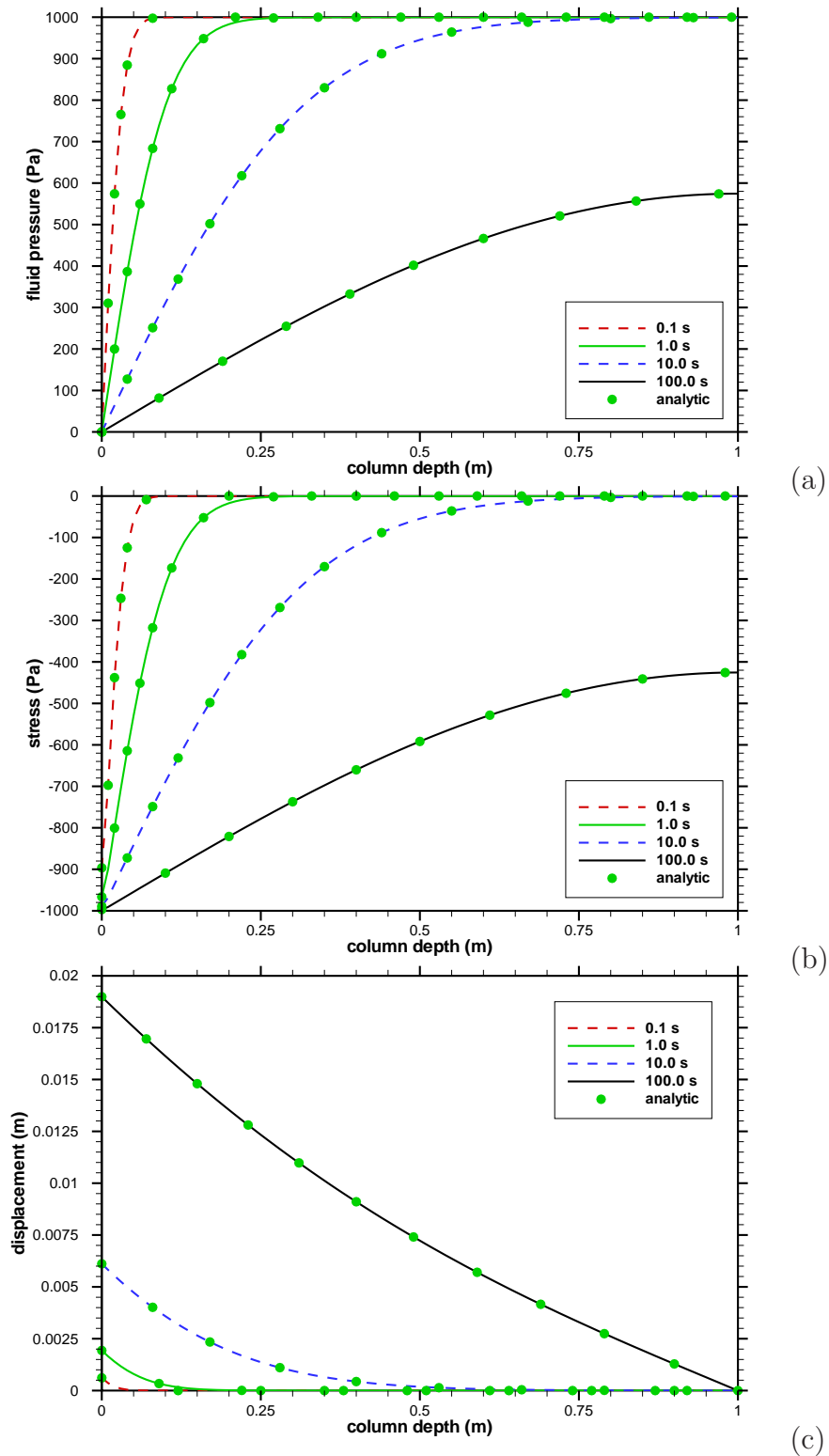


Figure 8.25: One-dimensional consolidation. Fluid pressure p (a), stress σ (b) and vertical displacement u (c) (ordinate) versus depth (abscissa) of deformable column.

8.4 Hydraulic-mechanical analysis of partially saturated porous media

In partially saturated soil mechanics it is difficult to find suitable tests for the verification of numerical formulations and algorithms. Thus, the examples presented in this section are compared against simulated reference values taken from the literature. The example of localization analysis of a rigid footing in Sec. 8.4.3 consist of several variations that are intended to demonstrate specific effects arising from the fluid-solid coupling of plastic soils.

8.4.1 Formulation of the problem

In case of a partially saturated ($S^l + S^g = 1$) medium, the solid phase (φ^s) and the volumetric sum of water (^w) and air (^a) in the liquid (^l) and in the gaseous (^g) phase have to be considered. We employ the *Richards's* approximation, i.e. air remains at atmospheric pressure and the multiphase flow can be represented in a single-phase formulation. The resulting set of governing equations is summarized in Box 8.2.

8.4.2 Liakopoulos experiment

In this section, multiphase flow in a deforming porous medium is studied. The presented test example is a drainage test based on an experiment by Liakopoulos (1965) [66]. Desaturation takes place due to gravitational effects. This example was studied previously by several authors, for example Liakopoulos [66], Narasimhan & Witherspoon [77], Zienkiewicz et al. [112] or Schrefler & Zhan [89]. Therefore, this example is well suited as benchmark, despite the lack of any analytical solutions for this type of coupled, non-linear problems.

The physical experiment of Liakopoulos was conducted in a column packed with so-called Del Monte sand. Moisture content and tension at several points along the column were measured with tensiometers (cf. Figs. 8.27 and 8.26).

The capillary pressure $p_c(S^w)$ is a function of the saturation and can be given as

$$p_c = \left(\frac{1 - S^w}{1.9722} \times 10^{11} \right)^{\frac{1}{2.4279}} \text{ Pa} \quad (8.18)$$

as well as the relative permeability relationship $k_{\text{rel}}(S^w)$

$$k_{\text{rel}}^w = 1 - 2.207(1 - S^w)^{1.0121} \text{ m}^2. \quad (8.19)$$

These equation fits the measured data in case of saturations larger than 0.84 and are therefore suitable for the following numerical simulation.

Box 8.2: Thermally affected hydraulic-mechanically coupled multi-phase flow. One-phase flow formulation (*Richards's* approximation). The solid grains are assumed to be incompressible ($\alpha = 1$) and the effects of thermal expansion are neglected in the fluid phase. Set of governing equations.

I. Balance equations

Conservation of mass (volumetric form) – cf. Eq. (2.56)

$$nS^w \frac{1}{K^w} \frac{\partial p^w}{\partial t} + n \frac{\partial S^w}{\partial p^w} \frac{\partial p^w}{\partial t} - (S^w \beta_T^s (1-n) + nS^w \beta_T^w) \frac{\partial T}{\partial t} + \frac{1}{\rho^w} \nabla \cdot \mathbf{J}^{ws} + S^w \nabla \cdot \frac{\partial \mathbf{u}}{\partial t} = 0.$$

Conservation of heat energy – cf. Eq. (2.62)

$$((1-n)c^s \rho^s + n(S^w c^w \rho^w + S^g c^g \rho^g)) \frac{\partial T}{\partial t} + \nabla \cdot \mathbf{J}_t + c^w \mathbf{J}^{ws} \cdot \nabla T = 0.$$

Conservation of linear momentum – Eq. (3.7)

$$\nabla \cdot (\boldsymbol{\sigma} - \alpha S^w p^w \mathbf{1}) + \rho_b \mathbf{g} = \mathbf{0}$$

II. Constitutive equations

Fluid flux – cf. Eq. (6.62)

$$\mathbf{J}^{ws} = nS^w \rho^w (\mathbf{v}^w - \mathbf{v}^s) = \rho^w \frac{k_{rel}^w \mathbf{k}}{\mu^w} (-\nabla p^w + \rho^w \mathbf{g})$$

Effective stresses – Eq. (3.1)

$$\boldsymbol{\sigma} = \lambda \operatorname{tr} \boldsymbol{\varepsilon}^{el} \mathbf{1} + 2G \boldsymbol{\varepsilon}^{el}$$

where

$$\boldsymbol{\varepsilon}^{el} = \boldsymbol{\varepsilon} - \boldsymbol{\varepsilon}^t \quad \boldsymbol{\varepsilon}^t = \alpha_T (T - T_{ref}) \mathbf{1}$$

in case of thermal expansion or in case of plastic deformations

$$\boldsymbol{\varepsilon}^{el} = \boldsymbol{\varepsilon} - \boldsymbol{\varepsilon}^{pl} \quad \boldsymbol{\varepsilon}^{pl} = \mathbf{e}^{pl} + \boldsymbol{\varepsilon}_v^{pl}.$$

Heat conduction – cf. Eq. (6.64)

$$\mathbf{J}_t = -\mathbf{D} \nabla T, \quad \mathbf{D} = \lambda_b \mathbf{1}$$

$$\text{where} \quad \lambda_b = (1-n) \lambda_s + n S^w \lambda^w + n S^g \lambda^g.$$

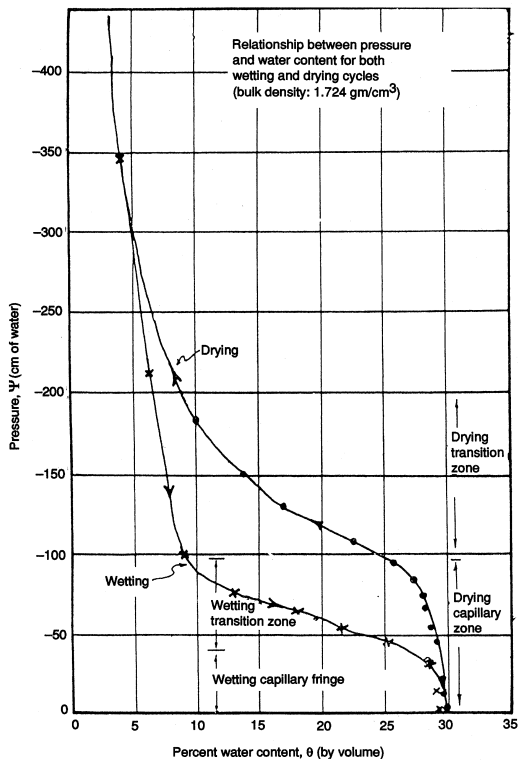


Figure 8.26: Hydraulic head versus water content, with $\Psi = p^w/\rho^w g$ and $\theta = nS^w$ ([66]).

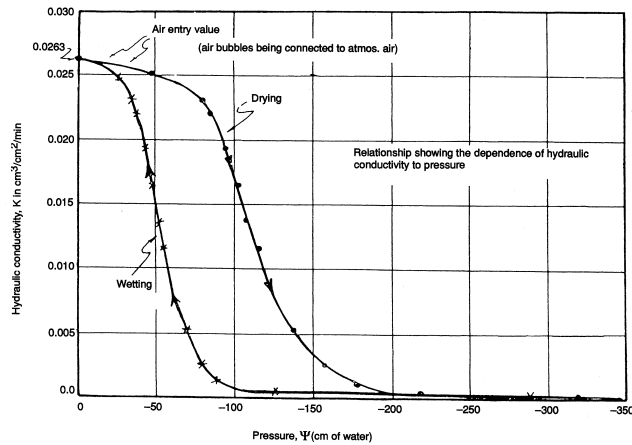


Figure 8.27: Hydraulic conductivity versus pressure, with $K = k\rho^w g/\mu^w$ and $\Psi = p^w/\rho^w g$ ([66]).

The model set-up is depicted in Fig. 8.28. The material parameters, taken from Lewis and Schrefler (1998) [64], are summarized in Tab. 8.9.

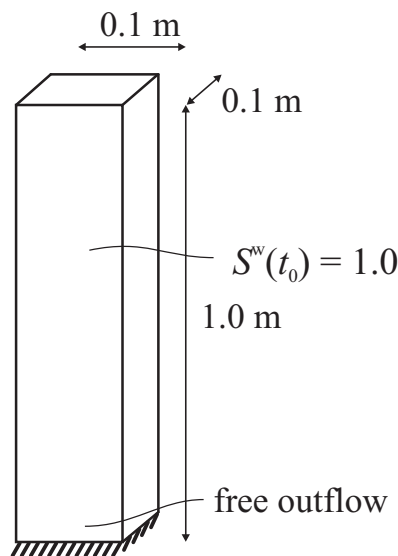


Figure 8.28: Liakopoulos experiment. Set-up.

Table 8.9: Liakopoulos benchmark. Material properties.

Parameter		Value	Unit
Young's modulus	E	1.3	MPa
Poisson's ratio	ν	0.4	
Solid grain density	ρ^s	2000	kg m^{-3}
Liquid density	ρ^w	1000	kg m^{-3}
Porosity	n	0.2975	
Permeability	k	4.5×10^{-13}	m^2
Water viscosity	μ^w	10^{-3}	Pa s
Gravity	g	9.806	m s^{-2}

In Figs. 8.29 and 8.30 the numerical results are shown: water pressure p^w , water saturation S^w and vertical solid displacement u_z^s along the column height. The reference values, taken from [64], are very close to the RockFlow results.

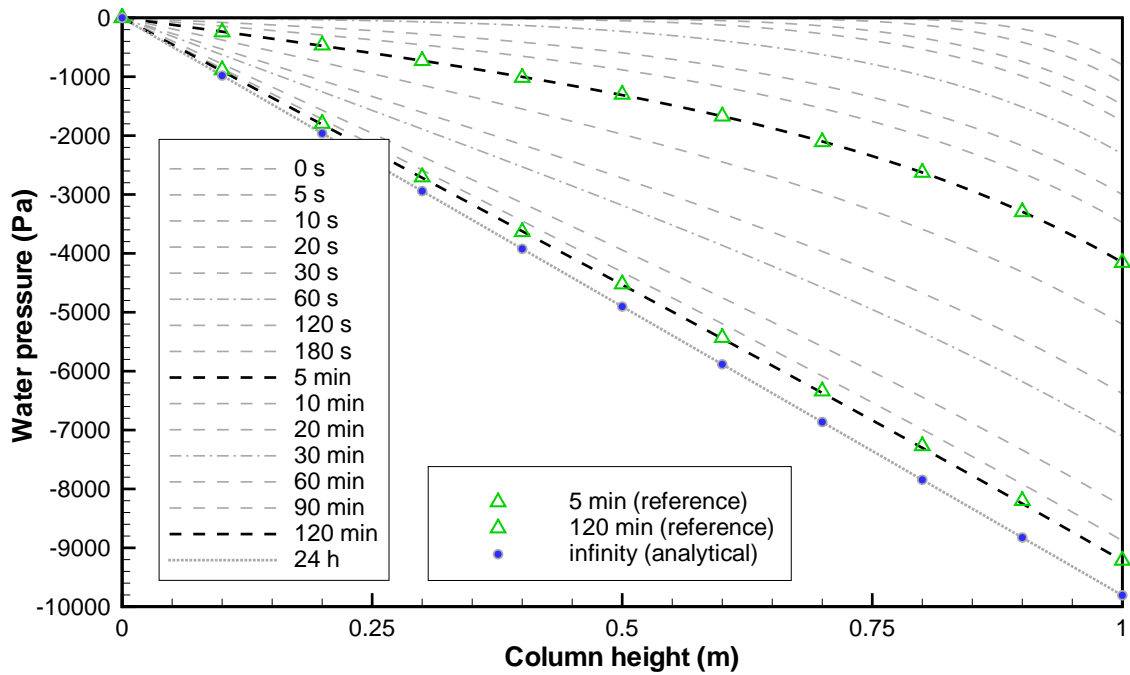


Figure 8.29: Liakopoulos experiment. Water pressure p^w versus height (abscissa) of deformable column ($t = \{5 \text{ s}, 10 \text{ s}, 20 \text{ s}, 30 \text{ s}, 1 \text{ min}, 2 \text{ min}, 3 \text{ min}, 5 \text{ min}, 10 \text{ min}, 20 \text{ min}, 30 \text{ min}, \dots, 120 \text{ min and } 24 \text{ h}\}$).

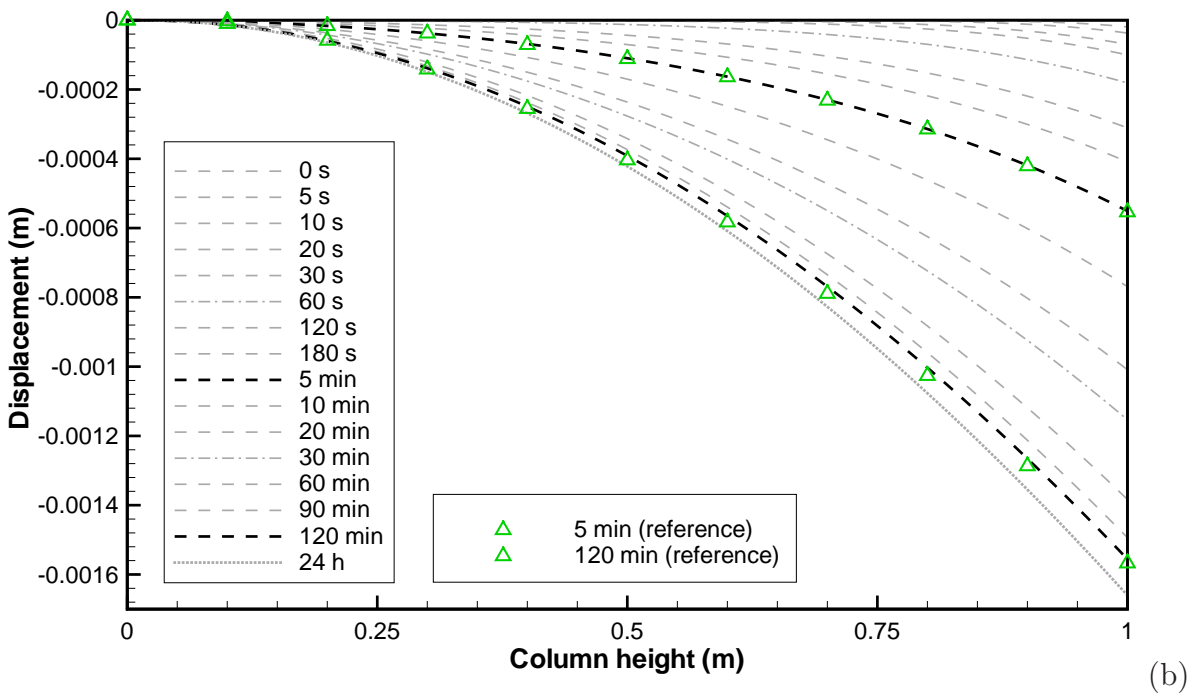
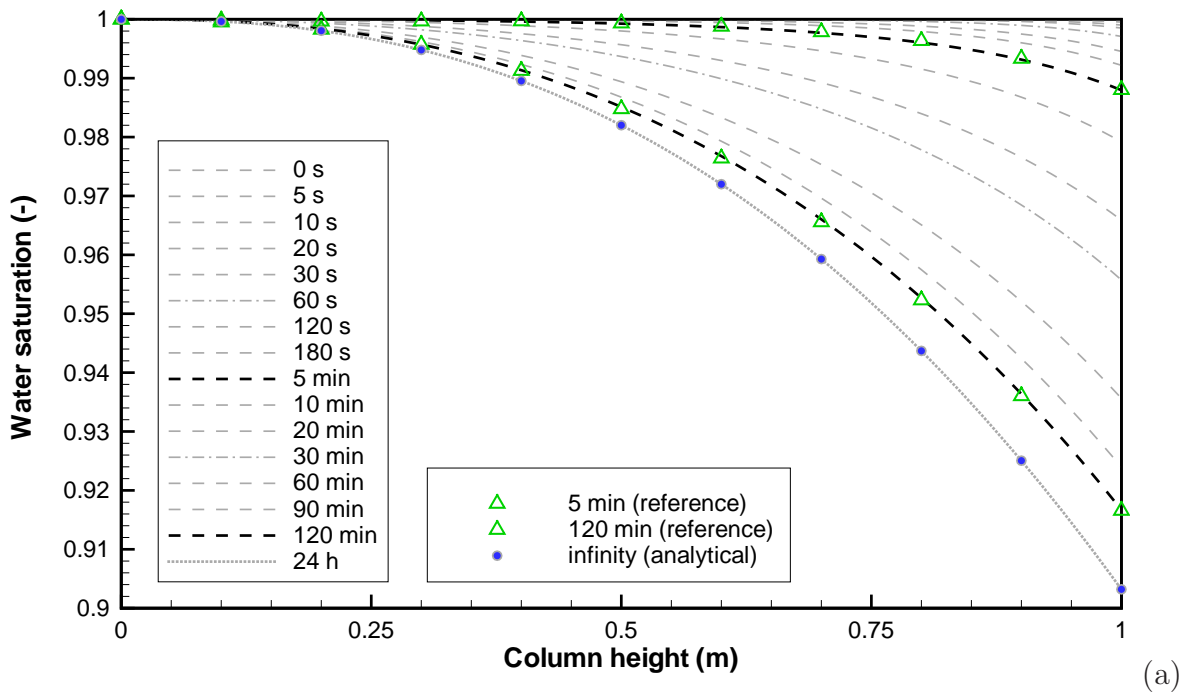


Figure 8.30: Liakopoulos experiment. Water saturation S^w (a) and vertical displacement u_z^s (b) (ordinate) versus height (abscissa) of deformable column ($t = \{5 \text{ s}, 10 \text{ s}, 20 \text{ s}, 30 \text{ s}, 1 \text{ min}, 2 \text{ min}, 3 \text{ min}, 5 \text{ min}, 10 \text{ min}, 20 \text{ min}, 30 \text{ min}, \dots, 120 \text{ min and } 24 \text{ h}\}$).

8.4.3 Localization analysis in a rigid footing

8.4.3.1 Introduction

In the present section, multiphase flow in an elasto-plastic porous medium is considered. Geometrically linear and non-linear analysis of the problem presented here can be found in Steinmann (1999) [97] and Sanavia et al. (2002) [87], respectively.

The following example is a square domain investigated under plane strain conditions and loaded by a rigid footing. The footing is represented by a prescribed time dependent displacement boundary condition. The model set-up is depicted in Fig. 8.31.

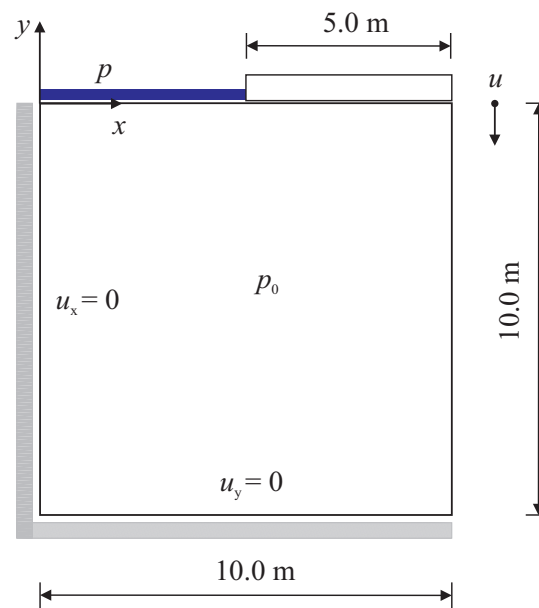


Figure 8.31: Rigid footing. Set-up.

The material is assumed to be perfectly plastic. A *von Mises* material type has been chosen as a reference material. Additionally, the *Drucker-Prager* type material has been used to show dilatant and contractant behavior that initiates direct interactions from the mechanical problem to the flow problem. The material properties are summarized in Table 8.10.

8.4.3.2 Non-dilatant plastic material

The numerical simulations presented in this section have been performed in order to provide reference results using a standard plastic material of *von Mises* type.

Undrained conditions. A comparison of the fully saturated and the partially saturated formulation is shown in Figs. 8.32 -8.35. Due to the chosen *von Mises* material without plastic dilatancy the pressure field or the saturation field are not affected by

Table 8.10: Rigid footing. Material properties.

Parameter		Value	Unit
Young's modulus	E	10.0	MPa
Poisson's ratio	ν	0.3	
Solid grain density	ρ^s	2000	kg m^{-3}
Liquid density	ρ^w	1000	kg m^{-3}
Porosity	n	0.2	
Permeability	k	1.0×10^{-11}	m^2
Water viscosity	μ^w	10^{-3}	Pa s
Gravity	g	9.806	m s^{-2}

plastic deformation. Only little positive volumetric elastic response can be identified in the top left-hand corner. Here a temporary suction of $p = -2.0$ kPa can be observed. Consequently, both formulations show almost the same results in the pressure field and in the plastic zone.

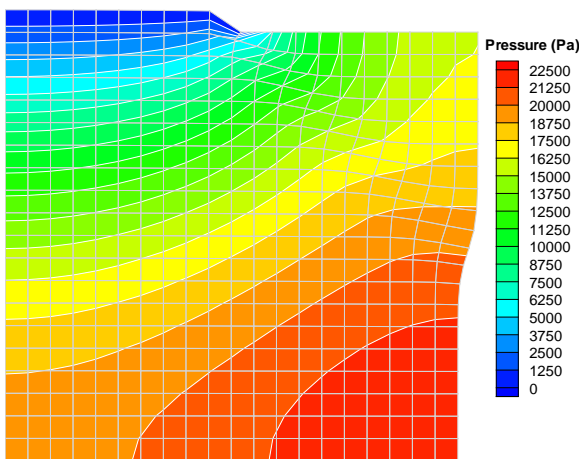


Figure 8.32: Fully saturated flow formulation. Fluid pressure field using the *von Mises* yield criterion.

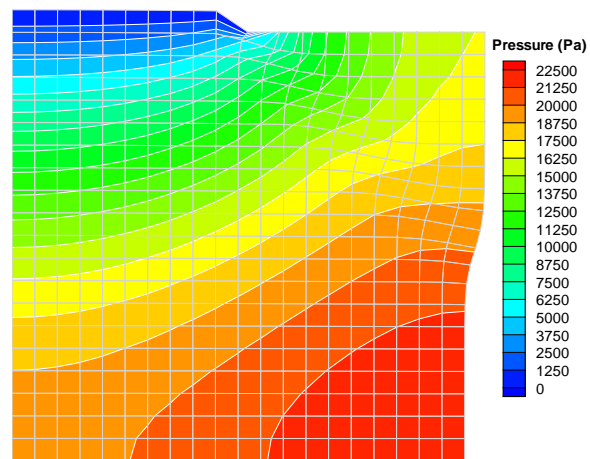


Figure 8.33: Partially saturated flow formulation. Fluid pressure field using the *von Mises* yield criterion.

Drained conditions. The plastic behavior of a partially saturated medium shall be investigated. The medium is assumed to have the same property of capillary pressure and relative permeability as the Del Monte sand applied in Sec. 8.4.2. The simulation starts with an initial saturation of 90% ($p_0 = -10$ kPa). A boundary conditions of suction of $p = -10$ kPa is prescribed at the left half of the top boundary.

As the *von Mises* model, predicting no volumetric plastic strain, is used here, only minor coupling effects can be identified in the saturation field. Nevertheless, low volumetric elastic strain rates within the plastic zone become apparent in the pressure/saturation field. The maximum extent at time step $t = 150$ s is shown in Figs. 8.36 and 8.37.

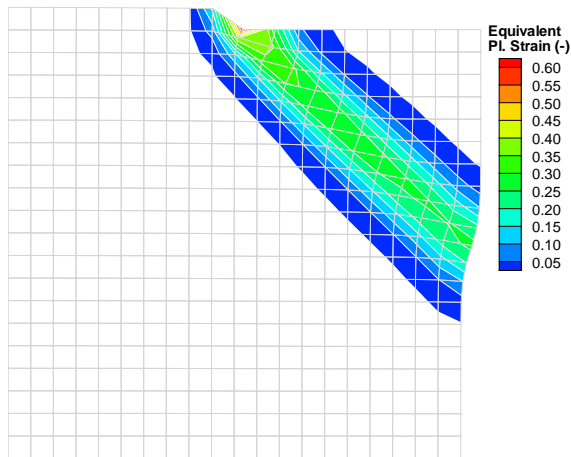


Figure 8.34: Fully saturated flow formulation. Equivalent plastic strain using the *von Mises* yield criterion.

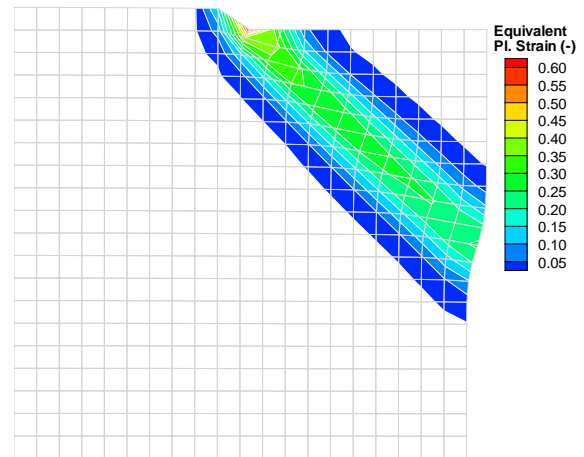


Figure 8.35: Partially saturated flow formulation. Equivalent plastic strain using the *von Mises* yield criterion.

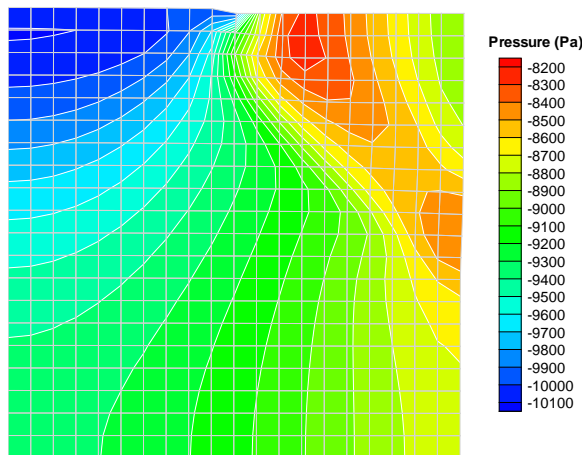


Figure 8.36: Partially saturated rigid footing. Fluid pressure using the *von Mises* yield criterion.

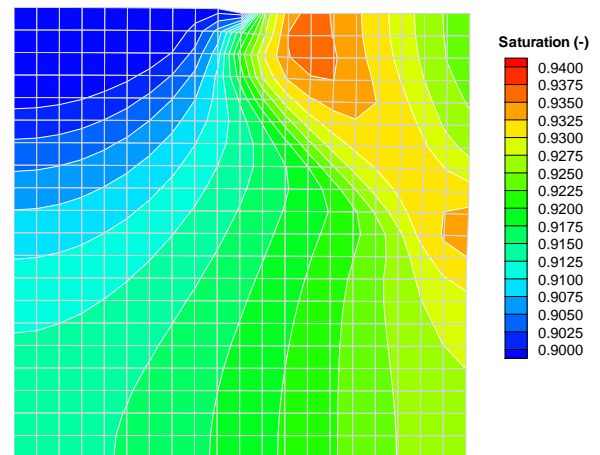


Figure 8.37: Partially saturated rigid footing. Fluid saturation using the *von Mises* yield criterion.

8.4.3.3 Analysis of a dilatant/contractant plastic material

In this section the *Drucker-Prager* plasticity model is used. In case of plastic deformation, positive or negative volumetric plastic strain rates occur, characterizing *dilatant* or *contractant* behavior, respectively. The material is dilatant if the angle of dilatancy ψ is positive.

Comparison of dilatant and contractant material behavior. Dilatant material behavior with an angle of dilatancy $\psi = 10^\circ$ is depicted in Fig. 8.38 and Fig. 8.39. The

equivalent contractant behavior with a negative angle of dilatancy $\psi = -10^\circ$ is depicted in Fig. 8.40 and Fig. 8.41. The fluid velocity is represented by blue arrows indicating the dilatant or contractant behavior in the shear zone.

It can be seen that the extent of the shear zone is affected by the increase or decrease of fluid pressure accompanied by changes in the effective mean stress. The effective mean stress finally influences the shear strength of the material defined by the conical yield surface of the *Drucker-Prager* model.

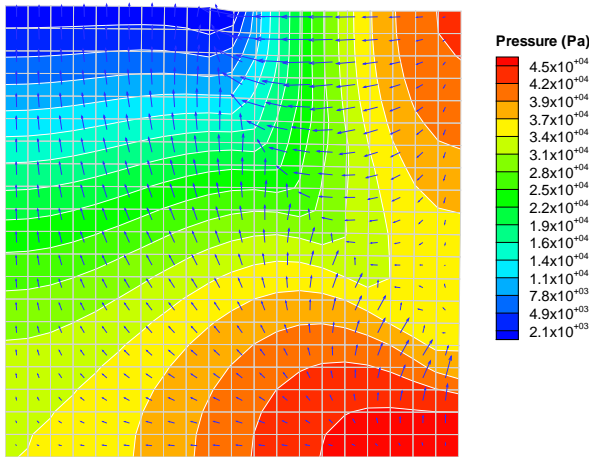


Figure 8.38: Saturated rigid footing. Fluid pressure and fluid velocity in a dilatant *Drucker-Prager* material.

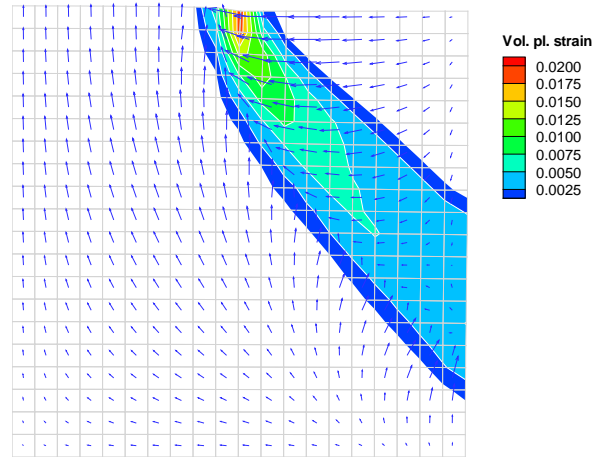


Figure 8.39: Saturated rigid footing. Accumulated volumetric plastic strain and fluid velocity in a dilatant *Drucker-Prager* material.

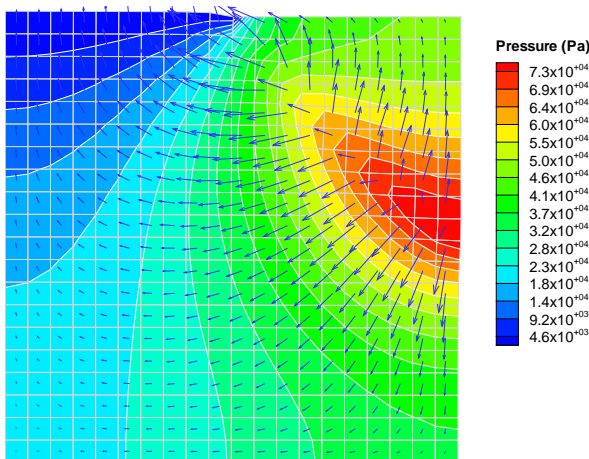


Figure 8.40: Saturated rigid footing. Fluid pressure and fluid velocity in a contractant *Drucker-Prager* material.

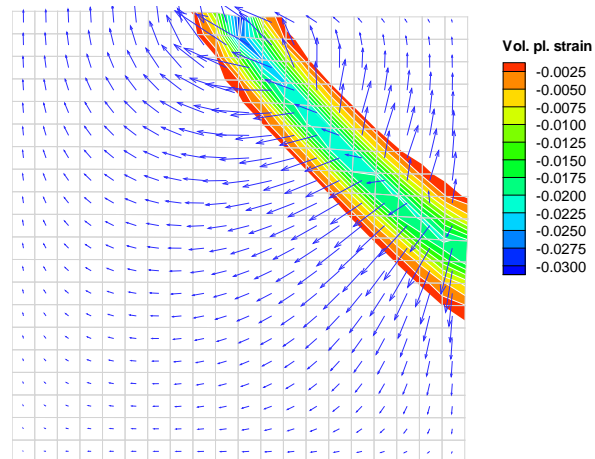


Figure 8.41: Saturated rigid footing. Accumulated volumetric plastic strain and fluid velocity in a contractant *Drucker-Prager* material.

Chapter 9

Applications

We can't solve problems by using the same kind of thinking we used when we created them.

Albert Einstein (1879 - 1955).

9.1 Coupled linear analysis of saturated poroelastic media

9.1.1 Poro-elastic consolidation – strip footing

9.1.1.1 Introduction

The examples presented in this section are a two dimensional plane strain and a three dimensional poro-elastic consolidation. In both examples the vertical load of a strip footing is assumed to act on the soil represented by a fluid-filled porous solid. The effects of gravitational forces remain disregarded.

Due to the load, the saturated porous medium beneath the footing is compressed and the pore fluid is pressed out. Consequently, the effective stresses in the porous structure are increasing in the same way as the fluid pressure is decreasing.

Among others, this test benchmark was studied by Lewis and Schrefler (1989) [64] or Korsawe et al. (2006) [59]. Thus, the benchmark is ideal to study solver characteristics for coupled systems. The two-dimensional and three-dimensional simulations are carried out with meshes of equal element sizes in order to receive comparable results.

9.1.1.2 Strip footing. Geometry and model set-up

In Fig. 9.1 the set-up of the strip footing consolidation problem is depicted and the simulation and mesh data is given in Table 9.1. The material parameters for the footing benchmarks are summarized in Table 9.2.

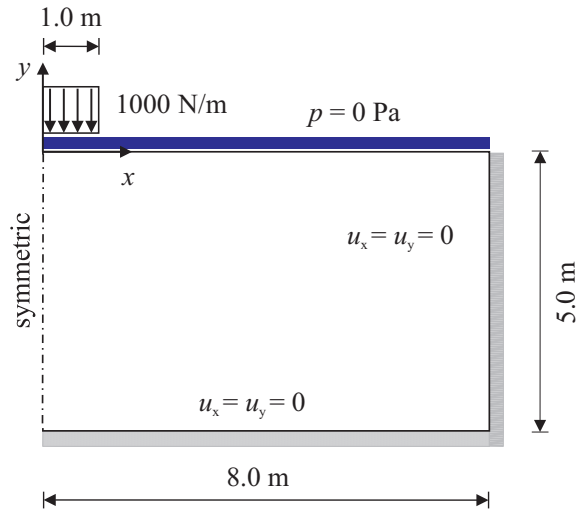


Figure 9.1: Geometry and boundary conditions.

Table 9.1: Strip footing. Mesh properties and temporal discretization.

Parameter	Symbol	Value
Element size	$\Delta x = \Delta y$	0.125 m
Element size	Δz	0.5 m
Degr. of freedom	#DOF 2d	23563
Degr. of freedom	#DOF 3d	94986
Time step length	Δt	1 s

Table 9.2: Strip footing. Material properties.

Parameter	Symbol	Value	
Young's modulus	E	30.0	MPa
Poisson's ratio	ν	0.2	
Permeability	k	1.0×10^{-10}	m^2
Water viscosity	μ^w	10^{-3}	Pa s
Gravity	g	0.0	m s^{-2}
Biot coefficient	α	1.0	

9.1.1.3 Numerical results

The consolidation process is illustrated in Fig. 9.2 presenting the deformed mesh (left) and the fluid pressure field added by fluid velocity vectors (right). As expected, two and three dimensional simulations show identical results. The resulting pressure fields are also given in Fig. 9.4. Fluid pressure and stress distributions along the vertical cross section at $x = 0$ m are depicted in Fig. 9.3. The results agree well with those of Lewis and Schrefler (1998) [64] or Korsawe et al. (2006) [59].

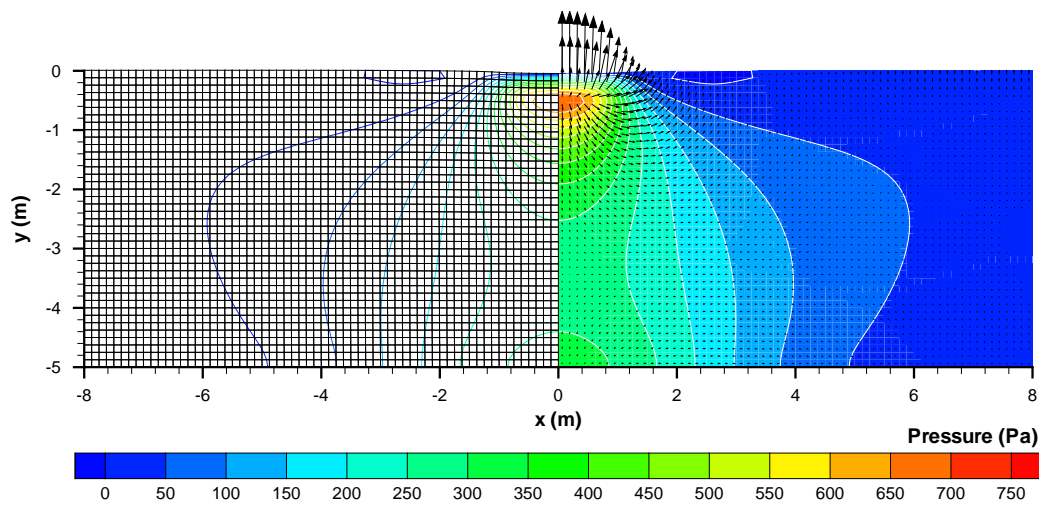


Figure 9.2: Mesh, fluid velocity and pressure field for $t = 10$ s.

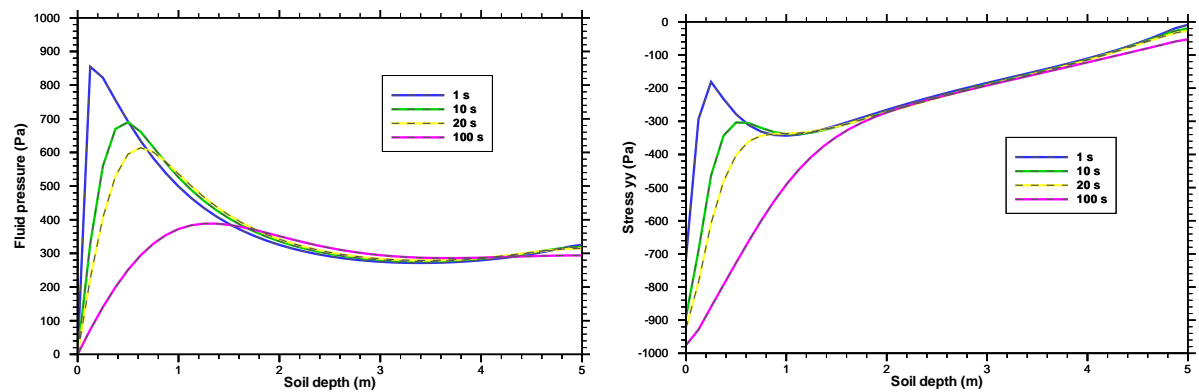


Figure 9.3: Fluid pressure (left) and stress σ_{yy} (right) along vertical cross section at $x = 0$ m for time steps 1, 10, 20 and 100 s evaluated in two (solid line) and three (dashed line) dimensional simulations.

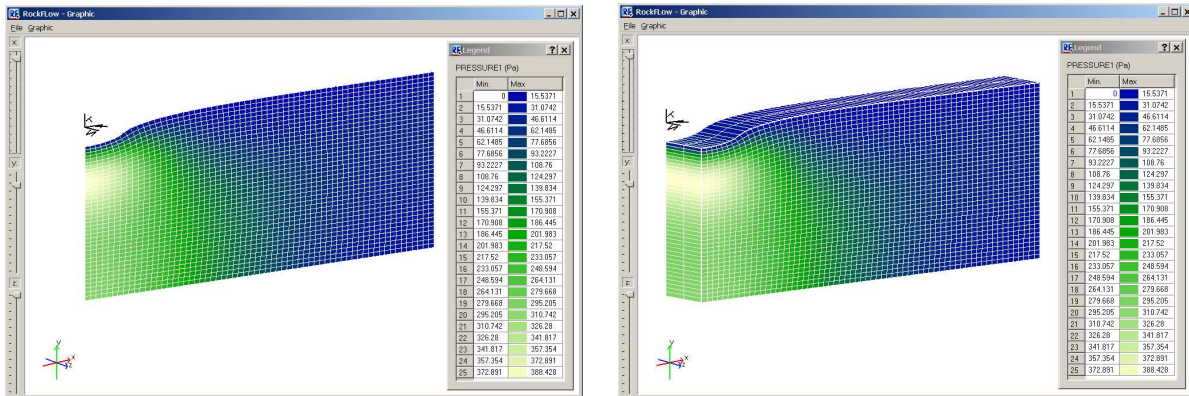


Figure 9.4: Pressure fields of two and three dimensional consolidation at $t = 100$ s. Displacements are scaled by factor 10.

9.1.2 Transport in an incompressible hydraulic system

9.1.2.1 Introduction

The example presented here is a hydro-mechanically coupled system with solute transport. A poro-elastic medium is filled with fluid that contains matter of different concentrations in its three parts depicted in Fig. 9.5. A prescribed cyclic displacement on top of the left cylinder generates a compression of the porous solid that results in a change of fluid pressure and a simultaneous expansion of the right cylinder. This cyclic compression and expansion causes a transport of solute and a continuous mixing.

9.1.2.2 Geometry and model set-up

The initial concentration and the discretized domain is depicted in Fig. 9.6. The joining element is assumed to have a significantly higher stiffness than the left and the right cylinder. Thus, its deformations are negligible. The porosity in the joining element is only $n = 0.1$ which leads to an increase in fluid velocity compared to other bodies. Thus, the advective transport is more dominant here. The material properties of solid medium and liquid phase are summarized in Table 9.3.

9.1.2.3 Numerical results

In addition to the visible coupling effects shown in Fig. 9.7, the results of a converging concentration and constant displacement maxima and minima presented in Fig. 9.8 can be interpreted as evidence of a correct conservation of fluid mass and solute matter, respectively.

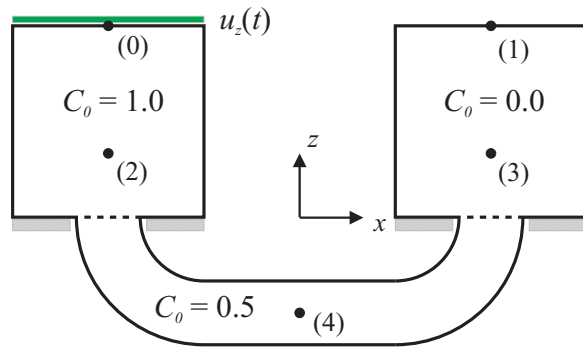


Figure 9.5: Model set-up.

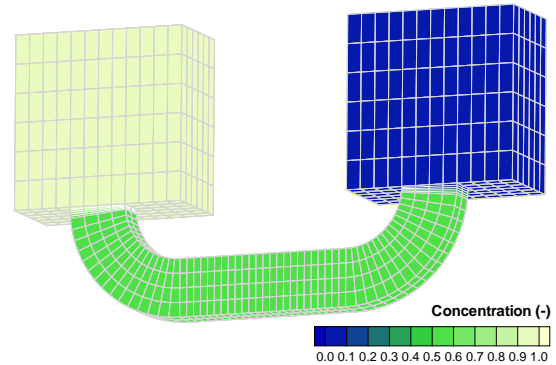


Figure 9.6: Domain and initial concentration.

Table 9.3: Hydro-mechanically coupled transport: material parameters.

Parameter	Symbol	Values		
		left cylinder	right cylinder	joining element
Young's modulus	E	100 MPa	100 MPa	100 GPa
Poisson's ratio	ν	0.2	0.2	0.2
Porosity	n	0.9	0.9	0.1
Permeability	k	$1 \times 10^{-10} \text{ m}^2$	$1 \times 10^{-10} \text{ m}^2$	$1 \times 10^{-10} \text{ m}^2$
water				
Diffusion coeffic.	D	$1 \times 10^{-8} \text{ m}^2 \cdot \text{s}^{-1}$		
Dispersion length	β	0.05 m		
Water viscosity	μ	$10^{-3} \text{ Pa} \cdot \text{s}$		
Gravity	g	$0.0 \text{ m} \cdot \text{s}^{-2}$		

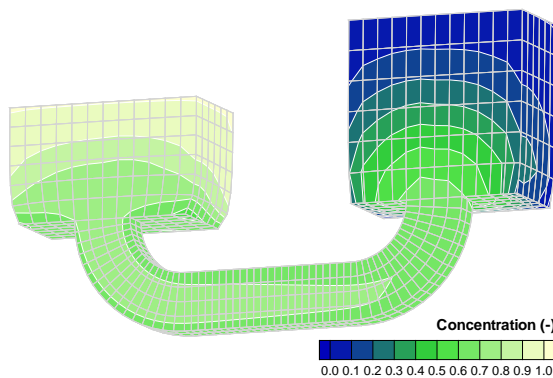


Figure 9.7: Deformed domain and concentration after 2.25 cycles at 540 s.

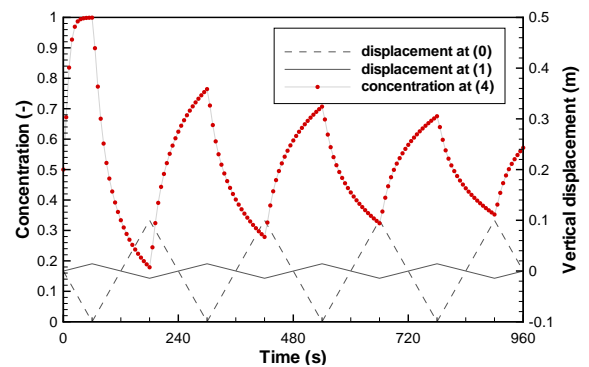


Figure 9.8: Displacements of left and right top and temporal concentration curves in point (4).

9.2 Coupled analysis of thermo-poroelastic media

9.2.1 DECOVALEX-III – Task 3

9.2.1.1 Introduction

The *DECOVALEX* project is an international cooperative project initiated by SKI, the Swedish Nuclear Power Inspectorate, with participation of several international organizations. The general goal is to encourage multidisciplinary interactive and cooperative research on modeling coupled processes in fractured rocks and buffer materials, in support of the performance assessment for radioactive waste storage.

In the present section, the *Benchmark Test 1 - Part B* (BMT 1-B) is described. This benchmark is part of Task 3 within DECOVALEX-III. It is concerned with thermo-hydro-mechanical simulation of a repository. The definition of the benchmark is based on a hypothetical set-up of a nuclear waste repository described in Nguyen et al. (2003) [78]. The part B of BMT 1 consists of performing scoping calculations for a typical repository in a homogeneous rock, in order to look at the implications of THM coupling on safety issues related to the near-field. The results given here are restricted to thermomechanical analysis.

9.2.1.2 Geometry and model set-up

The geometry of a typical tunnel of a hypothetical repository is depicted in Fig. 9.9 located in 1000 m depth. Due to symmetry conditions only a quarter of the whole domain need to be analyzed. For thermal and thermomechanical analysis two meshes of different discretizations have been used. The model consists of the following materials: homogeneous rock mass, backfill, buffer, waste and overpack. The material properties are listed in Table 9.4.

Table 9.4: Task 3. BMT 1-B. Material properties.

Material parameter	Rock mass	Backfill	Buffer	Waste & overpack
Youngs modulus, E (MPa)	61.0×10^3	5.0	100.0	200.0×10^3
Poissons ratio, ν	0.303	0.4	0.4	0.3
Thermal exp. coeff., α_T (K^{-1})	8.21×10^{-6}	8.21×10^{-6}	8.21×10^{-6}	1.64×10^{-6}
Effective porosity, n (%)	0.379	30	20	0.0379
Density, ρ (kg/m^3)	2746	1750	1800	7800
Specific heat, c (J/(kgK))	900	826.087	826.087	460
Thermal conduct., λ , (W/mK)	2.6	1.46213	1.36760	53

The initial conditions and the boundary conditions to be applied for excavation and transient analysis are depicted in Fig. 9.10. For the transient analysis a heat source boundary has to be prescribed according to the heat output curve shown in Fig. 9.11.

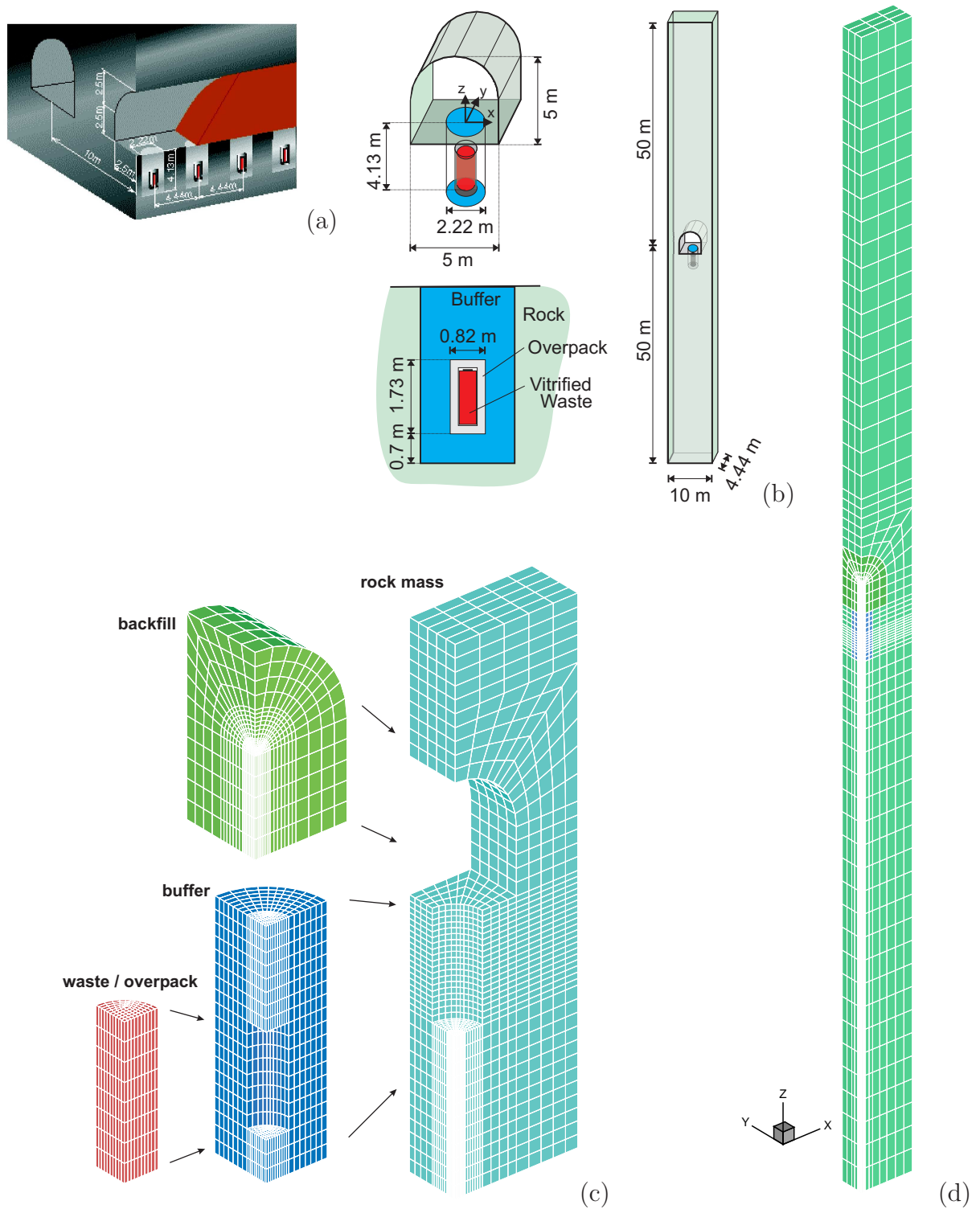


Figure 9.9: Task 3. BMT 1-B. Conceptual design of a hypothetical repository [47] (a). Conceptual representation of repository near-field (b). Near-field parts of the fine mesh for temperature analysis consisting of waste/overpack, buffer, fracture, backfill and rock mass (c). Mesh used for thermomechanical analysis (d).

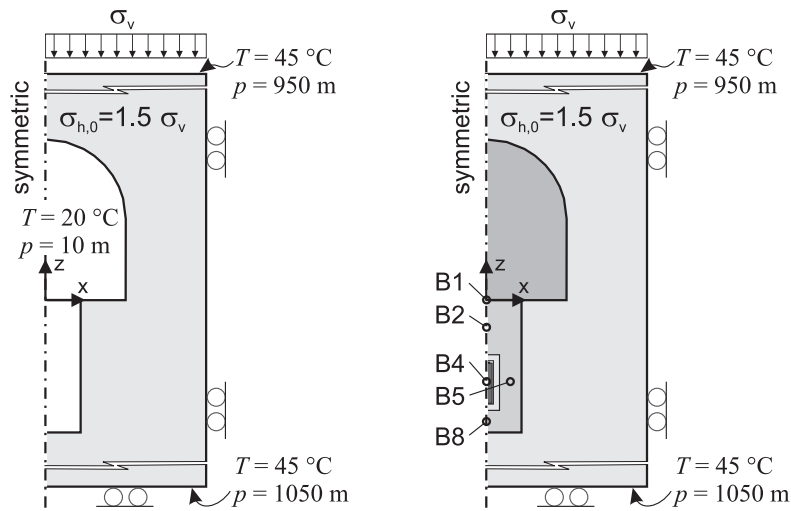


Figure 9.10: Task 3. BMT 1-B. Initial and boundary conditions prescribed for excavation (left) and ensuing transient analysis (right).

9.2.1.3 Results of transient thermal analysis

Two reasonable scenarios for the initial state are possible: (i) a steady state heat flow according to the boundary conditions for the excavation phase given in Fig. 9.10 (left) or (ii) starting with an initial temperature of 45°C in the whole domain assuming a short excavation phase with minor influence on the temperature of the far-field. Here the results of case (ii) are presented. In order to verify a sufficient mesh quality, the thermal analysis is performed on a finer mesh than the thermomechanical analysis. The resulting temperature is depicted in Fig. 9.11.

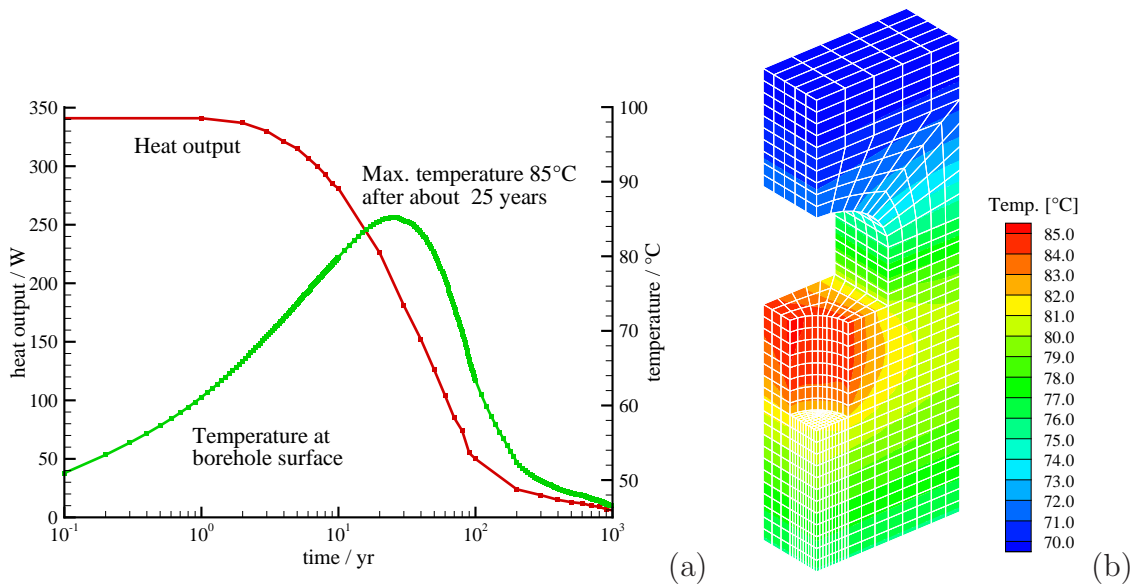


Figure 9.11: Heat output curve, resulting temperature curve (a) and temperature in the near-field after 30 years (b).

9.2.1.4 Results of transient thermo-mechanical analysis

The temperature and stress fields resulting from the thermo-mechanical analysis at time $t = 10$ years are depicted in Fig. 9.12. The resulting temperature and stress curves at selected points in the buffer (B1, B2, B8 cf. Fig. 9.10) are given in Fig. 9.13 and Fig. 9.14. The heat producing waste affects the temperature field. Starting with an assumed initial temperature of 45 °C a maximum temperature is predicted and the influence on the mechanical behavior of the solid structure can be seen. Effects of vaporization of water or vapor transport are not incorporated.

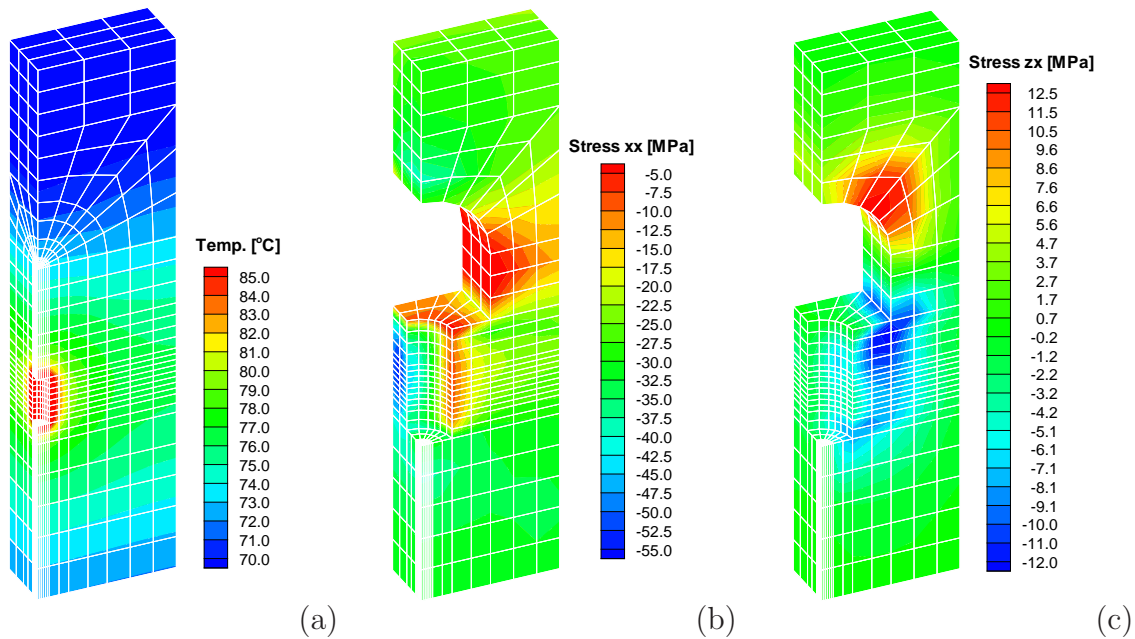


Figure 9.12: Temperature field (a), horizontal stress σ_{xx} (b) and shear stress σ_{zx} (c) after 10 years.

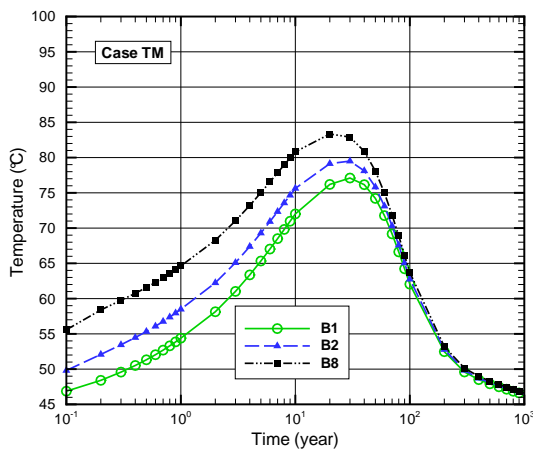


Figure 9.13: Temperature versus time.

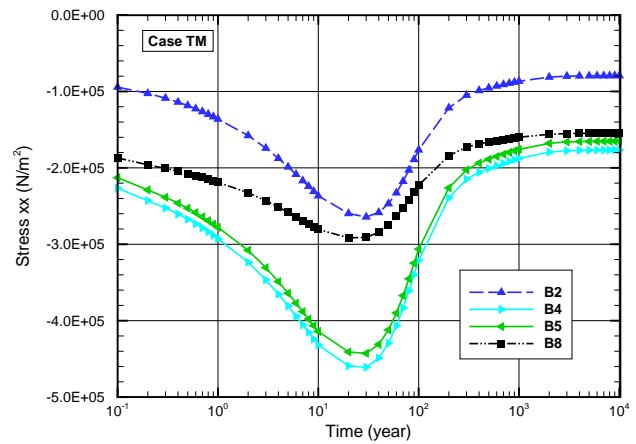


Figure 9.14: Stress σ_{xx} versus time.

9.2.2 Density driven flow in a thermo-poro-elastic medium

9.2.2.1 Introduction

In geothermal applications heat transport by injected water mass is the main process. Nevertheless, density driven flow may occur due to density gradients in the fluid caused by thermal expansion. The process of thermal convection in a thermo-hydro-mechanically coupled porous medium is presented in this example.

9.2.2.2 Geometry and model set-up

The schematic set-up of the model is depicted in Fig. 9.15. Its three-dimensional representation is illustrated in Fig. 9.16. On the right hand side a constant temperature of 45 °C is prescribed representing a geothermal activity. A cooling on the left hand side, prescribed by a constant thermal heat sink, represents an extraction well. The fluid volume remains constant as no fluid is injected or extracted. The solid material is chosen to be equivalent to rock mass but with higher porosity n and significantly higher permeability k . The fluid is supposed to be water. The material properties are summarized in Table 9.5.

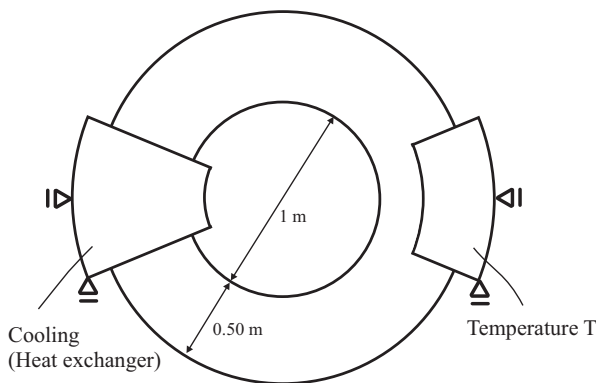


Figure 9.15: Torus. Set-up.

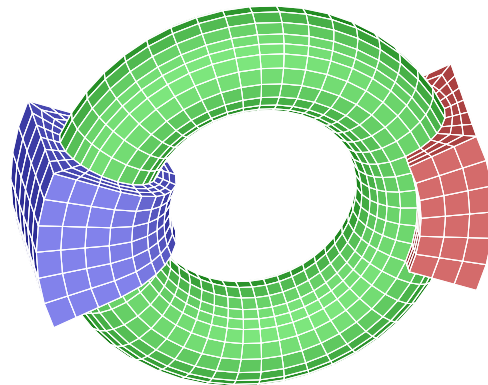


Figure 9.16: Torus. Mesh of differently colored partitions.

9.2.2.3 Results of thermo-hydro-mechanical analysis

The fluid flow in the torus is controlled by density gradients. The circulating fluid causes an advective transport of heat energy. The fluid flow field is in a steady state as soon as the thermal flow has heated up the system according to its specific heat. The resulting steady state fields of temperature and displacement are depicted in Fig. 9.17 and Fig. 9.18.

Table 9.5: Material properties.

Material parameter	Symbol	Value	
Rock			
Youngs modulus	E	61.0×10^3	MPa
Poissons ratio	ν	0.303	
Thermal expansion coeff.	α_T	8.21×10^{-6}	K^{-1}
Porosity	n	0.1	
Permability	k	1×10^{-7}	m^2
Density	ρ^s	2746 kg m^{-3}	
Specific heat	c^s	900	$\text{J kg}^{-1} \text{K}^{-1}$
Thermal conductivity	λ^s	2.6	$\text{W m}^{-1} \text{K}^{-1}$
Water			
Viscosity	μ^w	10^{-3}	Pa s
Density	ρ^w	1000 kg m^{-3}	
Specific heat	c^w	4200	$\text{J kg}^{-1} \text{K}^{-1}$
Thermal conductivity	λ^w	0.6	$\text{W m}^{-1} \text{K}^{-1}$

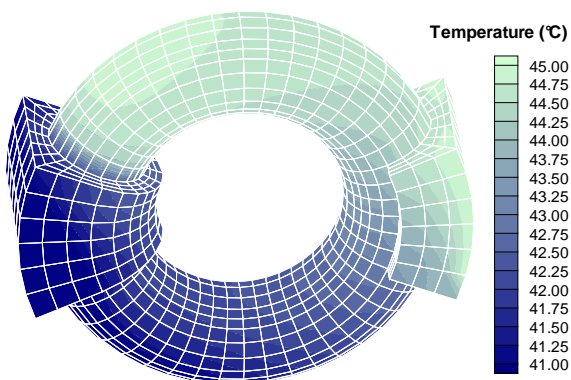


Figure 9.17: Resulting steady state temperature field.

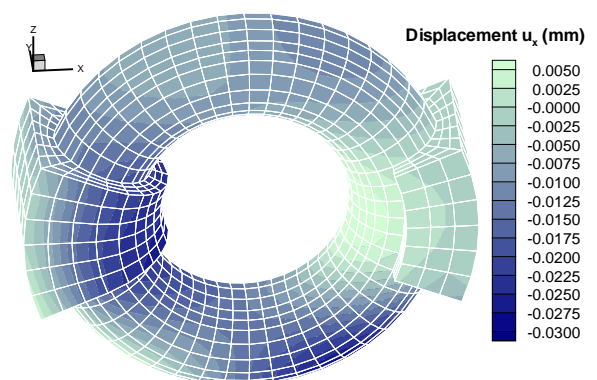


Figure 9.18: Resulting steady state displacement field.

9.3 Coupled analysis of partially saturated thermoelastic and elasto-plastic media

This section is concerned with fully coupled thermo-hydro-mechanical modeling combined to non-linear flow and deformation processes. Non-linearities occur due to flow in partially saturated media, saturation induced swelling of expansive material or elasto-plastic behavior of fully or partially saturated soils.

9.3.1 DECOVALEX-THMC – Task D

9.3.1.1 Introduction

The application presented in this section originated in the framework of the DECOVALEX-THMC international project which is a continuation of the project DECOVALEX-III. It has been introduced in Sec. 9.2.1. The latter is a multi-disciplinary interactive and co-operative research effort in modeling *Thermo-Hydro-Mechanical-Chemical* (T-H-M-C) processes in fractured rocks and buffer materials. In addition to coupled code development, the project investigates the role of T-H-M-C processes in *Performance Assessment* (PA) for radioactive waste storage.

In the recent project stage of DECOVALEX-III the THM modeling work on two large-scale in situ heater experiments had been included: the *FEBEX* experiment at Grimsel in Switzerland and the *Drift Scale Test* (DST) at *Yucca Mountain* in the USA. In continuation, the new project DECOVALEX-THMC applies the knowledge gained from modeling the above mentioned short-term in situ tests, with a test period between one and eight years, to the evaluation of long term processes. Two generic repository types are considered according to the FEBEX and Yucca Mountain experiments. The regulatory compliance periods in these types of repositories span over thousands to ten-thousands of years.

Task D investigates thermo-hydro-mechanical as well as thermo-hydro-chemical processes. Thus, two sub-tasks of different objectives have been defined. The task definition that focuses on geomechanical processes is referred to as D_THM, and the other one focusing on geochemical processes is referred to as D_THC. The simulation presented in this work concentrates on the thermo-hydro-mechanical sub-task D_THM. For more details concerning the other sub-task, the interested reader should refer to Barr et al. (2004) [2].

9.3.1.2 General model set-up

Description of repository scenarios. As mentioned above, two different generic repository settings are considered named *Yucca Mountain* type and *FEBEX* type. Consequently, both sub-tasks are further sub-divided into (1) THC1/THM1 and (2) THC2/THM2. The repository type (1) is supposed to be located in saturated crystalline rock, where emplacement tunnels are backfilled with buffer material of *FEBEX*

type, while the emplacement of type (2) is defined to be proceeded in open gas-filled tunnels of *Yucca Mountain* type. The similarities and differences of both scenarios are summarized in Table 9.6.

Table 9.6: Task D. Summary of similarities and differences between repository scenarios [2].

	Repository Scenario (1): FEBEX Type	Repository Scenario (2): Yucca Mountain Type
Compl. Period	To be defined	10,000 years
Geometry	Similar	Similar
Initial Heat Load	290 W/m	1,450 W/m Ventilation effects reduce this load during 50-year period.
Tunnel	Bentonite-filled	Open, no buffer.
Flow in Tunnel	Initially unsaturated; swelling effects. Two-phase flow under thermal gradient.	Gas flow
Rock	Sparsely fractured crystalline rock.	Densely fractured volcanic rock.
Flow in Rock	Saturated in far-field rock. Initially unsaturated in near-field rock.	Unsaturated. Two-phase flow under thermal gradient.

Geometric data. The model set-up is similar for both *Yucca Mountain* and *FEBEX* type. A schematic general description of the model geometry, the boundary conditions, the specific areas of focus, and profiles/locations for which simulation outputs should be derived is presented in Fig. 9.19. Due to symmetry conditions only a single drift has to be considered, representing a repository of infinite length and width. Consequently, this approach represents an extreme setting as interactions with the surrounding area are restricted to top and bottom boundaries. The specific data of sub-task THM1, to be analyzed in this work, is given in detail in the next section.

9.3.1.3 Specific model set-up of sub-task THM1

Model dimensions. According to the general definitions given in Fig. 9.19, the model dimensions for Task THM1 are summarized in Table 9.7.

Material properties. The material properties of the rock is summarized in Table 9.8. The bentonite buffer material is of FEBEX type. The material properties of the bentonite are summarized in Table 9.9. The water retention curve is a modified and a standard

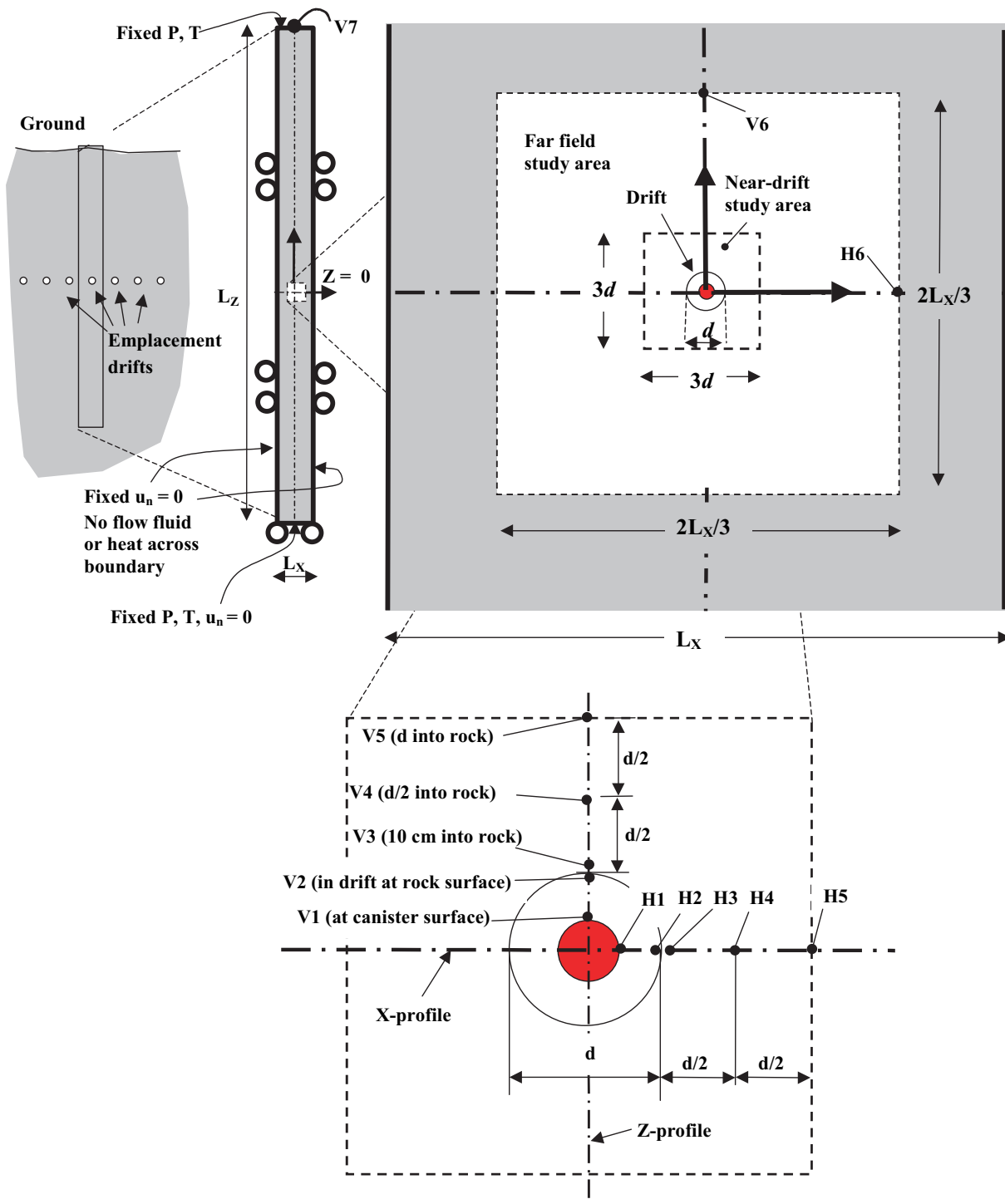


Figure 9.19: General model description for Task D, THM. Model geometry and boundary conditions (above). Locations of points, lines and areas for model output (below) [2].

van Genuchten function for the bentonite and the rock, respectively. The curves are depicted in Fig. 9.20.

Table 9.7: Task D_THM1. Model dimensions.

Dimension	Value
Vertical length, L_z	1,000 m
Horizontal length, L_x	35 m
Drift diameter, d	2.28 m
Diameter of waste canister	0.9 m

Table 9.8: Task D_THM1. Material properties of the rock.

Parameter	Value
Density, ρ	2,700 kg m ⁻³
Porosity, n	0.01
Biot's constant, α	1.0
Young's modulus, E	35 GPa
Poisson's ratio, ν	0.3
Specific heat c	900.0 J kg ⁻¹ K ⁻¹
Thermal conductivity, λ	3.0 W m ⁻¹ K ⁻¹
Thermal expansion coeff., α_T	1.0×10^{-5} K ⁻¹
Permeability, k	1.0×10^{-17} m ²
Rel. Permeability, k_{rel}	$k_{\text{rel}} = \sqrt{S} (1 - (1 - (S^{1/0.6})^{0.6})^2)$
Water retention, $S(p_c)$	$S = (1 + (\frac{p_c}{1.47 \text{ MPa}})^{2.5})^{-0.6}$

Table 9.9: Task D_THM1. Material properties of the bentonite buffer.

Parameter	Value
Dry density, ρ	1,600 kg m ⁻³
Porosity, n	0.41
Biot's constant, α	1.0
Young's modulus, E	100 MPa
Poisson's ratio, ν	0.35
Moisture swelling coefficient, β_{sw}	0.238
Dry specific heat, c_s	767 J kg ⁻¹ K ⁻¹ , $((1.38 \text{ K}^{-1} \cdot T + 732.5) \text{ J kg}^{-1} \text{ K}^{-1})$
Thermal conductivity, λ_m	1.3 Wm ⁻¹ K ⁻¹ , $((1.28 - \frac{0.71}{1+e^{(S-0.65)/0.1}}) \text{ Wm}^{-1}\text{K}^{-1})$
Thermal expansion coeff. α_T	1.0×10^{-5} K ⁻¹
Permeability, k	1.0×10^{-21} m ²
Rel. permeability, k_{rel}	$k_{\text{rel}} = S^3$
Water retention, $S(p_c)$	$S = 0.01 + 0.99 (1 + (\frac{p_c}{35 \text{ MPa}})^{1.43})^{-0.3} (1 - \frac{p_c}{4000 \text{ MPa}})^{1.5}$

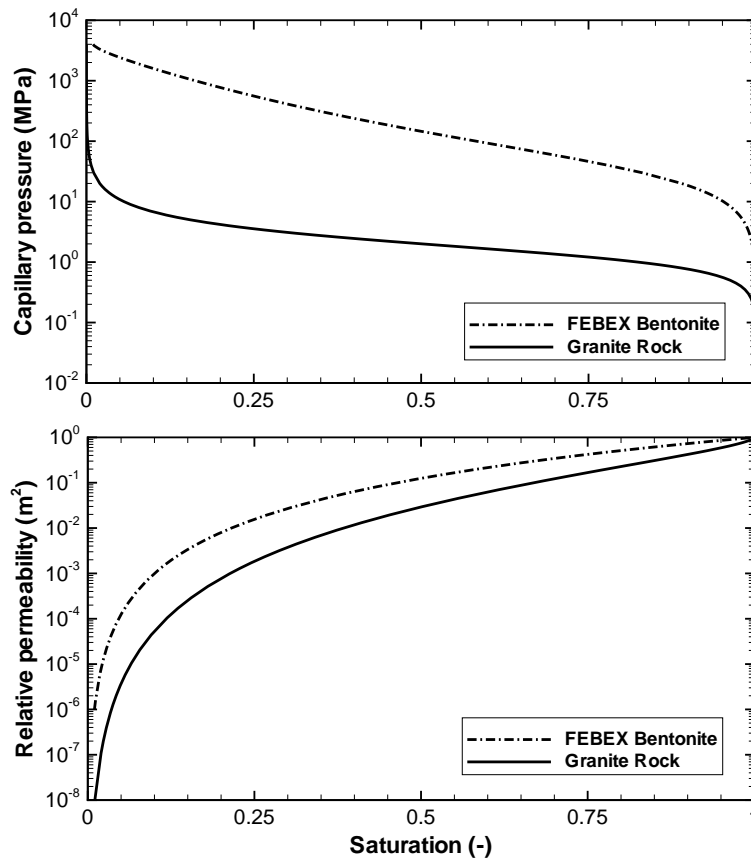


Figure 9.20: Water retention and relative permeability curves for granite rock (standard *van Genuchten*) and FEBEX bentonite material (modified *van Genuchten*) as defined in Table 9.8 and Table 9.9.

Heat output. The thermal power emitted by a reference *Pressurized Water Reactor* (PWR) element is depicted in Fig. 9.21. Assuming that the waste is 30 years old at emplacement time, the current heat output is 400 W per PWR element. Considering an alignment of four PWR elements per canister of 4.54 m length and a canister spacing of 2 m results in an average thermal power per meter drift of $4 \times 400 \text{ W}/6.54 \text{ m} = 245 \text{ W/m}$. The temporal evolution of this value is according to the decay curve depicted in Fig. 9.21 in consideration of the initial disposal time of 30 years.

In situ stress field. The in situ stress field is assumed to depend linearly on the depth D . The horizontal total stress is prescribed by the function $\sigma_h = 0.055 \text{ MPa/m} \cdot D + 4.6 \text{ MPa}$ while the vertical stress is evaluated by the stress of the overlying rock mass. Thus, at the drift axis the initial value of the horizontal stress is 32.1 MPa while the vertical stress is about 13.5 MPa.

Modeling sequence. The modeling sequence demanded in Task THM1 is concerned with (a) the pre-excavation conditions, (b) the simulation of the excavation, (c) the

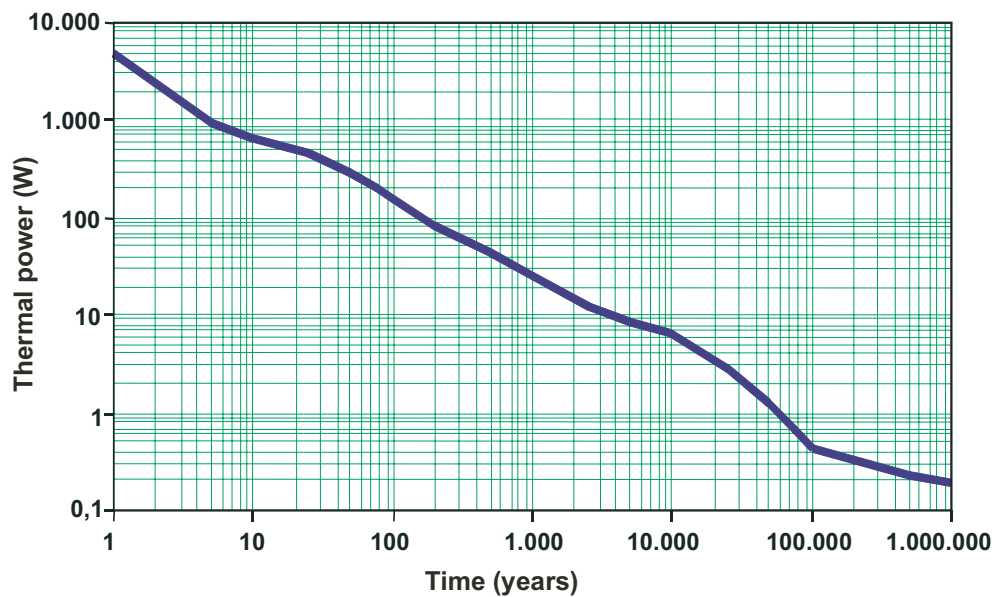


Figure 9.21: Thermal power decay function of a reference fuel PWR element [2].

installation of bentonite buffer and finally (d) the transient simulation of the post-closure thermo-hydro-mechanical behavior of the repository. The sequences and the associated initial and boundary conditions are depicted in Fig. 9.22. The numerical predictions for these sequences are presented in the next sections.

9.3.1.4 Numerical simulation of pre-excavation conditions

The pre-excavation is simulated in order to check the correctness of the initial values of the numerical model. As the stress and fluid pressure fields are correct and the strain is equal to zero, the simulation of the next phases can be initiated. The results are presented in the following three sections.

9.3.1.5 Numerical simulation of the excavation

With the pre-excavation model at hand, the excavation is simulated by disregarding the rock mass elements. The deformation and the stress increase due to excavation is depicted in Fig. 9.23. It also shows the decrease of fluid pressure around the tunnel causing an overall settlement of the drift and the overlying rock mass.

9.3.1.6 Numerical simulation of installation of bentonite buffer

The installation of the bentonite buffer is finally simulated by replacing the rock mass elements by bentonite elements. No initial stresses are applied. The initial saturation is 65 %. This phase immediately runs over into the transient phase which is presented in the next section.

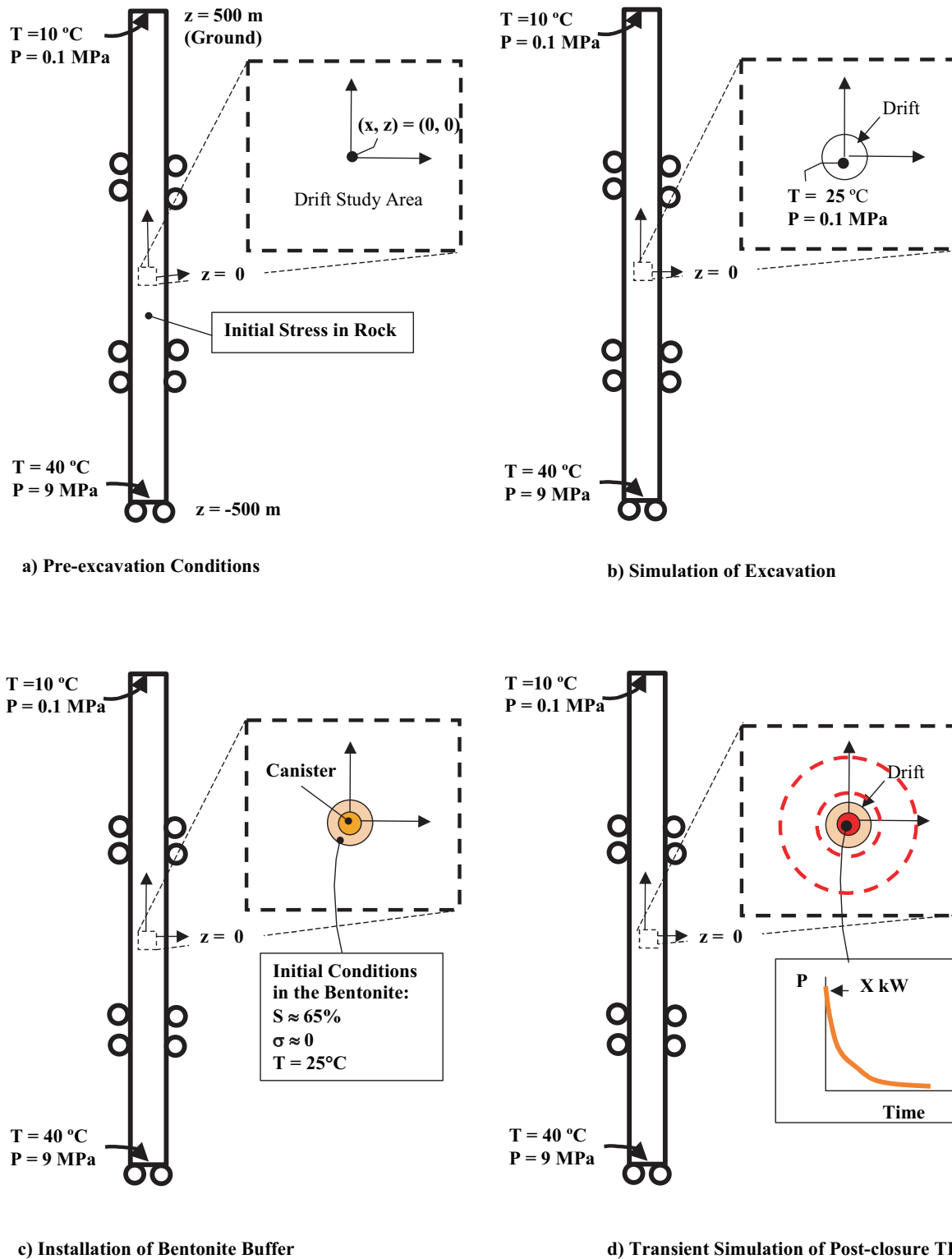


Figure 9.22: Specific modeling sequence, initial and boundary conditions for Task D, THM1 [2].

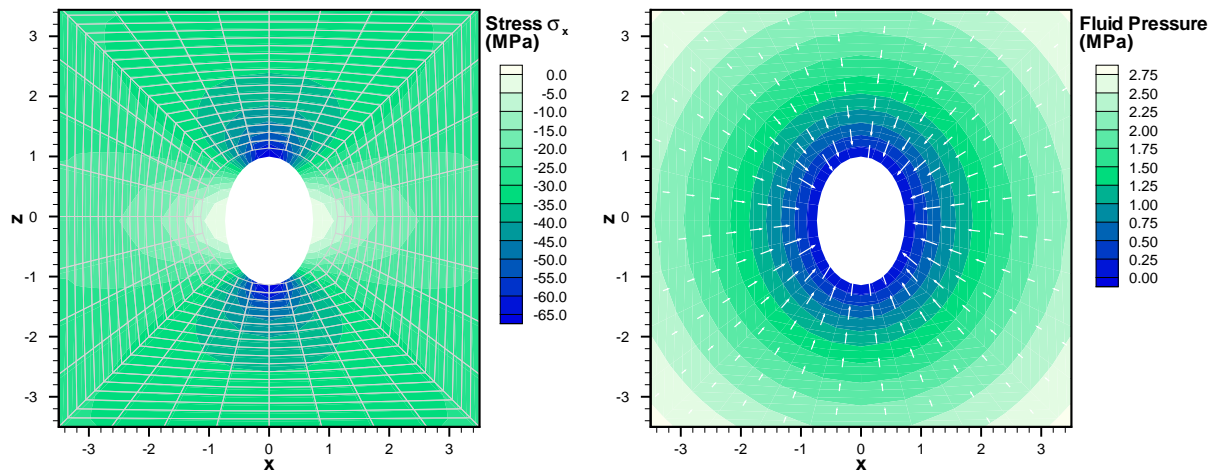


Figure 9.23: Horizontal stress (left) in the deformed near field due to excavation. The undeformed mesh represents the initial configuration. The settlement of the drift is due to the transient pressure field (right) influenced by the drainage caused by the atmospheric pressure in the drift wall. The displacements are scaled by factor 250.

9.3.1.7 Numerical simulation of the transient thermo-hydro-mechanical response

The transient simulation predicts the thermo-hydro-mechanical response of the repository for a time range of 100,000 years. The RockFlow results, presented in the following, are compared to predictions carried out with two different codes, namely TOUGH2 and ROCMAS. The reference values obtained with TOUGH2 and ROCMAS are taken from Birkhölzer et al. (2005) [10]. The presentation of the resulting values is according to the model output specifications given in Fig. 9.19.

Temperature evolution. The evolution of the temperature is depicted in Fig. 9.24 and Fig. 9.25. The peak temperature of 93.2 °C is reached after 11 years. As the temperature strongly depends on the heat output, the maximum temperature is very sensitive to the interpolation of the thermal power decay function depicted in Fig. 9.21. Its logarithmic decrease has to be reflected in the time step size in order to ensure a correct integration in time. Regarding the temperature field, the length of the time period for the reestablishment of initial state conditions is more than 100,000 years.

Evolution of water saturation and fluid pressure. The fluid pressure profiles of the RockFlow, TOUGH2 and ROCMAS simulations are shown in Fig. 9.26 and Fig. 9.27. During the steady-state analysis of the excavation sequence, the overburden is drained due to prescribed atmospheric pressure in the drift. After emplacement of the PWR canisters and backfilling the tunnel with a partially saturated bentonite mixture, the closing of the drift is initiated. In the model, the closing is described by releasing the fluid pressure boundary condition at the wall of the drift. Thus, the hydrostatic gradient

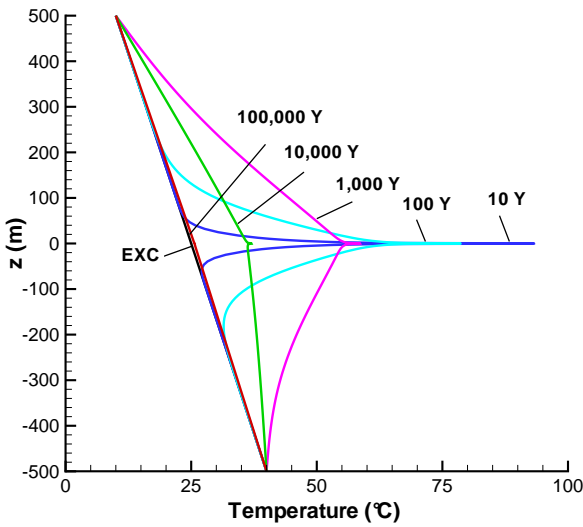


Figure 9.24: RockFlow simulation results of vertical temperature profiles.

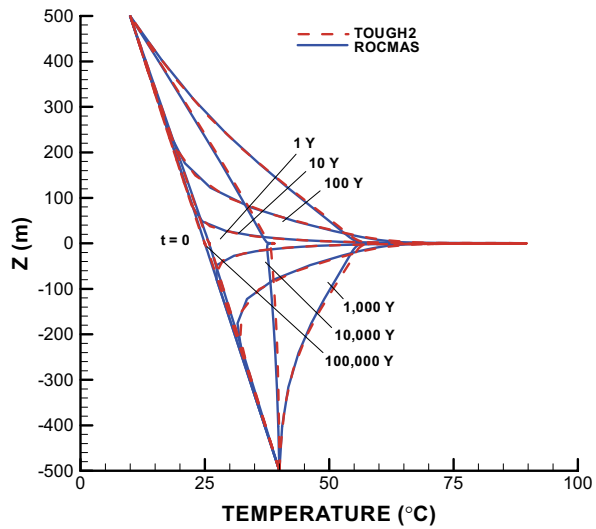


Figure 9.25: Comparison of TOUGH-FLAC (TOUGH2) and ROCMAS simulation results of vertical temperature profiles [10].

of fluid pressure is slowly reestablished within the whole domain of bentonite and rock mass. The resaturation of the bentonite takes about 30 years, but it has to be mentioned that no evaporation and moisture transport has been taken into account. Regarding the fluid pressure field, the length of the time period for the reestablishment of the initial state is more than 100 years.

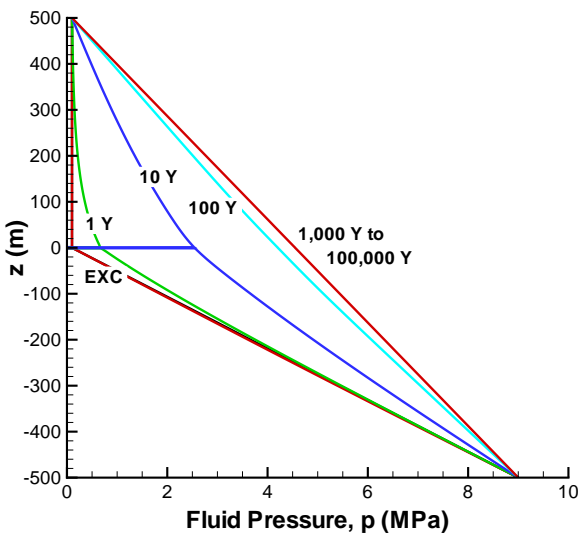


Figure 9.26: RockFlow simulation results of vertical pressure profiles.

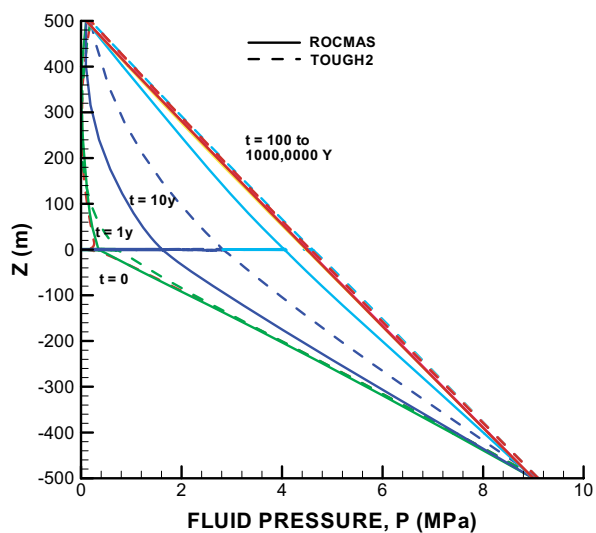


Figure 9.27: Comparison of TOUGH2 and ROCMAS simulation results of vertical pressure profiles [10].

Evolution of stress. The vertical profiles of the horizontal and vertical component of the total stress are presented in Fig. 9.28 and Fig. 9.29. The total stress is defined to be compound by the effective stress σ and the fluid pressure p reduced by the saturation S in case of unsaturated conditions

$$\sigma^{\text{tot}} = \sigma - p S \quad (9.1)$$

Remark: In contrast to the convention of negative compressive stress used within this work, in the ROCKMAS code the convention is vice versa as a positive compressive stress is usually preferred in soil mechanics. Due to this fact the values of the stress profiles depicted in the following figures are of opposite sign.

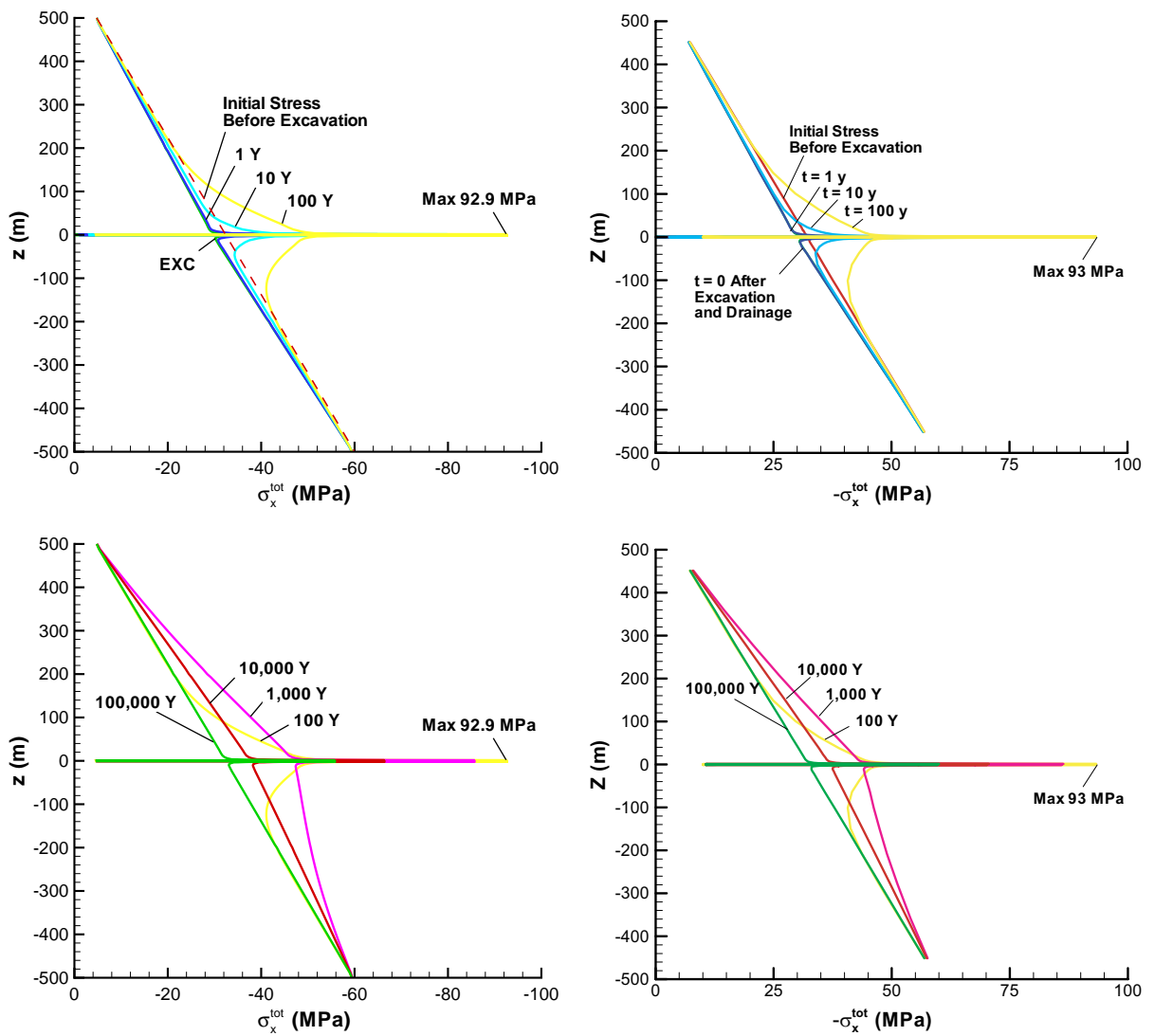


Figure 9.28: Simulation results of vertical profiles of total horizontal stress. RockFlow (left) and ROCKMAS (right) [10].

In the total stress plots not only the variation of thermal stresses becomes obvious but changes in fluid pressure can also be identified as well. After excavation, the total stress is lower than the initial stress, which is induced by the decrease of water pressure due to the drainage process. At the end of the simulation time of 100,000 years, when the initial water pressure field is build up again, the stresses increase linearly with depth. Neglecting the disturbance by the drift, the stresses at level $z = 0$ m would result in the initial stress values of -32.1 MPa in horizontal direction and about -13.5 MPa in vertical direction.

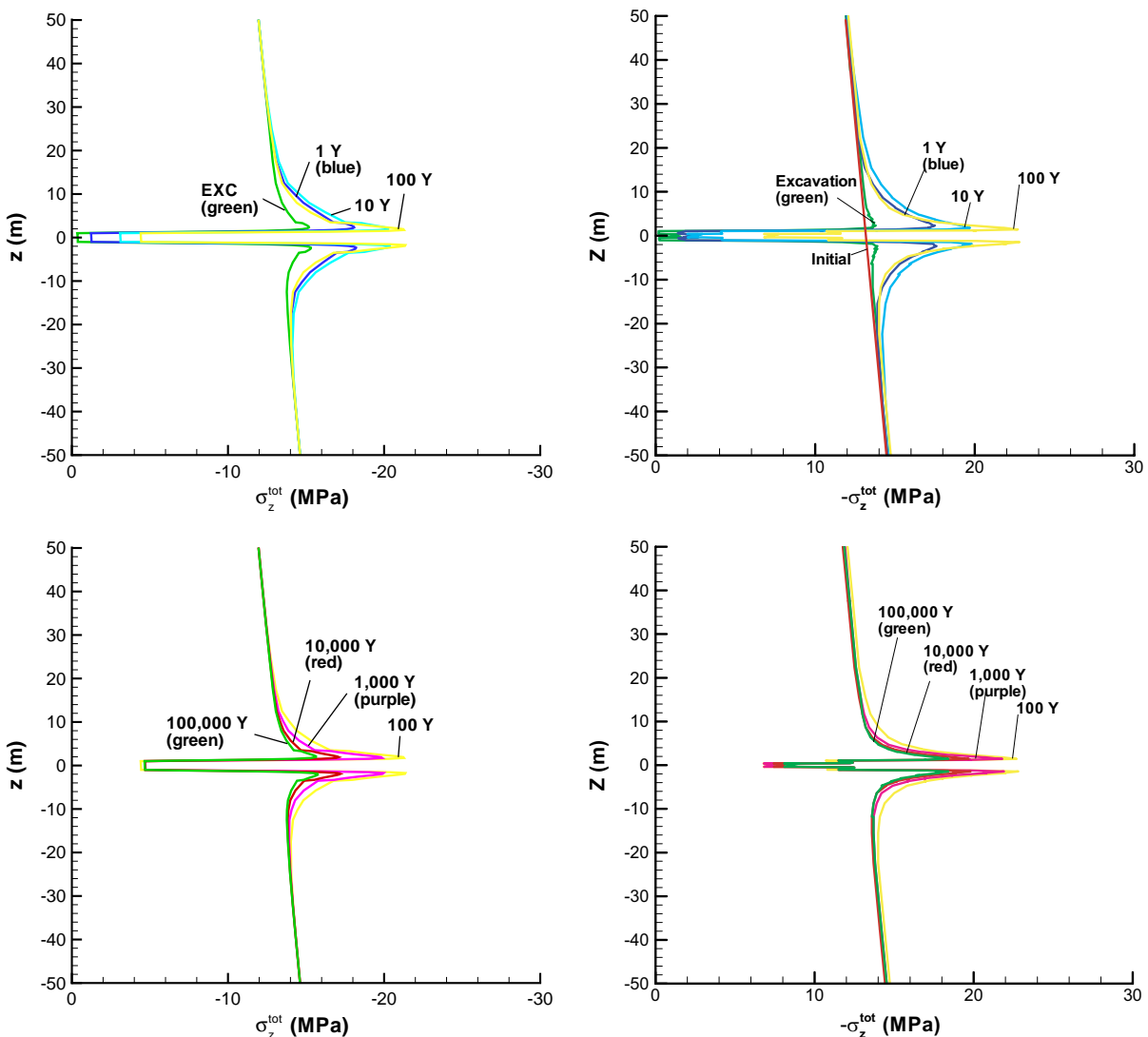


Figure 9.29: Simulation results of vertical profiles of vertical stress. RockFlow (left) and ROCMAS (right) [10].

Evolution of displacement. The profiles of the vertical displacement are presented in Fig. 9.30 and Fig. 9.31. The initial settlement of the entire column is caused by the drainage of water into the open drift during the excavation phase. During the excavation phase, the water pressure above the drift is assumed to be equal to atmospheric pressure. After closing the drift, the reestablishment of water pressure and the temperature increase due the prescribed heat power output cause an upwardly directed displacement of the drift and the whole column.

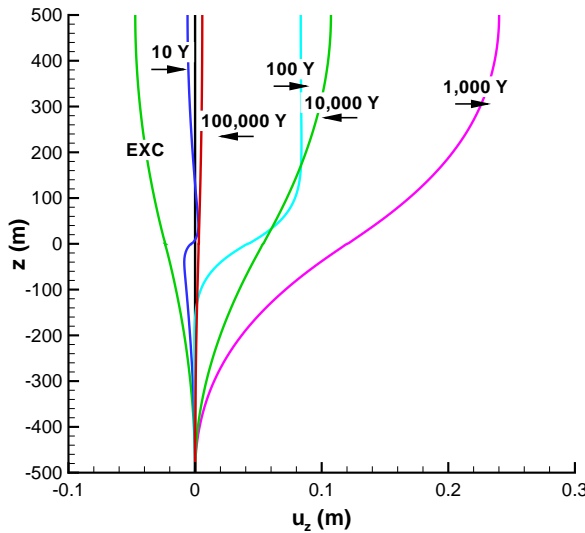


Figure 9.30: RockFlow simulation results of vertical displacement profiles.

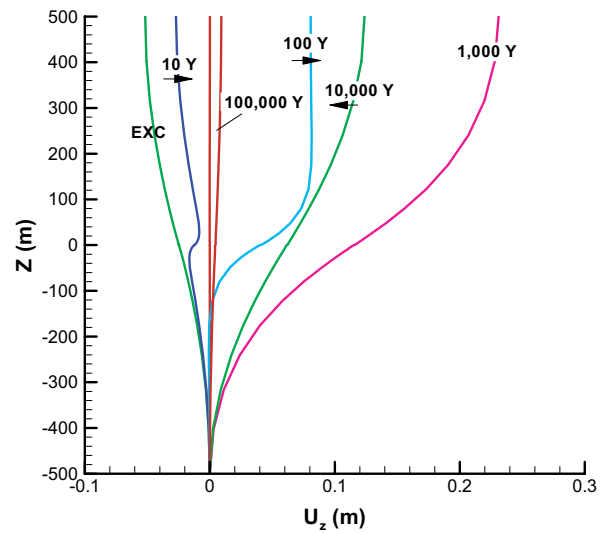


Figure 9.31: ROCMAS simulation results of vertical displacement profiles [10].

9.3.1.8 Conclusions

The numerical predictions achieved in the RockFlow simulations are in good agreement to the results predicted by the other research teams involved in Task D.

The partially saturated bentonite buffer and the time period of resaturation is of special interest. It becomes obvious that the resaturation is limited by the low conductivity of the barrier material. The influence of swelling pressure on the porosity and permeability could be of interest.

As the temperature is significantly below the boiling point of water, the effect of evaporation and the moisture transport forced by the thermal gradient is neglected here, but might be of considerable importance, especially if high temperatures occur at the canister.

9.3.2 Embankment problem

9.3.2.1 Introduction

This example is concerned with the two-dimensional simulation of a multiphase flow through an embankment. Numerical results of this problem are given for example by Ehlers et al. [35]. The embankment is depicted in Fig. 9.32. It has a height of 10 m and a slope of 1:3 at both sides. The ground level is assumed to have a low permeability of the same magnitude as the central sealing unit. Geometries of steeper slope are investigated in order to identify situations of possible failure.

9.3.2.2 Model set-up

The set-up of the embankment problem and its boundary conditions are depicted in Fig. 9.32. The material properties of the different parts of the dam are summarized in Table 9.10.

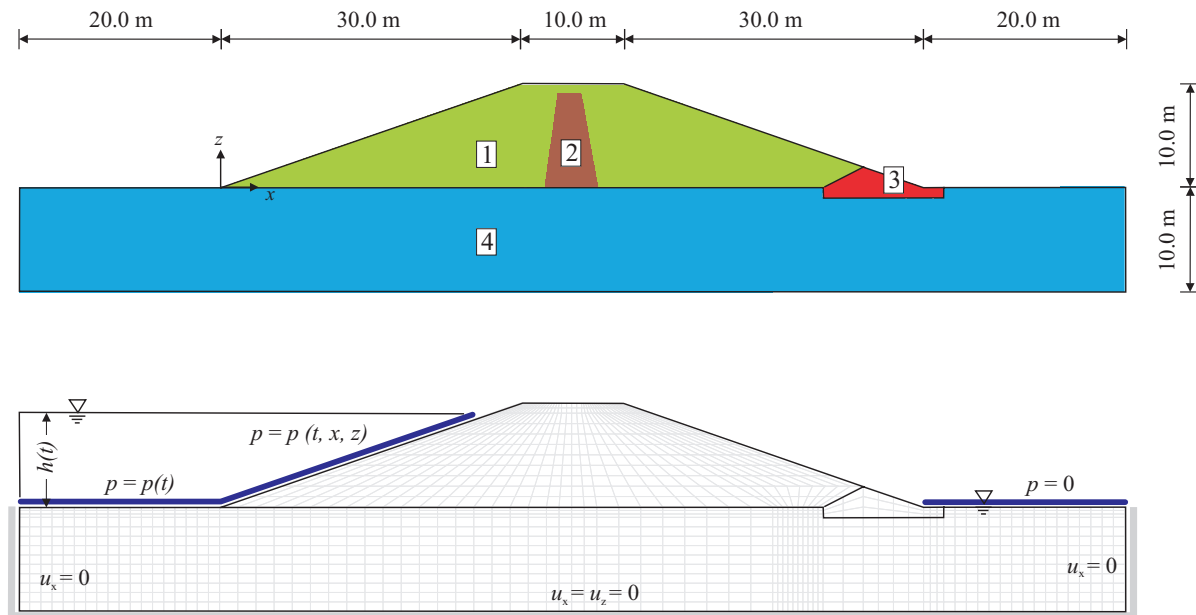


Figure 9.32: Embankment problem. Model set-up and boundary conditions.

The capillary pressure relation is defined by a *van Genuchten* function. For more details refer to van Genuchten (1980) [106]. The relation is defined as follows

$$S_{\text{eff}}^l(p_c) = [1 + (\alpha_{\text{gen}} p_c)^{j_{\text{gen}}}]^{-h_{\text{gen}}} \quad (9.2)$$

where S_{eff}^l is the effective liquid (water) saturation defined as follows

$$S_{\text{eff}}^l := \frac{S^l - S_{\text{res}}^l}{1 - S_{\text{res}}^l - S_{\text{res}}^g} \quad (9.3)$$

Table 9.10: Embankment problem. Material properties.

Parameter		Dam (1)	Central seal (2)	Dam (3)	Foundation (4)
Young's modulus	E (MPa)	14.516	14.516	14.516	100.0
Poisson's ratio	ν (-)	0.3	0.3	0.3	0.3
Permeability	k (m ²)	1.0×10^{-12}	1.0×10^{-15}	1.0×10^{-9}	1.0×10^{-15}
Solid grain density	ρ^s (kg m ⁻³)	2700	2700	2700	2700
Porosity	n (-)	0.46	0.46	0.46	0.46

and S_{res}^l and S_{res}^g are residual saturation of the liquid and gaseous phase, respectively.

The relative permeability saturation relation is

$$k_{\text{rel}}^l = (S_{\text{eff}}^l)^{\varepsilon_{\text{gen}}} [1 - [1 - (S_{\text{eff}}^l)^{1/h_{\text{gen}}}]^{h_{\text{gen}}}]^2. \quad (9.4)$$

The chosen parameters are $\alpha_{\text{gen}} = 2 \times 10^{-5}$, $j_{\text{gen}} = 2.3$, $h_{\text{gen}} = 1.5$ and $\varepsilon_{\text{gen}} = 0.5$.

The hydraulic-mechanical simulation of unsaturated flow in the embankment predicts the transient change in the location of saturated and unsaturated zones caused by varying water depths in a range of 2 m to 8 m. Moreover, the coupled simulation allows the estimation of zones of possible failure if the stress field is evaluated by an appropriate yield criterion.

9.3.2.3 Numerical simulation of multiphase flow

A transient simulation with a periodic variation of the water depth has been carried out. The resulting saturation fields in the embankment at water levels h of 2 m and 8 m are depicted in Fig. 9.33. The evaluation of a *Drucker-Prager* type yield function indicates that no plastic deformation occurs if this kind of standard embankment configuration is applied.

9.3.2.4 Numerical prediction of zones of possible failure

Hydraulic-mechanical simulations of the embankment configuration presented above have proven that no mechanical failure occurs. The major reasons are the central seal, the mild slope of 1:3 and a moderate change in water level.

Investigations has also been carried out for an embankment consisting of a slope of $1 : \sqrt{2}$. In case of a quick drop-out of the water level, the water remains in the dam and a relatively high water pressure arises on the seaward side. The pressure field, depicted in Fig. 9.34, causes possible failure at the seaward dam base as can be seen in the evaluation of a *Drucker-Prager* type yield criterion parameterized by a friction angle of $\phi = 10^\circ$ and a cohesion of $C = 40$ kPa.

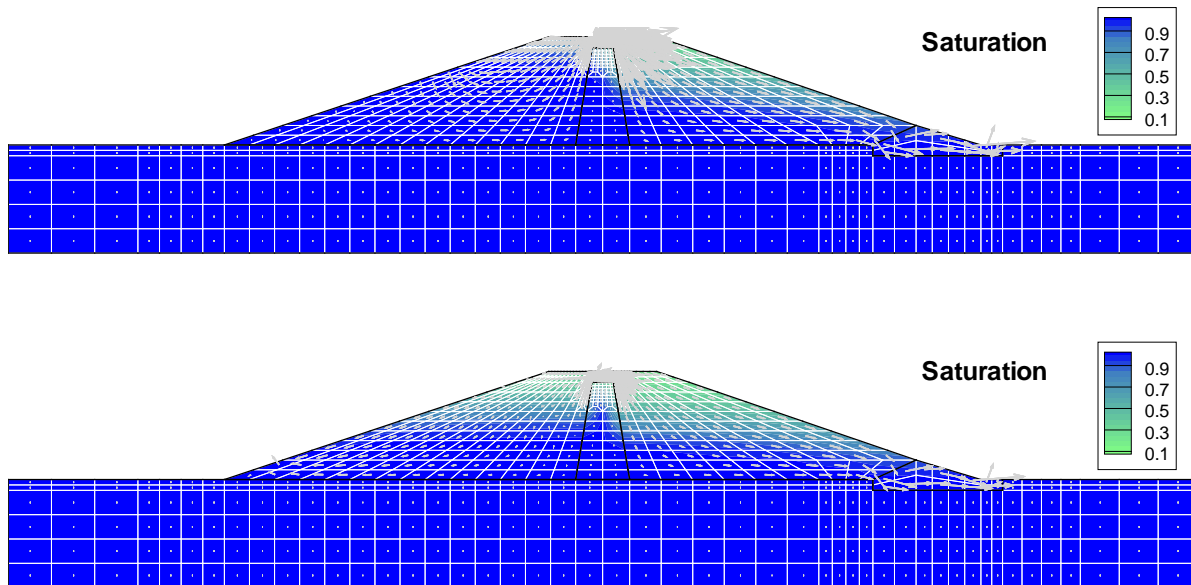


Figure 9.33: Embankment problem. Saturation fields and velocity vectors indicating the direction of fluid flow at a water level of $h = 8$ m (above) and $h = 2$ m (below) predicted in a transient simulation.

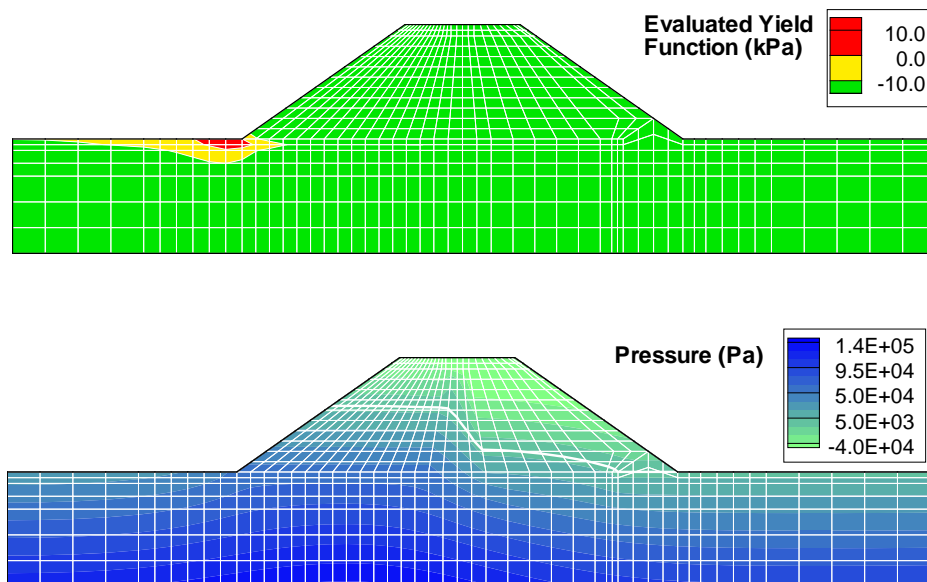


Figure 9.34: Embankment problem. Evaluation of the *Drucker-Prager* yield function (above) and excess pore pressure (below). Saturated and partially saturated zones are separated by a white line in the pressure field.

9.3.3 Slope stability problem

9.3.3.1 Introduction

The slope stability analysis is a crucial aspect in geotechnical applications. In saturated or partially saturated soils the pore water pressure reduces the mean effective stress in the porous skeleton and may cause failure. The impact of a rising water table on the stability of a slope is addressed in the present section. First, a reference simulation is carried out in a purely mechanical approach, which is comparable to drained conditions. Afterwards the results are compared to a hydraulic-mechanical simulation considering the excess pore pressure of the water table.

9.3.3.2 Geometry and model set-up

The purpose of this application is to investigate the stability of a slope with an inclination of 1:1. Similar simulations are given by Panesso (1998) [79], Regueiro and Borja (1999) [83] or Ehlers et al. (2004) [35], amongst others. Gravitational acceleration and an extra load due to a rigid footing at the top of the slope are considered. The footing is represented by an almost rigid body loaded by an increasing distributed load. The load is controlled by an increasing load factor λ within an interval of $[0 \dots \lambda_{\text{crit}}]$. The resulting set-up of the model is depicted in Fig. 9.35. The soil is supposed to be a water saturated porous medium. Its constitutive behavior is approximated by the plasticity model of *Drucker-Prager*. The material parameters are summarized in Table 9.11.

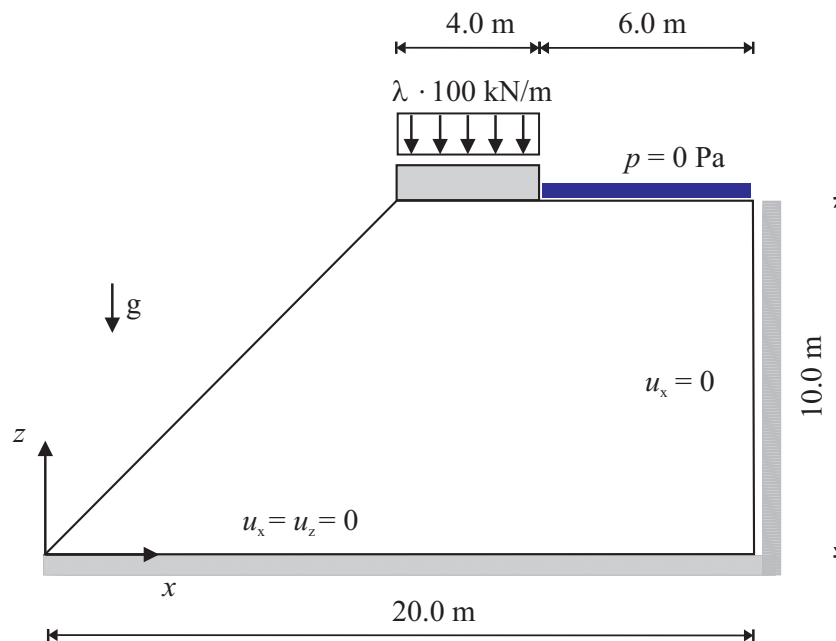


Figure 9.35: Slope stability problem. Geometry and boundary conditions.

Table 9.11: Slope stability problem. Material properties.

Parameter	Symbol	Value	
Young's modulus	E	10.0	MPa
Poisson's ratio	ν	0.3	
Cohesion	C	65.0	kPa
Internal friction angle	ϕ	10.0	°
Dilatancy angle	ψ	0.0	°
Permeability	k	1.0×10^{-10}	m^2
Water viscosity	μ^w	10^{-3}	Pa s
Water density	ρ^w	1000	kg m^{-3}
Solid grain density	ρ^s	2700	kg m^{-3}
Porosity	n	0.2	
Gravity	g	9.81	m s^{-2}
Biot coefficient	α	1.0	

9.3.3.3 Numerical results

In order to investigate the impact of a rising water pressure two different simulations are carried out. The first one is a purely mechanical approach without hydraulic effects while the second one is a fully coupled simulation including the hydrostatic fluid pressure field. The deformation of the solid skeleton induces a flow of the pore water, but the corresponding pressure build-up is insignificant due to relatively high permeable soil.

For both cases the simulation is performed with an increasing load. The simulation is carried on until the critical load is reached. The differing critical load factors determined for both systems indicate the influence of the hydrostatic pore water pressure.

Failure analysis in a purely mechanical approach. The resulting shear band in a purely mechanical simulation, representing soil in drained conditions without pore pressure arising, is depicted in Fig. 9.36. The critical state is reached with a load factor of $\lambda_{\text{crit}} = 0.44$.

Failure analysis of fully saturated soil. The resulting shear band in fully saturated conditions is depicted in Fig. 9.37. With $\lambda_{\text{crit}} = 0.31$ the resulting critical load is significantly lower than in the previous simulation. Simultaneously, the lower stability results in a bigger shear band zone. This reflects the crucial impact of pore water excess pressure in geotechnical analysis.

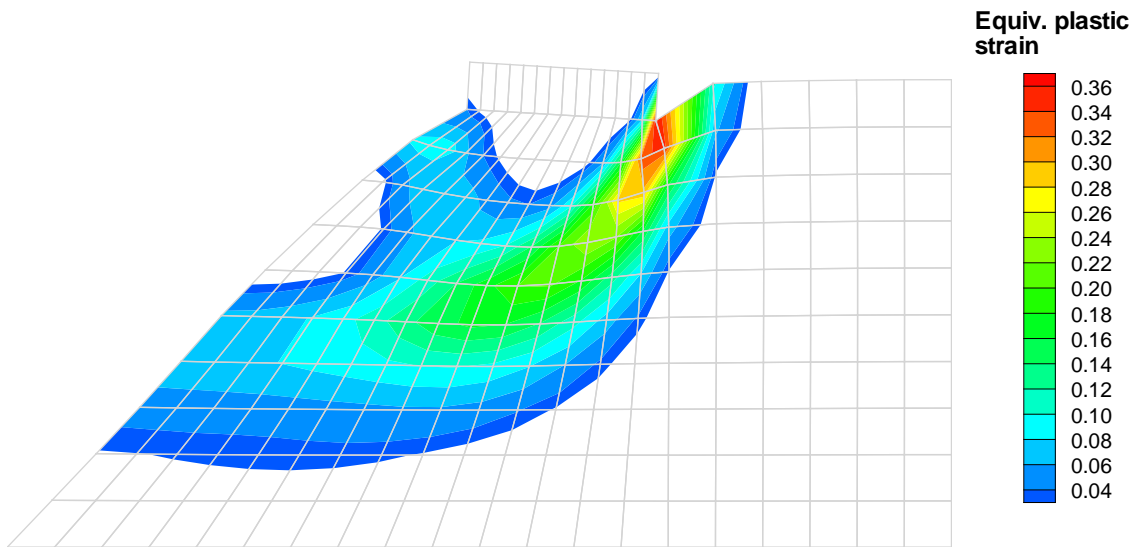


Figure 9.36: Slope stability problem in case of drained conditions. Shear bands in the deformed slope at $\lambda_{\text{crit}} = 0.44$.

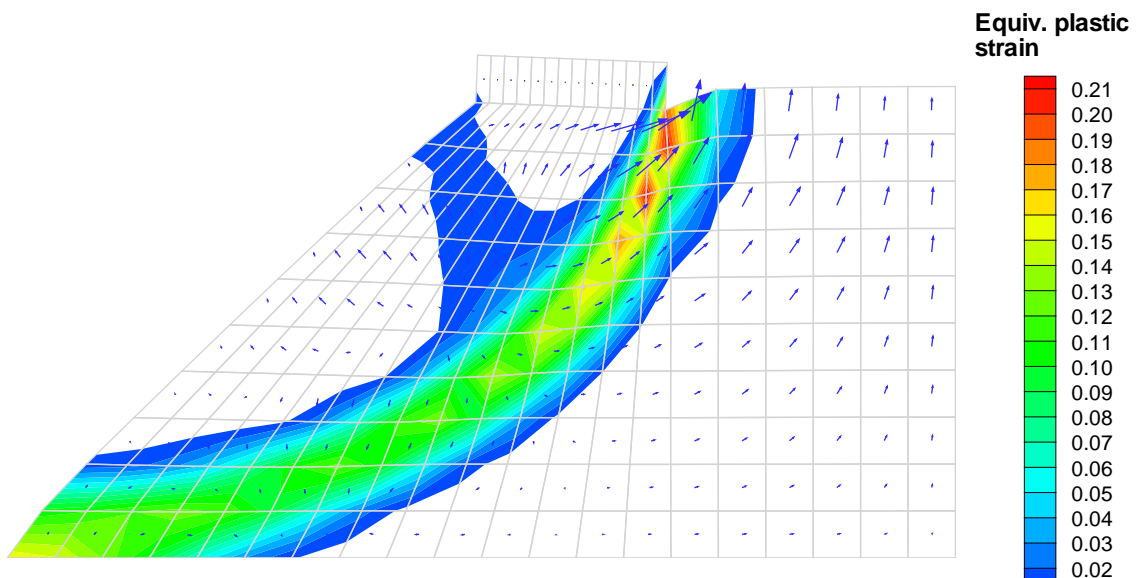


Figure 9.37: Slope stability problem in case of fully saturated conditions. Shear bands in the deformed slope at $\lambda_{\text{crit}} = 0.31$ with arrows indicating the flow direction of the pore water.

Chapter 10

Conclusions and recommendations

10.1 Conclusions

In the framework of the finite element method, this work investigates coupling phenomena occurring in geotechnical problems. The formulations are based on the well established Theory of Porous Media presented in Chapter 2. The mixture theory, the kinematical description and the conservation equations of the coupled thermo-hydro-mechanical processes are addressed here. The resulting set of governing equations describing the behavior of saturated and partially saturated flow in a deformable porous medium is given in Chapter 3. The problem is solved numerically by applying the finite element method outlined in Chapter 4 which also gives an overview of the numerical and iterative methods needed for solving non-linear equations arising in coupled problems.

Several coupling phenomena may occur in thermo-hydro-mechanical modeling. Those of most importance are mentioned in Chapter 5 also presenting some numerical aspects of the required solution procedure for algebraic equations of coupled problems. Couplings become even more important if they affect the constitutive behavior of the medium or the fluid. Chapter 6 gives a short overview of the phenomenological constitutive behavior of soils and describes the required algorithmic treatment.

The applied computational methods and used software concepts for developing a finite element code for research as well as for practical purposes are described in Chapter 7. The used strategy of implementing separate formulations for each process added by the needed coupling formulations leads to a flexible structure. Thus, piecewise activation of particular processes and couplings is combined with a useful and extendible control and steering facility. The developed graphical user interface provides a broad insight into the simulation cycle and the calculated results. With the implementation of new algorithms, methods and data structures a modern and self-documenting finite element code for coupled thermo-hydro-mechanical analysis has been established.

In Chapter 8 the developed finite element algorithms for coupled thermo-hydro-mechanical processes and their implementation are verified by benchmarks based on analytical solutions or other well-founded numerical research results.

With the verified implementations at hand, numerical simulations of coupled problems are carried out. The applications portrayed in Chapter 9 give an overview of coupled thermo-hydro-mechanical modeling in the field of partially saturated media and demonstrate the applicability of the developed strategy of a process oriented implementation.

Applications in geotechnical engineering like Performance Assessment of Engineered Barrier Systems or the slope stability analysis of unsaturated soils show the usability of the implemented formulations. They also identify possible subjects of future developments in the context of a more accurate and stable multiphase flow formulation and the importance of the consideration of vapor transport modeling.

10.2 Recommendations

The strategy of separate implementation of coupled processes and couplings presented in this work and the developed computational framework of a graphically assisted and documented finite element code give the opportunity to realize even more complex coupled modeling software. Some interesting aspects shall be mentioned.

Non-isothermal multiphase flow formulations are available and the numerical simulation of highly non-linear phase change effects are possible. Future research has to verify that these formulations can successfully be incorporated into a thermo-hydro-mechanical framework.

The significance of geometric non-linearities should be considered for reliable predictions in non-linear analyses of geotechnical materials. Due to the coupling phenomena, these non-linear effects also influence flow specific material properties of the solid and thus strongly affect the flow field and consequently other coupled processes.

Further activities should focus on the consideration of reactive transport processes in order to provide possible changes of material properties by leaching, precipitation induced by radionuclide release or by displacement of solute.

Notation

Typefaces

Typeface	Meaning
\mathbf{v}, \mathbf{M}	vector or matrix notation
\mathbf{T}	tensor notation
s	scalar value
\bullet^i	index
\bullet^{id}	identifier

Accents

Accent	Meaning
$\hat{\bullet}$	nodal value
$\bar{\bullet}$	boundary value
$\bullet^{(e)}$	finite element contribution

Operators

Partial derivatives. Let $f : \mathbb{R}^{\text{n}_{\text{dim}}} \rightarrow \mathbb{R}$ and $x_1, \dots, x_{\text{n}_{\text{dim}}}$ are Euclidean coordinates, corresponding to the orthonormal basis $\mathbf{e}_1, \dots, \mathbf{e}_{\text{n}_{\text{dim}}}$. We use the following notations

$$\partial_i f = \frac{\partial}{\partial x_i} f \quad \text{where } i = 1, \dots, \text{n}_{\text{dim}}.$$

$$\partial_t f = \frac{\partial}{\partial t} f,$$

where t is the time. The notation $f_{,i} = \partial_i f$ will not be used.

The gradient operator. Let $f : \mathbb{R}^{\text{n}_{\text{dim}}} \rightarrow \mathbb{R}$. If $x_1, \dots, x_{\text{n}_{\text{dim}}}$ are Euclidean coordinates, corresponding to the orthonormal basis $\mathbf{e}_1, \dots, \mathbf{e}_{\text{n}_{\text{dim}}}$, then the gradient operator ∇ can be considered as a vector-valued differential operator. In n_{dim} -dimensional Euclidean space it is written as

$$\nabla = \sum_i^{\text{n}_{\text{dim}}} \frac{\partial}{\partial x_i} \mathbf{e}_i.$$

The symmetric gradient operator. The symmetric gradient operator ∇^{sym} applied on a vector field $\mathbf{v} \in \mathbb{R}^{\text{n}_{\text{dim}}}$ is considered as a tensor-valued differential operator. With the standard basis $\{\mathbf{e}_i\}$ in $\mathbb{R}^{\text{n}_{\text{dim}}}$ it is written as follows

$$\nabla^{\text{sym}} \mathbf{v} := \frac{1}{2} [\nabla \mathbf{v} + (\nabla \mathbf{v})^\top] = \frac{1}{2} (\partial_i v_j + \partial_j v_i) \mathbf{e}_i \otimes \mathbf{e}_j \quad \text{where } i, j = 1, \dots, \text{n}_{\text{dim}}.$$

Directional derivatives. Let $f : \mathbb{R}^{\text{ndim}} \rightarrow \mathbb{R}$ be continuously differentiable. Then, the gradient ∇f is also defined by the property

$$\mathbf{D}_{\mathbf{v}} = \nabla f \cdot \mathbf{v} \quad \forall \quad \mathbf{v} \in \mathbb{R}^{\text{ndim}}$$

where $\mathbf{D}_{\mathbf{v}}$ is the directional derivative with respect to \mathbf{v} .

The divergence operator. The divergence operator is expressed by

$$\nabla \cdot \mathbf{v} = \frac{\partial v_x}{\partial x} + \frac{\partial v_y}{\partial y} + \frac{\partial v_z}{\partial z}$$

where \mathbf{v} is a vector or a tensor field.

Vector norms

The 1-norm. The 1-norm of the vector $\mathbf{v} = (v_1, \dots, v_n)^T \in \mathbb{R}^n$ is defined by

$$\|\mathbf{v}\|_1 = \sum_{i=1}^n |v_i|.$$

The 2-norm. The 2-norm, of the vector $\mathbf{v} = (v_1, \dots, v_n)^T \in \mathbb{R}^n$ is defined by

$$\|\mathbf{v}\|_2 = (\mathbf{v}^T \mathbf{v})^{1/2} = \left\{ \sum_{i=1}^n |v_i|^2 \right\}^{1/2}.$$

The 2-norm is called *Euclidean* norm and will also be denoted by $\|\mathbf{v}\|$.

The ∞ -norm. The ∞ -norm of the vector $\mathbf{v} = (v_1, \dots, v_n)^T \in \mathbb{R}^n$ is defined by

$$\|\mathbf{v}\|_{\infty} = \max_{i=1}^n |v_i|.$$

Nomenclature

Temporal quantities

Symbol	SI-Unit	Meaning
t	s	time
Δt	s	time step length
λ	—	load factor

Spatial quantities

Symbol	SI-Unit	Meaning
\mathbf{X}	m	material coordinates
\mathbf{x}	m	spatial coordinates
a	m ²	surface element
v	m ³	volume element

Material quantities

Symbol	SI-Unit	Meaning
c	J kg ⁻¹ K ⁻¹	specific heat capacity
C	N m ⁻²	cohesion
\mathbb{C}	N m ⁻²	elasticity tensor
D	m ² s ⁻¹	diffusion coefficient
\mathbf{D}	W m ⁻¹ K ⁻¹	diffusion tensor
E	N m ⁻²	<i>Young's</i> modulus
f	N m ⁻²	yield function
g	N m ⁻²	plastic potential function
G	N m ⁻²	shear modulus
h		hardening type
\mathbf{k}	m ²	permeability tensor
k_{rel}	—	relative permeability
K	Pa	bulk modulus
n	—	porosity
\mathbf{n}	m	normal unit vector
\mathbf{q}		set of internal variables
\mathbf{r}	—	direction of plastic flow
S	Pa ⁻¹	storativity

(continued)

Symbol	SI-Unit	Meaning
α	—	Biot's coefficient
α_T	K^{-1}	linear thermal expansion coefficient
β	m	dispersion length
β_T	K^{-1}	linear volumetric thermal expansion coefficient
β_{sw}		linear volumetric swelling coefficient
$\boldsymbol{\beta}$	N m^{-2}	back stress
γ	—	consistency parameter
λ	$\text{W m}^{-1} \text{K}^{-1}$	thermal conductivity
λ	N m^{-2}	<i>Lamé's</i> constant
μ	Pa s	dynamic viscosity
ν	—	<i>Poisson's</i> ratio
ρ	kg m^{-3}	density
$\boldsymbol{\sigma}$	N m^{-2}	effective stress tensor
$\boldsymbol{\sigma}^{\text{tot}}$	N m^{-2}	total stress tensor
σ_Y	N m^{-2}	yield stress
φ^α		phase of constituent α
φ		mixture
ϕ	°	angle of internal friction
ψ	°	angle of dilatancy

State quantities

Symbol	SI-Unit	Meaning
\boldsymbol{u}	m	solid displacement
p	Pa	fluid pressure
S	—	saturation
T	K, °C	temperature
C	—	concentration

Derived quantities

Kinematical quantities

Symbol	SI-Unit	Meaning
\boldsymbol{F}	—	deformation gradient
\boldsymbol{H}	—	displacement gradient
$\boldsymbol{\varepsilon}$	—	linearized strain tensor
\boldsymbol{e}	—	deviatoric part of linearized strain tensor

Stresses quantities

Symbol	SI-Unit	Meaning
$\boldsymbol{\sigma}$	N m^{-2}	stress tensor
\boldsymbol{s}	N m^{-2}	deviatoric part of the stress tensor
p	N m^{-2}	hydrostatic part of the stress
$\sigma_1, \sigma_2, \sigma_3$	N m^{-2}	principle values of the stress tensor
s_1, s_2, s_3	N m^{-2}	principle values of the deviatoric stress tensor
I_1, I_2, I_3	$\text{N m}^{-2}, \text{N}^2 \text{m}^{-4}, \text{N}^3 \text{m}^{-6}$	first, second and third invariant of the stress tensor
J_1, J_2, J_3	$\text{N m}^{-2}, \text{N}^2 \text{m}^{-4}, \text{N}^3 \text{m}^{-6}$	first, second and third invariant of the deviatoric part of stress the tensor
θ	$^\circ$	<i>Lode</i> angle

Flux quantities

Symbol	SI-Unit	Meaning
\boldsymbol{J}	$\text{kg m}^{-2} \text{s}^{-1}$	volume averaged advective and diffusive mass flux densities
\boldsymbol{J}_t	$\text{J m}^{-2} \text{s}^{-1}$	volume averaged conductive thermal energy flux density

Velocity and acceleration

Symbol	SI-Unit	Meaning
\boldsymbol{v}	m s^{-1}	velocity
\boldsymbol{q}	m s^{-1}	volume averaged velocity of the liquid relative to the solid of saturated porous media ($\boldsymbol{q} = n \boldsymbol{v}^{\text{ls}}$)
\boldsymbol{a}	m s^{-2}	acceleration
g	m s^{-2}	acceleration due to gravity
\boldsymbol{g}	m s^{-2}	acceleration vector to gravity

Source quantities

Symbol	Meaning
Q	production term (internal)
q	source term (external)
t	load term (external)

Indices

Symbol	Meaning
α	phase index
i	iteration index
n	time step index

Identifiers

Symbol	Meaning
algo	algorithmic (consistent)
b	body
c	capillary
crit	crit
eff	effective
el	element
g	gaseous
iso	isotropic
kin	kinematic
l	liquid
m	mixture
n	node
pl	plastic
rel	relative
s	solid
$(\bullet)^{\alpha s}$	quantity $(\bullet)^{\alpha}$ with respect to the solid displacement
t	thermal
tot	total
trial	trial
w	water

Finite element quantities

Symbol	Meaning
n_{el}	number of elements
n_n	number of nodes per element
n_{gp}	number of evaluation points for Gaussian quadrature (Gauss points)

Bibliography

- [1] C. Barlag. *Adaptive Methoden zur Modellierung von Stofftransport im Kluftgestein*. PhD thesis, Institut für Strömungsmechanik und Elektronisches Rechnen im Bauwesen, Universität Hannover, 1997.
- [2] D. Barr, J. Birkhölzer, J. Rutqvist, and E. Sonnenthal. Draft Description for DECOVALEX-THMC. Task D: Long-Term Permeability/Porosity Changes in EDZ and Near Field, due to THM and THC Processes in Volcanic and Crystalline-Bentonite Systems. REV02 December 2004, Office of Repository Development, U.S. Dept. of Energy; Earth Sciences Division, LBNL, USA, Berkeley, 2004.
- [3] K.-J. Bathe. *Finite Element Procedures*. Prentice Hall, Englewood Cliffs, 1996.
- [4] J. Bear and Y. Bachmat. *Introduction to Modeling of Transport Phenomena in Porous Media*. Kluwer Academic Publishers, Dordrecht, 1990.
- [5] N. Bicanic and K. H. Johnson. Who was '-Raphson'. *International Journal for Numerical Methods in Engineering*, 14(1):148–152, 1979.
- [6] M. A. Biot. General theory of three dimensional consolidation. *Journal of Applied Physics*, 12:155–164, 1941.
- [7] M. A. Biot. Theory of propagation of elastic waves in a fluid-saturated porous solid, I. Low frequency range. *The Journal of the Acoustical Society of America*, 28:168–178, 1956.
- [8] M. A. Biot. Theory of propagation of elastic waves in a fluid saturated porous solid, II. Higher frequency range. *The Journal of the Acoustical Society of America*, 28:179–191, 1956.
- [9] M. A. Biot and D. G. Willis. The elastic coefficients of a theory of consolidation. *Journal of Applied Mechanics*, 79:594–601, 1957.
- [10] J. Birkholzer, J. Rutqvist, E. Sonnenthal, and D. Barr. DECOVALEX-THMC. Task D: Long-Term Permeability/Porosity Changes in EDZ and Near Field due to THM and THC Processes in Volcanic and Crystalline-Bentonite Systems. Status Report October 2005, Earth Sciences Division, LBNL, USA; Office of Repository Development, DOE, USA, Berkeley, 2005.
- [11] R. I. Borja and A. Aydin. Computational modeling of deformation bands in granular media, I: Geological and mathematical framework. *Computer Methods in Applied Mechanics and Engineering*, 193(27-29):2667–2698, 2004.

-
- [12] R. I. Borja and S. R. Lee. Cam-clay plasticity, Part I: Implicit integration of elastoplastic constitutive relations. *Computer Methods in Applied Mechanics and Engineering*, 78(1):49–72, 1990.
- [13] R. M. Bowen. Thermodynamics of diffusion. In A. C. Eringen, editor, *Continuum physics*, volume 3: Mixtures and EM field theories, pages 1–127. Academic Press, New York, 1976.
- [14] R. M. Bowen. Incompressible porous-media models by use of the theory of mixtures. *International Journal of Engineering Science*, 18(9):1129–1148, 1980.
- [15] R. M. Bowen. Compressible porous-media models by use of the theory of mixtures. *International Journal of Engineering Science*, 20(6):697–735, 1982.
- [16] D. Braess. *Finite Elements. Theory, Fast Solvers and Applications in Solid Mechanics*. Cambridge University Press, Cambridge, 2nd edition, 2002. reprint.
- [17] C. Braun. *Ein Upscaling-Verfahren für Mehrphasenströmungen in porösen Medien*. PhD thesis, Institut für Wasserbau, Universität Stuttgart, 2000.
- [18] F. Brezzi. On the existence, uniqueness and approximation of saddle-point problems arising from Lagrangian multipliers. *Revue française d'automatique, d'informatique et de recherche opérationnelle*, 8(2):129–151, 1974.
- [19] W. F. Chen and G. Y. Baladi. *Soil Plasticity, Theory and Implementation*. Elsevier, Amsterdam, 1985.
- [20] H. Class and R. Helmig. Numerical simulation of non-isothermal multiphase multicomponent processes in porous media. 2. Applications for the injection of steam and air. *Advances in Water Resources*, 25(5):551–564, 2002.
- [21] H. Class, R. Helmig, and P. Bastian. Numerical simulation of non-isothermal multiphase multicomponent processes in porous media. 1. An efficient solution technique. *Advances in Water Resources*, 25(5):533–550, 2002.
- [22] J. Crank and P. Nicolson. A practical method for numerical evaluation of solutions of partial differential equations of the heat-conduction type. *Proceedings of the Cambridge Philosophical Society*, 43(1):50–67, 1947.
- [23] R. de Boer. *Theory of Porous Media. Highlights in Historical Development and Current State*. Springer, 2000.
- [24] R. de Boer and W. Ehlers. *Theorie der Mehrkomponentenkontinua mit Anwendung auf bodenmechanische Probleme. Forschungsberichte aus dem Fachbereich Bauwesen, 40*. Universität-Gesamthochschule Essen, 1986.
- [25] R. de Borst and A. E. Groen. A note on the calculation of consistent tangent operators for von Mises and Drucker-Prager plasticity. *Communications in Numerical Methods in Engineering*, 10(12):1021–1025, 1994.
- [26] R. de Borst and A. E. Groen. Some observations on element performance in isochoric and dilatant plastic-flow. *International Journal for Numerical Methods in Engineering*, 38(17):2887–2906, 1995.

- [27] R. de Borst and A. E. Groen. Towards efficient and robust elements for 3d-soil plasticity. *Computers & Structures*, 70(1):23–34, 1999.
- [28] C. S. Desai and H. J. Siriwardane. *Constitutive Laws for Engineering Materials, With Emphasis on Geological Materials*. Prentice Hall, Englewood Cliffs, 1984.
- [29] H. J. G. Diersch and O. Kolditz. Coupled groundwater flow and transport: 2. Thermo-haline and 3D convection systems. *Advances in Water Resources*, 21(5):401–425, 1988.
- [30] D. C. Drucker and W. Prager. Soil mechanics and plastic analysis or limit design. *Quarterly of Applied Mathematics*, 10(2):157–165, 1952.
- [31] W. Ehlers. *Poröse Medien: ein kontinuumsmechanisches Modell auf der Basis der Mischungstheorie. Forschungsberichte aus dem Fachbereich Bauwesen, 47*. Universität-Gesamthochschule Essen, 1989.
- [32] W. Ehlers. A single-surface yield function for geomaterials. *Archive of Applied Mechanics*, 65(4):246–259, 1995.
- [33] W. Ehlers. Foundations of multiphasic and porous materials. In W. Ehlers and J. Bluhm, editors, *Porous Media*. Springer, Berlin, 2002.
- [34] W. Ehlers and J. Bluhm. *Porous Media*. Springer, Berlin, 2002.
- [35] W. Ehlers, T. Graf, and M. Ammann. Deformation and localization analysis of partially saturated soil. *Computer Methods in Applied Mechanics and Engineering*, 193(4):2885–2910, 2004.
- [36] G. Eipper. *Theorie und Numerik finiter elastischer Deformationen in fluidgesttigten porsen Festkörpern*. PhD thesis, Institut für Mechanik (Bauwesen), Universität Stuttgart, 1998.
- [37] J. W. Elder. Steady free convection in a porous medium heated from below. *Journal of Fluid Mechanics*, 27:29–48, 1967.
- [38] P. Fillunger. *Erdbaumechanik?* Selbstverlag des Verfassers, Wien, 1936.
- [39] A. L. Florence and J. N. Goodier. Thermal stress at spherical cavities and circular holes in uniform heat flow. *Journal of Applied Mechanics*, 26:293–294, 1959.
- [40] N. E. Gibbs, W. G. Poole, and P. K. Stockmeyer. An algorithm for reducing bandwidth and profile of a sparse matrix. *SIAM Journal on Numerical Analysis*, 13(2):236–250, 1976.
- [41] H. Habbar. *Direkte und Inverse Modellierung reaktiver Transportprozesse in klüftig-porösen Medien*. PhD thesis, Institut für Strömungsmechanik und Elektronisches Rechnen im Bauwesen, Universität Hannover, 2001.
- [42] S. M. Hassanizadeh and W. G. Gray. General conservation equations for multi-phase systems: 1. averaging procedure. *Advances in Water Resources*, 2:131–144, 1979.
- [43] S. M. Hassanizadeh and W. G. Gray. General conservation equations for multi-phase systems: 2. mass, momenta, energy, and entropy equations. *Advances in Water Resources*, 2:191–203, 1979.

- [44] P. Haupt. *Continuum mechanics and theory of materials*. Springer, Springer, 2000.
- [45] R. Helmig. *Theorie und Numerik der Mehrphasenströmungen in geklüftet-porösen Medien*. PhD thesis, Institut für Strömungsmechanik und Elektronisches Rechnen im Bauwesen, Universität Hannover, 1993.
- [46] T. J. R. Hughes. *The Finite Element Method: Linear Static and Dynamic Finite Element Analysis*. Dover Publications, Mineola, New York, 2000. Reprint.
- [47] JNC (Japan Nuclear Cycle Development Institute). H12: Project to establish the scientific and technical basis for HLW disposal in Japan, 2000.
- [48] K. Johannsen. The Elder problem - Bifurcations and steady state solutions. In *Developments in Water Science*, volume 47, pages 485–492, 2002.
- [49] M. Kachanov, B. Shafiro, and I. Tsukrov. *Handbook of Elasticity Solutions*. Kluwer Academic Publishers, Dordrecht, 2003.
- [50] R. Kaiser. *Gitteradaption für die Finite-Elemente-Modellierung gekoppelter Prozesse in geklüftet-porösen Medien*. PhD thesis, Institut für Strömungsmechanik und Elektronisches Rechnen im Bauwesen, Universität Hannover, 2001.
- [51] C. Kanzow. *Numerik linearer Gleichungssysteme: direkte und iterative Verfahren*. Springer, Berlin, 2005.
- [52] A. S. Khan and S. Huang. *Continuum Theory of Plasticity*. John Wiley & Sons, New York, 1995.
- [53] P. Knabner and L. Angermann. *Numerical Methods for Elliptic and Parabolic Partial Differential Equations*. Springer, New York, 2003.
- [54] M. Kohlmeier, R. Kaiser, O. Kolditz, and W. Zielke. Finite element simulation of consolidation and bentonite swelling in the framework of unsaturated porous media. In *Developments in Water Science*, volume 47, pages 57–64, 2002.
- [55] M. Kohlmeier, R. Kaiser, and W. Zielke. Numerical simulation of variably coupled thermo-hydro-mechanical processes in fractured porous media. In O. Stephansson, J. A. Hudson, and L. Jing, editors, *Coupled Thermo-Hydro-Mechanical-Chemical Processes in Geo-Systems: Fundamentals, Modelling, Experiments and Applications*, pages 199–204. Elsevier, Amsterdam, 2004.
- [56] M. Kohlmeier, G. Ziefle, and W. Zielke. Coupling of thermo-hydro-mechanical processes for the simulation of partially saturated systems. In *Proc. 5. Workshop 'Porous Media' - Blaubeuren, Dec. 02-03, 2004*, 2005.
- [57] O. Kolditz, A. Habbar, R. Kaiser, H. Kasper, T. Rother, M. Schulze-Ruhfus, C. Thorenz, and W. Zielke. Software concept of simulating coupled processes in subsurface hydrosystems. In *Proceedings of the 3rd International Conference on Hydroinformatics, Copenhagen, Denmark, August 24-26*, pages 613–618, 1998.
- [58] O. Kolditz, R. Ratke, H. J. G. Diersch, and W. Zielke. Coupled groundwater flow and transport: 1. Verification of variable density flow and transport models. *Advances in Water Resources*, 21(1):27–46, 1988.

- [59] J. Korsawe, G. Starke, W. Wang, and O. Kolditz. Finite element analysis of poro-elastic consolidation in porous media: Standard and mixed approaches. *Computer Methods in Applied Mechanics and Engineering*, 195(9-12):1096–1115, 2006.
- [60] K.-P. Kröhn. *Simulation von Transportvorgängen im klüftigen Gestein mit der Methode der Finiten Elemente*. PhD thesis, Institut für Strömungsmechanik und Elektronisches Rechnen im Bauwesen, Universität Hannover, 1991.
- [61] P.V. Lade. Elastoplastic stress-strain theory for cohesionless soil with curved yield surfaces. *International Journal of Solids and Structures*, 13:1019–1035, 1977.
- [62] P.V. Lade and J.M. Duncan. Elastoplastic stress-strain theory for cohesionless soil. *Journal of the Soil Mechanics and Foundations Division*, 101(10):1037–1053, 1975.
- [63] T. Lege. *Modellierung des Kluftgesteins als geologische Barriere für Deponien*. PhD thesis, Institut für Strömungsmechanik und Elektronisches Rechnen im Bauwesen, Universität Hannover, 1995.
- [64] R. W. Lewis and B. A. Schrefler. *The Finite Element Method in the Static and Dynamic Deformation and Consolidation of Porous Media*. John Wiley & Sons, Chichester, 1998.
- [65] R. W. Lewis, B. A. Schrefler, and L. Simoni. Coupling versus uncoupling in soil consolidation. *IJNAMG*, 15(8):533–548, 1991.
- [66] A. Liakopoulos. Retention and distribution of moisture in soils after infiltration has ceased. *Bulletin of the International Association for scientific hydrology*, 10:58–69, 1965.
- [67] B. Loret and J. H. Prevost. Accurate numerical-solutions for Drucker-Prager elastic-plastic models. *Computer Methods in Applied Mechanics and Engineering*, 54(3):259–277, 1986.
- [68] B. Loret and J. H. Prevost. Dynamic strain localization in fluid-saturated porous-media. *Journal of Engineering Mechanics*, 117(4):907–922, 1991.
- [69] R. Mahnken and M. Kohlmeier. Finite element simulation for rock salt with dilatancy boundary coupled to fluid permeation. *Computer Methods in Applied Mechanics and Engineering*, 190(32-33):4259–4278, 2001.
- [70] J. Maßmann, G. Ziefle, M. Kohlmeier, W. Zielke, and H. Shao. Coupled hydro-mechanical modeling of seasonally affected unsaturated claystone. In *Proc. of the 2nd International Conference on Coupled T-H-M-C Processes in Geosystems & Engineering (Geo-Proc2006), May 22-25, 2006, Nanjing, P. R. China, 2006*.
- [71] H. Matsuoka and T. Nakai. Stress-deformation and strength characteristics of soil under three different principal stresses. *Proceedings of Japan Society of Civil Engineers*, 232:59–70, 1974.
- [72] C. Miehe. *Kanonische Modelle multiplikativer Elasto-Plastizität: thermodynamische Formulierung und numerische Implementation*. Institut für Baumechanik und Numerische Mechanik, Universität Hannover, 1993.
- [73] K. Mittendorf. *Hydromechanical Design Parameters and Design Loads for Offshore Wind Energy Converters*. PhD thesis, Institut für Strömungsmechanik und Elektronisches Rechnen im Bauwesen, Leibniz Universität Hannover, 2006.

- [74] S. Moenickes. *Grid Generation for Simulation of Flow and Transport Processes in Fractured-Porous Media*. PhD thesis, Institut für Strömungsmechanik und Elektronisches Rechnen im Bauwesen, Universität Hannover, 2004.
- [75] I. Müller. A thermodynamic theory of mixture fluids. *Archive for Rational Mechanics and Analysis*, 28:1–39, 1968.
- [76] M. A. Murad and A. F. D. Loula. Improved accuracy in finite element analysis of Biot’s consolidation problem. *Computer Methods in Applied Mechanics and Engineering*, 95:359–382, 1992.
- [77] T. N. Narasimhan and P. A. Witherspoon. Numerical model for saturated-unsaturated flow in deformable porous media. *Water Resources Research*, 14:1017–34, 1978.
- [78] T. S. Nguyen, M. Chijimatsu, J. De Jonge, L. Jing, M. Kohlmeier, A. Millard, A. Rejeb abd J. Rutqvist, M. Souley, and Y. Sugita. Implications of coupled thermo-hydro-mechanical processes on the safety of a hypothetical nuclear fuel waste repository. In *Proc. of the 1st International Conference on Coupled T-H-M-C Processes in Geosystems & Engineering (GeoProc2003), October 13-15, 2003, Stockholm, Sweden, 2003*.
- [79] J. M. Panesso. *Lokalisierung und Stabilität der Deformation wassergesättigter bindiger und granularer Böden*. Institut für Baumechanik und Numerische Mechanik, Universität Hannover, 1998.
- [80] C. Paniconi and M. Putti. A comparison of picard and newton iteration in the numerical-solution of multidimensional variably saturated flow problems. *Water Resources Research*, 30(12):3357–3374, 1994.
- [81] J. Plischka. *Die Bedeutung der Durchschnittsbildungstheorie für die Theorie poröser Medien*. PhD thesis, Universität-GH Essen, 1992.
- [82] J. N. Reddy. *Energy principles and variational methods in applied mechanics*. John Wiley & Sons, Hoboken, 2nd edition, 2002.
- [83] R. A. Regueiro and R. I. Borja. A finite element model of localized deformation in frictional materials taking a strong discontinuity approach. *Computer Methods in Applied Mechanics and Engineering*, 33(4):283–315, 1999.
- [84] A. Rejeb and O. Stephansson. DECOVALEX IV THMC. Excavation Damaged Zone (EDZ) in the Argillaceous Tournemire Site (France). Report of Task C1. May 2005, Institute of Radioprotection and Nuclear Safety, France; GeoForschungsZentrum-Potsdam, Germany, 2006.
- [85] T. Rother. *Geometric Modelling of Geo-Systems*. PhD thesis, Institut für Strömungsmechanik und Elektronisches Rechnen im Bauwesen, Universität Hannover, 2001.
- [86] K. Runesson. Implicit integration of elastoplastic relations with reference to soils. *International Journal for Numerical and Analytical Methods in Geomechanics*, 11(3):315–321, 1987.

- [87] L. Sanavia, B. A. Schrefler, and P. Steinmann. Geometrical and material non-linear analysis of fully and partially saturated porous media. In W. Ehlers and J. Bluhm, editors, *Porous Media*. Springer, Berlin, 2002.
- [88] B. A. Schrefler and R. Scotta. A fully coupled dynamic model for two-phase fluid flow in deformable porous media. *Computer Methods in Applied Mechanics and Engineering*, 190(24-25):3223–3246, 2001.
- [89] B. A. Schrefler and X. Y. Zhan. A fully coupled model for water flow and airflow in deformable porous media. *Water Resources Research*, 190(29):155–67, 1993.
- [90] J. Schröder. *Theoretische und algorithmische Konzepte zur phänomenologischen Beschreibung anisotropen Materialverhaltens*. PhD thesis, Institut für Baumechanik und Numerische Mechanik, Universität Hannover, 1996.
- [91] M. Schulze-Ruhfus. Adaptive Verfeinerung und Vergrößerung gekoppelter 1D/2D/3D-Elemente. Diploma thesis, Institut für Strömungsmechanik und Elektronisches Rechnen im Bauwesen, Universität Hannover, 1996.
- [92] H. Shao. *Simulation von Strömungs- und Transportvorgängen in geklüfteten porösen Medien mit gekoppelten Finite-Element- und Rand-Element-Methoden*. PhD thesis, Institut für Strömungsmechanik und Elektronisches Rechnen im Bauwesen, Universität Hannover, 1994.
- [93] H. Shao, T. Nowak, Ch. Lege, H. Kunz, and V. Brüuer. Hydro-mechanical behaviour of saturated-unsaturated clay materials – experimental and numerical investigations of gas migration. In *Proc. of the 2nd International Conference on Coupled T-H-M-C Processes in Geosystems & Engineering (GeoProc2006), May 22-25, 2006, Nanjing, P. R. China*, 2006.
- [94] J. C. Simo and T. J. R. Hughes. *Computational Inelasticity*. Springer, New York, 1998.
- [95] J. C. Simo and R. L. Taylor. Consistent tangent operators for rate-independent elasto-plasticity. *Computer Methods in Applied Mechanics and Engineering*, 48(1):101–118, 1985.
- [96] E. Stein, P. Wriggers, A. Rieger, and M. Schmidt. Benchmarks. In E. Stein, editor, *Error-Controlled Adaptive Finite Elements in Solid Mechanics*. John Wiley & Sons, Chichester, 2002.
- [97] P. Steinmann. A finite element formulation for strong discontinuities in fluid-saturated porous media. *Mechanics of Cohesive-Frictional Materials*, 4:133–152, 1999.
- [98] B. Szabó and I. Babuška. *Finite Element Analysis*. John Wiley & Sons, New York, 1991.
- [99] K. Terzaghi. *Erdbaumechanik auf bodenphysikalischer Grundlage*. Franz Deuticke, Leipzig, 1925.
- [100] K. Terzaghi. *Theoretical Soil Mechanics*. John Wiley & Sons, New York, 1954.
- [101] C. Thorenz. *Model adaptive simulation of multiphase and density driven flow in fractured and porous media*. PhD thesis, Institut für Strömungsmechanik und Elektronisches Rechnen im Bauwesen, Universität Hannover, 2001.

- [102] S. P. Timoshenko and J. N. Goodier. *Theory of Elasticity*. MacGraw-Hill, New York, 3rd edition, 1970.
- [103] C. Truesdell. Thermodynamics of diffusion. In C. Truesdell, editor, *Rational Thermodynamics*, pages 219–236. Springer, New York, 2nd edition, 1984.
- [104] C. Truesdell and R. A. Toupin. The classical field theories. In S. Flügge, editor, *Handbuch der Physik III/1*, pages 226–793. Springer, Berlin, 1960.
- [105] H. A. van der Vorst. Bi-CGSTAB - A fast and smoothly converging variant of Bi-CG for the solution of nonsymmetric linear systems. *SIAM Journal on Scientific and Statistical Computing*, 13(2):631–644, 1992.
- [106] M. Th. van Genuchten. A closed-form equation for predicting the hydraulic conductivity of unsaturated soils. *Soil Sci. Soc. Am. J.*, 44:892–898, 1980.
- [107] J. Wollrath. *Ein Strömungs- und Transportmodell für klüftiges Gestein und Untersuchungen zu homogenen Ersatzsystemen*. PhD thesis, Institut für Strömungsmechanik und Elektronisches Rechnen im Bauwesen, Universität Hannover, 1990.
- [108] P. Wriggers. *Nichtlineare Finite-Element-Methoden*. Springer, Berlin, 2001.
- [109] M. Wulkau. *Entwicklung einer Struktur- und Datenverwaltung zur objektorientierten Umsetzung eines flexiblen Konzepts der Dateneingabe im FE-Programm RockFlow*. Student thesis, Institut für Strömungsmechanik und Elektronisches Rechnen im Bauwesen, Universität Hannover, 2005.
- [110] G. Zieffle, M. Kohlmeier, J. Maßmann, and W. Zielke. DECOVALEX IV (THMC) - Task C. Excavation Disturbed Zone (EDZ) in the Argillaceous Tournemire Site (France). Part I. Report, September 2005, Institut für Strömungsmechanik und Elektronisches Rechnen im Bauwesen, Universität Hannover, 2005.
- [111] G. Zieffle, M. Kohlmeier, and W. Zielke. Einbeziehung gekoppelter HM-Modellierung in die Materialbeschreibung teilgesättigter Medien. In *Proc. 5. Workshop 'Porous Media' - Blaubeuren, Dec. 02-03, 2004*, 2005.
- [112] O. C. Zienkiewicz, Y. M. Xie, B. A. Schrefler, A. Ledesma, and N. Bicanic. Static and dynamic behaviour of soils: a rational approach to quantitative solutions, ii. semi-saturated problems. *Proceedings of the Royal Society of London Series A-Mathematical Physical and Engineering Sciences*, 429:11–21, 1990.
- [113] O.C. Zienkiewicz and R.L. Taylor. *The Finite Element Method*, volume 1. Its Basis & Fundamentals. Butterworth-Heinemann, Oxford, 6th edition, 2005.
- [114] O.C. Zienkiewicz and R.L. Taylor. *The Finite Element Method*, volume 3. For Fluid Mechanics. Butterworth-Heinemann, Oxford, 6th edition, 2005.
- [115] O.C. Zienkiewicz and R.L. Taylor. *The Finite Element Method*, volume 2. For Solid and Structural Mechanics. Butterworth-Heinemann, Oxford, 6th edition, 2005.

Appendix A

Numerical methods and derivations

A.1 Convergence of iterative solution procedures

Linear convergence. Suppose that the sequence $\{x_i\}$ is convergent with $\lim_{i \rightarrow \infty} x_i = x^*$. Convergence is linear if there exists a constant $0 < r < 1$ such that

$$\frac{\|x_{i+1} - x^*\|}{\|x_i - x^*\|} \leq r. \quad (\text{A.1})$$

The number r is called the rate of convergence.

Superlinear convergence. The convergence of a sequence is superlinear if

$$\frac{\|x_{i+1} - x^*\|}{\|x_i - x^*\|} \rightarrow 0. \quad (\text{A.2})$$

Quadratic convergence. We have a quadratic order of convergence if

$$\frac{\|x_{i+1} - x^*\|}{\|x_i - x^*\|^2} \leq C \quad (\text{A.3})$$

with a constant C .

Note: Quadratic convergence implies superlinear convergence, to see this, multiply both sides of the equation by $\|x_i - x^*\|$.

A.2 Derivation of finite elements

Gauss's theorem (divergence theorem). Let $\Omega \subseteq \mathbb{R}^3$ be a region which is the interior of a closed surface Γ . The unit normal vector, denoted by \mathbf{n} , is pointing outward. Let \mathbf{J} be a continuous differentiable vector field defined on an open set containing interior Ω and the surface Γ .

Then, we can formulate the following *divergence theorem*

$$\int_{\Omega} \nabla \cdot \mathbf{J} \, d\Omega = \int_{\Gamma} \mathbf{J} \mathbf{n} \, d\Gamma \quad (\text{A.4})$$

which means that the volume integral of the divergence of \mathbf{J} over the interior coincides with the flux integral of \mathbf{J} over the bounding surface Γ .

Weak formulation. In this section, the procedure of deriving the weak form of a partial differential equation is briefly described. The problem under consideration is the *Poisson* problem. This *boundary value problem* (BVP) is defined as follows: For a given $f \in \mathbb{L}^2(\Omega)$, $u_D \in \mathbb{H}^1(\Omega)$, and $g_D \in \mathbb{L}^2(\Gamma)$ we are searching the solution $u \in \mathbb{H}^1(\Omega)$ which satisfies the *Poisson* equation

$$-\nabla \cdot (\nabla u) = f \quad (\text{A.5})$$

with *Dirichlet* boundary conditions $u = u_D$ on Γ_D and *Neumann* boundary conditions $\nabla u \mathbf{n} = g$ on Γ_N .

The weak formulation of this BVP is obtained by multiplying the equation (A.5) with $\omega \in \mathbb{H}_D^1(\Omega) := \{\omega \in \mathbb{H}^1(\Omega) | \omega = 0 \text{ on } \Gamma_D\}$ and integration over Ω

$$-\int_{\Omega} \nabla \cdot \nabla u \cdot \omega \, d\Omega = \int_{\Omega} f \cdot \omega \, d\Omega. \quad (\text{A.6})$$

Application of *Green's* theorem on the divergence operator in Eq. (A.6), that means integration by parts and application of *Gauss's* theorem, results in the following

$$\int_{\Omega} \nabla \cdot (\nabla u) \cdot \omega \, d\Omega = \int_{\Omega} \nabla u \cdot \nabla \omega \, d\Omega - \int_{\Gamma_N} \nabla u \mathbf{n} \, d\Gamma. \quad (\text{A.7})$$

With Eq. (A.7) we finally get the weak formulation of the *Poisson* problem

$$\int_{\Omega} \nabla u \cdot \nabla \omega \, d\Omega = \int_{\Omega} f \cdot \omega \, d\Omega + \int_{\Gamma_N} g \cdot \omega \, d\Gamma. \quad (\text{A.8})$$

where the *Neumann* boundary conditions g on Γ_N are included simultaneously. *Dirichlet* boundary conditions u_D can be considered by assuming a homogeneous solution $v \in \mathbb{H}_D^1(\Omega)$, given by $v = u - u_D$ which satisfies $v = 0$ on Γ_D .

The solution $u = v + u_D$ of the *Poisson* equation is obtained by finding $v \in \mathbb{H}_D^1(\Omega)$ such that

$$\int_{\Omega} \nabla v \cdot \nabla \omega \, d\Omega = \int_{\Omega} f \cdot \omega \, d\Omega + \int_{\Gamma_N} g \cdot \omega \, d\Gamma + \int_{\Omega} \nabla u_D \cdot \nabla \omega \, d\Omega. \quad (\text{A.9})$$

Transformation from global to local coordinates and the Jacobian. Transformation from global $\mathbf{x} = (x, y, z)^\top$ to local $\boldsymbol{\xi} = (\xi, \eta, \zeta)^\top$ coordinates allows to evaluate the matrices in unit coordinates. Usually, *isoparametric* elements are used. These elements use the same shape functions (interpolations) to define the geometry as were used to define the the primary unknowns, for example the displacements. So the geometry is approximated by

$$\mathbf{x}(\boldsymbol{\xi}) \approx \hat{\mathbf{x}}(\boldsymbol{\xi}) = \sum_{i=1}^{n_n} \mathbf{N}_i(\boldsymbol{\xi}) \mathbf{x}_i . \quad (\text{A.10})$$

The Jacobian matrix relating the natural coordinate derivatives to the local coordinate derivatives, see for example [98, 3, 115], is defined in the following way

$$\begin{pmatrix} \partial/\partial\xi \\ \partial/\partial\eta \\ \partial/\partial\zeta \end{pmatrix} = \mathbf{J} \begin{pmatrix} \partial/\partial x \\ \partial/\partial y \\ \partial/\partial z \end{pmatrix} \quad \text{where} \quad \mathbf{J} = \begin{pmatrix} \partial x/\partial\xi & \partial y/\partial\xi & \partial z/\partial\xi \\ \partial x/\partial\eta & \partial y/\partial\eta & \partial z/\partial\eta \\ \partial x/\partial\zeta & \partial y/\partial\zeta & \partial z/\partial\zeta \end{pmatrix} . \quad (\text{A.11})$$

So the global derivatives of the shape functions can be calculated by using the local derivatives and the inverse Jacobian matrix

$$\begin{pmatrix} \partial N(\boldsymbol{\xi})/\partial x \\ \partial N(\boldsymbol{\xi})/\partial y \\ \partial N(\boldsymbol{\xi})/\partial z \end{pmatrix} = \mathbf{J}^{-1} \begin{pmatrix} \partial N(\boldsymbol{\xi})/\partial\xi \\ \partial N(\boldsymbol{\xi})/\partial\eta \\ \partial N(\boldsymbol{\xi})/\partial\zeta \end{pmatrix} \quad (\text{A.12})$$

with

$$\mathbf{J}(\boldsymbol{\xi}) = \sum_{i=1}^n \begin{pmatrix} \partial N_i(\boldsymbol{\xi})/\partial\xi \\ \partial N_i(\boldsymbol{\xi})/\partial\eta \\ \partial N_i(\boldsymbol{\xi})/\partial\zeta \end{pmatrix} \begin{pmatrix} x_i \\ y_i \\ z_i \end{pmatrix}^\top . \quad (\text{A.13})$$

Numerical integration. For evaluating the element integrals Gauss quadrature can be used. With the isoparametric concept this yields to

$$\int_{\Omega^e} [\bullet] d\Omega^e = \int_{-1}^1 \int_{-1}^1 \int_{-1}^1 [\bullet] \det \mathbf{J} dr ds dt = \sum_{k=1}^{n_{gp}} [\bullet]_k w g_k J_k \quad (\text{A.14})$$

where n_{gp} are the sampling points with the weights $w g_k$. J_k is the determinant of the Jacobian matrix \mathbf{J} , defined in Eq. (A.11, evaluated at sampling point k .

Appendix B

Application of the finite element method on a hydraulic-mechanically coupled saturated flow problem

In the present section, the finite element formulation for the hydraulic-mechanically coupled problem of fully saturated flow in poro-elastic porous media, as presented in Sec. 3.2, is derived.

B.1 Finite element formulation

Weak formulation. The weak form of the hydraulic-mechanical part of the problem summarized in Sec. 3.2 is achieved by applying the standard Galerkin method as presented in Sec. A.2. This weak integral formulation is derived within finite elements resulting in a set of matrices given in App. B.2. Thus, the coupled problem can be written in the following form

$$\mathbf{K} \frac{d\hat{\mathbf{u}}}{dt} + \mathbf{Q} \frac{d\hat{\mathbf{p}}}{dt} = \frac{d(\mathbf{f}_u^{\text{ext}} - \mathbf{f}_u^{\text{int}})}{dt} \quad (\text{B.1})$$

$$\mathbf{Q}^T \frac{d\hat{\mathbf{u}}}{dt} + \mathbf{C}\hat{\mathbf{p}} + \mathbf{S} \frac{d\hat{\mathbf{p}}}{dt} = \mathbf{f}_p^{\text{ext}}, \quad (\text{B.2})$$

Temporal discretization. The equations have to be discretized in time. Introducing a time step $\Delta t_n = t_{n+1} - t_n$, the time derivatives in the differential equation can be replaced by finite differences. For the temporal integration between time t_n and t_{n+1} different methods can be used. In order to achieve a stable scheme without dependence of the time step length, the implicit Euler backward method usually is used.

$$\mathbf{K}\Delta\hat{\mathbf{u}} + \mathbf{Q}\Delta\hat{\mathbf{p}} = \mathbf{f}_u^{\text{ext}}(n+1) - \mathbf{f}_u^{\text{int}}(n) \quad (\text{B.3})$$

$$\mathbf{Q}^T \frac{\Delta\hat{\mathbf{u}}}{\Delta t} + \mathbf{C}\hat{\mathbf{p}}_{(n+1)} + \mathbf{S} \frac{\Delta\hat{\mathbf{p}}}{\Delta t} = \mathbf{f}_p^{\text{ext}}(n+1) \quad (\text{B.4})$$

After applying the temporal discretization, the equations has be rearranged in order to get the solution at time t_{n+1} . An incremental approach with the formulation of resulting

increments $\Delta(\hat{\bullet}) = (\hat{\bullet})_{n+1} - (\hat{\bullet})_n$, a direct formulation of the solution vector $(\hat{\bullet})_{n+1}$ or a mixture of both is possible, as applied in the following set of equations

$$\mathbf{K}\Delta\hat{\mathbf{u}} + \mathbf{Q}\hat{\mathbf{p}}_{(n+1)} = \mathbf{f}_{\mathbf{u}}^{\text{ext}}{}_{(n+1)} - \mathbf{f}_{\mathbf{u}}^{\text{int}}{}_{(n)} - \mathbf{Q}\hat{\mathbf{p}}_{(n)} \quad (\text{B.5})$$

$$\frac{\mathbf{Q}^{\text{T}}}{\Delta t}\Delta\hat{\mathbf{u}} + \mathbf{C}\hat{\mathbf{p}}_{(n+1)} + \frac{\mathbf{S}}{\Delta t}\hat{\mathbf{p}}_{(n+1)} = \mathbf{f}_{\mathbf{p}}^{\text{ext}}{}_{(n+1)} - \frac{\mathbf{S}}{\Delta t}\hat{\mathbf{p}}_{(n)} \quad (\text{B.6})$$

Linear system of equations. The final system of linear equations can directly be formulated. In case of linear material behavior the equation can be solved within a single step.

$$\begin{bmatrix} \mathbf{K}_{\text{uu}} & \mathbf{C}_{\text{up}} \\ \mathbf{C}_{\text{pu}} & \mathbf{K}_{\text{pp}} \end{bmatrix} \begin{Bmatrix} \Delta\hat{\mathbf{u}} \\ \hat{\mathbf{p}} \end{Bmatrix} = \begin{Bmatrix} \mathbf{R}_{\mathbf{u}} \\ \mathbf{R}_{\mathbf{p}} \end{Bmatrix} \quad (\text{B.7})$$

where

$$\mathbf{K}_{\text{uu}} = \mathbf{K} \quad (\text{B.8})$$

$$\mathbf{K}_{\text{pp}} = \mathbf{C} + \frac{\mathbf{S}}{\Delta t} \quad (\text{B.9})$$

$$\mathbf{C}_{\text{up}} = \mathbf{Q} \quad (\text{B.10})$$

$$\mathbf{C}_{\text{pu}} = \frac{\mathbf{Q}^{\text{T}}}{\Delta t} \quad (\text{B.11})$$

$$\mathbf{R}_{\mathbf{u}} = \mathbf{f}_{\mathbf{u}}^{\text{ext}}{}_{(n+1)} - \mathbf{f}_{\mathbf{u}}^{\text{int}}{}_{(n)} - \mathbf{Q}\hat{\mathbf{p}}_{(n)} \quad (\text{B.12})$$

$$\mathbf{R}_{\mathbf{p}} = \mathbf{f}_{\mathbf{p}}^{\text{ext}}{}_{(n+1)} - \frac{\mathbf{S}}{\Delta t}\hat{\mathbf{p}}_{(n)} \quad (\text{B.13})$$

The global coefficient matrices appearing in these algebraic equations are composed by the finite element matrices $[\bullet]^{(e)}$ given in App. B.2 for each sub-problem. The finite element assembly sums up the contributions of n_{el} elements according to the mesh connectivity and can be written as follows

$$[\bullet] = \mathbf{A} \sum_{e=1}^{n_{\text{el}}} [\bullet]^{(e)} \quad (\text{B.14})$$

where $[\bullet]$ and $[\bullet]^{(e)}$ are the is the global matrix and the finite element matrices, respectively.

The operator $\mathbf{A} \sum_{e=1}^{n_{\text{el}}}$ is called the standard finite element assembly operator.

B.2 Finite element matrices

In this section, the finite element matrices of both the fluid and the solid sub-problem are summarized in Table B.1 and Table B.2, respectively.

Table B.1: Fluid sub-problem.

Matrix / Vector	Meaning
$\mathbf{C}^{(e)} = \int_{\Omega_e} (\nabla N_p)^T \frac{\mathbf{k}}{\mu} \nabla N_p d\Omega_e$	Conductance matrix
$\mathbf{S}^{(e)} = \int_{\Omega_e} N_p S N_p d\Omega_e$	Storativity matrix
$(\mathbf{Q})^T = \int_{\Omega_e} N_p \alpha \mathbf{m} \mathbf{B} d\Omega_e$	Coupling matrix (volume)
$\mathbf{f}_p^{\text{ext}(e)} = \int_{\Omega_e} (\nabla N_p)^T \frac{\mathbf{k}}{\mu} \nabla N_p \rho^f \mathbf{g} z d\Omega_e + \int_{\Gamma_e \cap \Gamma_p^N} N_p \bar{q} d\Gamma_e$	External source vector

Table B.2: Solid sub-problem.

Matrix / Vector	Meaning
$\mathbf{K}^{(e)} = \int_{\Omega_e} \mathbf{B}^T \mathbf{C} \mathbf{B} d\Omega_e$	Stiffness matrix
$\mathbf{Q}^{(e)} = \int_{\Omega_e} \mathbf{B}^T \alpha \mathbf{m}^T N_p d\Omega_e$	Coupling matrix (pressure)
$\mathbf{f}_u^{\text{ext}(e)} = \int_{\Omega_e} \mathbf{N}_u \rho \mathbf{g} d\Omega_e + \int_{\Gamma_e \cap \Gamma_u^N} \mathbf{N}_u \bar{\mathbf{t}} d\Gamma_e$	External load vector
$\mathbf{f}_u^{\text{int}(e)} = \int_{\Omega_e} \mathbf{B}^T (\boldsymbol{\sigma} - \alpha p \mathbf{m}^T) d\Omega_e$	Internal force vector

The external source and load vectors \bar{q} and $\bar{\mathbf{t}}$ are the components of the stress tensor and fluid flux vectors normal to the boundary defined by the outward normal \mathbf{n} as follows

$$\bar{q} = \mathbf{q} \mathbf{n}, \quad \bar{\mathbf{t}} = \boldsymbol{\sigma} \mathbf{n} \quad (\text{B.15})$$

and \mathbf{m} is the vector representation of the first order unit tensor

$$\mathbf{m} = [1, 1, 1, 0, 0, 0]. \quad (\text{B.16})$$

Different ansatz spaces are used for the two sub-problems. In the hydraulic problem the pressure is approximated linearly, while quadratic shape functions are used for the approximation of the displacement field.

$$\mathbf{N}_u = \begin{bmatrix} N_u \\ N_v \\ N_w \end{bmatrix}, \quad \mathbf{B} = \begin{bmatrix} \partial_x N_{u,x} & 0 & 0 \\ 0 & N_{v,y} & 0 \\ 0 & 0 & N_{w,z} \\ N_{u,y} & N_{v,x} & 0 \\ 0 & N_{v,z} & N_{w,y} \\ N_{u,z} & 0 & N_{w,x} \end{bmatrix} \quad (\text{B.17})$$

$$N_u = N_v = N_w = \begin{Bmatrix} N_1^{(e)u} \\ N_2^{(e)u} \\ \vdots \\ N_{n_{\text{nod}}^{(e)u}}^{(e)u} \end{Bmatrix}, \quad N_p = \begin{Bmatrix} N_1^{(e)p} \\ N_2^{(e)p} \\ \vdots \\ N_{n_{\text{nod}}^{(e)p}}^{(e)p} \end{Bmatrix} \quad (\text{B.18})$$

Appendix C

Various derivations

C.1 Invariants of second order tensors

Stress tensor invariants

$$\begin{aligned} I_1 &= \text{tr}(\boldsymbol{\sigma}) = \sigma_{ii} = \sigma_{xx} + \sigma_{yy} + \sigma_{zz} \\ &= \sigma_1 + \sigma_2 + \sigma_3 \\ I_2 &= \frac{1}{2} \sigma_{ij} \sigma_{ij} = \sigma_{xx} \sigma_{yy} + \sigma_{yy} \sigma_{zz} + \sigma_{xx} \sigma_{zz} - \sigma_{xy}^2 - \sigma_{xz}^2 - \sigma_{yz}^2 \\ &= \sigma_1 \sigma_2 + \sigma_2 \sigma_3 + \sigma_3 \sigma_1 \\ I_3 &= \frac{1}{3} \sigma_{ij} \sigma_{jk} \sigma_{ki} = \det(\sigma_{ij}) = \begin{vmatrix} \sigma_{xx} & \sigma_{xy} & \sigma_{xz} \\ \sigma_{yx} & \sigma_{yy} & \sigma_{yz} \\ \sigma_{zx} & \sigma_{zy} & \sigma_{zz} \end{vmatrix} \\ &= \sigma_1 \sigma_2 \sigma_3 \end{aligned}$$

Deviatoric stress tensor invariants

$$\begin{aligned} J_1 &= \text{tr}(\mathbf{s}) = s_{ii} \\ &= s_1 + s_2 + s_3 \\ &= 0 \\ J_2 &= \frac{1}{2} \mathbf{s} : \mathbf{s} = \frac{1}{2} s_{ij} s_{ij} \\ &= \frac{1}{2} (s_1^2 + s_2^2 + s_3^2) \\ J_3 &= \det(s_{ij}) = \frac{1}{3} s_{ij} s_{jk} s_{kl} \\ &= s_1 s_2 s_3 \end{aligned}$$

$$J_2 = \frac{1}{3}(I_1^2 - 3I_2)$$

$$J_3 = \frac{1}{27}(2I_1^3 - 9I_1I_2 + 27I_3)$$

Further useful invariants

The mean stress σ also called *hydrostatic stress* p and the octahedral shear stress τ are defined as follows

$$\sigma = \frac{1}{3}(\sigma_1 + \sigma_2 + \sigma_3) = \frac{1}{3}I_1 \quad (\text{C.1})$$

$$\tau = \sqrt{\frac{2}{3}}\sqrt{J_2}. \quad (\text{C.2})$$

The equivalent stress q and the equivalent plastic strain e_q^{pl} are work-conjugate quantities. They are defined as follows

$$q = \sqrt{\frac{3}{2}}\|\mathbf{s}\| = \sqrt{3}\sqrt{J_2} \quad (\text{C.3})$$

$$e_q^{\text{pl}} = \sqrt{\frac{2}{3}}\|\mathbf{e}\|. \quad (\text{C.4})$$

Partial derivatives of stress tensor invariants

Some important derivatives of stress invariants are summarized below. With the assumption that $\mathbf{s} = \mathbf{s}^T$ the norm of the second order tensor \mathbf{s} is $\|\mathbf{s}\| = \sqrt{\mathbf{s} : \mathbf{s}} = \sqrt{\mathbf{s}\mathbf{s}^T} = \sqrt{\text{tr}(\mathbf{s}^T\mathbf{s})}$ and

$$\frac{\partial\|\mathbf{s}\|}{\partial\mathbf{s}} = \frac{\mathbf{s}}{\|\mathbf{s}\|}. \quad (\text{C.5})$$

For the evaluation of the plastic flow the derivatives of the invariants I_1, J_2, J_3 with respect to the stress tensor are required. They are as follows

$$\frac{\partial I_1}{\partial\boldsymbol{\sigma}} = \mathbf{1}, \quad (\text{C.6})$$

$$\frac{\partial J_2}{\partial\mathbf{s}} = \mathbf{s}, \quad (\text{C.7})$$

$$\frac{\partial J_3}{\partial\mathbf{s}} = \mathbf{s}^2 - \frac{2}{3}J_2\mathbf{1}. \quad (\text{C.8})$$

C.2 Thermoelasticity

Three-dimensional problem

The stress strain relations for three-dimensional problems are:

$$\begin{aligned}\varepsilon_x - \alpha_T(T - T_0) &= \frac{1}{E}(\sigma_x - \nu(\sigma_y + \sigma_z)) \\ \varepsilon_y - \alpha_T(T - T_0) &= \frac{1}{E}(\sigma_y - \nu(\sigma_x + \sigma_z)) \\ \varepsilon_z - \alpha_T(T - T_0) &= \frac{1}{E}(\sigma_z - \nu(\sigma_x + \sigma_y))\end{aligned}\quad (\text{C.9})$$

$$\gamma_{xy} = \frac{\tau_{xy}}{G} \quad \gamma_{yz} = \frac{\tau_{yz}}{G} \quad \gamma_{xz} = \frac{\tau_{xz}}{G} \quad (\text{C.10})$$

Two-dimensional problem

Three-dimensional thermoelastic problems can be formulated in only two dimensions if there is no temperature variation in the third direction. In case of thin plates or in case of equal cross sections a plane stress or plane strain state may be assumed, respectively.

Plane stress In a state of plane stress, with $\sigma_z = \tau_{xz} = \tau_{yz} = 0$, the stress-strain relations are as follows

$$\begin{aligned}\varepsilon_x - \alpha_T(T - T_0) &= \frac{1}{E}(\sigma_x - \nu\sigma_y) \\ \varepsilon_y - \alpha_T(T - T_0) &= \frac{1}{E}(\sigma_y - \nu\sigma_x)\end{aligned}\quad (\text{C.11})$$

$$\gamma_{xy} = \frac{\tau_{xy}}{G}. \quad (\text{C.12})$$

Plane strain In a state of plane strain, with $\varepsilon_z = \gamma_{xz} = \gamma_{yz} = 0$, the stress-strain relations are as follows

$$\begin{aligned}\varepsilon_x - (1 + \nu)\alpha_T(T - T_0) &= \frac{1 - \nu^2}{E}\left(\sigma_x - \frac{\nu}{1 - \nu}\sigma_y\right) \\ \varepsilon_y - (1 + \nu)\alpha_T(T - T_0) &= \frac{1 - \nu^2}{E}\left(\sigma_y - \frac{\nu}{1 - \nu}\sigma_x\right)\end{aligned}\quad (\text{C.13})$$

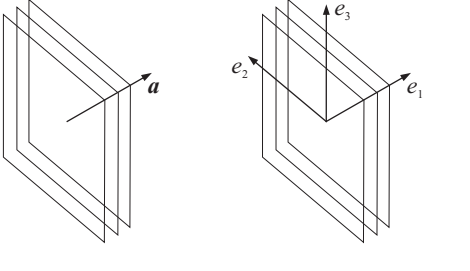
$$\gamma_{xy} = \frac{\tau_{xy}}{G}. \quad (\text{C.14})$$

These equations can be obtained from the equations of plane stress, Eqs. (C.11), by replacing E with $E/(1 - \nu^2)$, ν with $\nu/(1 - \nu)$ and α_T with $(1 + \nu)\alpha_T$. The analytical solution may be transformed in the same way (c.f. [102]).

C.3 Parameterization of transverse isotropy

Transverse isotropy in terms of engineering elastic properties

Table C.1: Invariant formulation of transverse isotropy. The axis of transverse isotropy is defined by \mathbf{a} and supposed to be x (1-direction).

		<p>direction perpendicular to plane of isotropy: 1 plane of isotropy: 23 ($\mathbf{a} = \mathbf{e}_1$)</p>
Invariants and their representation in five independent elastic parameters		
1	$\lambda = E_2(\nu_{23} + \nu_{13}\nu_{31})/D$	
2	$\alpha = E_2(\nu_{13}(\nu_{32} - \nu_{31}) - \nu_{32})/D$	
3	$\beta = (E_1(1 - \nu_{32}\nu_{23}) - E_2[(\nu_{23} + \nu_{13}\nu_{31})$ $+ 2(\nu_{13}(\nu_{32} - \nu_{31}) - \nu_{32})])/D - 4G_{12} + 2G_{23}$	
4	$G_L = G_{12}$	
5	$G_T = G_{23}$	
where		
$D = 1 - \nu_{32}^2 - 2\nu_{13}\nu_{31} - 2\nu_{13}\nu_{32}\nu_{31}$		
and		
$E_2 = E_3$		
$\nu_{12} = \nu_{13}$		
$\nu_{21} = \nu_{31}$		
$\nu_{23} = \nu_{32}$		
$\nu_{21} = \frac{E_1}{E_2}\nu_{12}$		
$G_{23} = \frac{E_2}{2(1 + \nu_{32})}$		

Transverse isotropy in terms of engineering elastic properties

Table C.2: Transverse isotropy in terms of engineering elastic properties E , G , and ν . The axis of transverse isotropy is x (1-direction).

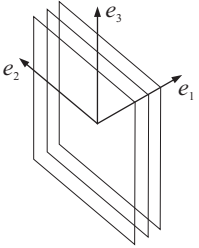
		<p>direction perpendicular to plane of isotropy: 1 plane of isotropy: 23</p>	
	Parameter	Relations	Definition
1	E_1		Young's modulus in direction (1) perpendicular to isotropic plane
2	E_2	$E_2 = E_3$	Young's modulus in plane of isotropy (23)
3	ν_{12}	$\nu_{12} = \nu_{13}$ $\nu_{21} = \nu_{31}$ $\nu_{12} = \nu_{21} E_2/E_1$	Poisson's ratio for the normal strain in the (1)-direction in the plane of isotropy (23) related to the normal strain in the (2)-direction in the perpendicular plane due to uniaxial stress in the (2) direction
4	ν_{23}	$\nu_{23} = \nu_{32}$	Poisson's ratio for the normal strain in the (1)-direction in the plane of isotropy (23) related to the normal strain in the (3)-direction due to uniaxial stress in (3) direction
5	G_{12}	$G_{12} = G_{13}$	Cross shear modulus between plane of isotropy (23) and perpendicular plane (12) or (13)
6	G_{23}	$G_{23} = \frac{E_2}{2(1 + \nu_{32})}$	Shear modulus in plane of isotropy (23) (G_{23} is a dependent parameter to be derived from the above mentioned.)

Table C.3: Transverse isotropy in terms of engineering elastic properties E , G , and ν . The axis of transverse isotropy is y (2-direction).

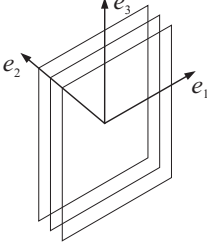
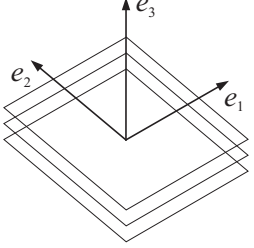
		<p>direction perpendicular to plane of isotropy: 2 plane of isotropy: 13</p>	
	Parameter	Relations	Definition
1	E_2		Young's modulus in direction (2) perpendicular to isotropic plane
2	E_1	$E_1 = E_3$	Young's modulus in plane of isotropy (13)
3	ν_{21}	$\nu_{21} = \nu_{23}$ $\nu_{12} = \nu_{32}$ $\nu_{21} = \nu_{12} E_1/E_2$	Poisson's ratio for the normal strain in the (2)-direction in the plane of isotropy (13) related to the normal strain in the (1)-direction in the perpendicular plane due to uniaxial stress in the (1) direction
4	ν_{13}	$\nu_{13} = \nu_{31}$	Poisson's ratio for the normal strain in the (2)-direction in the plane of isotropy (13) related to the normal strain in the (3)-direction due to uniaxial stress in (3) direction
5	G_{21}	$G_{21} = G_{23}$	Cross shear modulus between plane of isotropy (13) and perpendicular plane (21) or (23)
6	G_{13}	$G_{13} = \frac{E_1}{2(1 + \nu_{31})}$	Shear modulus in plane of isotropy (13) (G_{13} is a dependent parameter to be derived from the above mentioned.)

Table C.4: Transverse isotropy in terms of engineering elastic properties E , G , and ν . The axis of transverse isotropy is z (3-direction).

			<p>direction perpendicular to plane of isotropy: 3 plane of isotropy: 12</p>
	Parameter	Relations	Definition
1	E_3		Young's modulus in direction (3) perpendicular to isotropic plane
2	E_1	$E_1 = E_2$	Young's modulus in plane of isotropy (12)
3	ν_{31}	$\nu_{31} = \nu_{32}$ $\nu_{13} = \nu_{23}$ $\nu_{31} = \nu_{13} E_1 / E_3$	Poisson's ratio for the normal strain in the (3)-direction in the plane of isotropy (12) related to the normal strain in the (1)-direction in the perpendicular plane due to uniaxial stress in the (1) direction
4	ν_{12}	$\nu_{12} = \nu_{21}$	Poisson's ratio for the normal strain in the (3)-direction in the plane of isotropy (12) related to the normal strain in the (2)-direction due to uniaxial stress in (2) direction
5	G_{31}	$G_{31} = G_{32}$	Cross shear modulus between plane of isotropy (12) and perpendicular plane (31) or (32)
6	G_{12}	$G_{12} = \frac{E_1}{2(1 + \nu_{21})}$	Shear modulus in plane of isotropy (12) (G_{12} is a dependent parameter to be derived from the above mentioned.)

List of figures

2.1	Motion of a material body in a Euclidian space, represented in relative to a frame of reference.	9
2.2	Motion of a material body in a Euclidian space, represented in relative to the configuration at time t_0 as a chosen frame of reference.	10
2.3	Real geometric structure of the representative element volume (REV) (left) and its smeared representation of a porous medium (right).	10
2.4	The concept of volume fraction. Schematic representation of the real REV (left) with a total volume of dv and the porous medium (right) described by its partial volumes.	12
4.1	Single-step method. Explicit <i>Euler</i> . System state evaluation at current time t_n .	31
4.2	Single-step method. Implicit <i>Euler</i> . System state evaluation at new time t_{n+1} .	31
4.3	Multi-step method with approximation around t_n . <i>Leapfrog</i> : centered explicit. System state evaluation at current time t_n	31
4.4	Forward <i>Euler</i> (left endpoint).	32
4.5	<i>Crank-Nicolson</i> (trapezoidal).	32
4.6	Backward <i>Euler</i> (right endpoint).	32
4.7	The <i>Newton-Raphson</i> method.	34
4.8	Direct (<i>Picard</i>) iteration.	35
5.1	Schematic description of the set-up of a linear equation system with direct (monolithic) or indirect (partitioned) treatment of the couplings.	44
5.2	Standard storage of a structurally symmetric sparse matrix.	45
5.3	Column compressed storage of a structurally symmetric sparse matrix. The coefficient are addressed using the indices (i, l) instead of (k, l)	45
5.4	Hydraulic-mechanically coupled system of six elements. Matrix structure resulting from a block-wise composition of unknowns without grid node reordering.	47
5.5	Hydraulic-mechanically coupled system of six elements. Matrix structure resulting from a block-wise composition of unknowns with grid node reordering.	47
5.6	Hydraulic-mechanically coupled system of six elements. Matrix structure resulting from a node oriented composition with grid node reordering.	47
6.1	Tensile test. Set-up.	52
6.2	Tensile test. RockFlow results and reference values taken from Schröder (1996) [90].	54
6.3	Geometric interpretation of plastic loading ($\gamma > 0$) at angles $\Theta < 90^\circ$	57
6.4	Yield surface of <i>von Mises</i> criterion.	59
6.5	Yield surface of <i>Tresca</i> criterion.	59
6.6	Yield surface of <i>Drucker-Prager</i> criterion.	60

6.7	<i>Mohr-Coulomb</i> yield surface.	60
6.8	Single yield surface. Material properties are taken from Ehlers (2002) [33] (p. 58).	60
6.9	Approximation of the <i>Mohr-Coulomb</i> yield criterion by a model of <i>Drucker-Prager</i> type with compromise cone.	67
6.10	Approximation of the <i>Mohr-Coulomb</i> yield criterion by a <i>Drucker-Prager</i> model.	68
7.1	2-D and 3-D elements with linear (above) and quadratic (below) shape functions. The location of the integration points is depicted in 2-D for a reliable integration order of 2×2 for linear and 3×3 quadratic approximation.	76
7.2	Procedure for direct or indirect solution of a coupled process.	78
7.3	The non-linear solver object.	78
7.4	Classes of the GUI framework for RockFlow.	79
7.5	Wire frame representation of the finite element mesh with differently colored material groups.	80
7.6	Selection of one material group. Node and element numbers are visualized.	80
7.7	Visualization of a hydrostatic pressure field contour.	82
7.8	Visualization of material groups and deformation due to gravity. <i>Dirichlet</i> boundary nodes are marked by green dots. The displacements are scaled by the factor 1000.	82
7.9	Grimsel 2.75-D application [74]. 2.5-D fracture network and its concentration field. Windows view.	82
7.10	Grimsel 2.75-D application [74]. 3-D matrix blocks around 2.5-D fracture network and its pressure field. Linux view.	82
7.11	Visualization of an XML based keyword description.	83
8.1	Geometry of the plate with a hole benchmark problem.	86
8.2	Monotonic loading: local unloading in point (2).	87
8.3	Monotonic loading: equivalent stress at $\lambda = 4.65$	88
8.4	Monotonic loading: accumulated plastic strain at $\lambda = 4.65$	88
8.5	Cyclic loading: deformation at sequenced load steps.	88
8.6	Cyclic loading: displacement u_x in point (2) (a) and u_y in point (4) (b).	89
8.7	Cyclic loading: stress σ_{yy} in point (2).	89
8.8	Cyclic loading: equivalent stress at $\lambda = 4.5$	90
8.9	Cyclic loading: accumulated plastic strain at $\lambda = 4.5$	90
8.10	Heat flow around spherical cavity.	91
8.11	Heat flow around 2-D circular hole.	92
8.12	3-D spherical cavity. Domain with colored near field.	93
8.13	3-D spherical cavity. Temperature in the near field.	93
8.14	3-D spherical cavity. Stress σ_{xx} versus height in the near field.	94
8.15	3-D spherical cavity. Temperature versus height in the near field.	94
8.16	2-D circular hole. Domain with colored near field.	95
8.17	2-D circular hole. Temperature in the near field.	95
8.18	2-D circular hole. Stress σ_{xx} in the near field.	95
8.19	2-D circular hole. Temperature versus height in the near field.	95
8.20	3-D circular hole. Domain with colored near field.	96
8.21	3-D circular hole. Stress σ_{xx} in the near field.	96
8.22	3-D circular hole. Stress σ_{xx} versus height in the near field.	96
8.23	3-D circular hole. Temperature versus height in the near field.	96

8.24	One-dimensional consolidation. Geometry and boundary conditions.	99
8.25	One-dimensional consolidation. Fluid pressure p (a), stress σ (b) and vertical displacement u (c) (ordinate) versus depth (abscissa) of deformable column. . .	101
8.26	Hydraulic head versus water content, with $\Psi = p^w/\rho^w g$ and $\theta = nS^w$ ([66]). . .	104
8.27	Hydraulic conductivity versus pressure, with $K = k\rho^w g/\mu^w$ and $\Psi = p^w/\rho^w g$ ([66]).	104
8.28	Liakopoulos experiment. Set-up.	104
8.29	Liakopoulos experiment. Water pressure p^w versus height (abscissa) of deformable column ($t = \{5\text{ s}, 10\text{ s}, 20\text{ s}, 30\text{ s}, 1\text{ min}, 2\text{ min}, 3\text{ min}, 5\text{ min}, 10\text{ min}, 20\text{ min}, 30\text{ min}, \dots, 120\text{ min and }24\text{ h}\}$).	105
8.30	Liakopoulos experiment. Water saturation S^w (a) and vertical displacement u_z^s (b) (ordinate) versus height (abscissa) of deformable column ($t = \{5\text{ s}, 10\text{ s}, 20\text{ s}, 30\text{ s}, 1\text{ min}, 2\text{ min}, 3\text{ min}, 5\text{ min}, 10\text{ min}, 20\text{ min}, 30\text{ min}, \dots, 120\text{ min and }24\text{ h}\}$). .	106
8.31	Rigid footing. Set-up.	107
8.32	Fully saturated flow formulation. Fluid pressure field using the <i>von Mises</i> yield criterion.	108
8.33	Partially saturated flow formulation. Fluid pressure field using the <i>von Mises</i> yield criterion.	108
8.34	Fully saturated flow formulation. Equivalent plastic strain using the <i>von Mises</i> yield criterion.	109
8.35	Partially saturated flow formulation. Equivalent plastic strain using the <i>von Mises</i> yield criterion.	109
8.36	Partially saturated rigid footing. Fluid pressure using the <i>von Mises</i> yield criterion.	109
8.37	Partially saturated rigid footing. Fluid saturation using the <i>von Mises</i> yield criterion.	109
8.38	Saturated rigid footing. Fluid pressure and fluid velocity in a dilatant <i>Drucker-Prager</i> material.	110
8.39	Saturated rigid footing. Accumulated volumetric plastic strain and fluid velocity in a dilatant <i>Drucker-Prager</i> material.	110
8.40	Saturated rigid footing. Fluid pressure and fluid velocity in a contractant <i>Drucker-Prager</i> material.	110
8.41	Saturated rigid footing. Accumulated volumetric plastic strain and fluid velocity in a contractant <i>Drucker-Prager</i> material.	110
9.1	Geometry and boundary conditions.	112
9.2	Mesh, fluid velocity and pressure field for $t = 10\text{ s}$	113
9.3	Fluid pressure (left) and stress σ_{yy} (right) along vertical cross section at $x = 0\text{ m}$ for time steps 1, 10, 20 and 100 s evaluated in two (solid line) and three (dashed line) dimensional simulations.	113
9.4	Pressure fields of two and three dimensional consolidation at $t = 100\text{ s}$. Displacements are scaled by factor 10.	114
9.5	Model set-up.	115
9.6	Domain and initial concentration.	115
9.7	Deformed domain and concentration after 2.25 cycles at 540 s.	115
9.8	Displacements of left and right top and temporal concentration curves in point (4).	115

9.9	Task 3. BMT 1-B. Conceptual design of a hypothetical repository [47] (a). Conceptual representation of repository near-field (b). Near-field parts of the fine mesh for temperature analysis consisting of waste/overpack, buffer, fracture, backfill and rock mass (c). Mesh used for thermomechanical analysis (d). . . .	117
9.10	Task 3. BMT 1-B. Initial and boundary conditions prescribed for excavation (left) and ensuing transient analysis (right).	118
9.11	Heat output curve, resulting temperature curve (a) and temperature in the near-field after 30 years (b).	118
9.12	Temperature field (a), horizontal stress σ_{xx} (b) and shear stress σ_{zx} (c) after 10 years.	119
9.13	Temperature versus time.	119
9.14	Stress σ_{xx} versus time.	119
9.15	Torus. Set-up.	120
9.16	Torus. Mesh of differently colored partitions.	120
9.17	Resulting steady state temperature field.	121
9.18	Resulting steady state displacement field.	121
9.19	General model description for Task D, THM. Model geometry and boundary conditions (above). Locations of points, lines and areas for model output (below) [2].	124
9.20	Water retention and relative permeability curves for granite rock (standard <i>van Genuchten</i>) and FEBEX bentonite material (modified <i>van Genuchten</i>) as defined in Table 9.8 and Table 9.9.	126
9.21	Thermal power decay function of a reference fuel PWR element [2].	127
9.22	Specific modeling sequence, initial and boundary conditions for Task D, THM1 [2].	128
9.23	Horizontal stress (left) in the deformed near field due to excavation. The undeformed mesh represents the initial configuration. The settlement of the drift is due to the transient pressure field (right) influenced by the drainage caused by the atmospheric pressure in the drift wall. The displacements are scaled by factor 250.	129
9.24	RockFlow simulation results of vertical temperature profiles.	130
9.25	Comparison of TOUGH-FLAC (TOUGH2) and ROCMAS simulation results of vertical temperature profiles [10].	130
9.26	RockFlow simulation results of vertical pressure profiles.	130
9.27	Comparison of TOUGH2 and ROCMAS simulation results of vertical pressure profiles [10].	130
9.28	Simulation results of vertical profiles of total horizontal stress. RockFlow (left) and ROCMAS (right) [10].	131
9.29	Simulation results of vertical profiles of vertical stress. RockFlow (left) and ROCMAS (right) [10].	132
9.30	RockFlow simulation results of vertical displacement profiles.	133
9.31	ROCMAS simulation results of vertical displacement profiles [10].	133
9.32	Embankment problem. Model set-up and boundary conditions.	134
9.33	Embankment problem. Saturation fields and velocity vectors indicating the direction of fluid flow at a water level of $h = 8$ m (above) and $h = 2$ m (below) predicted in a transient simulation.	136

9.34	Embankment problem. Evaluation of the <i>Drucker-Prager</i> yield function (above) and excess pore pressure (below). Saturated and partially saturated zones are separated by a white line in the pressure field.	136
9.35	Slope stability problem. Geometry and boundary conditions.	137
9.36	Slope stability problem in case of drained conditions. Shear bands in the deformed slope at $\lambda_{\text{crit}} = 0.44$	139
9.37	Slope stability problem in case of fully saturated conditions. Shear bands in the deformed slope at $\lambda_{\text{crit}} = 0.31$ with arrows indicating the flow direction of the pore water.	139

List of tables

6.1	Load, material and geometric properties.	53
6.2	Engineering representation of elastic properties with axis of transverse isotropy in x -direction.	53
6.3	Engineering representation of elastic properties with axis of transverse isotropy in y -direction.	54
6.4	Parameters of the <i>Mohr-Coulomb</i> yield criterion approximated by a model of <i>Drucker-Prager</i> type with compromise cone.	67
6.5	Parameters of the Mohr-Coulomb yield criterion approximated by <i>Drucker-Prager</i> type.	67
7.1	THM _{plus} model. Available processes and associated keywords.	74
8.1	Geometry and load setup.	86
8.2	Material Properties.	86
8.3	Reference values and RockFlow results ($\lambda = 4.5$).	87
8.4	Material properties.	87
8.5	Model geometry and mesh size.	92
8.6	Material and heat flow parameters.	93
8.7	Comparison of analytical and numerical results.	97
8.8	One-dimensional consolidation. Geometry and material properties.	100
8.9	Liakopoulos benchmark. Material properties.	105
8.10	Rigid footing. Material properties.	108
9.1	Strip footing. Mesh properties and temporal discretization.	112
9.2	Strip footing. Material properties.	112
9.3	Hydro-mechanically coupled transport: material parameters.	115
9.4	Task 3. BMT 1-B. Material properties.	116
9.5	Material properties.	121
9.6	Task D. Summary of similarities and differences between repository scenarios [2].	123
9.7	Task D_THM1. Model dimensions.	125
9.8	Task D_THM1. Material properties of the rock.	125
9.9	Task D_THM1. Material properties of the bentonite buffer.	125
9.10	Embankment problem. Material properties.	135
9.11	Slope stability problem. Material properties.	138
B.1	Fluid sub-problem.	163
B.2	Solid sub-problem.	163

C.1	Invariant formulation of transverse isotropy. The axis of transverse isotropy is defined by \mathbf{a} and supposed to be x (1-direction).	168
C.2	Transverse isotropy in terms of engineering elastic properties E , G , and ν . The axis of transverse isotropy is x (1-direction).	169
C.3	Transverse isotropy in terms of engineering elastic properties E , G , and ν . The axis of transverse isotropy is y (2-direction).	170
C.4	Transverse isotropy in terms of engineering elastic properties E , G , and ν . The axis of transverse isotropy is z (3-direction).	171

Liste der bisher erschienenen Institutsberichte

(* = bereits vergriffen)

- 01/1970 * **Holz, K.-P.** *Ergänzung des Verfahrens finiter Elemente durch Ecksingularitäten zur verbesserten Berechnung schiefwinkliger Platten.* Dissertation, Techn. Univ. Hannover, 1970
- 02/1971 * **Ehlers, K.-D.** *Berechnung instationärer Grund- und Sickerwasserströmungen mit freier Oberfläche nach der Methode finiter Elemente.* Dissertation, Techn. Univ. Hannover, 1971
- 03/1971 * **Meissner, U.** *Berechnung von Schalen unter großen Verschiebungen und Verdrehungen bei kleinen Verzerrungen mit Hilfe finiter Dreieckselemente.* Dissertation, Techn. Univ. Hannover, 1971
- 04/1972 * **Grotkop, G.** *Die Berechnung von Flachwasserwellen nach der Methode der finiten Elemente.* Dissertation, Techn. Univ. Hannover, Sonderdruck aus dem Jahresbericht 1971 d. SFB 79, H. 2, 1972
- 05/1973 * **Schulze, K.-W.** *Eine problemorientierte Sprache für die Dynamik offener Gerinne.* Dissertation, Techn. Univ. Hannover, Mitteil. d. SFB 79, Heft 1, 1973
- 06/1977 * **Beyer, A.** *Die Berechnung großräumiger Grundwasserströmungen mit Vertikalstruktur mit Hilfe der Finite-Element-Methode.* Dissertation, Fortschrittberichte der VDI-Zeitschriften, Reihe 4, Nr. 34, 1977
- 07/1977 * **Ebeling, H.** *Berechnung der Vertikalstruktur wind- und gezeiten-erzeugter Strömungen nach der Methode der finiten Elemente.* Dissertation, Fortschrittberichte der VDI-Zeitschriften, Reihe 4, Nr. 32, 1977
- 08/1977 * **Gärtner, S.** *Zur Berechnung von Flachwasserwellen und instationären Transportprozessen mit der Methode der finiten Elemente.* Dissertation, Fortschrittberichte der VDI-Zeitschriften, Reihe 4, Nr. 30, 1977
- 09/1977 * **Herrling, B.** *Eine hybride Formulierung in Wasserständen zur Berechnung von Flachwasserwellen mit der Methode finiter Elemente.* Dissertation, Fortschrittberichte der VDI-Zeitschriften, Reihe 4, Nr. 37, 1977
- 10/1979 * **Hennlich, H.-H.** *Aeroelastische Stabilitätsuntersuchung von Linientragwerken.* Dissertation, Fortschrittberichte der VDI-Zeitschriften, Reihe 4, Nr. 49, 1979
- 11/1979 * **Kaločay, E.** *Zur numerischen Behandlung der Konvektions-Diffusions-Gleichung im Hinblick auf das inverse Problem.* Dissertation, Univ. Hannover, 1979

- 12/1980 * **Januszewski, U.** *Automatische Eichung für ein- und zweidimensionale, hydrodynamisch-numerische Flachwassermodelle.* Dissertation, Univ. Hannover, Fortschrittberichte der VDI-Zeitschriften, Reihe 4, Nr. 58, 1980
- 13/1982 * **Carbonel Huamán, C.A.A.** *Numerisches Modell der Zirkulation in Auftriebsgebieten mit Anwendung auf die nordperuanische Küste.* Dissertation, Univ. Hannover, 1982
- 14/1985 **Tuchs, M.** *Messungen und Modellierung am Deep Shaft.* Dissertation, Univ. Hannover, 1984
- 15/1985 **Theunert, F.** *Zum lokalen Windstau in Ästuarien bei Sturmfluten – Numerische Untersuchungen am Beispiel der Unterelbe.* Dissertation, Univ. Hannover, 1984
- 16/1985 **Perko, H.-D.** *Gasausscheidung in instationärer Rohrströmung.* Dissertation, Univ. Hannover, 1984
- 17/1985 **Crotogino, A.** *Ein Beitrag zur numerischen Modellierung des Sedimenttransports in Verbindung mit vertikal integrierten Strömungsmodellen.* Dissertation, Univ. Hannover, 1984
- 18/1985 **Rottmann-Söde, W.** *Ein halbanalytisches FE-Modell für harmonische Wellen zur Berechnung von Wellenunruhen in Häfen und im Küstenvorfeld.* Dissertation, Univ. Hannover, 1985
- 19/1985 **Nitsche, G.** *Explizite Finite-Element-Modelle und ihre Naturanwendungen auf Strömungsprobleme in Tidegebieten.* Dissertation, Univ. Hannover, 1985
- 20/1985 **Vera Muthre, C.** *Untersuchungen zur Salzausbreitung in Ästuarien mit Taylor'schen Dispersionsmodellen.* Dissertation, Univ. Hannover, 1985
- 21/1985 **Schaper, H.** *Ein Beitrag zur numerischen Berechnung von nichtlinearen kurzen Flachwasserwellen mit verbesserten Differenzenverfahren.* Dissertation, Univ. Hannover, 1985
- 22/1986 **Urban, C.** *Ein Finite-Element-Verfahren mit linearen Ansätzen für stationäre zweidimensionale Strömungen.* Dissertation, Univ. Hannover, 1986
- 23/1987 **Heyer, H.** *Die Beeinflussung der Tidedynamik in Ästuarien durch Steuerung – Ein Beitrag zur Anwendung von Optimierungsverfahren in der Wasserwirtschaft.* Dissertation, Univ. Hannover, 1987
- 24/1987 * **Gärtner, S.** *Zur diskreten Approximation kontinuumsmechanischer Bilanzgleichungen.* Institutsbericht, davon 4 Abschnitte als Habilitationsschrift angenommen, Univ. Hannover, 1987
- 25/1988 **Rogalla, B.U.** *Zur statischen und dynamischen Berechnung geometrisch nichtlinearer Linientragwerke unter Strömungs- und Wellenlasten.* Dissertation, Univ. Hannover, 1988
- 26/1990 * **Lang, G.** *Zur Schwebstoffdynamik von Trübungszonen in Ästuarien.* Dissertation, Univ. Hannover, 1990

- 27/1990 **Stittgen, M.** *Zur Fluid-Struktur-Wechselwirkung in flexiblen Offshore-Schlauchleitungen.* Dissertation, Univ. Hannover, 1990
- 28/1990 * **Wollrath, J.** *Ein Strömungs- und Transportmodell für klüftiges Gestein und Untersuchungen zu homogenen Ersatzsystemen.* Dissertation, Univ. Hannover, 1990
- 29/1991 **Kröhn, K.-P.** *Simulation von Transportvorgängen im klüftigen Gestein mit der Methode der Finiten Elemente.* Dissertation, Univ. Hannover, 1991
- 30/1991 **Lehfeldt, R.** *Ein algebraisches Turbulenzmodell für Ästuar.* Dissertation, Univ. Hannover, 1991
- 31/1991 * **Prüser, H.-H.** *Zur mathematischen Modellierung der Interaktion von Seegang und Strömung im flachen Wasser.* Dissertation, Univ. Hannover, 1991
- dito * **Schröter, A.** *Das numerische Seegangmodell BOWAM2 1990 – Grundlagen und Verifikationen – .* Univ. Hannover, 1991
- 32/1992 **Leister, K.** *Anwendung numerischer Flachwassermodelle zur Bestimmung von Wasserlinien.* Dissertation, Univ. Hannover, 1992
- 33/1993 **Ramthun, B.** *Zur Druckstoßsicherung von Fernwärmenetzen und zur Dynamik von Abnehmeranlagen.* Dissertation, Univ. Hannover, 1993
- 34/1993 * **Helmig, R.** *Theorie und Numerik der Mehrphasenströmungen in geklüftet-porösen Medien.* Dissertation, Univ. Hannover, 1993
- 35/1994 **Plüß, A.** *Netzbearbeitung und Verfahrensverbesserungen für Tidedemodelle nach der Finiten Element Methode.* Dissertation, Univ. Hannover, 1994
- 36/1994 **Nöthel, H.** *Statistisch-numerische Beschreibung des Wellen- und Strömungsgeschehens in einem Bühnenfeld.* Dissertation, Univ. Hannover, 1994
- 37/1994 **Shao, H.** *Simulation von Strömungs- und Transportvorgängen in geklüfteten porösen Medien mit gekoppelten Finite-Element- und Rand-Element-Methoden.* Dissertation, Univ. Hannover, 1994
- 38/1994 **Stengel, T.** *Änderungen der Tidedynamik in der Deutschen Bucht und Auswirkungen eines Meeresspiegelanstiegs.* Dissertation, Univ. Hannover, 1994
- 39/1994 **Schubert, R.** *Ein Softwaresystem zur parallelen interaktiven Strömungssimulation und -visualisierung.* Dissertation, Univ. Hannover, 1994
- 40/1994 **Alm, W.** *Zur Gestaltung eines Informationssystems im Küsteningenieurwesen.* Dissertation, Univ. Hannover, 1994
- 41/1994 **Benali, H.** *Zur Kopplung von FEM- und CAD-Programmen im Bauwesen über neutrale Datenschnittstellen.* Dissertation, Univ. Hannover, 1994
- 42/1995 **Schröter, A.** *Nichtlineare zeitdiskrete Seegangssimulation im flachen und tieferen Wasser.* Dissertation, Univ. Hannover, 1995

- 43/1995 **Blase, Th.** *Ein systemtechnischer Ansatz zur Modellierung von Hydraulik, Stofftransport und reaktionskinetischen Prozessen in Kläranlagen.* Dissertation, Univ. Hannover, 1995
- 44/1995 **Malcherek, A.** *Mathematische Modellierung von Strömungen und Stofftransportprozessen in Ästuaren.* Dissertation, Univ. Hannover, 1995
- 45/1995 **Lege, T.** *Modellierung des Kluftgesteins als geologische Barriere für Deponien.* Dissertation, Univ. Hannover, 1995
- 46/1996 **Arnold, H.** *Simulation dammbruchinduzierter Flutwellen.* Dissertation, Univ. Hannover, 1996
- 47/1996 **Kolditz, O.** *Stoff- und Wärmetransport im Kluftgestein.* Habilitation, Univ. Hannover, 1996
- 48/1996 **Hunze, M.** *Numerische Modellierung reaktiver Strömungen in oberflächenbelüfteten Belebungsbecken.* Dissertation, Univ. Hannover, 1996
- 49/1996 **Wollschläger, A.** *Ein Random-Walk-Modell für Schwermetallpartikel in natürlichen Gewässern.* Dissertation, Univ. Hannover, 1996
- 50/1997 **Feist, M.** *Entwurf eines Modellierungssystems zur Simulation von Oberflächengewässern.* Dissertation, Univ. Hannover, 1997
- 51/1997 **Hinkelmann, R.** *Parallelisierung eines Lagrange-Euler-Verfahrens für Strömungs- und Stofftransportprozesse in Oberflächengewässern.* Dissertation, Univ. Hannover, 1997
- 52/1997 **Barlag, C.** *Adaptive Methoden zur Modellierung von Stofftransport im Kluftgestein.* Dissertation, Univ. Hannover, 1997
- 53/1997 **Saberi-Haghighi, K.** *Zur Ermittlung der verformungsabhängigen Windbelastung bei Hängedächern.* Dissertation, Univ. Hannover, 1997
- 54/1998 **Krüger, A.** *Physikalische Prozesse im Nachklärbecken – Modellbildung und Simulation.* Dissertation, Univ. Hannover, 1998
- 55/1998 **Wolters, A. H.** *Zur Modellierung des instationären thermohydraulischen Betriebsverhaltens von Fernwärmeanlagen.* Dissertation, Univ. Hannover, 1998
- 56/1999 **Jankowski, J. A.** *A non-hydrostatic model for free surface flows.* Dissertation, Univ. Hannover, 1999
- 57/1999 **Kopmann, R.** *Mehrdimensionale Effekte in dimensionsreduzierten Gewässergütemodellen.* Dissertation, Univ. Hannover, 1999
- 58/1999 * **Kahlfeld, A.** *Numerische Seegangmodellierung als Bestandteil einer funktionellen Hafenplanung.* Dissertation, Univ. Hannover, 1999
- 59/1999 *Festschrift zum 60. Geburtstag von Prof. Dr.-Ing. Werner Zielke.* Univ. Hannover, 1999
- 60/2000 * **Kolditz, O., Zielke, W., Wriggers, P., Dürbaum, H.-J., Wallner, M.** *3. Workshop Kluft-Aquifere - Gekoppelte Prozesse in Geosystemen.* Univ. Hannover, 2000

- 61/2001 * **Malcherek, A.** *Hydromechanik der Fließgewässer.* Habilitation, Univ. Hannover, 2001
- 62/2001 **Thorenz, C.** *Model Adaptive Simulation of Multiphase and Density Driven Flow in Fractured and Porous Media.* Dissertation, Univ. Hannover, 2001
- 63/2001 **Kaiser, R.** *Gitteradaption für die Finite-Elemente-Modellierung gekoppelter Prozesse in geklüftet-porösen Medien.* Dissertation, Univ. Hannover, 2001
- 64/2001 **Rother, T.** *Geometric Modelling of Geo-Systems.* Dissertation, Univ. Hannover, 2001
- 65/2001 **Habbar, A.** *Direkte und inverse Modellierung reaktiver Transportprozesse in klüftig-porösen Medien.* Dissertation, Univ. Hannover, 2001
- 66/2002 * **Weilbeer, H.** *Strömung und Kolkung an Wasserbauwerken.* Dissertation, Univ. Hannover, 2002
- 67/2002 **Hoyme, H.** *Mesoskalige morphodynamische Modellierungen am Beispiel der Meldorfer Bucht.* Dissertation, Univ. Hannover, 2002
- 68/2004 **Moenickes, S.** *Grid generation for simulation of flow and transport processes in fractured porous media.* Dissertation, Univ. Hannover, 2004
- 69/2004 **Strybny, J.** *Ein phasenauflösendes Seegangmodell zur Ermittlung von Bemessungsparametern für Küstenstrukturen.* Dissertation, Univ. Hannover, 2004
- 70/2004 **Weilbeer, J.** *Modellierung des Partikeltransports in Nachklärbecken als Mehrphasenströmung.* Dissertation, Univ. Hannover, 2004
- 71/2006 **Mittendorf, K.** *Hydromechanical Design Parameters and Design Loads for Offshore Wind Energy Converters.* Dissertation, Leibniz Universität Hannover, 2006
- 72/2006 **Kohlmeier, M.** *Coupling of thermal, hydraulic and mechanical processes for geotechnical simulations of partially saturated porous media.* Dissertation, Leibniz Universität Hannover, 2006
- 73/2006 **Schumacher, S.** *Leistungsbestimmende Prozesse in Nachklärbecken - Einflussgrößen, Modellbildung und Optimierung.* Dissertation, Leibniz Universität Hannover, 2006